NNT : 2016SACLC067

THESE DE DOCTORAT
DE
L'UNIVERSITE PARIS-SACLAY
PRÉPARÉE À
CENTRALESUPELEC

ECOLE DOCTORALE N°575 EOBE
Electrical, optical, bio-physics and engineering

Spécialité de Doctorat
Genie électrique

Par

M. Moussa KAFAL

Imaging techniques for soft fault location in different wiring networks

Thèse présentée et soutenue à Gif-sur-Yvette, le 20 Septembre 2016 :

Composition du Jury :

M. Yann Le Bihan	Professeur des Universitaires, GeePs	Président
M. Philippe Besnier	Directeur de recherche au CNRS, IETR	Rapporteur
M. Julien De Rosny	Directeur de recherche au CNRS, Langevin	Rapporteur
Mme. Maud Franchet	Ingénieur de recherche, EDF	Examinatrice
M. Andrea Cozza	Professeur, CentraleSupélec	Directeur de thèse
M. Lionel Pichon	Directeur de recherche au CNRS, GeePs	Co-directeur de thèse

Acknowledgements

This is an articulated very emotional moment of my life where I am moving from one stage to another. This long journey wouldn't have seen the light without those who have embraced me with their support, encouragement, confidence, friendship, affection, patience and love.

My thesis was held at the Laboratory of the Group of electrical engineering, Paris (GeePs) in the Department of research in Electromagnetism (DRE) at CentraleSupélec. I would first like to thank Prof. Claude Marchand, research director at the CNRS and the director of GeePs laboratory in addition to the direction of CentraleSupélec, firstly for hosting me during my thesis and, secondly, for providing me with the necessary conditions and good ambiance for my work.

I would like to express my deep gratitude to Prof. Andrea Cozza, my thesis director and supervisor. Thank you first for giving me the opportunity to enroll with your research team as a Ph.D student and for enlightening me the first glance of research. Thank you for your devoted time to guide me throughout these three years. Thank you for your invaluable advice, ongoing support, and endless patience. Thank you for your modesty and temperance at both the intellectual and human level. I had a great pleasure and honor to work with such an outstanding researcher as you.

My sincere thanks to my thesis co-director, Prof. Lionel Pichon, for his trust in me with this research work. Thank you for your help and valuable comments. Thank you for your availability, support and kindness.

I would like also to thank Prof. Philippe Besnier, research director at the CNRS in the IETR laboratory, and Prof. Julien De Rosny, research director at the CNRS at the Langevin institute for accepting to be the reviewers of my thesis manuscript. I would like to equally thank Prof. Yann Le Bihan, universities' professor at GeePs laboratory, and Dr. Maud Franchet, research engineer at EDF for giving me the pleasure of taking the role of the examiners in my defense.

The acknowledgment list elongates but I'll still take a few more lines to extend my thanks to all members of L2S and GeePs laboratories. So I would like to thank Mohammed Serhir, Florian, Laurence, Marc, Christopher, Frederic, Vincent, Safaa, Henri, Philippe, Giacomo, Takis, Mouad, Mohamed Farouq, Hidayet and of course my office mates Pierre-luc and Serge. I have surely forgotten

some because the list is long, but I thank all those whom I might have omitted to mention. I am really grateful to all the scientific and non-scientific discussions we had (at table for lunch, coffee break,...). You were a real great daily support.

Well, I would like also to catch the opportunity to thank Mahmoud and Jad for their support, advice and nice discussions. Big thanks for Mohammad Toufayli, Elie, Moustafa, Issa, Fatima, and Soukna for your friendship, which is so dear to me, thank you for your solidarity, thank you for these wonderful years we spent together, thank you for all those unforgettable moments, you have been really my second family in France. Thanks also to Mohammad koteich, Azary, Mohammad Ayoub, Hassan Cheaito, Lama, and many other friends I got to know during my stay in France. Although the list of friends became so long, but I can't miss to thank Abdallah, Hasan Termos and Haidar Taki for their brotherhood friendship.

All this little dream would have never been possible without the love, trust, and support of my family. I am so grateful to my dear dad Ahmad and my dearest mom Huda for their immense love and encouragement, for their continuous support and patience. Thank you for being by my side with all my successes and my failures without distinction. Thank you for giving me so much joy and warmth of life. Thank you for always been there for me. Thank you for teaching me to never give up. And To you, my dear sister Douja and my dearest brothers Kassem and Ibrahim, big thanks for every lovely moment we had together.

Last but not least, I would like to express my greatest gratitude to my future wife Zahraa. Your support, encouragement, quiet patience and unwavering love were undeniably the bedrock upon which the past ten months of my life have been built. Your tolerance of my occasional vulgar moods is a testament in itself of your unyielding devotion and love. I shall thank you for the patience to endure my worst faults, mood swings, negligence, vanities, my fears and my doubts. Thank you for being my life.

Finally, I thank my GOD who has filled me with His gifts, for the inexhaustible mercy, power and blessings He afforded me. In the major storms, I have been always able to anchor in His hands! Thank You ! I would like to thank also the unknown soldiers of God on earth, whom if not of them I wouldn't have been able to be where I am standing right now.

The doctoral journey has been a wonderful and enriching experience for me, but also a long, painful marathon at some time. Finally, I leave you with these simple words:

"***Do not let your difficulties fill you with anxiety, after all it is only in the darkest nights that stars shine more brightly***"

-Ali Ibn Abu-Talib-

Contents

List of Figures

List of Tables

General Introduction

Issues and Context

Electrical cables are everywhere in many fields where the transfer of energy and information is necessary to guarantee a proper functioning and a good performance of a system. In the last few decades, we have witnessed a paradigm shift of hydraulic, pneumatic, mechanical, control and auxiliary systems in most of nowadays appliances to electrical systems. In fact, this increasing usage of electrical components was accompanied by an increase in the demand of electrical cables, where they can be found in transportation systems, industrial machinery, power plants, infrastructures, in addition to most of today's human facilities and utilities. For instance, the cumulated length of electrical wires in a modern car is more than 4 km, compared to a few hundred meters 30 years ago, higher than 40 km in modern fighter aircrafts, it is close to 200 km in high speed trains and 400 km in recent civil planes and can be estimated around 5000 km in a nuclear power plant. Considering more than 40000 km of railways in a large country, one can see that this kind of infrastructure can use almost 1 million km of electrical cables. Consequently, electrical wires are playing a primary role where wiring networks have become fundamental subsystems whose proper functioning is of critical importance.

One day or another, a cable in a network will show signs of weakness attributed to either external reasons, as chemical contamination, mechanical aggression, etc., or due to internal causes manifested by manufacturing defects, local heating, etc. Among the most often met wiring faults are short and open circuits which are usually referred to as *hard faults*, and are characterized by the fact that they prevent any signal from going further away. On the other side, any minor alteration that affects a cable is classified as a *soft fault* namely insulation damage, cracks etc.; these can be of very different kinds and are more difficult to detect. Besides, they are a preliminary step towards the occurrence of *hard faults*.

In many systems, a great number of electrical wires are dedicated to safety and control operations, thus any shortening in their performance due to the appearance of a defect might be highly expensive in terms of lives and from an economical aspect. Particularly, the National Transportation Safety Board (NTSB) investigation revealed that it was the electrical wiring fault that caused the Boeing 747 TWA Flight 800 disaster in 1996 and the crash of a Swissair MD-11 in 1998 taking the lives of hundreds of passengers. Unfortunately, wiring faults have been accounted as the major reason behind fires in human occupied and non-occupied facilities where in 2014, there were 1,298,000 fires reported in the United States of America, causing 3,275 civilian deaths, 15,775 civilian injuries, and $11.6 billion property damage.

Accordingly, ensuring the reliable use of cables requires the availability of techniques capable of detecting the presence of faults that could potentially put in jeopardy a whole system. One estimate is that highly trained technicians spend between 1 million to 2 million man-hours each year at the operational level to troubleshoot and repair wiring system problems in the U.S navy alone. In fact, techniques relying on the human senses' intervention (visual inspection, X-ray methods, etc.) have shown to be time consuming, highly expensive and inefficient in most of the cases. Consequently, the need for novel techniques dedicated to accurately locate faults in cables became persistent, where several methods have evolved throughout the last few decades including low frequency and DC methods, capacitive and inductive methods, medium frequency techniques in addition to several other techniques. Despite the fact that several electric and non-electric wire diagnosis methods have been studied and developed throughout the last few decades, reflectometry-based techniques are still in the center stage of research and industrial applications in this domain. They have been introduced since the middle of the twentieth century, where their general concept rely on the propagation of an electromagnetic waveform in the wire network to be tested, followed by monitoring the reflected one in order to detect the presence, position, and nature of an impedance discontinuity. Depending on the domain of analysis of the reflected wave, reflectometry methods can be categorized into two main families: Time Domain Reflectometry (TDR) and Frequency Domain Reflectometry (FDR). They have been providing effective results with hard faults due to their high reflection coefficients, but have shown to be less reliable whenever soft faults are addressed. As a matter of fact, soft faults are usually characterized by weak reflectiveness which produce echoes that can pass unnoticed compared to those caused, e.g., by junctions within a network under test, particularly when noisy conditions are present, e.g., in live testing. Add to that, they showed weakness with complex networks as multiple echoes in the reflected signal, resulting from the presence of junctions and impedance discontinuities in the network, mask the signature of an eventual fault. Furthermore, the detection of multiple faults is also mostly limited to hard faults.

Thesis Objective

Based on a radically different concept, the DORT method, standing for decomposition of the time reversal operator, was originally developed in acoustics as a remote-sensing technique for the detection and location of scatterers within homogeneous media. Basically, it allows defining signals bound to focus on one of the scatterers, thus providing a visual method for inferring the position of a previously unknown scatterer. This idea was recently transposed to guided-wave propagation, e.g., wire networks, and shown to precisely detect and locate single soft faults even within complex network configurations. On the other hand, while passing from a single scatterer to several is trivial with waves propagating in homogeneous media, we will show in this thesis that in the case of wire networks this is no longer true. Multiple faults cannot be resolved separately, because of their strong coupling via guided propagation.

The objective of this thesis is to propose new approaches that aim at locating single as well as multiple soft faults in different complexity networks. The standard DORT method will be recalled, where we will present the process of obtaining testing signals from the network's scattering matrix that once injected into the network's model will lead to focal spots aiming to locate the position of the fault. As mentioned earlier several limitations hindered the standard version of DORT from locating multiple faults in wiring configurations, henceforth an alternative formulation of the DORT based on an updating scheme is proposed. Notably, this novel approach, referred to as EDORT, allowed extracting the signature of each fault solely which is characterized by its corresponding single-fault scattering matrix from the multiple faulty scattering matrix initially measured. The input signals used for imaging the faults were shown to focus selectively on single faults, allowing a clear identification. No spurious focusing was observed, thus reducing the probability of false alarms. Experimental validations also confirmed these conclusions, when considering both very weak faults and non-trivial network layouts. These results give credibility to the practical usefulness of the proposed method in critical real-life configurations that are hardly addressed in current literature. In addition to that, the proposed procedure allowed an accurate estimate of the severity of each fault, a feature of practical interest when monitoring the state of a cable in a wiring network. Notably, the proposed method has shown a remarkable robustness in the presence of noise proving a significant applicability in noisy measuring environments of signal-to-noise ratio (SNR) below 0 dB. Besides, this efficiency improved when the network's complexity increased. Additionally, DORT method has shown to be tolerant against changes in the lengths of cables composing the network models used for the injection of the testing signals.

On the other hand, any method based on time-domain analysis, belonging to TDR or DORT methods, relies on the availability of potentially large bandwidths, in order to create the conditions for spatial resolution. Limitations are thus introduced by the ability of cables in a network under test to support low bandwidths, as in the case of low-frequency networks such as power grids. With this background in mind, we studied the possibilities offered by time-reversal (TR) multiple signal classification, also known as TR-MUSIC. It has already been applied with success to other detection problems and appears to bring an effective answer to all of the limitations recalled so far. TR-MUSIC is mainly applied for detecting and locating scatterers in a background medium; indeed, soft faults can also be treated as weak scatterers. The most striking feature of TR-MUSIC is that it ensures *sub-wavelength spatial resolution* while working on a single-frequency basis. Besides, it is by far less sensitive to fault coupling prior to multiple faults and returns *super-resolution* estimates for their locations.

TR-MUSIC shares the same foundations as DORT-based methods, namely, the availability of a multistatic (or multiport) characterization of the wiring network, but they follow two distinguished ways to translate multistatic data into a fault position. DORT-based methods use a sub-space approach in defining signals that, once fed into a numerical model of the network, will focus back to the position of a fault; this propagation phase is carried out in the time domain, and therefore undergo most of the same limitations of any other time-domain method, particularly the need for large bandwidth to create spatial resolution. On the contrary, TR-MUSIC, does operate on a different sub-space approach, based on the Green function of the network; no back-propagation phase is used and actually a correlation process is defined. TR-MUSIC operates on phase patterns provided by Green function as a mean of identifying positions in a complex medium. The performance of TR-MUSIC is studied for detecting and locating single as well as multiple soft faults in different network configurations. Experimental results confirm the practical potential of this novel approach. TR-MUSIC is also shown to allow retrieving the reflection coefficient of each fault, thus giving a direct evaluation of the risk they pose to the integrity of the network. This step is accomplished without having to measure the reflections of test signals, as no test signal is used in TR-MUSIC. It is important to point out that TR-MUSIC has also shown a great robustness towards noisy measured scattering data proving its feasibility of working in environments of low SNR.

Thesis Organization

The following thesis is composed of five chapters.

Chapter 1 presents an overview of the context of our study, starting with defining electrical cables, their types and their fields of application, followed by introducing the main reasons behind the appearance of wiring faults. After that, we will list some of the consequences that these cable defects led to along with introducing the most common methods used for investigating the wire health. The general principle of reflectometry techniques will be presented with their different varieties, along with illustrating their major advantages and limitations.

Chapter 2 is dedicated to build the basis that will allow understanding the proposed methods namely the principles of wave propagation along transmission lines. In fact, the concepts and tools we used to model and simulate the guided propagation will be described. We will recall the transmission line theory tools that are going to be needed in our study, and also multiport modeling using the S-parameter matrices used to define our simulator. Space-time and energy diagrams are also introduced; they represent the tools we adopted to observe voltage propagation and energy in the tested networks thus facilitating the development of the fault location criteria. Finally in this chapter the use of the *difference system* in the case of soft is discussed, which is a method first introduced in acoustics for removing the effect of clutter from the medium containing a weak target. This is accomplished after establishing a comparison between the free-space propagation and the guided propagation case, where we will also present the drawbacks of not having a perfect *difference system* on the applicability of soft fault location techniques.

Chapter 3 will focus on the concepts of time reversal in free-space while presenting two of its major methodologies: DORT method and TR-MUSIC techniques. For instance, we will address the theoretical basis of these two methods, their areas of applications and the merits and demerits they endure.

Chapter 4 addresses the adaptation of DORT method from free space to guided wave propagation along transmission lines. The standard version of DORT (SDORT) will be recalled while showing its feasibility in locating single soft faults in different complexity networks. This will be followed by illustrating the limitations it faced when multiple faults occur in a wiring configuration, after which we will introduce a formal mathematical analysis on the separation of the multiple faulty scattering matrix into single-fault ones. After that, an assessment of the procedure of retrieving the fault's reflection coefficient will be presented. Based on this analysis, we will examine the alternative DORT method (EDORT) while showing its different steps, which allowed detecting and locating multiple soft faults in different complex networks. In fact, this will be validated numerically and experimentally. This will be followed by showing the results that intend to compute the severities of the soft faults of the tested networks. The last part of this chapter, will be dedicated to handle the robustness and tolerance of DORT method towards noise and model cable length changes.

Chapter 5 deals with the application of TR-MUSIC to transmission lines and the *super resolution* results obtained with continuous wave excitation signals on the accurate detection and location of single as well as multiple soft faults in different networks under test. A numerical and experimental study will validate the novel approach. This is accompanied by presenting the process followed for computing the faults' reflection coefficients while presenting their corresponding results. Last but not least, an assessment of the robustness of TR-MUSIC to noise will be examined.

Chapter 1

State of the Art

Contents

1.1 Introduction

In the last few decades, we have witnessed a huge paradigm reckoning on the extensive use of electrical cables in nearly all modern systems. They played a primary role in energy and signal distribution where wiring networks became fundamental subsystems whose proper functioning is of critical importance. In this first chapter we are going to present the main applications that rely on the presence of healthy cables where we will be listing briefly the increasing demand on the cumulative lengths of cables in today's systems. This will be accompanied with presenting the different types of cables present nowadays with their fields of applications, after which we are going to introduce the types of faults that threaten the healthy situation of a cable. Accordingly, the negative impacts, whether economical or human wise consequences, resulting from the deterioration of these wiring defects will be shed light on. In fact, the serious jeopardy wiring faults led to, necessitated the development of techniques capable of providing an early detection and location of them. Notably, we will present two main groups of such techniques some of which are non-reflectometry based while others are the well known reflectometry techniques. Finally, a comparison is done between different fault detection and location methods.

1.2 Electrical Cables

Getting an electrical signal from point A to point B is pretty a standard thing. Put a piece of copper wire between A and B and the job is done. A century of development has left us with increased specialization in wiring, connection devices, and everything in between point A and B. In particular, the first known typical electrical cable satisfying this job ages back to 1892, when Thomas Edison, an American inventor, filed a U.S patent [1] shown in Fig. 1.1, of what he called an electrical conductor surrounded by insulating material which is resistant to both fire and moisture.

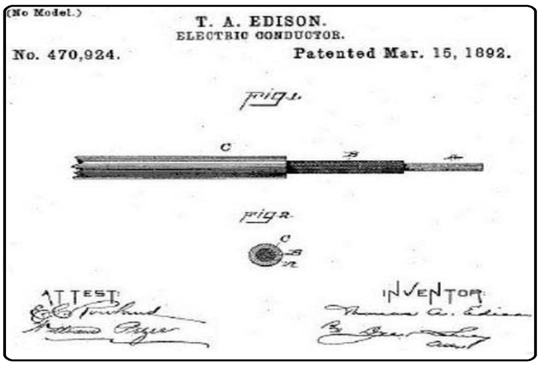

Figure 1.1 The first known electrical cable invented by Thomas Edison in 1892. *Source: [1]*

As a matter of fact, the emergence of electrical employments geared the indispensable use of electrical cables in nearly all modern systems. They became their backbone structures where it won't be an exaggeration to resemble them as the nerves and veins of a human body. Signals, commands and power are delivered to their destinations via these wires whose presence is vital for the transfer of energy and information that is necessary to guarantee the normal functioning and optimal performance of a system.

Electrical cables are everywhere in many fields where their presence is not limited to transportation systems, nuclear power plants, industrial machinery, human facilities, infrastructure and buildings. The increasing complexity accompanied with modern systems such as that in the automotive and avionics industry have witnessed a huge reckoning on the extensive use of electrical wires. For instance, todays vehicles are no longer equipments used just for transporting individuals, on the contrary they have included leisure and entertainment facilities (AC, radio, TV, navigation systems, etc.) which necessitate the presence of wiring networks. Besides, in the last few years we are witnessing an evolution to a new concept in the automotive industry better known as the *X-by-wire* technology which is based on the usage of electrical or electro-mechanical systems (motor, ABS brakes, etc) for performing vehicle functions traditionally achieved solely by mechanical linkages. Fig. 1.2 is a demonstration of an electrical cable network in a typical modern car showing bundles of long cables with their connectors, where statistics conducted have shown that about 35% of the total vehicle infrastructure is electrical based. Consequently, from few hundred of meters in vehicles few decades ago, modern cars contain about 4 km, in fact, wire lengths have also increased to several hundred km in civil and military airplanes which even escalates in transport ships to more than 1200 Km. The demonstration of Fig. 1.3 describes the evolution of cable lengths in different transport systems. Moreover, estimates have shown that about 5000 km are present in a nuclear power plant which can skyrocket to 40000 km of cables in railway infrastructures of large countries, one can see that the later kind of infrastructure can use almost 1 million km of electrical wires [10]. All these examples, show that the massive use of wiring networks in nowadays systems became crucial.

Generally, we can differentiate between cables depending on the nature of the transmitted signals which can be either analog or digital [11], having low or high power, propagating at low, medium or high frequencies. Another key point is the environment in which the cable is placed which can widely vary between air, as for power transmission networks, the sea, as internet cables, or underground as for power cables [12]. It is worthy to note here that the paradigm shift in the technology of semiconductors led to a huge development in computers and smart systems which are extensively used in every application. Notably, these applications use two main types of cables: the coaxial [13] and the twisted pair cables [14]. Significantly, an aircraft as the Airbus A340 presented in Fig. 1.4 could contain a large variety of a big number of different cable types.

In general, there exist three main types of cables: power, coaxial and twisted pair cables. Power cables are usually used for the transmission of electrical power at high voltage, whether in the AC or DC mode. They originate from power plants to distribution stations which are responsible for supplying this electrical power to different electricity using facilities. Underground power cables as the ones presented in Fig. 1.5 (b) clearly show that they have big cross-sections. Each unit as

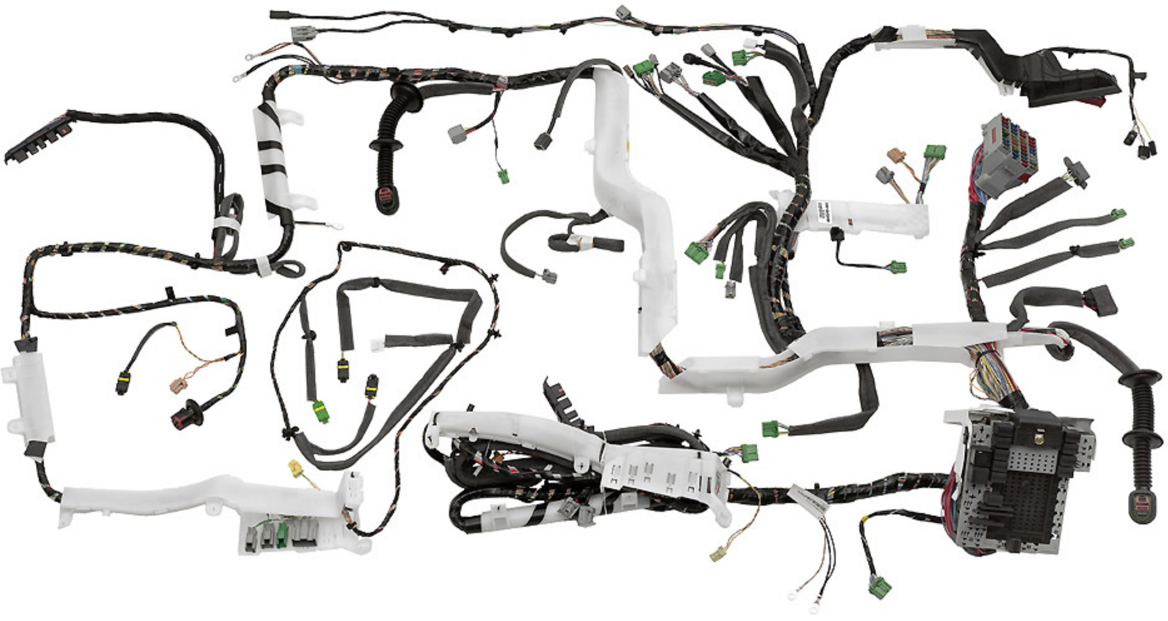

Figure 1.2 A complete network of electrical cables of a typical modern car with bundles of cables in addition to their connectors referred to as the automotive wire harness. *Source: [2]*

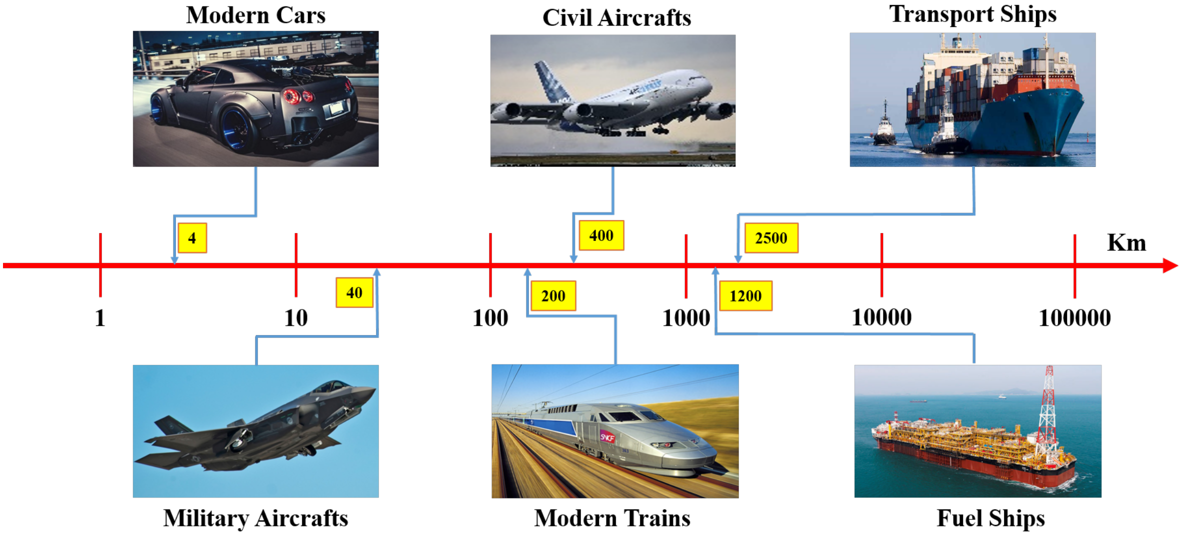

Figure 1.3 Cumulated lengths of electrical cables in transportation systems.

detailed in Fig. 1.5 (a), is fundamentally composed of several conductor lines in the core, in addition to various shielding insulation which are responsible of providing a high level of protection against corrosion or external damage.

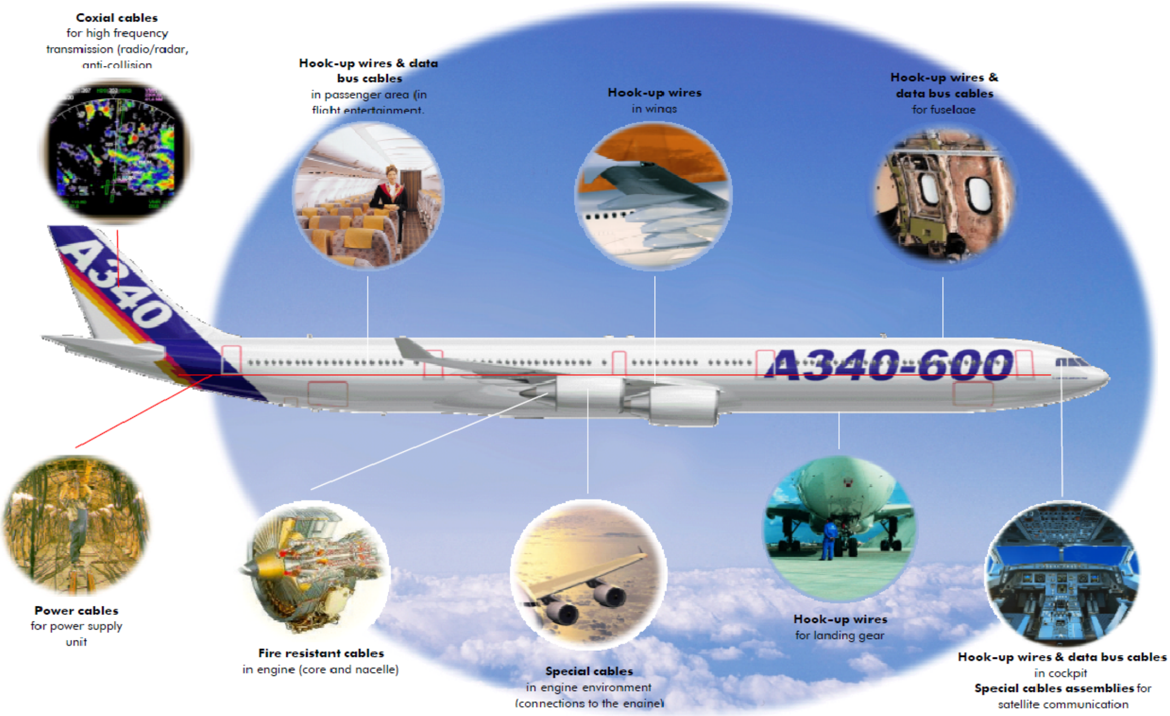

Figure 1.4 A map showing different cable types with their function in an airbus A340 aircraft. *Source: [2]*

Twisted pair cables were first introduced by Alexander Graham Bell in 1881 [15], for telephone applications. Basically, a twisted pair is the ordinary copper wire that connects home and many business computers to the telephone company [14]. To reduce crosstalk or electromagnetic induction (EMI) between pairs of wires, two insulated copper wires are twisted around each other, where each connection on a twisted pair requires both wires (a forward and a return conductor of a single circuit). Since some telephone sets or desktop locations require multiple connections, twisted pair is sometimes installed in two or more pairs, all within a single cable. For some business locations, twisted pair is enclosed in a shield that functions as a ground. This is known as the shielded twisted pair (STP) cable used typically in Token Ring networks as shown in Fig. 1.6 (b), whereas, the unshielded twisted pair (UTP) is the ordinary wire used in ethernet networking as demonstrated in Fig. 1.6 (a). While the twisted pair cable is used by older telephone networks and is the least expensive type of local area network (LAN) cable, most networks still contain some twisted-pair cabling at some point along the network. Other types of cables used for LANs include fiber optic cables and coaxial cables.

In general, a coaxial cable is a type of cable that has an inner conductor surrounded by a tubular insulating layer, which is in turn surrounded by a tubular conducting shield. In general, many coaxial cables have an insulating outer sheath or jacket covering the conducting shield for protection purposes as demonstrated in Fig. 1.6 (c). In particular, the term coaxial comes from the fact that

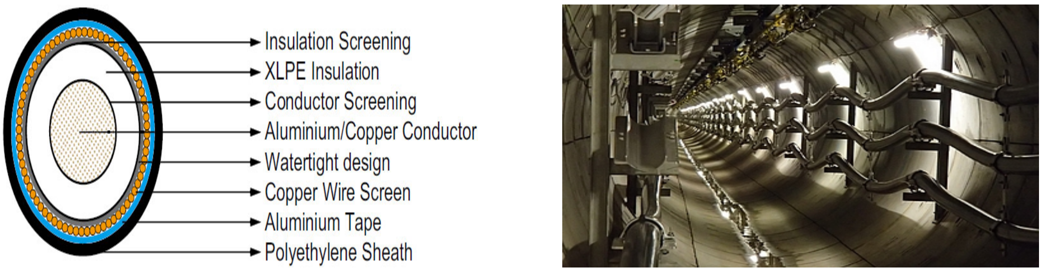

(a) (b)

Figure 1.5 A High voltage power cable where: (a) shows a cross-sectional cut displaying all elements it is composed of, (b) displays bundles of underground power lines.

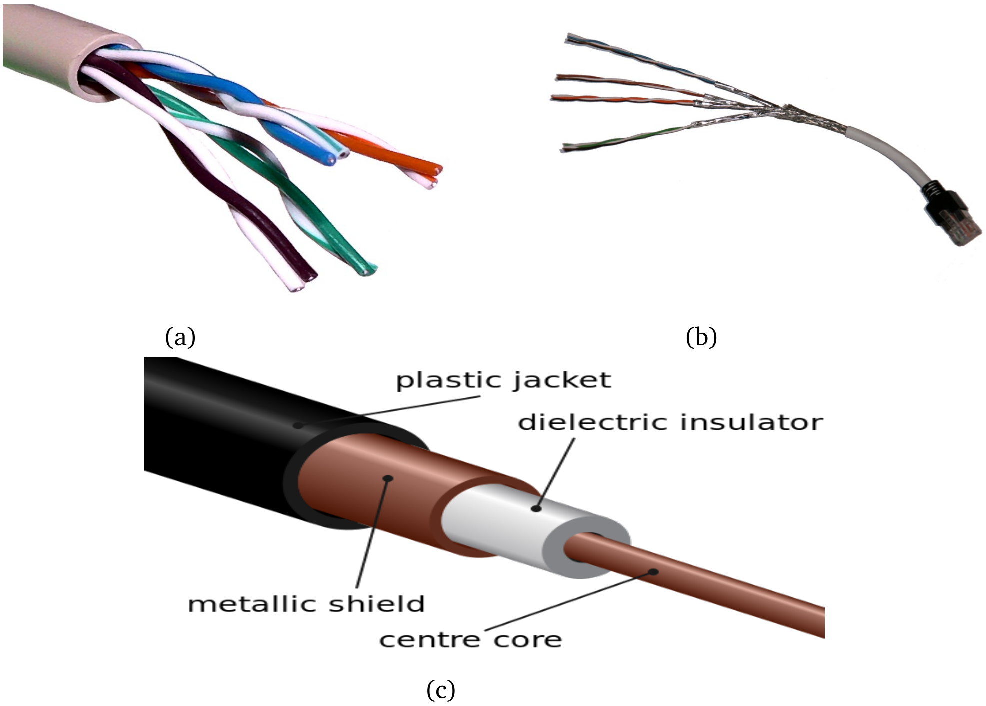

(a) (b)

(c)

Figure 1.6 The twisted pair and coaxial cables, where: (a) shows the unshielded twisted pair (UTP), (b) presents the shielded twisted pair cable (STP), while (c) demonstrates a front cut of the coaxial cable showing its different elements. *Source: wikipedia*.

the inner conductor and the conducting shield share the same geometric axis. It was invented by an English engineer and mathematician Oliver Heaviside, who patented the design in 1880 [16]. In fact, the dimensions of the coaxial cable which are controlled to give a precise, constant conductor spacing, that is needed to provide an efficient function resembling a transmission line, creates the difference compared to other shielded cables used for carrying lower-frequency signals. Coaxial cables are mainly used as transmission lines for radio frequency signals. Their applications include feedlines connecting radio transmitters and receivers with their antennas, computer network (Internet) connections, digital audio (S/PDIF), and distributing cable television signals. Most coaxial cables have a characteristic impedance of either 50, 52, 75, or 93 Ω, where the RF industry uses standard type-names for coaxial cables. For instance, RG-6 is the most commonly used coaxial cable for home use, RG-7 is used for television, satellite television and cable modems, etc. We can differentiate several types of coaxial cables, where there exists hard lines used in broadcasting as well as many other forms of radio communication, radiating lines, tri and twin axial cables, semi rigid cables in addition to rigid coaxial cables.

It is worthy to note here that in our numerical model we used uniform two-wire transmission lines in order to validate the proposed methods for locating faults, while coaxial cables were used in the experimental measurements. Notably, the latter kind of cables allowed comparing the experimental results with the numerical ones, besides they have connectors compatible with most vector network analyzers used for measurements. Furthermore, creating faults was feasible and controllable using such kind of cables especially the semi-rigid coaxial ones as will be explained later in the coming chapters.

It can be realized from the presented examples that the massive use of wiring networks in nowadays systems became essential, especially that some of these cables are integrated in control and safety operations of many of these systems. On the other hand, one day or another, a cable in a network will show signs of weakness or aging leading to the appearance of defects. These anomalies can be the origin of dysfunctions and imply serious consequences for the system or the environment. In fact these defects, hereafter referred to as wiring faults, can be categorized in two main families: hard or soft faults. In the next section, we will illustrate the main reasons behind the occurrence of each of them and present later on the techniques used to detect such kinds of faults throughout history.

1.3 Wiring Faults

Despite the fact that cable manufactures have paid lots of research and efforts to protect cables against damaging factors, wires are still subject to unwanted modifications and breakdowns. In many sectors, a great number of embedded systems dedicated to safety and comfort, communicate with increasingly important data rates in order to fulfill severe real-time constraints. These constraints imply to have at disposal a trustworthy physical support to guarantee both quality of service and reliability. Depending on the areas of application, the consequences of such a performance degradation might be catastrophic and fatal especially when it comes to areas inhabited by humans.

In fact, statistics showed that over 90% of home, building, and factory fires are attributed to electrical caused fires, although it is not totally clear how many are due to installed wiring faults, it can be still inferred that most of them result from similar defects [4]. On the other hand, studies conducted on the avionics industry indicated that the crashes of both TWA 800 off New York's Long Island in 1996 and Swissair 111 near Nova Scotia in 1998 were strongly correlated to the faulty wiring systems onboard [17]. With an average age of more than 22 years [18], the aviation industry fleet is suffering from readiness problems. Many of the aircrafts and spacecrafts have served well beyond the age they were designed for, which is typically 15 to 20 years, leading to the appearance of a big variety of wiring faults as demonstrated in the pie chart of Fig. 1.7. The virtually invisible wire faults make these aged work horses prone to disasters. Although wire faults are found more frequently in aging aircraft, newer designs are not immune to wiring problems. Airbus's flagship A380, for example, had to delay its delivery schedule due to wiring problems and the price tag for that incident was six billion dollars [19]. Fortunately the problem was discovered before hitting the market. In May of 1986, a NASA Delta 3925 rocket booster carrying a GOES (Geostationary Operational Environmental Satellite) weather satellite failed due to a momentary short caused by a chafed wire. An Air Force Titan 4B broke up when a short circuit occurred, and 13 years earlier, the failure of another Delta was also due to a chafed wire that caused short circuits [20]. Numerous incidents like these have happened and billions of dollars have been wasted. It was not until the TWA tragedy in 1996 that governments and industries started seriously looking for solutions to this problem. Generally, the main causes of the degradation and the appearance of defects in cables can be either of external or internal origins [21, 22].

1. **Faults from an external origin**

   These reasons can be summarized in what follows:

   (a) Chemical contamination (hydraulic fluids, fuel, and corrosion products cleaning);

   (b) water penetration to the external complex (between the protection sheath and the conductor), following a deterioration due to excessive local thermo-mechanical stresses during the operation of the cable;

   (c) damage and mechanical aggression (vibration, etc.);

   (d) an incorrect application: e.g. underestimation of the maximum current, voltage, or thermal resistance of the environment;

   (e) oxidation, corrosion, or environmental effects (temperature, humidity, etc.), as the two faults shown in Fig. 1.8 attests, where Fig. 1.8(a) is due to humidity while Fig. 1.8(b) is a result of high temperature.

   Whereas, internal reasons can be summarized as follows:

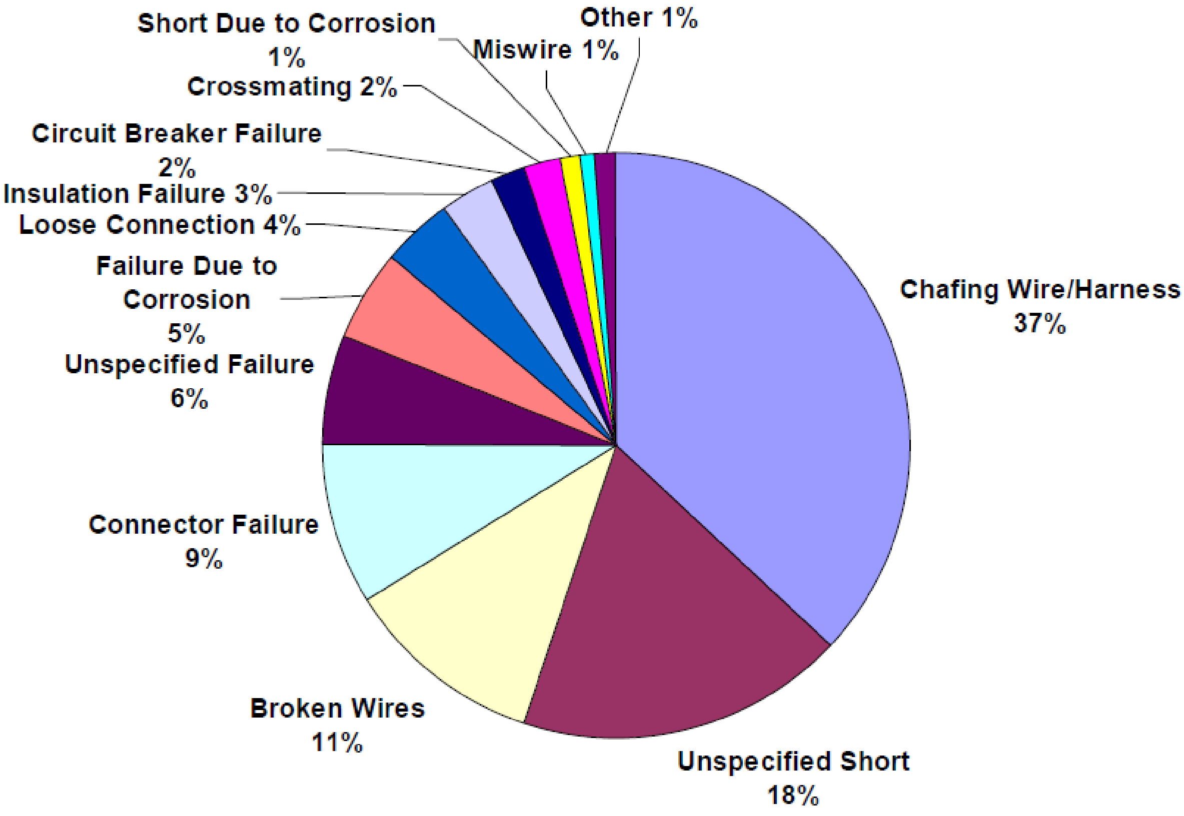

Figure 1.7 A pie chart showing detailed types of wiring faults in aircrafts belonging to the NASA. *Source: [3].*

2. **Faults from an internal origin**
   (a) Manufacturing defects that are not detected during factory safety product tests (vacuoles, impurities creating partial discharges leading to the progressive degradation of the insulation);
   (b) important local heating;
   (c) insulation aging [23, 24]: where heat accelerates drying and cracking of the insulation, moisture accelerates the corrosion of terminals, contacts and connectors.

Among the most often met defects are short and open circuits which are the sources of many fires or signal losses [25]. They are called "*hard faults*", and are characterized by the fact that they prevent any signal from going further away. In fact, hard faults are the first among two main wiring fault families. "*Soft faults*", are the second group of wiring defects which are basically of very different kind and are usually more difficult to detect [3]. Generally, any fault which is not considered hard shall be defined as a soft one, these include insulation damage, cracks, frays, etc. Significantly, a precise knowledge of the fault's reflection coefficient might allow a better assessment

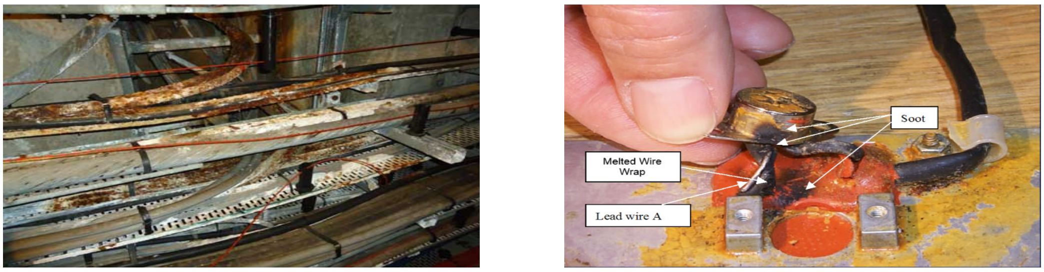

(a) (b)

Figure 1.8 Samples of damaged cables: (a) due to moisture and humidity, (b) aircraft cable damage due to heating.

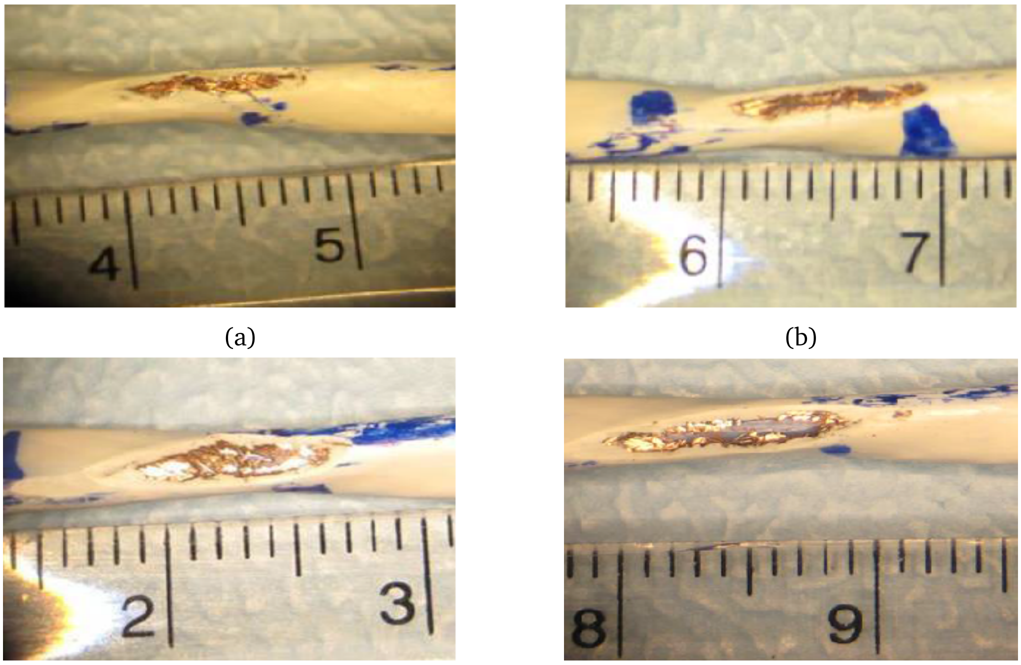

(a) (b)

(c) (d)

Figure 1.9 A progressive chafing example of an aircraft cable where: (a) shows degradation after 4K flight cycles where the shield is relatively intact, (b) after 6K cycles where holes start to appear in the shield, (c) after 8K cycles where the dielectric of the inner conductor starts to be exposed, (d) finally after 10K cycles where the inner dielectric is scraped but intact. *Source: [3].*

of the category the soft fault lies in and consequently detect its severeness and the dangerousness on its corresponding system. As a matter of fact, this will also give a direct evaluation of the risk they might pose to the integrity of the network allowing to know whether they might posses instant breakdown of the system for an urgent fixing or not. It is worthy to note here that a study made by the Aging Transport Systems Rulemaking Advisory Committee (ATSRAC) [26] on 6 different aircrafts has shown that chaffing (a kind of a soft fault), defined as "*localized damage to the insulation or shielding of a wire*" accounts 30% to 50% of all detected wiring faults. Fig. 1.9 shows an example of a progressive chaffing of an aircraft cable, where the situation of the fault seems to deteriorate with time from a normal non-severe soft fault to an intenser severe one which might develop to become a hard fault leading to catastrophic casualties if not early rectified.

It shall be important to point out here that the two main families of wiring defects, *hard* and *soft* faults, are basically *permanent* faults, that is they will appear continuously once they occur. With this in mind, there exists wiring faults that occur commonly in aircrafts, and referred to as *intermittent* arc faults (about 37%), these are the most frustrating, mysterious and extremely difficult to detect and locate because they can disappear in a few milliseconds due to vibrations or other reasons [27] and then disappear.

Consequently, the searching phase for the detection and repair of a wiring fault becomes essential and vital especially that examples have shown that a wiring fault might lead to destructive consequences which is both expensive economically and in terms of human lives. Thus, proper and efficient wire diagnosis tools become strongly recommended to prevent the drastic consequences that may occur.

1.4 Fault Location Techniques: State of the Art

1.4.1 Introduction

Although avionic tragedies namely the TWA 800 Boeing 747 and the Swissair MD-11, are cited as the impetus to research and development efforts in addressing aging wiring problems, there have been a considerable number of incidents that have not resulted in crashes but have been attributed to electrical wiring failures. Replacement of the complete wiring system is ofcourse a solution, and might be feasible in some areas as in automotive or aircraft industries, but replacing a complete wiring system is indeed much more expensive than repairing the faulted wire section. For instance, replacing the wiring system in a typical aircraft is estimated to cost $1-7 million, depending on the aircraft, compared to few thousands in the case of repairing [4].

In the previous section, we presented different types of defects that might exist in electrical cables, and the reasons behind their appearance. We have also seen that these defects may cause serious electrical system malfunctions in addition to severe catastrophic consequences. It is therefore necessary to have diagnostic tools that enable anticipating or detecting the occurrence of faults in wiring networks (hard or soft faults). In fact, many methods have been developed throughout the last few decades to test the condition of cables, most of which were devoted for locating hard faults which are usually at the origin of incident occurrence, such as fires and breakdowns. Generally, such kinds of faults are easier to detect and locate as they are characterized by high reflection coefficients [28]. However, studies have reported that a vast majority of wiring defects are considered to be soft, these types of faults might seem to be non-dangerous as they posses no direct threat for a system breakdown. Despite this fact, they shall not be underestimated, since a soft fault will develop sooner or later into a hard one, thus leading to devastating damages.

Accordingly, ensuring the reliable use of cables requires the availability of techniques capable of detecting the presence of faults that could potentially put in jeopardy a whole system. In what follows, we will present the most common techniques used to detect and locate faults (hard and soft ones), where we will categorize them into two major families: Non reflectometry based methods and reflectometry based ones. The reason behind this kind of categorization is that reflectometry based techniques are the most widely used methods in this domain as they have presented effectual results compared to other traditional methods, besides they are in a continuous development to overcome the limitations they possess.

1.4.2 Non-Reflectometry Based Methods

In this section, we try to present some of the traditional familiar methods which were firstly introduced to detect and locate the presence of faults in wiring systems. In fact, several of such techniques are still used nowadays especially that the ones that will be presented are less expensive than modern techniques and do not require high expertise for their utilization. At the same time, some of the drawbacks faced by such methods will be illustrated.

Visual Inspection

Visual examination is a simple diagnostic method used to identify and/or locate a wiring fault once symptoms or malfunction appears in a system. It is the most intuitive technique that depends totally on the human sensual *raw* visual intervention trying to detect faults such as chafes, cracks, holes in insulation, and signs of arc faults by checking the wires. However, this method is non-efficient due to several reasons that hinder its way. In the first place, wiring faults are often hidden under clamps or walls, within bundles, and other places, and therefore cannot easily be found. Besides, fault inspection requires twisting or turning of the wire, which might cause more harm to the wire than good. Moreover, this inspection might require special designed glasses to check microscopic narrow cross-section cables, which is not available in most of the times. Furthermore, this method is totally unsuitable for the examination of an intermittent arc fault because such faults appear only under particular conditions. With all this in mind, studies done in the automotive industry proved that the searching phase of detecting and repairing a wiring fault done by mechanics would be both expensive and time consuming. This is accompanied with an inability of detection in many of the cases where studies reported that 70% of checked vehicles were returned fault free although they were defected [10]. Consequently, it can be concluded that visual inspection is a tedious, time-consuming and non-efficient process especially with today's cumulated long lengths of cables and complex wiring networks. Hence, more effective tools and techniques became pressing.

Radiographic inspection

These methods are usually based on X-rays and other radiographic techniques. They are designed to allow a technician check not only the state of the outer layer of the cable but also the condition of insulation and conductors located inside. However, a fault is only detected once it is realized by the technician, thus, and since it is based on the human senses intervention, errors will arise. For instance, X-ray based methods rely on the presence of an X-ray generator as well as special detectors and instruments resulting in a heavy and complex setup where cables must be positioned near these devices in order to be inspected leading to non-practicability in many of the cases. Consequently, we can say that this technique is only applicable to cables which are easy to access [29].

Capacitive and Inductive Methods

These methods are based on the measurement of the capacitance or inductance of the cable [30]. The measurement of the capacity is used to locate an open circuit while the measurement of the inductance is used to locate a short circuit on the cable. Generally, there are several methods for measuring the capacity or the overall inductance of a cable, where we can use the divider bridges, oscillators or other methods for measuring an impedance. Although inductance and capacitance techniques, are powerful and easy to the extent that they are used to diagnose the state of a point-to-point cable, they are not suitable for the analysis of complex wired networks, or when the cable is in operation.

In fact, the capacitance of an open circuited wire and the inductance of a short circuited one are linearly proportional to their lengths. There are numerous methods for measuring capacitances and inductances, where customized sensors designed for this objective are capable of measuring the length of a wire based on its capacitance or inductance.

For two circular parallel conductors (round wires) the capacitance and inductance can be calculated according to the following equations where

$$C = \frac{\pi\epsilon}{\cosh^{-1}\left(\frac{D}{d}\right)} \quad (F) \tag{1.1}$$

while

$$\begin{aligned} L &= \frac{\mu}{\pi}\cosh^{-1}\left(\frac{D}{d}\right) \quad (H) \qquad \text{for high frequencies,} \\ &= \frac{\mu}{\pi}\left[\frac{1}{4}+\cosh^{-1}\left(\frac{D}{d}\right)\right] \quad (H) \quad \text{for low frequencies.} \end{aligned} \tag{1.2}$$

It is noted that, d is the diameter of the conductors, D is the distance between the centers of the conductors, ϵ is the permitivity of the insulation, while μ is the magnetic permeability of the dielectric. Consequently, computing the distance to the open or short circuit of the cable under test becomes easy as the capacitance C or inductance L for each type of cable is usually known [30].

Other Non-Reflectometry Techniques		
Method	Advantages	Disadvantages
Ultrasound guided wave	1. Detects insulation defects	1. Necessitates complete access to the cable 2. Fails with branched wires
End-to-End resistance measurements	1. Simple 2. Inexpensive 3. Locates broken cables	1. Needs disconnecting the cable from its network 2. Fails with soft faults
Infrared thermal imaging	1. Provides location information	1. Requires complex imaging systems 2. Not suited for every kind of fault (the fault must create a hot spot)
Low Frequency and DC methods	1. Estimate the location of an insulation fault 2. locate hard faults	1. Necessitates a disconnection of the cable from the network 2. Fails with complex networks and soft faults

Table 1.1 A list of several non-Reflectometry based diagnosis methods with their advantages and disadvantages.

As any testing technique, there are some potential sources of error that shall be considered. Since the capacitance or inductance of a wire changes along its path due to reasons related to nearby metallic components on unshielded or untwisted wires, significant changes in the orientation or separation of the wire and its associated "ground" or paired wire, or from discrete components added to the system, the capacitance or inductance of these additional effects will also be measured and will create errors in the length measurements. In addition to that, these methods are not suitable for locating faults on branched wires, as only the lumped capacitance or inductance is being measured. It can be noted also that they can not be applied to locating soft faults as they are only devoted for hard ones.

In spite of these limitations, these methods are still simple and inexpensive and can provide excellent location of open and short circuits on wires. They are ideally suited for integration in hand held test equipments, and can provide an easy-to-use alternative to the manual search methods.

Despite the fact that the explained methods are the most well known non-reflectometry techniques dedicated for detecting and locating wiring faults, there exist a number of other techniques that will be briefly summarized in table 1.1.

While several electric and non-electric wire diagnosis methods were studied and developed, reflectometry-based techniques are still forming the pivotal focus of research in this domain. Essentially based on a high frequency mechanism, reflectometry injects a probe signal into the network under test (NUT) and monitors the reflected one trying to detect the presence, position, and nature of an impedance discontinuity.

1.4.3 Reflectometry Based Techniques

Reflectometry is a high frequency technique of investigation, imaging or nondestructive testing, dated back to the late 1930's as a technique catching the attention of mainly geologists and other scientists. It was later developed as a result of World War 2 research and was used for defining dielectric properties of soil, rocks and other materials and their moisture content. The basic principle is simple to implement: a probe signal is sent to the system or environment to diagnose, this signal travels under the laws of propagation of the medium studied and when it encounters an obstacle a portion of its energy is returned to the point of injection. The analysis of the reflected signal to the incident one is used to infer information about the system or the environment.

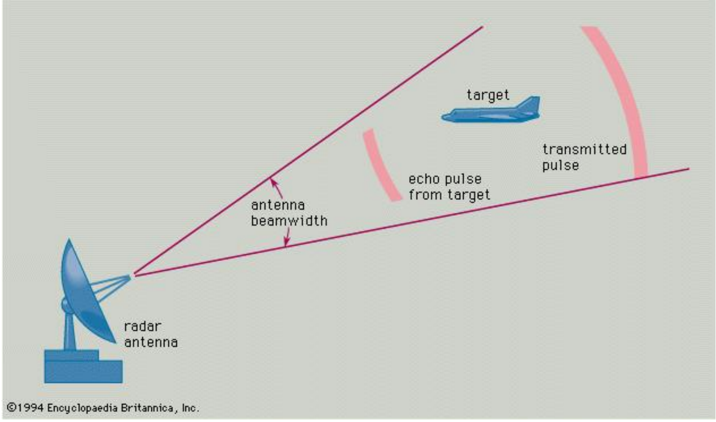

Figure 1.10 Radar systems using reflectometry principle for locating targets, *Source: Wikipedia*.

In fact, reflectometry has found its place in many diverse applications starting from radar systems where it has been used extensively for detecting and measuring the distance to a target (e.g aircraft) as shown in Fig. 1.10. Besides, it has been utilized in the characterization of rheological properties to determine parameters such as viscosity, or viscoelasticity of some materials [31], for the characterization of semiconductor and dielectric thin films [32], in addition to nondestructive testing (NDT) which is widely used in industry to reliably detect the presence of various anomalies in materials such as corrosion evaluation or inspection of composite materials [33–35]. Geotechnology [36], hydrology [37], construction [38], and telecommunication networks are other forms of reflectometry applications [39]. Notably, reflectometry is also a widely common used method for determining the properties of cables. In particular, it allows the detection, location and characterization of electrical defects [17], where it was first introduced for such applications in 1950.

The electronic measuring instrument used for characterizing and locating faults with reflectometry in electric cables is called a *reflectometer*. The reflectometer setup is composed of a signal generator, a coupler, an oscilloscope and the tested cable as shown in Fig. 1.11, where the corresponding tool used to demonstrate the results is referred to as the reflectogram. The process of detecting a fault can be summarized as follows: the signal generator emits for example a step-like pulse which propagates along the cable. Once this pulse encounter an impedance discontinuity (fault), part will be reflected back and another will continue propagating along the cable. The reflected wave front goes back to the injection point where an oscilloscope records the signal amplitude variations over time, and consequently the analysis of the reflected signal can infer information about the system (position of the fault) or the medium under consideration. This information is very rich and valuable for maintenance operators. In fact, the reflection coefficient Γ_f of the impedance discontinuity can also be retrieved which gives a measure of how much signal is returned and is given by

$$\Gamma_f = \frac{V_{reflected}}{V_{incident}} = \frac{Z_c - Z_f}{Z_c + Z_f}; \tag{1.3}$$

where Z_c is the characteristic impedance of the transmission line and Z_f is the impedance of the discontinuity (fault). For instance, the reflection coefficient for an open circuit ($Z_f = \infty$) is 1, while it is -1 for a short circuit ($Z_f = 0$). The time or phase delay between the incident and the reflected signals tells the distance of the fault, while the magnitude describes its reflection coefficient.

As a matter of fact, reflectometry showed promising results when dealing with hard faults but failed when addressing soft ones depicted by weak reflectivities[4]. In order to better illustrate this point, the reflectogram of Fig. 1.12 showing the spread spectrum reflectometry (SSTDR) responses, where SSTDR is a type of reflectometry methods, is considered for fault impedances ranging from 20 to 2000 Ω for a 50 Ω coaxial cable. It can be inferred that faults with high impedance discontinuities (20% of Z_c) are relatively easy to detect and locate due to their relatively high peaks. On the other hand, fault impedances below this value become progressively more difficult to identify as their response is much smaller than even the measurement errors. Besides, there are also several sources of error in reflectometry, as those related to hardware errors, where classical measurement error (any changes in the cable under test (CUT), in the connection, etc.) can affect negatively the feasibility of precisely locating the position of the faults. Furthermore, another significant source of error in reflectometry which is quite important in avionics industry is referred to as the "blind spot" occurs with cables of relatively short lengths. This is usually caused by the fact that the reflected signal overlaps the incident one as a result of the so small time delay.

With a basic understanding of reflectometry and the errors that are inherent in its use, and in the domain of wire detection and location, there are several reflectometry methods that are distinguished by the type of waves used and the domain of analysis of the reflected signal. Basically, we can differentiate between two main reflectometry families, time domain family methods which are based on the time domain analysis and another frequency domain family whose methods are based on the frequency domain analysis.

Reflectometry Techniques based on the Frequency Domain Analysis

Frequency Domain Reflectometry (FDR) which is also called swept frequency reflectometry (SFR) sends a set of stepped-frequency sine waves along the cable under test. These waves travel to the end

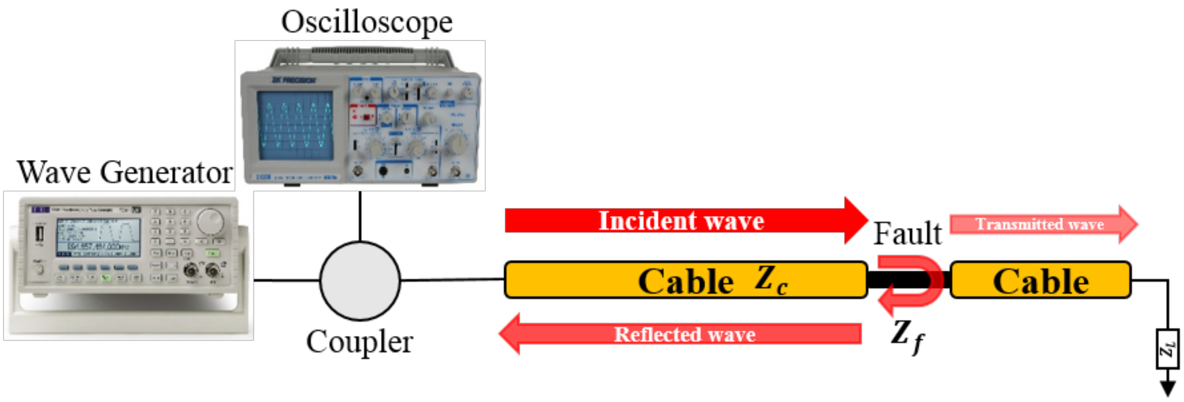

Figure 1.11 A scheme showing the principal of reflectometry.

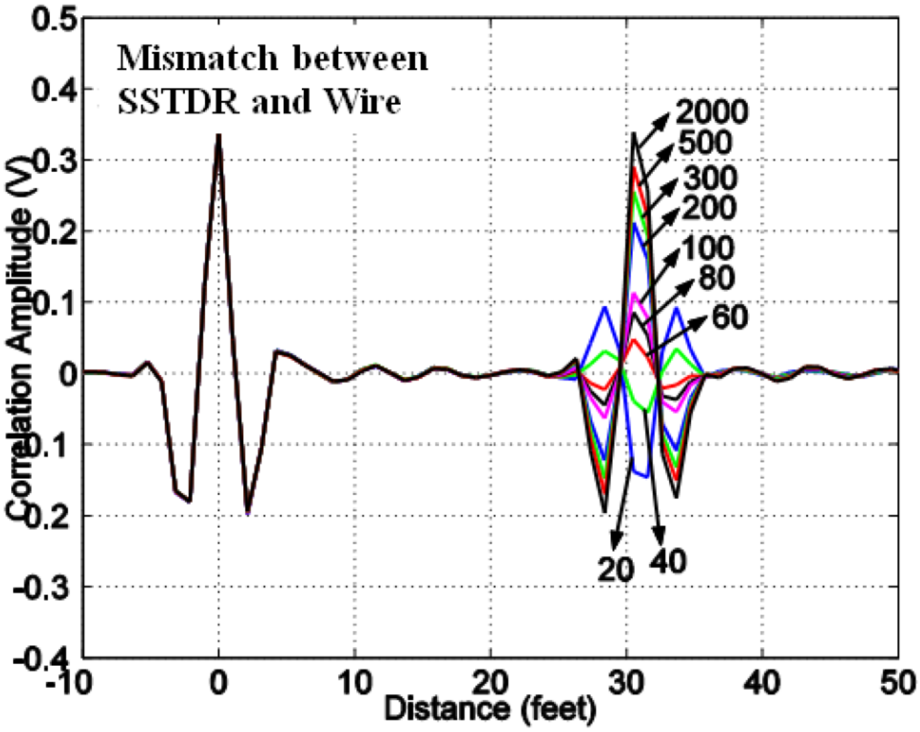

Figure 1.12 A reflectogram showing the responses of a spread spectrum reflectometry (SSTDR) for different load impedances for a 50 Ω coaxial cable. *Source:[4].*

of the cable and are reflected back to the source, where either the reflected waves or the standing wave produced by the superposition of the incident wave and that reflected by heterogeneities are analyzed [40, 41]. The signal of Fig. 1.13 represents a frequency "chirp" signal whose frequency variation is linear. This signal is defined as follows:

$$x(t) = A.\sin(\theta(t) + \phi) \tag{1.4}$$

$$\theta(t) = \int_0^t \pi f(u) du \tag{1.5}$$

$$f(t) = F_{min} + \frac{F_{max} - F_{min}}{t_{max}} t \qquad 0 \le t \le t_{max} \tag{1.6}$$

Upon the injection of the signal into the cable under test, it is necessary to use an electronic system which will allow to measure and analyze the signal in the incident plane in order to determine the characteristics of the line (length , load impedance, capacitance, inductance, resistance and hard fault location).

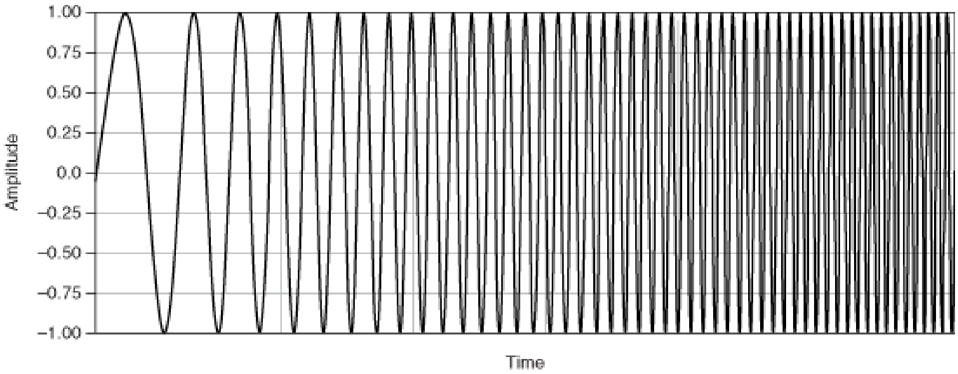

Figure 1.13 Signal "chirp" for a linear frequency FDR implementation. *Source: National Instruments*.

In fact, there are three main types of frequency domain reflectometry that are commonly used in radar applications but have been also adapted to fault detection along wires.

1. Standing Wave Reflectometry (SWR) [37, 42] is the simplest among FDR methods, which is based on the measurement of the maxima and the nulls in the standing wave resulting from the constructive and destructive interferences of the transmitted and reflected wave respectively. Null detection is the form of SWR measuring the nulls in the standing wave while mixed signal reflectometry (MSR) is the one measuring the magnitudes of the standing wave peaks.

2. Frequency modulated carrier wave (FMCW) varies the sine wave quickly, in a ramp function, and measures the frequency shift ΔF between the incident and the reflected signals, that once converted to time delay along with the knowledge of the velocity of wave propagation

can be converted to a distance thus estimating the location of the fault [43] as:

$$\Delta F = \frac{\Delta t}{T}\delta F \tag{1.7}$$

$$d = \frac{v_p T \Delta F}{2\delta F} \tag{1.8}$$

with δF being the bandwidth of the injected signal, v_p the velocity of wave propagation and T the signal's period.

3. Phase detection frequency domain reflectometry (PD-FDR) measures instead of the frequency shift as done in FMCW, the phase shift between the transmitted and reflected waves [40].

Reflectometry Techniques based on the Time Domain Analysis

Time Domain Reflectometry (TDR) is the most well known reflectometry method used for fault detection and location [17]. In its standard form, TDR uses a short rise time voltage step as an incident signal where reflected voltages from impedance discontinuities are also step functions. Consequently, the position of the fault d is retrieved from the round trip time delay τ between the incident and reflected waves and the velocity of wave propagation (v_p) of the cable which is given by:

$$d = \frac{v_p \tau}{2}. \tag{1.9}$$

Basically, standard TDR is accomplished offline, where the tested cable is disconnected from its corresponding system in order to apply the method. For online operation, there exists the online TDR method (OTDR) which is capable of applying the TDR technique while the system is functioning by using high power signals. Unfortunately, this form of operation is not recommended as the power of the injected signals may disrupt or damage electronic systems connected to the cable [7]. It is important to note that the energy of the pulse signals used in TDR is limited, which is a drawback in countering the cable's propagation attenuation, thus there exists a need to increase the signal's energy. Notably, this can be accomplished by using pulse compression [44] which is done by using a binary pseudo random signal and calculating the correlation of the measured signal to the injected one to obtain the reflectogram [45]. The idea of linking TDR with spread spectrum techniques led to novel methods using the pseudo random binary sequences as testing signals, which were later defined as Sequence Time Domain Reflectometry (STDR) [46] and Spread spectrum TDR (SSTDR) [47]. STDR uses pseudo noise (PN) as testing signals as the one shown in Fig. 1.14, which usually have very small magnitudes well below the noise floor especially in aircraft applications. The signal at the source end (a combination of incident and reflected waves) is correlated with a test copy of the PN code where the distance of the fault is easily determined from the correlation data. Markedly, this correlation enables STDR to run on live wires far better than any other reflectometry-based method. For a better performance of STDR for live wire testing, a sine wave modulated PN code (as shown in Fig. 1.14) is used instead as a testing signal, where this new technique is known as the Spread Spectrum TDR (SSTDR). In fact, this has lead to sharper correlation peaks than that obtained with the STDR leading to more accurate estimates of the fault's position.

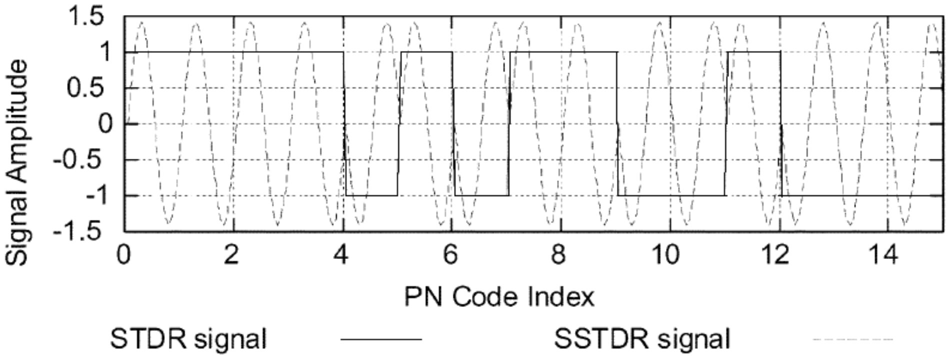

Figure 1.14 STDR and SSTDR testing signals. *Source: [5].*

Joint Time Frequency Domain Reflectometry

Joint Time Frequency Domain Reflectometry (JTFDR) is a method that captures the advantages of both TDR and FDR while avoiding some of their limitations by employing an interrogating incident signal that can be customized based upon the application and advanced post-processing of the reflected signal [6, 48–50]. This innovative technique utilizes a reference signal that is localized in both the time and frequency domains, which is composed of a Gaussian envelope applied to a linear chirp signal. A distinct advantage of this reference signal is its configurability; the user can properly select the parameters of the reference signal, including frequency bandwidth, center frequency, and time duration, by considering the frequency characteristics of the wire under test. After obtaining the time-frequency distributions of the reference and reflected signals, JTFDR computes the time-frequency cross-correlation of the two distributions and uses the peaks of the correlation to detect the defects and determine their locations. JTFDR has proven to accurately and sensitively detect both hard and soft defects on coaxial cables.

To better illustrate the potential benefits JTFDR has provided compared to TDR techniques, Fig. 1.15 was considered. Figs. 1.15 (a) -(b) show the experimental JTFDR results using the proper reference signal design and the time-frequency cross-correlation function under the same experimental conditions used to produce the TDR results in Fig. 1.15(c). The top portion of the figure shows the time-domain incident and reflected signals from the end of the tested cable cable. In fact, Fig. 1.15 (b) illustrates how the time-frequency cross-correlation function of the reference and reflected signals can detect, locate, and assess the defects in the cable. For detection, the time-frequency cross–correlation function quantifies the existence of the signal component associated with the reference signal in terms of time and frequency signatures. This function is normalized between 0 and 1 so that the detection of the defects can be quantified within bounded values; i.e., the function indicates the probability of reflection from potential defects. Again, the reflection from the hotspot is not easily observed in the time domain only (see Fig. 1.15 (c)). However, the time-frequency cross-correlation function at the bottom of Fig. 1.15 (b) clearly shows the detection and location of the hotspot. In addition, because this function provides time resolution and reveals the local time center, it can be used to accurately locate the defect in the cable under test. A new approach called the "Cluster Time Frequency Domain Reflectometry" (CTFDR) applies JTFDR method to improve the detection of soft faults in wire strands [51]. The originality of this approach is, in particular, the use of electromagnetic coupling phenomena in multiconductor structures [52].

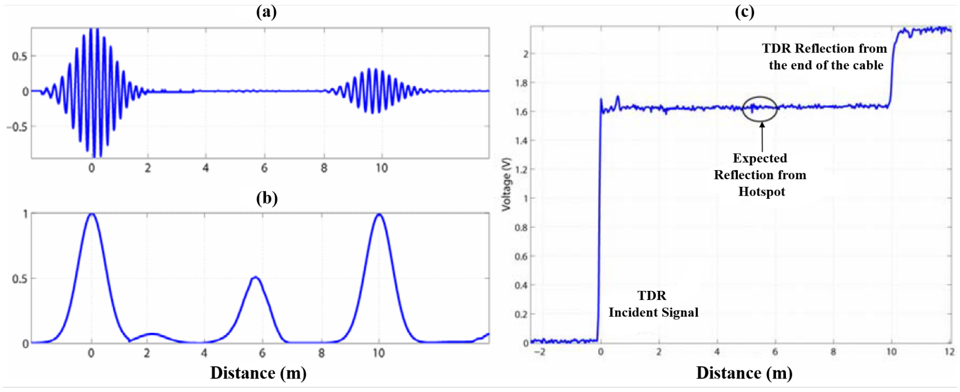

Figure 1.15 Comparisons of JTFDR in (a-b) with (c) classical TDR for the detection of a hotspot. *Source: [6].*

1.4.4 Performance Analysis of Reflectometry Based Methods

Reflectometry techniques described in what preceded have shown a feasibility in detecting and locating wiring faults, where they were mainly differentiated by the types of signals used, their measuring principle and the nature of the defect to be detected. In fact, some methods presented more efficient results towards several issues of the cable under test when other techniques failed. In what follows we are going to present the main advantages and disadvantages presented by some of these reflectometry based methods.

For instance, FDR systems are relatively inexpensive compared to TDR, as the electronics they use are simpler and cheaper, besides they present very little frequency dispersion with clearer peak locations since they are not as broadband as TDR techniques [4]. Furthermore, FDR methods showed to be applicable for testing live wires, under the condition that the test frequency is not within the frequency range of the existing signal on the cable, and the FDR is below the noise margin of the signal. However, this makes it non-optimal and unideal for live wire testing as the necessitated conditions can not be always satisfied which may easily corrupt the FDR response [4, 40]. As a matter of fact, FDR methods seem unsuited for testing complex networks, that is networks made up of several branches and junctions as the single Y-junction network of Fig. 1.17, where the interactions of a great number of shifted waves becomes very difficult to analyze. Besides, the resolution of the obtained responses are very dependent on the sweeping frequency, where increasing the testing bandwidth improves the accuracy of location. It is important to realize, that the applicability of the FDR methods was limited to hards faults and failed in detecting soft ones with low reflection coefficients.

Despite the fact that, FDR techniques were easier and cheaper to implement, the huge development and improvement of electronic components during the past decade (FPGA's, DSP's. etc.) made it simpler to implement TDR based methods. With this in mind, it is worthy to note that TDR techniques use simpler architecture than FDR methods while providing a better resolution of the locations of the faults. Besides, STDR and SSTDR have proved to be feasible and efficient in testing live wires with a high immunity against noise as they operate below the noise level. Perhaps, one of the most significant advantages of the SSTDR is that since it is testing while the wires are live, intermittent hard faults (short duration open or short circuit) could be detected. Although this is true, but TDR based techniques still fail once soft faults are addressed in a network. On the other hand, they were well suited for the diagnosis of complex topology networks as the single Y-junction configuration of Fig. 1.17 (a) where the corresponding reflectogram present peaks associated with each discontinuity along the cables of the network as shown in Fig. 1.16 .

Most TDR methods described can achieve a location accuracy of only a few percents of the length of the wire under test up to a few hundred meters long. Long cables suffer from attenuation and dispersion which greatly reduce the location accuracy. Indeed, the peaks of the reflectogram (Fig. 1.16) must be very sharp if one wants to provide a precise estimation of their location. But sharp peaks mean the use of high frequency (if standard TDR is used) or high data rate signals (for STDR-based methods). So, the precise detection of the edge of the peaks requires powerful data processing or very quick sampling, which increases the complexity and the cost of the diagnosis system [4, 10, 43]. However, another limitation to accuracy is due to the precision of the knowledge of the propagation speed v_p of the signal. TDR systems only measure a round trip time τ , then the distance to the defect is obtained as given by 1.9. Any uncertainty on the value of v_p will decrease the accuracy on the value of the distance to the defect since the propagation speed depends on the frequency. Then, as the probe signal's bandwidth may be quite large, it is not possible to precisely define the propagation speed for the whole signal. Furthermore, TDR methods face the so-called "blind zone" limitation. If the TDR system is not matched to the intrinsic impedance of the cable, a part of the energy of the injected signal is directly sent back, without even going inside the cable. This creates an additional high amplitude peak at the beginning of the reflectogram which may hide a defect close to the injection point. One way to counter this is to use distributed reflectometry [7] where instead of using a single testing port as used in standard TDR techniques, multiple testing ports are used. In the single Y-junction network of Fig. 1.17(b) a standard TDR injects a single testing signal using one of the three ports, on the other hand distributed TDR might use up to three testing ports. Accordingly, two important limitations can be bypassed, firstly this new technique would be removing the "blind zone" effect by using several testing ports rather than only the affected one, besides it is capable of eliminating any ambiguity on the fault's location with respect to the branches of the network. Another key point, is that TDR methods rely on the presence of large bandwidths for obtaining a good spatial resolution for the location of the fault, which is twofold. This could allow identifying it as a potential method for locating soft faults if an extremely accurate initial baseline, which is reference model of the wiring network to be tested, is available [4, 28]. However, there are both practical and theoretical reasons that makes it impossible to obtain such a baseline as will be discussed in the next chapter. On the other hand, large bandwidths are not always satisfied especially with band-limited systems and when developed equipment and processing tools are not available. Notably, one of the fault detection techniques (TR-MUSIC) that will be presented in this thesis has shown a great efficiency in locating soft faults with a continuous wave excitation (single tone, no bandwidth).

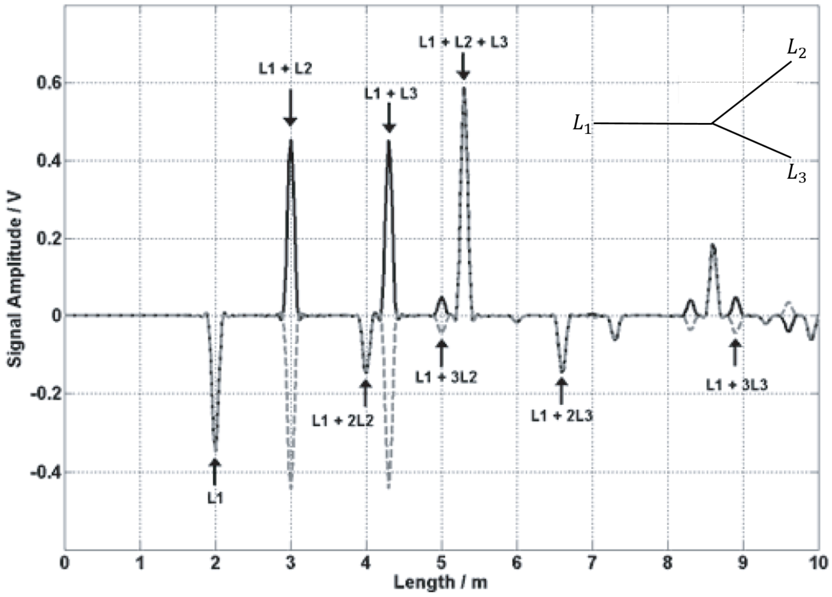

Figure 1.16 Reflectogram of a time domain reflectometry applied for a single Y-junction network. *Source: [7].*

Last but not least, it was also surprising that all the presented techniques didn't handle the problem of addressing multiple faults in a wiring network. As a matter of fact, several defects (hard and soft) might occur in a wiring configuration at the same time thus putting in danger the whole system if only one of them was identified, while the second might be developing without being noticed. Consequently, developing techniques capable of locating multiple faults became crucial, where a recent work [53] aiming at locating multiple faults based on TDR techniques along with a teaching–learning based optimization technique succeeded in this mission. Although, it showed efficient with hard faults it failed when soft ones were addressed.

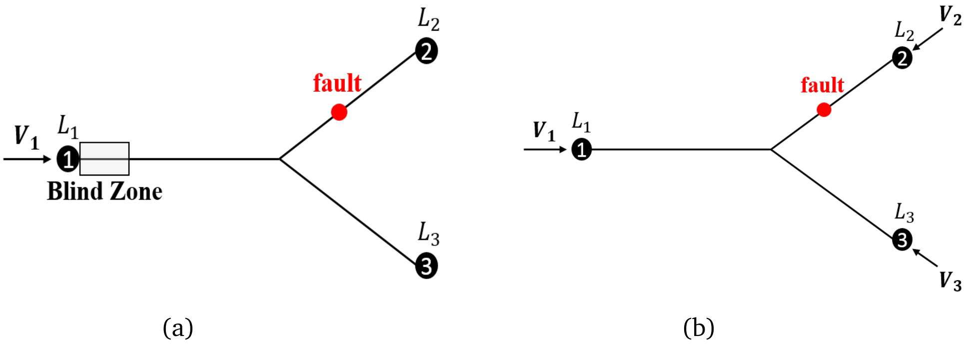

(a) (b)

Figure 1.17 A single Y-junction network where TDR method was applied in (a) standard version using a single testing port, (d) distributed form using multiple testing ports.

1.5 Conclusion

In this chapter, we presented an overview of different electrical cable types that have become widely used in almost all modern systems. Their cumulative length can exceed hundreds of kilometers in many networks employed today where as any system, they are subject to wearing and accidents that can make them non-operational. In fact, we distinguished between two major families of defects that can occur on a cable: hard faults (open or short circuits) and soft faults that feature minor alterations, such as insulation wearing; in this case, signals can still propagate along a cable, and a network is in no danger of breaking down. Yet, a partial wearing may evolve into a stronger degradation, eventually leading to a hard fault. We then illustrated some of the fatal consequences that a wiring breakdown can lead to in many of its application fields where we presented statistical examples of the losses they have caused notably in the avionics industry. Hence, developing robust procedures for the identification and location of faults becomes important, as an early-warning approach for ensuring the safe operation of a critical infrastructure. Consequently, we highlighted on two main groups of fault detection and location methods namely non-reflectometry based methods and reflectometry based ones. Yet, we have seen that the reflectometry based techniques which have formed the pivot of nearly all modern studies in this field, can be distinguished according to the analysis domain of the reflected signals. Specifically, we have seen time domain (TDR) methods and frequency domain (FDR) ones in addition to an uprising technique working jointly on both domains (JTFDR).

To sum up, we presented the main well known reflectometry based methods that have been studied and developed in the last few decades. In fact, they have shown great performances but also witnessed limitations towards some issues. One of these specific problems is that they almost shared an inability of providing efficient results with increased network complexity which arises when we deal with complex networks, involving the presence of one or several junctions, discontinuities, mismatched loads, etc. Another key point, is that we noticed a common inconvenience for all the methods except the JTFDR where they start to fail as soon as the fault becomes ’softer’, that is when the fault's response becomes weak compared to that of a hard fault. In fact, the situation rapidly worsens when multiple faults appear in a wiring network, where none of the presented techniques showed to be feasible in detecting several defects simultaneously while handling soft faults.

Chapter 2

Theoretical Basis of Transmission Lines

Contents

2.1 Introduction

To better understand the fault detection and location new methods that will be presented in later chapters, it is necessary to understand how an electromagnetic wave propagates in a transmission line. The aim of this chapter is first to position our work within the framework of the transmission line theory and in the context of the wiring modeling techniques and then present a method for modeling wiring networks followed by presenting the concept of the "difference system". We will begin with a brief state of the art of methods used for solving the equations of wave propagation along transmission lines in two different domains: frequency and time. These two domains of analysis have been differentiated to describe the behavior of a system since the early studies on electromagnetic modeling. However, although these two domains are theoretically equivalent, they have different provisions for their implementation.

In our study, we will adopt the frequency domain analysis as it has presented important advantages. Notably, it has provided an easy way of equations' discretization, a relatively short duration calculation time and immediate dispersion modeling. However, two major disadvantages, which are, firstly, the need to know in advance the frequency characteristics of the system and, secondly, the difficulty to model nonlinearities, contributed to the renewed interest of the analysis time. This will be followed introducing the methods used to implement and analyze wiring networks and the techniques used to obtain the results namely the space-time diagram. Finally, we will show in the last part of this chapter the usefulness and purpose of applying the difference system concept, after which we will present the major drawbacks resulting from its impossible application in the case of fault detection study field.

2.2 Transmission Lines: Principle

In the most general terms, a transmission line is a system of metal conductors and/or dielectric insulating media that is capable of "guiding" the energy transfer between a generator and a load. From this point of view, a one dimensional propagation phenomenon takes place on a transmission line.

There are many types of transmission lines, of which some examples are shown in Fig. 2.1. The various line types are used for different applications in specific frequency ranges. We are rather interested in this dissertation with structures consisting of two metal conductors, such as coaxial cables. The fundamental assumption of wave propagation mode for these types of transmission lines, whether for a two-conductor line or a multiconductor one (MTL), is that the field distribution surrounding the conductors obeys a Transverse ElectroMagnetic (TEM) distribution. At low frequencies, the wavelength λ is greater than the length l of the transmission line, thus the wave is almost constant at any point on the line, regardless of the load impedance. In this case, it is unnecessary to introduce the concept of propagation. However, as we are working on high frequencies where λ becomes less than the length l of the line, the amplitude of the wave

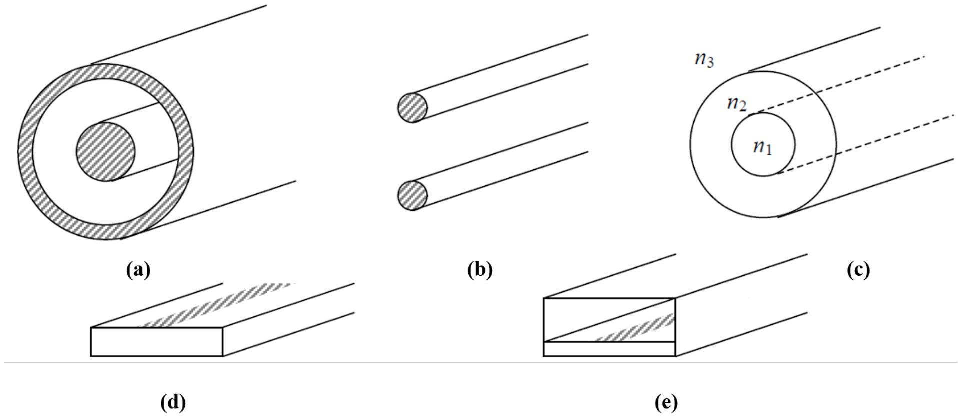

Figure 2.1 Examples of transmission lines: (a) coaxial cable, (b) two wire line, (c) optical fiber, (d) microstrip , (e) stripline.

is no longer constant throughout the line, which therefore introduces regularly spaced minima's and maxima's. In this case, we must take into account the propagation phenomenon. To model this phenomenon, we must recall the propagation theory of electromagnetic waves which mainly depends on various underlying assumptions [54]:

1. The conductors shall have a uniform geometric shape in length and in cross-section where they shall be present in a single homogeneous and isotropic dielectric medium.
2. The propagation mode of the wave traversing the line is considered a transverse electromagnetic wave that is all the transverse and longitudinal dimensions (conductors diameters, heights, spacing between conductors) are smaller than the wavelength λ.

2.3 Transmission Lines: Behavior and Concept

For our case study considering two-conductor transmission lines, and under the assumption that the electric and magnetic fields are transverse to the axis of propagation (TEM wave), a set of coupled partial differential equations referred to as the transmission line equations are obtained. Consequently, a TEM transmission line can be represented with a lumped element circuit where we can model an infinitesimal length section dx of the line as shown in Fig. 2.2 which is better known as the "$RLCG$" model [54]. In fact this section dx is composed of four lumped elements R and L account for loss and energy storage in the conductors, while C and G for installation and loss in the insulator, which are explained as follows:

1. The per unit length resistance R in (Ω/m). This resistance varies with frequency due to the skin and proximity effects in addition to temperature.

2. The per unit length inductance L in (Henry/m). This inductance depends on the diameter of the conductors, the spacing between the two conductors and permeability of materials.

3. The per unit length capacitance C in (Farad/m). This capacitance depends on the permittivity of the dielectric located between the conductors.

4. The per unit length conductance G in (Siemens/m) which reflects the losses due to the dielectric. This conductance depends on the distributed capacitance and dielectric loss angle.

The application of Kirchoff's laws to the $RLCG$ model will provide the following equations:

$$\frac{\partial v(x,t)}{\partial x} = -Ri(x,t) - L\frac{\partial i(x,t)}{\partial t} \tag{2.1}$$

$$\frac{\partial i(x,t)}{\partial x} = -Gv(x,t) - C\frac{\partial v(x,t)}{\partial t} \tag{2.2}$$

where for the case of lossless transmission lines ($R = G = 0$), Telegraph's equations then describe the relationship between the voltage $v(x,t)$ and the current $i(x,t)$ as

$$\frac{\partial^2 v(x,t)}{\partial x^2} = -LC\frac{\partial^2 v(x,t)}{\partial t^2} \tag{2.3}$$

$$\frac{\partial^2 i(x,t)}{\partial x^2} = -LC\frac{\partial^2 i(x,t)}{\partial t^2} \tag{2.4}$$

This model can be extended to bundles of cables as the case of MTLs to account for crosstalk and line interference phenomenon [51]. In fact, the solution to Telegraph's equations given by eqs. 2.3 & 2.4 can be either obtained by an analysis in the time domain or the frequency domain.

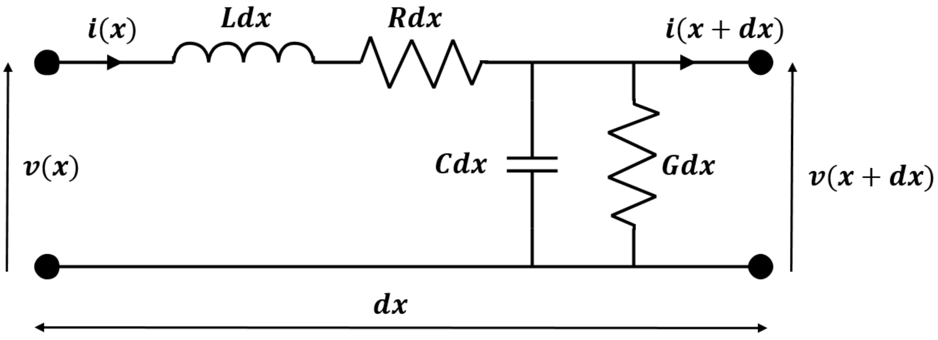

Figure 2.2 Equivalent circuit of a small of a transmission line, showing the per-unit-length parameters R, L, C, and G.

2.3.1 Time Domain Analysis

Time domain analysis allows to follow the signals as they propagate through the cables in a network. There exist several commercial full Maxwell solvers, such as CST MWS [55], that permit to simulate wire networks using different circuit analysis methods such as matrix formulation, state variable, etc. Notably, the Finite Difference Time Domain (FDTD) method [56] is today's one of the most popular techniques for the solution of electromagnetic problems. It has been successfully applied to an extremely wide variety of problems, such as scattering from metal objects and dielectrics, antennas, microstrip circuits, and electromagnetic absorption in the human body exposed to radiation. It is based on solving the electromagnetic problem by simply discretizing Maxwell's equations, both in time and space, with a central difference approximation [56]. Besides, it provides a quick result, as it only requires a 1D mesh of the wire to be tested [57], where voltage and current values are computed at integer and half integer values of the cell size dx using a standard leapfrog scheme scheme [58]. FDTD simulation can help understand the propagation of signals along the wire or in a bundle [59] but it cannot take into account the variations of R and G with frequency. To sum up FDTD methods have presented several advantages over other methods where we are going to list some:

1. *Short development time*, thanks to the simple discretization procedure, where it became easy to implement.

2. *Ease of understanding*, thanks again to the simple discretization procedure, the FDTD method is easily understandable and directly follows the differential form of Maxwell's equations.

3. *Explicit nature*, no linear algebra or matrix inversions are required, and as such there is no inherent limit to the size of a simulation; computer time is the only limitation.

However, there are also a number of disadvantages of the FDTD method:

1. *Stair-stepping edges*, the orthogonal grid structure of the FDTD method implies that edges of structures within the simulation have edges that follow the grid structure;

2. *Computational time*, For simulations with large spaces or multiple scales (largely varying wavelengths), this means the simulation must be run for a very long time.

As a matter of fact, the proposed methods in this thesis require the use of non-harmonic signals to define an origin in space and time; this notwithstanding, rather than directly working in the time domain, it will be by far simpler to start our analysis in the frequency domain and switching back to the time domain afterwards.

2.3.2 Frequency Domain Analysis

It is possible to express the current and the voltage along a cable of length l as shown in Fig. 2.3 , as $V(x,t) = V(x)\exp^{j\omega t}$ and $I(x,t) = I(x)\exp^{j\omega t}$ where $V(x)$ and $I(x)$ are the complex amplitudes associated with the voltage $V(x,t)$ and $I(x,t)$ respectively, while $\omega = 2\pi f$ being the radian frequency in rad.s^{-1}, f being the cyclic frequency of excitation, and j being the imaginary unit. In the case of sinusoidal steady-state, the voltage and current will take the form of single-tone sine waves given by:

$$V(x,t) = Re\left\{V(x)e^{j\omega t}\right\} \tag{2.5}$$

$$I(x,t) = Re\left\{I(x)e^{j\omega t}\right\}, \tag{2.6}$$

with "Re" being the real part of the enclosed complex quantity. Thereupon, Telegraph's equations (eqs. 2.3 & 2.4) will reduce so that the voltage and current at any position x can be found by solving the two wave equations:

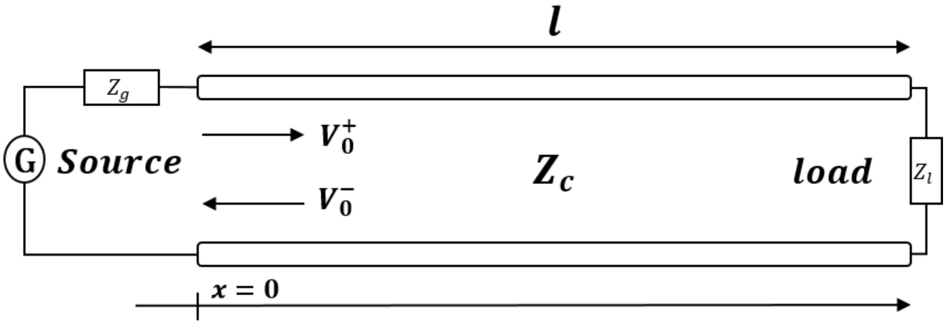

Figure 2.3 Two Conductor Transmission Line of characteristic impedance Z_c and terminated by a load of impedance Z_l.

$$\begin{aligned}\frac{\partial^2 V(x)}{\partial x^2} &= ZYV(x)\\ &= \gamma^2 V(x);\end{aligned} \tag{2.7}$$

$$\begin{aligned}\frac{\partial^2 I(x)}{\partial x^2} &= ZYI(x)\\ &= \gamma^2 I(x),\end{aligned} \tag{2.8}$$

where $Z = R + j\omega L$ is the impedance in Ω/m, $Y = G + j\omega C$ is the admittance in Siemens/m, and γ is the complex propagation constant given by:

$$\gamma = \sqrt{(R + j\omega L)(G + j\omega C)} = \alpha + j\beta; \tag{2.9}$$

with α and β being the attenuation constant in Nepers$/m$ and the phase constant in radians$/m$ respectively.

For the two parallel conductors of Fig. 2.3 , the solution of the second order ordinary differential wave equations (eqs. 2.7 & 2.8) results in

$$V(x) = V_0^+ e^{-\gamma x} + V_0^- e^{\gamma x} \tag{2.10}$$

$$I(x) = I_0^+ e^{-\gamma x} + I_0^- e^{\gamma x} \tag{2.11}$$

where $V_0^+ e^{-\gamma x}$ and $I_0^+ e^{-\gamma x}$ are the forward propagating voltage and current waves, while $V_0^- e^{\gamma x}$ and $I_0^- e^{\gamma x}$ are the backward propagating voltage and current waves. The terms V_0^+, V_0^-, I_0^+, and I_0^- are complex constants depending on the terminal conditions at the two ends of the line, i.e., at the source and the load positions. It is worthy to note that the location variable x can be replaced by $v_p t$ with v_p being the velocity of wave propagation along the line.

As a matter of fact, the current along the line can be written as a function of the voltage in the form of

$$I(x) = \frac{V_0^+}{Z_c} e^{-\gamma x} + \frac{V_0^-}{Z_c} e^{\gamma x}, \tag{2.12}$$

where Z_c is the characteristic impedance of the line. Specifically, Z_c is the limit towards which the input impedance of an infinitely long line tends to, i.e., a line on which a signal propagates without ever being reflected towards the entrance. So at any point x in this infinite line, the ratio of the voltage and current of a wave traveling along the line is its corresponding characteristic impedance given as follows:

$$Z_c = \frac{V(x)}{I(x)} = \sqrt{\frac{Z}{Y}} \quad \Omega \tag{2.13}$$

which may reduce to

$$Z_c = \sqrt{\frac{L}{C}} \tag{2.14}$$

for lossless transmission lines.

The existence of a reflected wave on a line can be explained by the presence of an impedance discontinuity along the line. This parameter is very important when studying fault detection and location methods. For instance, for a uniform transmission line of characteristic impedance Z_c ending by an impedance load Z_l, the incident wave will be reflected at the load. To quantify this reflection, a reflection coefficient is defined, which is given by the ratio of the forward propagating to backward propagating traveling waves at each point x as:

$$\Gamma(x) = \frac{V_{reflected}}{V_{incident}} = \frac{V_0^- e^{\gamma x}}{V_0^+ e^{-\gamma x}}. \tag{2.15}$$

Significantly, the reflection coefficient Γ_f at any discontinuity Z_f along the line which is terminated by a load of impedance Z_l is given by:

$$\Gamma_f = \frac{Z_f - Z_c}{Z_f + Z_c}. \tag{2.16}$$

It is therefore important to point out, that faults are characterized by this reflection coefficient. Certainly, hard faults whether open or short circuits result in an absolute reflection coefficient equal to 1 ($|\Gamma_f| = 1$), whereas any other kind of defect will result in a $|\Gamma_f| < 1$. Consequently, the smaller Γ_f is, i.e., as much as it tends to zero the "*softer*" the fault becomes. Notably, the reflection coefficient at the end of a matched load circuit $Z_c = Z_l$, is indeed zero that is $\Gamma_l = 0$.

In what preceded, we have been considering the case of a uniform two-parallel conductor transmission lines as the one presented in Fig. 2.3. In practice wires are components forming a network, where the corresponding wiring configurations are composed of several branches, junctions and interconnections. As a matter of fact, we will consider wiring networks in our study to present the potential benefits our methods has come with in the domain of fault detection and location. Accordingly, an analysis model is needed in order to simulate these branched networks for validating the methods we intend to present in this thesis.

2.4 Wiring Networks: Methods of Analysis

In real-life environments such as aerospace and automotive, wired networking interconnect dozens or even hundreds of electrical systems together. These wired networks consist of a set of wires, usually of the same type, interconnected according to well defined topology standards. In fact, there exist several network topologies which come in the form of a bus, star, mesh, ring, tree, etc. as shown in Fig. 2.4. In our case study, we are rather interested in the tree topology which is formed of wires that are connected as branches through junctions, where several complex branched configurations will be considered.

Numerous transmission line techniques have been used for modeling wired networks. In general, these techniques can be categorized into three different generations. The first generation modeling techniques as the Bounce/Lattice diagram method [60] and the Bergeron diagram method [61] utilize graphical approaches to trace the wave propagation. These methods are able to perform quick estimation graphically with little training. However, the capabilities of these graphical methods are limited to very simple cases. Additionally, the idealized wave propagations rarely provide sufficient fidelity to match real world measurement results with the level of detail needed to locate small faults. The second generation techniques enhance the wave tracing capabilities by logically dividing the transmission lines into a number of small sections or grids. These techniques are based on time domain analysis and can be distinguished between two main families: analytical & graphical methods such as the slight flow graph (SFG) and its extended version methods [62], in addition to discrete based time domain analysis techniques as the FDTD and the generalized bounce diagram (GBD) methods [56, 63]. In fact, with the assistance of modern computing power, these methods can model much more complicated fault scenarios such as multi-sections and branched networks. One of the biggest drawbacks for these methods is inefficiency. Since the wires are divided into many small subsections, increasing resolution to model small faults increases the computational burden substantially and slows the process dramatically. This is especially serious for long wires with very small faults where high resolution is needed. Another problem for these second generation methods is that the modeling is often performed in time domain, so many of the frequency dependent parameters are not properly represented. Although time domain methods have frequently been used for simulation purposes in [60, 64, 65] these methods are rarely used for inversion purposes, in which high fidelity and high efficiency are both needed.

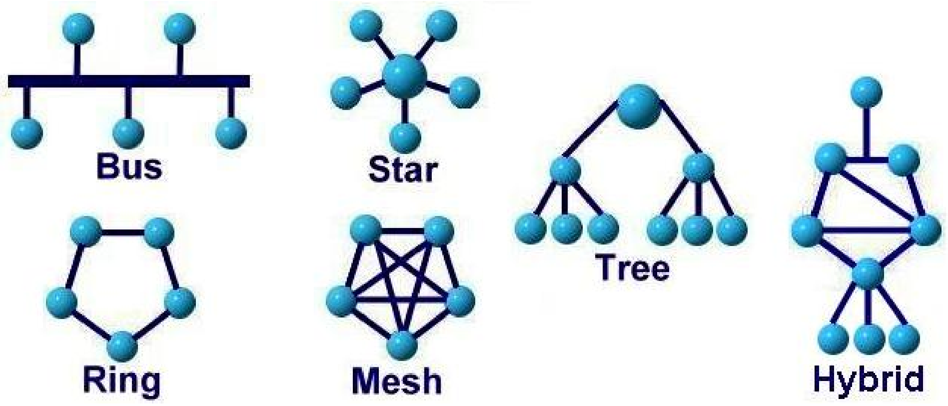

Figure 2.4 Wiring network topologies. *Source: Wikipedia*.

The third generation modeling methods are generally performed in the frequency domain, where results may be later transformed back into the time domain. Since the modeling is performed in the frequency domain, the frequency dependent parameters are taken into account. Without having to divide the wires into many small sections or meshes, the resolution has less impact on the overall efficiency of the method. This is seen more clearly for configurations with long wires requiring high resolutions such as small faults (high fidelity) on long wires. Moreover, the frequency dependent parameters are not properly accounted for in the first and second generation methods unless the results are converted between the time and frequency domains where filtering can be applied. In order to accommodate the high efficient and frequency dependent properties that are needed for high fidelity inverse solutions, new methods have been used. Most of the newer methods are based on either the formalisms of the scattering parameters [66] or the ABCD matrix [67]. Notably, these two formalisms have allowed to derive a model of a soft fault. In our thesis, we have used the scattering parameters' method as it has offered excellent fidelity and computational efficiency.

2.4.1 Scattering Parameter Modeling of Wiring Networks

Scattering parameters (S-parameters) which usually form what is referred to as the scattering matrix denoted as **S**, have been widely used in microwave applications where the scattering analysis has proved to be a very powerful tool that provides the system parameters of an N-port network [68–70]. In the S-parameter approach, an electrical network is regarded as a 'black box' containing various interconnected basic electrical circuit components or lumped elements such as resistors, capacitors, inductors and transistors, which interacts with other circuits through ports. The network is characterized by a square **S** matrix of complex numbers, which can be used to calculate its response to signals applied to the ports. To better illustrate this approach we are going to consider a 2-port network as the one presented in Fig. 2.5, where the transmission lines are characterized by a characteristic impedance Z_c, each of length L_i, a propagation constant γ, and connecting a null length discontinuity considered as a black box B. The voltage $V_1(x)$ and current $I_1(x)$ at any point of the transmission line L_1 at the first port are given by :

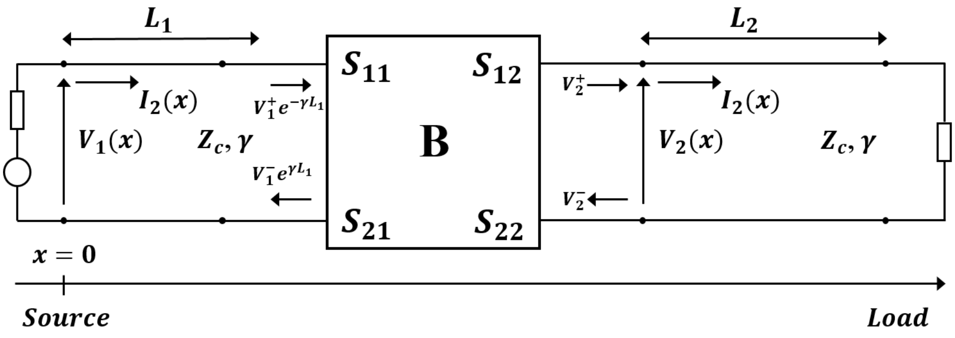

Figure 2.5 A two conductor transmission line containing a discontinuity represented as a block (B) whose length is null.

$$V_1(x) = V_1^+ e^{-\gamma x} + V_1^- e^{\gamma x} \tag{2.17}$$

$$I_1(x) = \frac{V_1^+}{Z_c} e^{-\gamma x} + \frac{V_1^-}{Z_c} e^{\gamma x} \tag{2.18}$$

Similarly, $V_2(x)$ and $I_2(x)$ at any point of L_2 are given by

$$V_2(x) = V_2^+ e^{-\gamma(x-L_1)} + V_2^- e^{\gamma(x-L_1)} \tag{2.19}$$

$$I_2(x) = \frac{V_2^+}{Z_c} e^{-\gamma(x-L_1)} + \frac{V_2^-}{Z_c} e^{\gamma(x-L_1)} \tag{2.20}$$

The incident waves at the discontinuity B ($V_1^+ e^{-\gamma L_1}$ and V_2^-) can be related to the reflected waves ($V_1^- e^{\gamma L_1}$ and V_2^+) as

$$\begin{bmatrix} V_1^- e^{\gamma L_1} \\ V_2^+ \end{bmatrix} = S \begin{bmatrix} V_1^+ e^{-\gamma L_1} \\ V_2^- \end{bmatrix} \tag{2.21}$$

where the scattering matrix S linking these waves is given by

$$S = \begin{bmatrix} S_{11} & S_{12} \\ S_{21} & S_{22} \end{bmatrix} \tag{2.22}$$

It is worthy to note that, the parameters S_{ii} are the voltage reflection coefficients of the discontinuity B which in the case of a fault indicates its softness, while the S_{ij} parameters are the transmission coefficients. For instance, S_{21} describes the part of the wave that has been transmitted from section (1) of the network to section (2) with

$$S_{21} = \frac{V2^+}{V_1^+ e^{-\gamma L_1}}. \tag{2.23}$$

For the case of a uniform lossless two conductor transmission line of length L as that of Fig. 2.3, the attenuation constant $\alpha = 0$, and consequently $\gamma = j\beta$. In other words, the difference between the forward propagating waves V_1^+ and V_2^+ is just the phase delay, as no attenuation or dispersion affects the propagation of the waves, this also applies for the backward propagating waves V_1^- and V_2^-. Accordingly , the corresponding scattering matrix S is given by:

$$S = \begin{bmatrix} 0 & e^{-\gamma L} \\ e^{-\gamma L} & 0 \end{bmatrix} \tag{2.24}$$

In our simulations we considered perfect lossless junctions, which means that the capacitive and inductive parasitic effects are not taken into account.

The case of a 3-branch junction is illustrated in Fig. 2.6. In the general case of an n-branch junction, the continuity of the voltage allows to form $(n-1)$ equations, and the current continuity single equation. The other n equations are obtained by imposing the continuity conditions at the extremities of the port, as invoked earlier. For the case of Fig. 2.6, where we considered that the three branches have the same characteristic impedance Z_c for simplification purposes, the voltage continuity conditions at the junction are

$$V_1^+ + V_1^- = V_2^+ + V_2^- \tag{2.25}$$

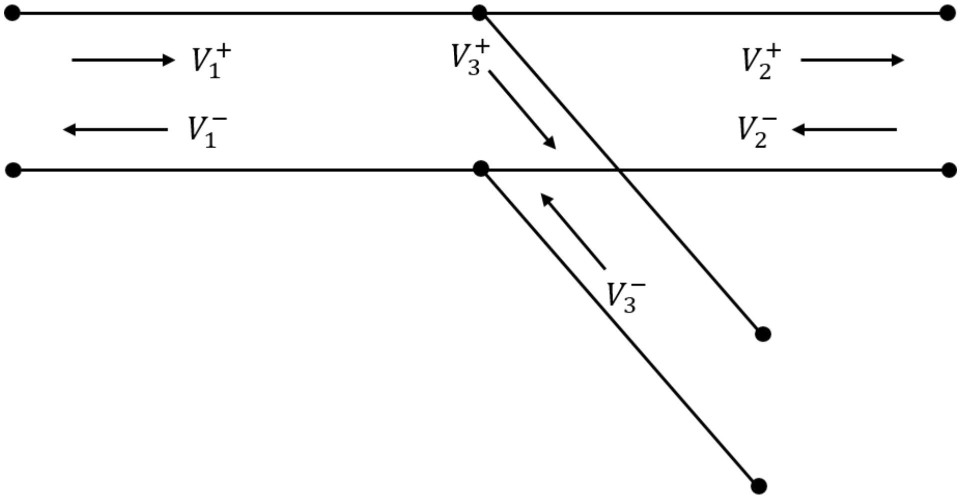

Figure 2.6 A perfect single junction 3-branch network.

and

$$V_1^+ + V_1^- = V_3^+ + V_3^- \tag{2.26}$$

The current continuity condition at the junction, or Kirchhoff's nodal law, implies that the sum of the currents flowing into the junction is equal to the sum of currents flowing out of the junction. If expressed in terms of the voltage waves, the condition is

$$\frac{V_1^+}{Z_c} - \frac{V_1^-}{Z_c} = \frac{V_2^+}{Z_c} - \frac{V_2^-}{Z_c} + \frac{V_3^+}{Z_c} - \frac{V_3^-}{Z_c} \tag{2.27}$$

which implies that **S** satisfying the following equation

$$\begin{bmatrix} V_1^- \\ V_2^+ \\ V_3^+ \end{bmatrix} = S \begin{bmatrix} V_1^+ \\ V_2^- \\ V_3^- \end{bmatrix} \tag{2.28}$$

is given by

$$S = \begin{bmatrix} -\frac{1}{3} & \frac{2}{3} & \frac{2}{3} \\ \frac{2}{3} & -\frac{1}{3} & \frac{2}{3} \\ \frac{2}{3} & \frac{2}{3} & -\frac{1}{3} \end{bmatrix} \tag{2.29}$$

The diagonal elements of **S** are the reflection coefficients at the junction; when a wave arrives at this position, it 'sees' two infinite lines, each can be represented by a parallel load whose value is Z_c. The equivalent impedance seen by this same wave is $Zc/2$ which is the equivalent of two parallel loads whose values are Z_c. Replacing the value of the load impedance Z_L by $Zc/2$ in eq. 2.16 leads to the reflection coefficient value already found.

As a matter of fact, the **S**-matrix formulation was the method we used in the numerical simulations we have performed throughout the work of this thesis which was done by the multi-paradigm numerical computing software *Matlab*. Besides, it has allowed faster and easier post-processing of the collected experimental data since they were frequency domain data obtained from measurements done by the use of a vector network analyzer (VNA).

It is important to note that our simulation code was made up of two main parts. The first, adopted an RSIM simulation tool which was originally designed for the simulation of railway systems [71]. In fact, RSIM afforded an efficient design and implementation of different complex wiring networks, allowing the computation of both the modal voltages and currents at each position of the network. The importance of this simulation tool is its easy interface with Matlab which necessary to demonstrate the obtained results, an advantage overshooting other commercial simulation tools (PSpice, Full wave simulators, etc.). Besides, it is capable of returning only beneficial data necessary to compute the scattering matrices compared to heavier uninteresting data produced by other commercial tools as the full wave simulators. As for the second part, it was based on the transmission line theory [54] which allowed computing the characteristic impedance, propagation constant, modal currents and consequently the voltage propagation at any point along the branches composing the studied networks, which in turn permitted calculating the corresponding scattering matrix **S**. The following section is devoted to highlight the main points followed to represent a network and the tools used to obtain the results.

2.4.2 Graphical Representation of Networks

In order to support our simulation model, some rules and standards have been adopted in our study in order to organize the process of obtaining results and their display. Graphical representation is a simple but effective way to represent different topologies of complex networks. In fact, we have used special symbols in order to demonstrate sources, discontinuities, and transmission lines, allowing to highlight the elements influencing the wave propagation in the network, while maintaining a simple representation of the latter. If we consider the general network structure, illustrated in Fig. 2.7, we first begin by assigning a number to each of the extremities where each designates a testing port, i.e the part of the network where we inject and receive signals. We will consider that the one numbered by (1), be the origin, and distances will be measured according to this origin, and consequently all graphs will plotted accordingly. Two kinds of discontinuities are present in our networks: junctions which connect several branches at a point and are represented by circles, in addition to faults that are designated by two red parallel lines. At this point, that is the discontinuity, the wave propagation at the corresponding position is disturbed by its presence, giving rise to reflection and transmission coefficients. As for the lengths of the branches, the values will be indicated in black on the figure, whereas the position of the fault is measured relative to the nearest point (testing port or junction) and indicated in red near the fault.

Uniform two-wire transmission lines were considered where the two conductors are 10 mm apart; each line has a total 1.5 mm cross-section distributed between a 1 mm core conductor and a 0.5 mm dielectric coating of relative permittivity $\epsilon_r = 3$ as shown in Fig. 2.8 (a). Soft faults are modeled by a partial removal of the coating surrounding the 1 mm core conductor of the line as shown in Fig. 2.8 (b), where the bigger the removed coating (length or thickness) the severer is the soft fault. In fact, the effect of such local modifications in the coating can be quantitatively assessed by computing the relative change R_f. In other words, $R_f = (|Z_f - Z_c|)/|Z_c|$ measures the deviation from the characteristic impedance Z_c of the line, after introducing a fault of impedance Z_f.

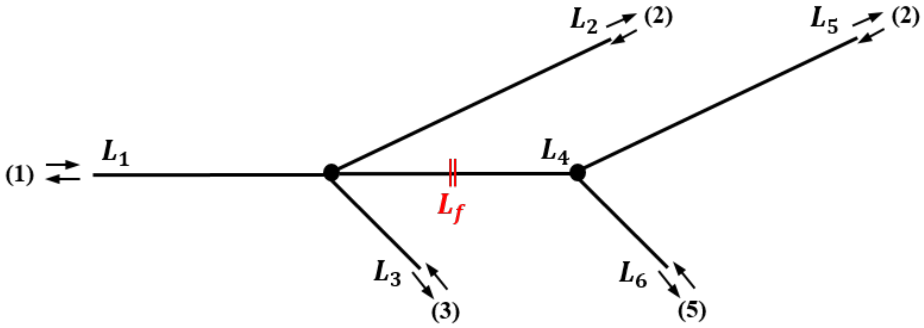

Figure 2.7 Graph representation of a double junction wiring network containing a fault between the two junctions.

2.4.3 Space Time (ZT) Diagram

In the first chapter, we have seen that the reflectogram is the tool used in standard TDR when trying to detect and locate the presence of an eventual fault in a network. The reflectogram allowed to observe the reflected voltage wave at the testing port position only, but wasn't able to afford observing the voltage propagation at different positions inside a network. This shall be a major drawback in our case study, especially that we are going to deal with fault location techniques in this thesis, namely in chapters 4 and 5, that necessitate tracking the voltage propagation at all points in a network. In order to solve this problem, an imaging tool, hereafter referred to as the space-time (or ZT) diagram, allowed tracking the voltage propagation inside a wiring network both in time and in space.

In order to use the ZT diagram tool for presenting the results, some rules concerning the networks shall be clarified. If we consider the wiring network of Fig. 2.9, we realize that it is composed of six branches and two junctions located at 2.5 m and 3.5 m from the testing port (1). The lengths of the branches, indicated on the same figure, were chosen arbitrarily. For simplification purposes, we consider that the extremities of the network are matched loads, which means that no reflection occur at these endings. Concerning the path designation, which is the path along which the voltage

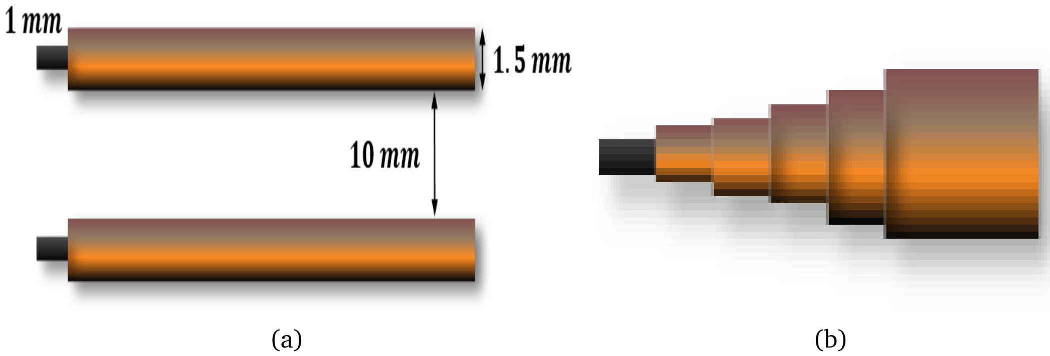

Figure 2.8 The uniform lossless transmission lines in: (a) showing the distance between the two lines, and the cross-section of both the conductor and the line as a whole, (b) showing a gradual degradation of the coating to form the soft fault.

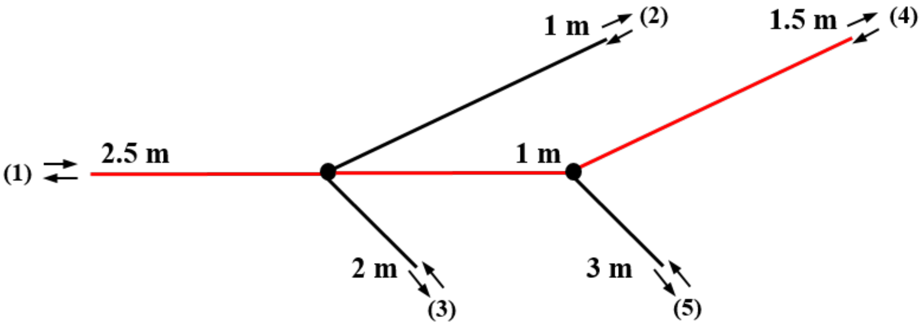

Figure 2.9 A wiring network composed of two junctions with matched end extremities The red line indicates the path along which we will plot the ZT diagram.

propagation on the ZT diagram will be observed, each path will be assigned a number that is the part of the network between the origin testing port and any of the other ports. As an example, in Fig. 2.9, the fourth path is the part of the network linking the origin to the testing port numbered (4).

Let us now introduce the ZT diagram observed along the fourth path which is marked in red in the double junction network of Fig. 2.9. The corresponding image is presented in Fig. 2.10, where the x-axis indicates the distance from the testing port (1), while the y-axis is the time axis. We consider a total bandwidth of 2 GHz, and a frequency sampling step of 20 MHz, which will allow to observe the evolution of the voltage propagation for a period of 0.5 ns, as indicated on the time axis. At time $t = 0$, we injected a normalized amplitude Gaussian pulse (bandwidth of 140 MHz at -3 dB) into the network where the speed of the corresponding propagating voltage wave is considered to be 0.8 times the speed of light. A closer look to the diagram of Fig. 2.10 shows that voltage wave propagates both in time and space, till it encounters the first junction at a distance of 2.5 m from the testing port. Consequently, the discontinuity reflects part of the wave

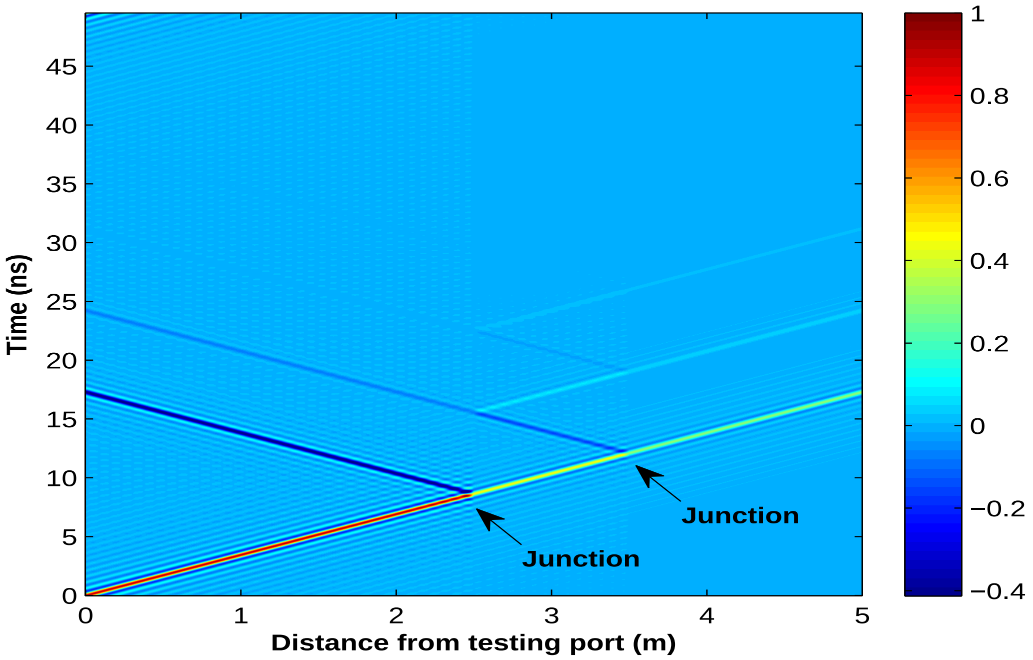

Figure 2.10 A ZT diagram tracking the voltage propagation along the fourth path of the network represented in Fig. 2.9 while all extremities are terminated by matched loads.

to the source where it reaches the origin after 17.29 ns which is the round-trip time to reach this junction. As for the other part of the wave, it will be transmitted through the network, where part of it will propagate along the second branch until it reaches the matched load and then disappears, similarly this will happen for the part propagating along the third branch. In fact, these two parts will not be visible in the ZT diagram of Fig. 2.10, as we are only observing the voltage along the fourth path. Accordingly, the corresponding transmitted voltage wave will continue propagating through the network until it encounters the second junction located at 3.5 m from the reference port where a similar reflecting-transmitting process as that of the first junction will occur until it reaches its end at the matched load extremity (4) and then disappears.

It is important to realize that for this simple case of matched load extremities it was easy to determine the position of the junctions present in the network. On the other hand, would we obtain the same result if open circuited ends were considered? The ZT diagram of Fig. 2.11 shows the result obtained with the same network of Fig. 2.9 where three of the four extremities were terminated by open circuits ((3), (4), and (5)) while (2) is matched. Notably, multiple reflections were obtained where barely the junctions were identified, this happens while we are aware that junctions are discontinuities characterized by higher reflection coefficients compared to soft faults. So, would it be possible to identify in this case soft faults characterized usually with weak reflectivities?

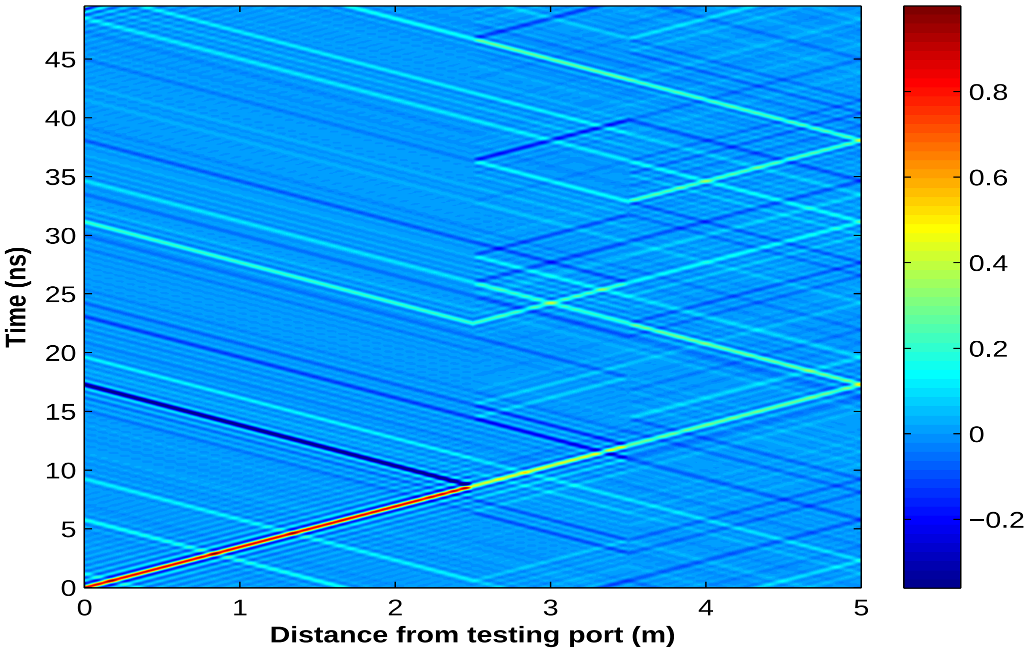

Figure 2.11 A ZT diagram tracking the voltage propagation along the fourth path of the network represented in Fig. 2.9 where extremities (3), (4) and (5) are terminated by open circuits while (2) by a matched load.

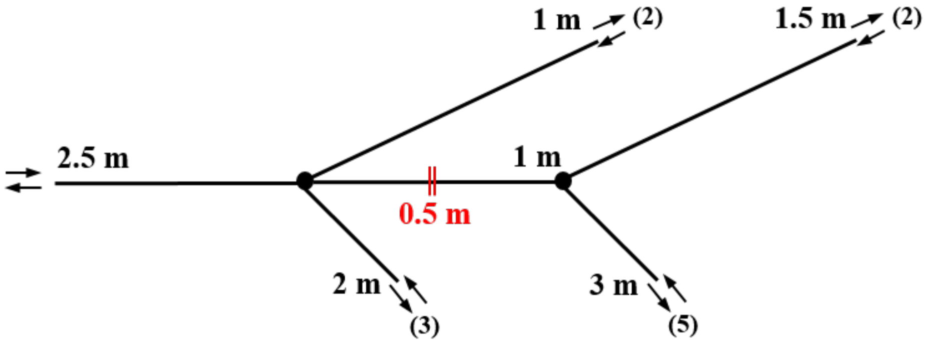

Figure 2.12 A wiring network composed of two junctions and a single soft fault located at 0.5 m from the first junction.

To answer these questions we will reconsider the double junction network but this time with a soft fault $R_f = 12\%$ situated between the two junctions at 3 m from (1) as shown in Fig. 2.12. Observing the voltage propagation along the fourth path of this network terminated by matched ends shows two remarkable reflections corresponding to the two junctions of the network in addition to a third weak one corresponding to the soft fault as shown in the ZT diagram of Fig. 2.13. On the other hand, ambiguity overwhelms the situation when three of the four extremities are ended now by open circuits where the location of the fault's reflection becomes vague as we can infer in the corresponding ZT diagram of Fig. 2.14. In fact, this appears to be the same problem as that of radar in open media, where the presence of clutter and multiple scattering masks the actual echo coming from the target. Consequently, to deal with this problem we are going to introduce the "*difference system*", a concept that allowed to ameliorate and clarify the signature of the fault and make it detectable.

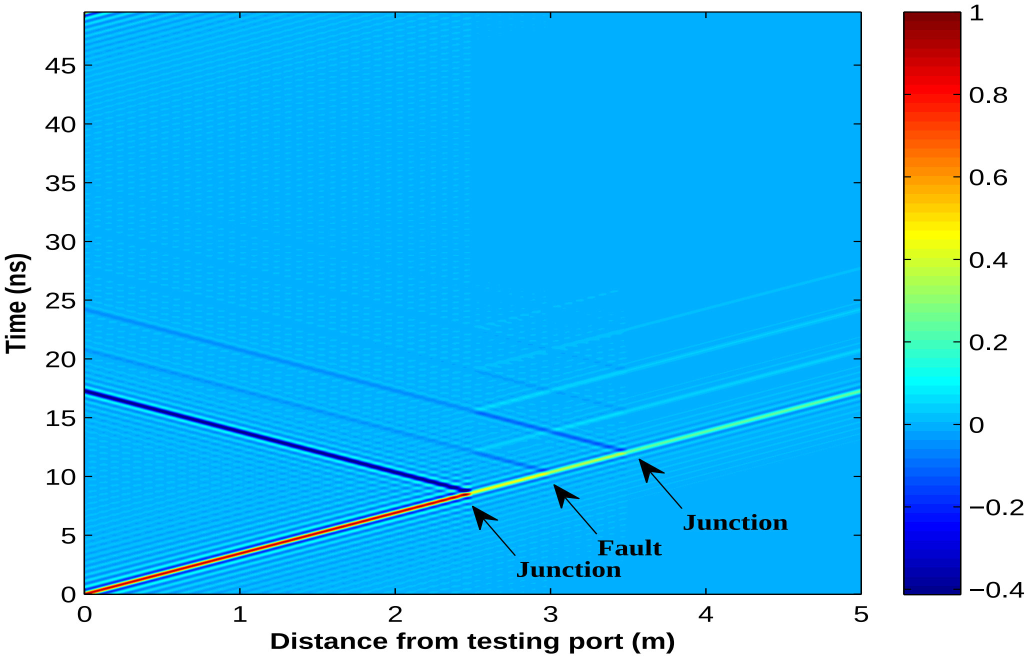

Figure 2.13 A ZT diagram tracking the voltage propagation along the fourth path of the double-junction single-fault network represented in Fig. 2.12 where all extremities end by a matched load.

2.5 Difference System

Clutter refers to echoes returned from targets which are uninteresting to the radar operators and interfere with the observation of useful signals. Such unwanted signals can be due to targets including natural objects such as ground, sea, precipitations (rain, snow or hail), sand storms, animals (especially birds), atmospheric turbulence, and other atmospheric effects, in addition to man-made objects such as buildings, etc. In this case, the echoes returned by a relatively weak reflectivity target might be masked by those produced by clutter leading to an impossibility of detection in some critical cases. Consequently, to overcome the problem of clutter in free space

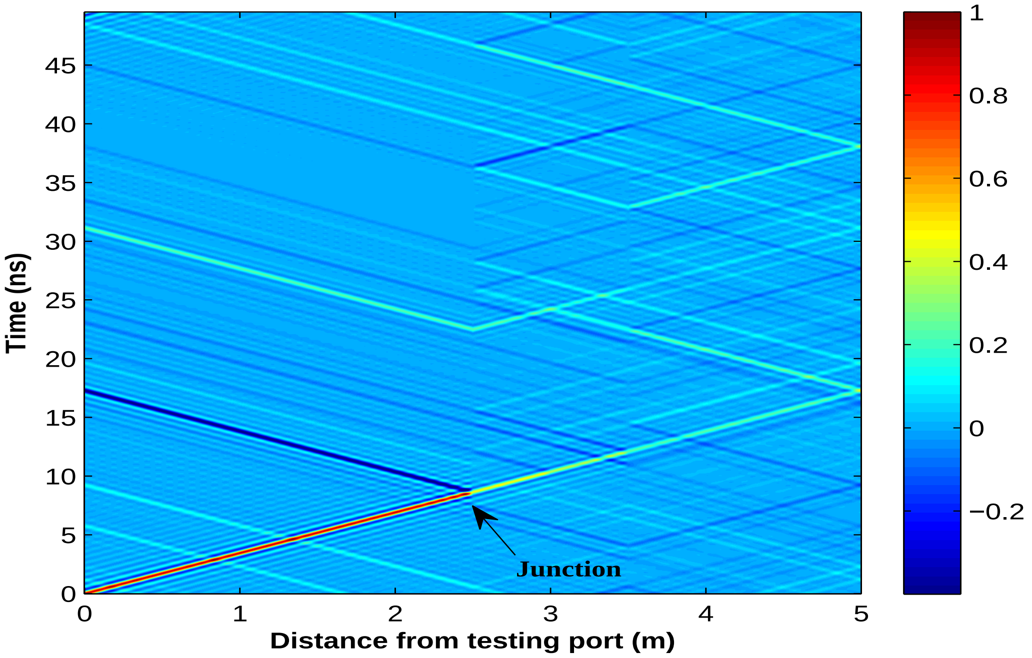

Figure 2.14 A ZT diagram tracking the voltage propagation along the fourth path of the network represented in Fig. 2.12 where extremities (3), (4) and (5) are terminated by open circuits while (2) by a matched load.

propagation, the basic idea was to try to minimize as much as possible the effect of the clutter, by considering what we will call the "*difference system*". In fact, this situation is supposed to be similar to wave propagation in guided structures, where the presence of discontinuities (as junctions) especially in complex networks serve as clutter that would mask the signature of a fault especially with soft faults that are basically characterized with weak reflectivities. In the following we are going to explain the basic concepts of the "*difference system*" in free space and then introduce its scenario in the case of wiring networks.

2.5.1 Difference System in Free space

We will firstly begin by considering the presence of an antenna which emits waves in a homogeneous medium, in the presence of several scatterers which are non-uniformities forcing a wave to deviate from its original trajectory as shown in Fig. 2.15 (a). Initially, no target is present in the medium so, the wave will propagate until it interacts with the scatterers. At this point, it is important to realize that in the presence of several scatterers a multiple scattering scenario is obtained, where a scatterer (X) not only reflects the initial emitted wave but also several reflections coming from other scatterers in the medium. On the other hand, for the case of distant scatterers, the first wave interaction is counted, which is referred to as the single scattering scenario, as the waves reflected from other scatterers are negligible. This is due to the fact that the wave reflected from a scatterer (X) and interacting with other scatterers is minimized as its amplitude decreases in terms of square the distance separating (X) from other scatterers.

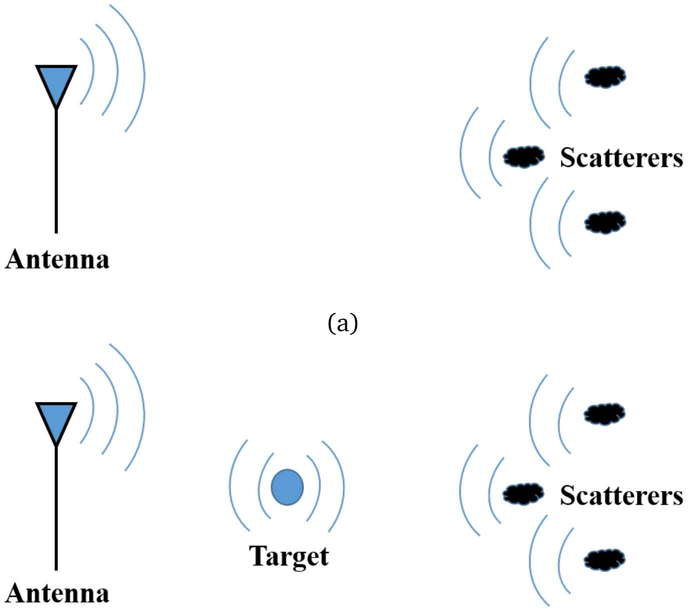

(a)

(b)

Figure 2.15 An example of free space propagation: (a) with the absence of a target, and (b) with its presence.

In the second case, we will add a target to the system so that Fig. 2.15 (b) will be obtained. The emitted wave will follow the same path it followed in the system with only the scatterers, until it encounters both the target and the scatterers which will result in multiple scattering. But, under the assumption of the single scattering scenario, only the most significant reflected wave resulting from the first interaction will be considered for both the case of the target and the scatterers. In fact, if we subtract now the total waves (incident and reflected) present in the second case from those of the first case, we will be left with only the reflected wave diffracted by the target. This is true if we assume that the perturbations brought by the weak target to the system are negligible, i.e, the reflected waves of the other scatterers are not affected by its presence, which is well known as the first-order Born approximation [72]. Ideally, the "new" system obtained by applying the difference of the systems with and without the target presence, only contains this target: it seems as the target was a secondary source, emitting isotropically in all directions. This system will be denoted as the "*difference system*"; it is the equivalent of a system whose transfer function is the result of the subtraction of two transfer functions (of two linear systems): the first one is the reference system without the target, or the baseline system, and the second one is the system with the presence of the eventual target.

Meanwhile, a fault in a wiring network is nothing else than a scatterer in a generic medium, where for complex wiring networks, a fault can be seen as a target, whereas discontinuities, including junctions and mismatched loads, could be considered as scatterers. In this case, single scattering refers to the first interaction of the incident voltage wave with a certain impedance discontinuity in the system, whilst multiple scattering refers to the multiple reflections that occur between these discontinuities.

It is worthy to note that the difference system have been of great importance for fault detection and location techniques. Perhaps, its importance becomes crucial in our case as we are dealing with soft faults due to two main reasons. An intuitive first reason is that the it will make the signature of the initially weak reflectivity soft fault more visible especially in complex networks, where this concept has been used by many researchers in this domain [4, 73]. Another reason is that we need to have the fault acting as a secondary source in order to derive and explain the fault location approaches presented in this thesis.

Although, a great resemblance is present for the difference system between free space and guided wave propagation, there exist major differences that shall be taken into account. While waves attenuate as a factor of $1/r$ in free space [74], guided waves experience negligible attenuation, therefore the single scattering approximation can not be applied directly even if the fault and the discontinuities are distant. However, a fair compromise would be to consider the perturbation brought by the fault to the system to be weak enough so as to consider it as a local perturbation rather than global (the Born approximation), as opposed to the case of a hard fault. Under the assumption of a soft fault, we can ideally remove the effect of the other elements of the system after the subtraction operation, and the fault can be treated as a secondary source, as seen for the target in the case of free-space propagation.

2.5.2 Difference System in Guided Wave Propagation

In the previous section we saw that applying the difference operation to a system's response in the presence and absence of a target (fault) allows eliminating most of the contributions of other elements in the system (other than the fault) that are not related to it's presence. However, due the presence of these elements and the multiple interactions with the target, a residual contribution of the elements exists and appears in the difference system response.

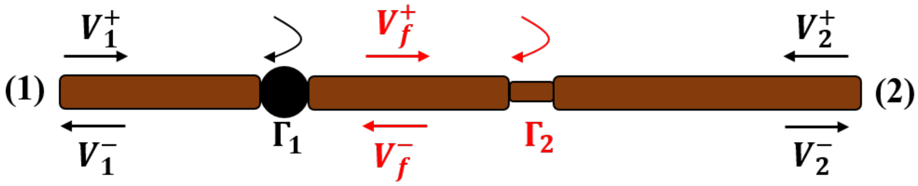

Figure 2.16 A transmission line containing an impedance discontinuity with a reflection coefficient denoted as Γ_1, and a fault with a reflection coefficient referred to as Γ_2.

In order to better understand such a contribution, we will consider a simple uniform lossless transmission line containing a discontinuity of reflection coefficient Γ_1 in addition to a fault having a reflection coefficient Γ_2 as illustrated in Fig. 2.16. For the sake of simplicity we consider that the lengths are equal to zero, and consequently no delay terms will appear in the calculus. The incident and reflected voltages at the extremities (1) and (2) are given by V_1^+, V_1^-, V_2^+, and V_2^- respectively. We assume that the system is in a steady state, and that the waves propagating in the faulty system between the discontinuity and the fault are referred to as V_f^+ and V_f^-. Under these assumptions, we can write

$$V_f^+ = V_1^+(1+\Gamma_1) + V_f^+\Gamma_1\Gamma_2 \tag{2.30}$$

thus

$$\frac{V_f^+}{V_1^+} = \frac{1+\Gamma_1}{1-\Gamma_1\Gamma_2} \tag{2.31}$$

The global reflection coefficient at the first port (1), denoted as

$$S_{11} = \left.\frac{V_1^-}{V_1^+}\right|_{V_2^+=0} \tag{2.32}$$

shall be calculated firstly in the reference system without the fault, where

$$S_{11}^b = \Gamma_1 \tag{2.33}$$

whereas in the faulty network it is given by

$$S_{11}^f = \Gamma_1 + \frac{\Gamma_2(1+\Gamma_1)^2}{1-\Gamma_1\Gamma_2} \tag{2.34}$$

knowing that in this case

$$V_1^- = \Gamma_1 V_1^+ + \Gamma_2(1+\Gamma_1)V_f^+. \tag{2.35}$$

Consequently, the global reflection coefficient of the "*difference system*" can be calculated as

$$S_{11} = S_{11}^f - S_{11}^b = \frac{\Gamma_2(1+\Gamma_1)^2}{1-\Gamma_1\Gamma_2}. \tag{2.36}$$

It can be clearly noticed that the difference system, hereafter referred to as baselining, didn't eliminate totally the contribution of the discontinuity which is designated by the terms containing Γ_1 in eq. 2.36. In fact, this explains the multiple scattering present prior to guided wave propagation. With this in mind, the harder the fault is, i.e the higher Γ_2 is, the more significant is the perturbation brought by the fault presence to the system. Consequently, in order to preserve the physical meaning of the difference system, and be able to apply the Born approximation invoked in the previous section, we decide to deal with soft faults in our work; this insures that a weak perturbation is caused by the fault's presence in the system. The following sections illustrate some qualitative examples.

2.5.3 Performance Analysis of Baselining in the Case of a Soft Fault

In order to better illustrate the concept of baselining for the case of a soft fault, we will consider the single junction network of Fig. 2.17, which contains a soft fault designated by a partial coating removal leading to $R_f = 8\%$. The reflectograms of Fig. 2.18 (a) show the TDR echo for the system containing the fault and that deprived of it, where a clear echo can be noticed on the position of the junction whereas a barely visible response can be detected at the position of the soft fault. Notably, applying the difference system to the responses of the two systems removed the effect of the junction and resulted in a stronger visible signature for the fault which can be now easily identified as shown in Fig. 2.18 (b). Accordingly, the main objective of baselining in making the soft fault's weak signature visible, was demonstrated and validated in this example.

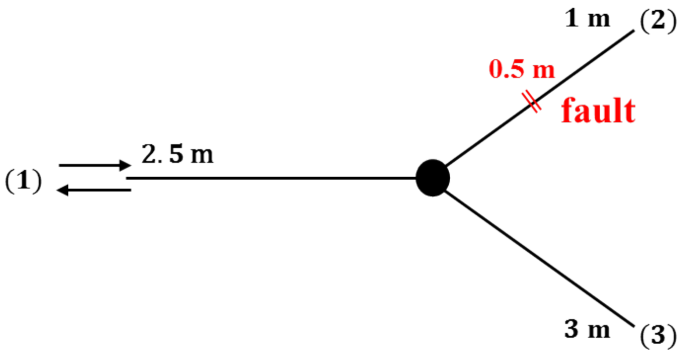

Figure 2.17 A single junction wiring network containing a soft fault $R_f = 8\%$ along its second branch.

On the other hand, it is important to point out that the obtained result was performed on the basis of a perfect baselining, that is to say a 100% identical network to that of the faulty topology was designed without a fault to serve as the baseline network. But what if a perfect baseline is not available?

Surely, this is a reasonable question especially that all methods using the difference system to improve the detectability of soft faults were either accomplished with simulations or with measurements done in a very controlled laboratory environment [4, 28, 73]. This baseline approach is a natural fit to find soft faults, but it is very difficult to obtain such a perfect one in a realistic environment. For instance, archiving baseline networks in specific applications as that in aircraft systems is possible, but it is limited to a very small number of networks as there exist enormous wiring configurations whose archiving process is a costly task. In addition, moving a wire, which is inevitable in high-vibration environments such as that in planes, can make impedance changes that

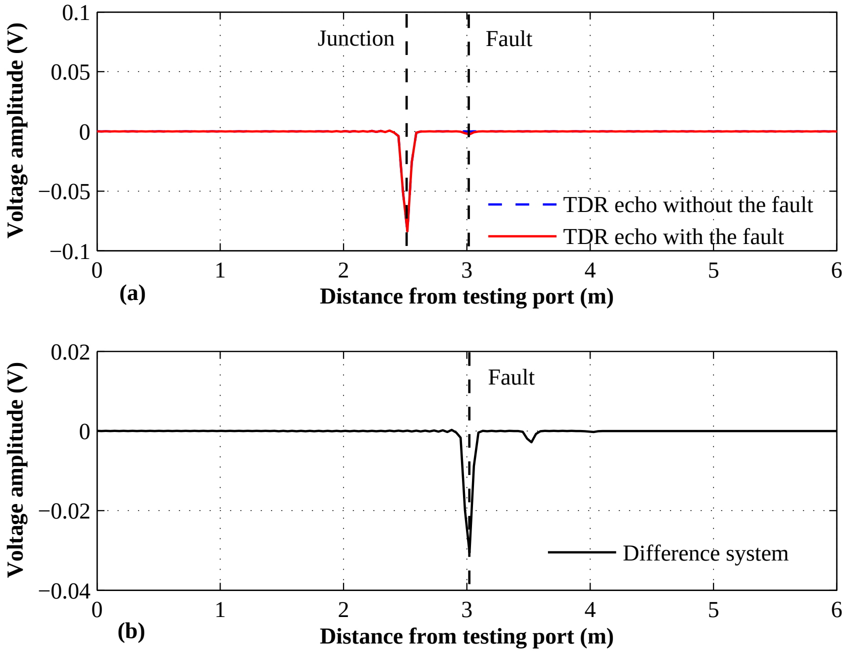

Figure 2.18 Reflectograms in the case of the network represented in Fig. 2.17. (a) shows the reflectograms of the reference and faulty systems, while (b) shows the difference signal. The fault is a soft fault $R_f = 8\%$ situated at 3 m from the testing port.

are as large or even larger than that of a soft fault. It was proven in [4] that simply moving a wire around in ways that could occur during regular use, created more impedance changes than frays (soft faults). In other words, regardless of how accurate and sensitive the systems are made, the environmental impedance changes can be expected to be larger than the fray impedance change, making it impossible to locate such frays using reflectometry methods [4].

Furthermore, this situation is expected to deteriorate once complex networks are considered. In this case, and due to the presence of discontinuities (junctions) that are basically stronger than soft faults, any change in the reference healthy network used to baseline the system would enhance the residual part of the discontinuity which might in some cases totally mask that of the soft fault. To better illustrate this point, we will reconsider the same single junction single fault network of Fig. 2.17, while considering four different reference healthy or baseline networks. The perturbation created was performed at the level of the position of the junction where we have modified for this purpose the length of the first branch linking the testing port (1) to the junction in four different situations, a 0.1%, 0.5%, 1%, and 5% change in this length. Standard TDR was applied to the faulty network and to the four baseline configurations, after which the difference system of each situation is computed, resulting in the reflectograms of Figs. 2.19. In fact, we can notice that even a 0.1% change in the baseline network have enhanced greatly the response on the junction compared to

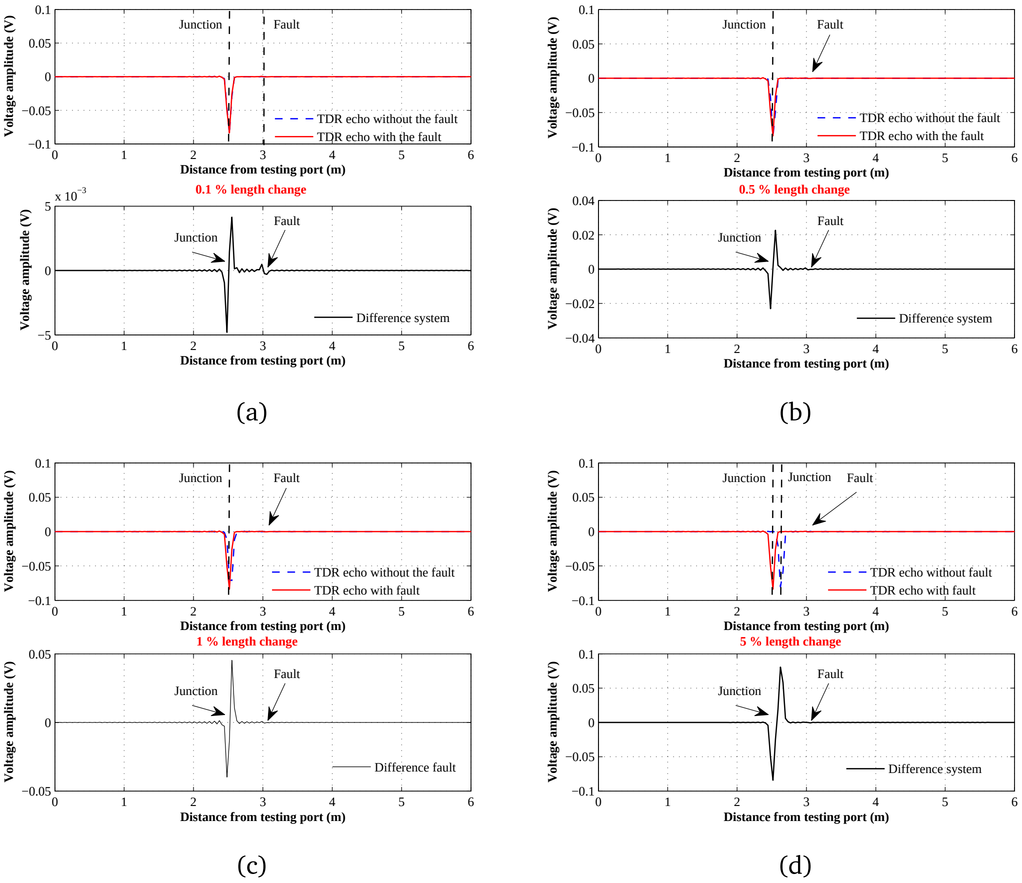

Figure 2.19 Reflectograms of the reference, faulty, and difference systems corresponding to the single-junction single-fault network of Fig. 2.17 while applying a change in the length of the first branch: (a) 0.1% change, (b) 0.5% change, (c) 1% change, and (d) 5% change.

that of the soft fault which becomes barely visible in the case of a 0.5% change and totally disappears when the change exceeds 1%. Notably, the most significant observation of this result is that soft faults on wires have a very critical reflectometry signature that is smaller than ordinary cable length changes in the network (as short-term modifications of the network topology, e.g., the distance between the conductors in a cable) as well as any other impedance change (due to movement, vibration, etc.), therefore, it is going to remain invisible to reflectometry methods. Even with further developments in the methods that might be able to make them sensitive enough to locate soft faults in idealized test environments, the normal impedance variation in the environment of the cable is greater than that due to the fault itself.

Under those circumstances, and due to the deficiency of reflectometry methods in dealing with soft faults, adopting new techniques for this purpose became crucial. From a formal point of view, the problem of soft fault location in a complex wire network is closely related to the problem of target location encountered in radar detection: increasing multiple scattering in the medium poses a significant difficulty when the target's signature is weak compared with other scatterers. To deal with this difficulty, time-reversal techniques can ensure a maximization of the fault-related echo by maximizing the energy impinging on the fault position with respect to the rest of the system under test. In fact, the signals applied to the network no longer aim at directly locating the fault but, rather, are meant to characterize the propagation of signals through the network. The eventual presence of a fault is subsequently inferred from the scattering matrix of the network rather than from echoes, as in TDR techniques. The proposed approach is, therefore, radically different from TDR-based techniques.

2.6 Conclusion

This chapter presented the basic tools and concepts we used to model guided propagation. We adopted a frequency domain analysis to implement our simulation tool, based on the S-matrix approach, due to its simplicity and its ease of implementation. Graph representation allows us to represent the studied networks in a simple manner, while the ZT diagrams give an insight of the voltage propagation in the network. Besides, we have showed that reflectometry methods are very sensitive to baselining which could not be obtained unless we have perfect conditions and is not feasible in practical applications. On the other hand, the difference system approach permit to have the soft fault acting as a secondary source; an idea that is going to be of great significance when addressing fault location techniques based on the time reversal concept.

Chapter 3

Time Reversal

Contents

3.1 Introduction

Because of the physical nature of waves, it is possible to focus waves back towards the source of its origin which can be accomplished by creating waves that behave as if they were propagating backwards in time. In this chapter we will present the principles of time-reversal (TR), a technique that in theory showed highly promising practical usage and has already given feasible results through experiments. Besides, it has attracted great attention due to the large variety of interesting potential applications where development of time-reversal is in continuous progress permitting its applicability to a wider range of areas. Examples are medicine, military operations and seismology. As long as there is some need of locating or focusing on an object of unknown origin which is able to reflect waves, we are within the boundaries of possible usage. In fact, two of the most commonly used TR methodologies, decomposition of the time reversal operator (DORT), and TR multiple signal classification (TR-MUSIC), will be exhibited while illustrating their background and concept, their wide range of applications, in addition to the advantages they have presented in effectively locating targets in open media. With this in mind, we will then show how these methods were adopted for the objective of locating faults along transmission lines.

3.1.1 Background and Motivation

A gunshot is fired at night in an area with lots of tall concrete buildings. Soon afterward a location is pinpointed and displayed on screen at the emergency department of the nearest hospital and also in a patrol car near by. What has happened is that the sound from the gunshot is recognized by microphones placed on the surrounding buildings and in a computer simulation projected back to the source. This might seem like science fiction and it is still, but with proper development it might not continue to be. Conceptually, this is referred to as time reversal; it can be thought of as a method that uses backward propagation of waves to focus wave energy onto a specific location in space and time.

TR concept as applied to waves dates back a number of years. In 1965, Parvulescu and Clay performed an experimentally transmitted signal from a source to a receiver, they time reversed the received signal and broadcast it from the source to the receiver again [75]. They termed this method as the matched signal technique which was able to focus the arrival of the waves in space, indeed, it was the first demonstration of TR known in science history. Studies in this field progressed until a unique mirror known as the Optical Phase Conjugator (OPC) was created in the period between the 1970s and 1980s firstly by researchers from the Soviet Union [76], and later in the United States [77]. This mirror provided the means to return an incoming wave back along the same incident ray path. Thus OPCs resemble TR by the concept of reversing wave energy while they differ in the waves they function with: OPCs work with quasi-monochromatic waves while TR functions with waves of any frequency bandwidth. TR was again studied in 1991 in underwater acoustics to correct for multi-path distortion and to improve the focusing of transmitted acoustic energy into a narrow beam [78]. An important practical outcome of this work was that TR provided the means of tracking a moving target. Advances in microelectronics and array technologies during the beginning of the 1990s, coupled with new theoretical tools, led to the development of the acoustic Time Reversal Mirror (TRM) by Fink and collaborators at the University of Paris VII, Laboratoire Ondes et Acoustique (LOA) [79], [80], [81],[82]. Later in 1994, professor Fink and his team successfully carried out an experiment of time reversing and made a seemingly chaotic signal focus back to its source [83].

TR as set finally, is a process of recording the signal from a remote source, time-reversing and back-propagating it to retro-focus around the source [84]. In the TR process, a probing pulse is used to illuminate the environment and the return echoes are recorded by an array of probes. Consequently, the received signals are time reversed and re-broadcasted into the media thus experiencing similar multipaths and scattering as those they have undergone in the forward direction. They will finally focus on the position of the initial source, a process similar in concept to playing a movie backwards. As a matter of fact, time reversal is a technique that is based on the principle of reciprocity. In particular, assume a source emits radiation that propagates through a complex media to a set of receiving antennas. The data that arrives early in time at a given receiver implicitly travels a shorter distance than data that arrives later in time. By reversing the received waveforms in time, and emitting them from their respective reception points, the data that traveled a longer distance is emitted early, and the data that traveled a shorter distance is emitted later, and all of the energy arrives at the original source in unison, approximately recreating the original excitation.

The list of possible applications of this time reversal technique is long. It can be applied for focusing energy created by an ultrasound transducer array on strongly scattering objects in the region of interest. This can be used for example in lithotripsy for localizing and destroying gall-stones in an automatic way [85, 86], for ultrasonic focusing through the skull [87], hyperthermia [88, 89], remote inspection of internal masses [90] or more generally in the application of medical imaging problems as the detection of breast cancer [91, 92]. Looking into the literature of seismic imaging, the application of time reversal can be found a very successful imaging strategy for detecting scattering interfaces in the Earth [93]. Moreover, it has shown a great feasibility in imaging buried objects beneath rough ground surface [94], through wall target localization [95], in addition to non-destructive testing methods for detecting defects and damages in materials and structures [96–98]. Besides, radar and sonar systems considered time reversal as a good promising tool for target location [99–101]. Recently, several iterative time-reversal schemes have been constructed for solving inverse problems arising in wireless communication thus opening new horizons in the vast domain of telecommunication [102].

3.1.2 Overview of Time Reversal

The concept of TR is based on the invariance of the wave equation in lossless and stationary medium, i.e., if $E(r,t)$ is the solution to the wave equation in (3.1), $E(r,-t)$ is also the solution.

$$\nabla^2 E(r,t) - \mu\epsilon \frac{\partial^2 E(r,t)}{\partial t^2} = 0 \tag{3.1}$$

According to the wave equation, the reverse of the field in time domain (or phase conjugation in frequency domain) would precisely retrace the path of the original wave back to the source where it is excited. $E(r,t)$ is the divergent wave which is usually called the scattered field while $E(r,-t)$ is the convergent wave which will focus on the source with physical or computational TR process.

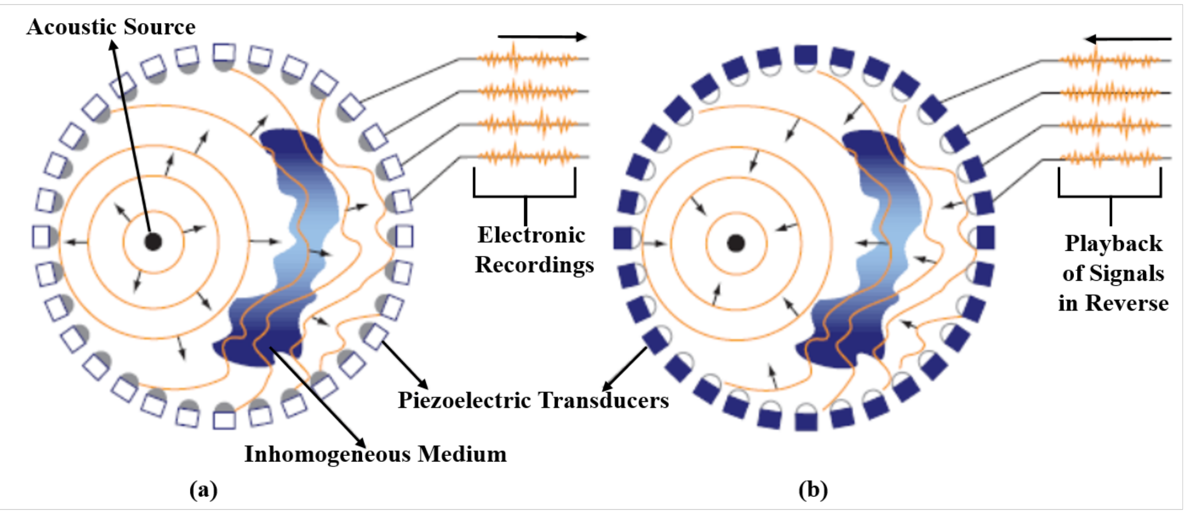

Figure 3.1 Acoustic TR of the TR cavity as presented in [8]. The process constitutes of two main steps. In the first step (a) a source emits sound waves (orange) that propagate out, perhaps being distorted by inhomogeneities in the medium. Each transducer in the mirror array detects the sound arriving at its location and feeds the signal to a computer. In the second step (b), each transducer plays back its sound signal in reverse in synchrony with the other transducers. The original wave is re-created, but traveling backward, retracing its passage back through the medium, untangling its distortions and refocusing on the original source point. *Source:[8].*

In order to better understand the functional concept of time reversal as firstly proposed in acoustics, Fig. 3.1 is considered. In an ideal TR experiment, an acoustic source as presented in Fig. 3.1 (a) located in a solid radiates a short elastic pulse (with longitudinal and transverse components of different velocities) that propagates through the solid and is transmitted into the inhomogeneous medium through the interface. These waves will experience attenuation and distortion due to the presence of discontinuities and inhomogeneities in the medium. Eventually, they will end to a set of transducers surrounding the source and better known as the TR cavity during which each transducer records the signal it detects [84]. This first step is the one known as the recording step.

This will be followed by the time-reversal and re-emission step demonstrated in Fig. 3.1 (b). During this step, the recorded signals are time reversed, and each transducer emits this signal in synchrony with the other transducers. The emitted waves travel back in time, retracing the original passage back through the medium, and refocusing on the initial source point. This is similar to playing a tape backward: the recorded signals are emitted in a reversed way, which means that the waves which were first recorded are re-emitted at the end, and so on. If the source has small dimensions, this technique allows to generate a wave that propagates through any complex interface and focuses back on the source. But some information on the source may be lost. Spatial details of the source smaller than the shortest wavelength are also lost, resulting from classical diffraction limits. If a short pulse (broadband spectrum) is emitted by a pointlike source, the acoustic field generated by the ideal TR method focuses on the source with a spot whose dimensions are of the order of the smallest wavelength contained in the original spectrum [84].

In practice, a closed TR cavity is difficult to realize and presents an ideal concept of focusing through inhomogeneous media. For instance, in non-destructive testing, one has to work in the pulse echo mode that is we can only place the probe on one side of the region of interest, besides sources are not active (transmit mode) as described before, in fact they are defects that behave passively (echo mode) and reflect an incident acoustic field [103]. This mode of operation is more practical and allows focusing from an array of transducers which is referred to as the TR mirror (TRM). Each transducer has its own electronics: detection amplifier, A/D and D/A converters, digital memory, and a programmable generator able to synthesize the temporally inverted signal stored in memory.

3.1.3 Time Reversal Mirrors (TRM)

A TRM array may be used according to the multi-step sequence, illustrated by Fig. 3.2, where it is used to convert waves emerging from a source in an unknown position, to waves converging onto the same source. The process starts when the array of transducers of the TRM generate wide incident pulses to illuminate the region of interest in the inhomogeneous medium as shown in 3.2 (a). If this region contains a scatterer, the reflected wavefronts are detected by the TRM, whose transducers work now in the receive mode, and the reflected pulses are converted into electrical signals that are recorded; this is known as the recording step of Fig. 3.2 (b). In the last step, a temporal window is used to select from the received wavefront the portion of signals that are time reversed and stored in electronic memories. The time-reversed signals are finally transmitted to the transducers, thus resulting in an ultrasonic wavefront that refocuses on the target through the interfaces as shown in Fig. 3.2 (c), noting that this process also compensates unknown deformation of the array.

In the case of several targets, the described latter process fails in producing a one-point focused wave on one of the targets [79]. But, since the TR process is very flexible it can easily be used in an iterative mode, that is the wave transmitted after one time reversal process leads to a second reflected wave that can also be measured and time reversed by an array of transducers. In fact, after n iterations of this process, the system will learn automatically to focus on the most reflective scatterer in the medium while a negligible focusing would occur on the weaker one [83].

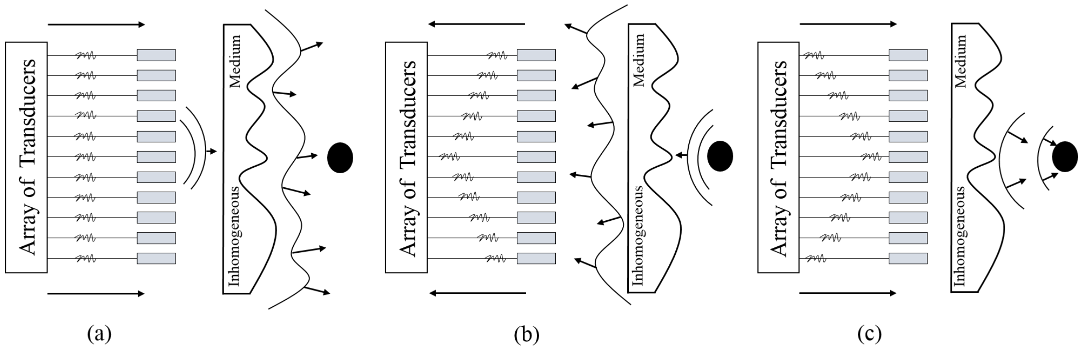

Figure 3.2 The TR process using the TRM. The step in (a) is the transmitting step where the TRM composed of an array of transducers emit pulses into the inhomogeneous medium towards the target. The scatterer will create a backscattered field which will be recorded by the TRM as shown in step (b) better known as the recording step. In the final step (c) a time reversed field will be retransmitted into the medium leading to a focusing on the position of the target.

In general, focusing on the source is either accomplished by physical or computational means in the TR process. The physical TR of electromagnetic waves have been successfully validated experimentally but has shown to be complex and highly costing [104]. As a result, computational TR was employed instead for radar imaging applications. TR imaging (TRI), decomposition of the time reversal operator (DORT), and TR multiple signal classification (TR-MUSIC) are the three main computational TR imaging methods applied in radar for target imaging.

3.1.4 TR Computational Methods

TRI is the most direct method used for the purpose of target location. The standard TRI is a procedure which can be briefly summarized as follows [84, 105, 106]: First, the radar transmits time domain signals to illuminate the unknown target where the scattered field from the target is measured by an array of receivers. After that, the received data is time reversed (or phase conjugated in frequency domain) and sent back to the same probing media from each receiver location. Finally, the time reversed wave from different receivers converges towards the target and focuses at the target's position. The TRI for electromagnetic waves was first applied for freespace imaging and later for seismic imaging and landmine detection. On the other hand, TRI is constrained to the diffraction limit due to the backpropagation of the reversed field. Besides, in the case of multiple scatterers TRI focuses more strongly on the dominant scatterer and masks the weaker ones. As the standard

TRI is iterated, a focusing limited to the strongest scatterer is only obtained. Standard TR iteration does not allow focusing on weaker scatterers unless time-gating is applied.

The DORT method (the French acronym of Decomposition de l'operateur de retournement temporel) overcomes this problem by exploiting the signal space of the multistatic response matrix (MDM) of the system and selectively focuses on different targets via different eigenvectors. DORT has been successfully applied for freespace and subsurface imaging, as well as medical imaging and recently for guided wave propagation. Selective focusing on different targets by DORT can be achieved for multiple scatterers. However, imaging quality degrades in the case of poorly-resolved targets [83, 107–109].

For an efficient dealing with this problem and for also improving the imaging efficiency, the TR-MUSIC algorithm which exploits the null space of the MDM was first proposed by Devaney in [110]. TR-MUSIC does not involve a complex solver for the implementation of the backpropagation of the time reversed field and thus is computationally very efficient. Simultaneously *super resolution* imaging of multiple scatterers can also be achieved. In fact, TR-MUSIC was firstly proposed in acoustics and later applied in electromagnetics [110–114].

In a final analysis of what preceded, iterative TR process allows auto-focusing and detection of defects, in addition to offering good signal-to-noise ratio (SNR). However, it requires programmable generators that are expensive and may not be available besides it couldn't focus on the weaker targets [115]. Unlike the iterative TR process, time reversal imaging methods based on subspace techniques of the MDM do not require programmable generators, and allow simultaneous detection and separation of several defects. As a matter of fact, different algorithms have been exploited to perform the TR imaging, but the most common methods that have been devised for this sake are the DORT and the TR-MUSIC techniques. They have presented advantages of high resolutions and multiple scatterer location. Their differences are in the method used for constructing the multistatic data matrix (MDM) and using the eigenspace elements for focusing on the desired scatterer.

3.2 The DORT method

3.2.1 Concept and Overview

Large arrays of transducers have become a common tool used for solving the problem related to ultrasonic detection and imaging of scatterers in an inhomogeneous medium. They have allowed the collection of a great amount of scattering data which can be used to extract the relevant information to detect or to form an image. Adaptive time delay focusing [116, 117] and acoustic TR imaging based on the TRMs [118–120] proved to be effectual techniques in bypassing this problem. Despite the fact that an iterative TR process operated by TRMs was able to provide focusing on the dominant scatterer in the case of multiple targets, they failed in providing a similar focusing on weaker scatterers.

To deal with this limitation, a theory developed in [121] describes the influence of several parameters such as the number of targets, their reflectivities, their positions with respect to the array, the properties of the propagation medium and the spatial resolution of the system, on the iterative TR process. Basically, this theory relies on the definition of the MDM and the time reversal operator (TRO). Significantly, it has successfully provided selective focusing on each scatterer of several well resolved scatterers of different reflectivities in a medium. The detection and focusing method derived from this result, has been called DORT by Prada et al. in [108, 119]; notably it allowed selective focusing without the need of iterations. In fact, this method was derived from the theoretical analysis of time reversal mirrors and relies on the matrix formalism used to describe a transmit-receive process. First developed for ultrasound, this method was also applied to the field of electromagnetic waves as shown by M Saillard and his team [122]. DORT has been widely used in various applications for non-destructive testing (NDT) [123], electromagnetic fields [124], and nonlinear waves [125].

3.2.2 DORT Technique in Open Media

The general principle of DORT method has been presented. In order to describe theoretically such a process, we give a simple formulation of any transmit and receive operation made with an array of reversible transducers. The idea is to express in a general manner the received signals as a function of the transmitted ones. An array of L transmit-receive transducers insonifying a scattering medium is considered as presented in Fig. 3.3. The whole system is supposed to be time-invariant and linear. In other words, it is assumed that the behavior of the transducers is linear and the waves obey the laws of linear acoustics.

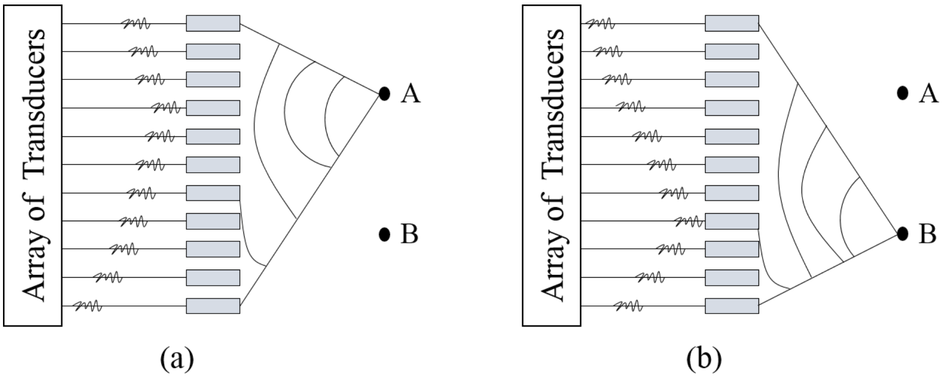

(a) (b)

Figure 3.3 Selective focusing accomplished by DORT method. In (a) the eigenvectors corresponding to the eigenvalue associated to scatterer (A) leads to a focusing on its position while the eigenvectors corresponding to the eigenvalue of (B) focuses on the position of target (B) as demonstrated in step (b).

The Inter-element Response

In the first place, the received signals shall be expressed as functions of the transmitted ones, for this purpose we define for each pair of transducers, an inter-element impulse response. This response includes all the propagation effects through the medium under investigation as well as the acousto-electric responses of the two elements. The inter-element impulse response $k_{lm}(t)$ from the element m to the element l is the signal received on the channel number l after a temporal Delta function is applied to the channel number m. According to the reciprocity theorem known for propagation in inhomogeneous medium, the position of a point source and an observer can be reversed without altering the acoustic field. Consequently, the inter-element impulse response from element number m to element number l is equal to the inter-element impulse response from element number l to element number m, so that $k_{lm}(t)$ is equal to $k_{ml}(t)$. The repetition of the process for each pair (m, l) of transmitting and receiving elements leads, at a given frequency, to the MDM or transfer matrix $\mathbf{S}(\omega)$ whose dimensions would be $L \times L$. It is worthy to note that, all the data and signal processing is performed in the frequency domain and is associated with a single frequency ω. Since all the expressions are associated with the given frequency, ω will be omitted from hereafter. In general, if the medium contains M pointlike scatterers the MDM $\mathbf{S}$ can be written as the product of three matrices [83]:

$$\mathbf{S} = \mathbf{HFH}^t \tag{3.2}$$

where $\mathbf{H}$ is the matrix describing the transmission and propagation from the L transducers to the M scatterers, $\mathbf{F}$ is the diagonal matrix describing the reflectivities of the scatterers on the MDM, in addition to $\mathbf{H}^t$ being transpose of $\mathbf{H}$ (t being the transpose symbol) which describes the backpropagation process from the M scatterers towards the L transducers.

The Time Reversal operator

The time reversal process can be described at a given frequency where the time reversal operation becomes equivalent to a phase conjugation in the frequency domain. The TRO, denoted as $\mathbf{K}$, will be defined as follows

$$\mathbf{K} = \mathbf{S}^{\dagger}\mathbf{S} \tag{3.3}$$

with † stands for the Hermitian transpose. In fact, the symmetry of $\mathbf{S}$ implies the TRO $\mathbf{K}$ is Hermitian, therefore the TRO can be diagonalized. It has been shown that the number of significant eigenvalues of this operator corresponds to the number of well-resolved scatterers. For instance, targets are said to be perfectly resolved if the time reversal focusing on one of them does not produce energy on the others. Furthermore, each eigenvector is the response of the corresponding scatterer to the array. Therefore, it provides the phase and amplitude information that should be applied to the transducer array in order to focus on the corresponding scatterer. Besides, the eigenvalues are functions of the apparent reflectivities Γ_i of the scatterers, and the largest eigenvalue corresponds to the strongest scatterer.

In fact, from a mathematical point of view, the eigenvalue decomposition of **K** is equivalent to the singular value decomposition (SVD) of the scattering matrix **S**. Indeed, the SVD of **S** is $\mathbf{S} = \mathbf{U}\boldsymbol{\Lambda}\mathbf{V}^{\dagger}$, where Λ is a real diagonal matrix of the singular values and **U** and **V** are unitary matrices. The eigenvalues of **K** are the squares of the singular values of **S**; its eigenvectors are the columns of **V**. In practice, and for simplicity, we will use the eigenvalue decomposition (EVD) of **K** rather than the SVD of the scattering matrix **S**, where we are going to analyze its eigenvalues and their corresponding eigenvectors.

The DORT procedure

The DORT method is a process composed of three main steps; its starts with the measurement step, followed by the diagonalization step and finalizing with the backpropagation step. In order to better illustrate this process we will reconsider the graphical representation of Fig. 3.3.

DORT commences by transmitting a temporal Delta function from each of the L transducers where these serve as transmitters and receivers at the same time. This operation is repeated for all the transducers where components of the scattering matrix **S** are obtained by a Fourier transform of each signal; this step is referred to as the measurement step.

After computing **S**, the TRO **K** shall be retrieved according to eq. 3.3 in order to accomplish the diagonalization step. In fact, diagonalizing **K** necessitates a Hermitian condition of it which is satisfied when **S** is symmetrical. But is practice, due to the presence of noise and because of the differences between the acousto-electric responses of the transducers this is no longer the case. Consequently, replacing each term k_{lm} with $\frac{1}{2}(k_{lm} + k_{ml})$ will result in a symmetrical transfer matrix. This shall be now followed by the eigenvalue decomposition of **K** at a chosen frequency which was first introduced by what is called the Central-Frequency DORT. But, this didn't allow obtaining much information about the scatterers neither facilitated the interpretation of data. As a result, the diagonalization process was switched to be performed over a large frequency range rather than a single frequency thus enabling a better understanding of the behavior of the resulting eigenvalues and their corresponding eigenvectors. Then it is very interesting to look at the eigenvalues distribution. In the case of point-like targets, the number of significant eigenvalues is exactly the number of targets, provided they are resolved by the system.

The third step is to backpropagate each eigenvector. This can be done either numerically or experimentally. The numerical backpropagation can be computed for an inhomogeneous medium with an array of well known geometry thus providing separated images of the different targets. The experimental backpropagation requires programmable generators controlled in a parallel like for the time reversal mirror. Pulsed signals are built from the monochromatic data given by the eigenvectors allowing us to focus on one of the targets without knowing the geometry of the array of transducers nor the properties of the propagating medium. In fact, if the targets are well resolved, and under the assumption that their number M is inferior to the transducer's number that is $M \leq L$, each eigenvector is associated to one of the targets: it is the output vector signal that would be obtained if a source is placed at the corresponding target position. The eigenvectors' propagation process amounts to image the medium thus providing separated images of the targets.

In the example we earlier considered in Fig. 3.3, the diagonalization of the TRO gives two significant eigenvalues, denoted as λ_1 and λ_2 (with $\lambda_1 > \lambda_2$) corresponding to the two targets A and B, and $L-2$ eigenvalues close to zero. So if we want to focus on the weaker target (B), we consider the eigenvector $\mathbf{v}_2$ corresponding to λ_2 and propagate each of its components through one of the transmitting transducers. The result is a wave focusing on (B); a similar result is also obtained when we propagate the eigenvector $\mathbf{v}_1$ corresponding to λ_1 in order to focus on (A), and thus selective focusing is achieved using the DORT method.

Eventually, this method offers several advantages in this domain; first it allows to determine the number of scatterers by analyzing the eigenvalues and eigenvectors of the TRO. As a matter of what presented, DORT allowed inferring the number of scatterers in the medium simply by observing the number of significant eigenvalues. Besides, since it is capable of isolating different scatterers, it can be used as a pre-processing step to improve the efficiency of the inverse scattering algorithms. This is accomplished by restricting the inverse problem to smaller domains considering the data provided by the method, thus leading to a faster convergence of these algorithms.

However, fundamental differences exist between the case of open media propagation and the one of guided wave propagation. Accordingly, an adaptation of the DORT method becomes essential to benefit from its advantages. In fact the process of adaptation will be detailed in the next chapter, which will present DORT method as applied for locating soft faults in guided wave propagating structures of transmission lines.

3.3 The MUSIC Method

3.3.1 Introduction

MUltiple **SI**gnal **C**lassification (MUSIC) was first introduced by R. O. Schimdt in 1979 [126] as a method used to provide asymptotically unbiased estimates of a general set of signal parameters of multiple wavefronts arriving at an antenna array from measurements made on the signals received at the array elements. In general, the number of signals, strengths and cross correlations among the directional waveforms, polarizations, the strength of noise or interference, and the direction of arrival (DOA) are the main elements the MUSIC approach covers. Essentially, MUSIC is widely known as a method of DOA estimation, where in signal processing literature, DOA denotes the direction from which a propagating wave arrives at a point, where usually a set of sensors are located. This set of sensors forms what is called a sensor array. In many signal processing applications a set of unknown parameters should be estimated from measurements collected by array of sensors.

As a matter of fact, high resolution DOA estimation is important in many applications such as radar, sonar and electronic surveillance [127]. Recent applications include array processing for wireless mobile communications at the base station for increasing the capacity and quality of these systems or design of large space structures. Among the methods proposed for solving the DOA problem, the class of techniques known as signal subspace algorithms is the most promising. These methods exploit the underlying data model, trying to separate the space spanned by the measured data into what are called noise and signal subspaces. Within this class of algorithms, MUSIC method has received an important attention and has been widely studied showing a great applicability to arrays with arbitrary geometry.

The literature of MUSIC algorithm shows that it has many varieties. Some of them are Spectral MUSIC, Root-MUSIC, Constrained MUSIC and Beamspace MUSIC [128–131]. In its standard form, also known as Spectral MUSIC, hereafter referred to simply as MUSIC, the method is a relatively simple and efficient eigenspace technique [129] which is based on the estimation of the noise subspace from available samples. Once the noise subspace has been estimated, a search for angle pairs is made by looking for steering vectors that are orthogonal to the noise subspace. This is normally accomplished by searching for peaks in the MUSIC spectrum.

3.4 MUSIC in Signal Processing

Spatial spectrum is an important concept in array signal processing theory. It presents the distribution of signals in every direction in space. Hence, if one can get the signal's spatial spectrum, one can retrieve the direction of arrival (DOA). Consequently, spatial spectrum estimation can be also called as DOA estimation.

Generally, there are various methods to estimate the DOA of radio signals on a sensor array, where we can broadly divide them into two main categories; namely non-subspace techniques and subspace based methods. For instance, conventional non-subspace methods including the delay-and-sum method [132], in addition to the maximum likelihood technique [133] depend on the spatial spectrum, where the DOAs are obtained as locations of peaks in the spectrum. These methods are conceptually simple and can be used in situations where we lack of information about properties of the signal, but they offer modest or poor performance in terms of resolution [134].

It is important to reemphasize here that *high resolution* DOA estimation is an important feature in many applications. Among the most promising methods proposed for solving the DOA problem with *high resolution*, was the class of techniques based on signal subspace. These methods by exploiting the underlying data model, try to separate the space spanned by the measured data into what are called noise and signal subspaces. Within this class of algorithms, the method that has received the most attention and has been widely studied is MUSIC algorithm which is applicable to arrays with arbitrary geometry and the price paid for this generality is that the array response must be measured and stored for all possible combinations of source parameters.

As a matter of fact, MUSIC has created a new era for spatial spectrum estimation algorithms. The promotion of the structure algorithm characterized rise and development, and it has become a crucial algorithm for theoretical system of spatial resolution. The basic idea is to conduct characteristic decomposition for the covariance matrix of any array output data, resulting in a signal subspace orthogonal with a noise subspace corresponding to the signal components. Then these two orthogonal subspaces are used to constitute a spectrum function, be got though by spectral peak search and detect DOA signals.

It is because MUSIC algorithm has a *high resolution*, accuracy and stability under certain conditions that it attracts a large number of scholar to conduct in-depth research and analyses. In general, it has the following advantages when it is used to estimate a signal's DOA.

1. The ability to simultaneously measure multiple signals.
2. High precision measurement.
3. *High resolution* for antenna beam signals.
4. Applicable to short data circumstances.
5. It can achieve real-time processing after using high-speed processing technology.

In order to better understand the process the MUSIC algorithm follows the following data model will be illustrated.

3.4.1 Data Model

If there are D signals incident on the array, the N received input data vector at the mth element array, $\mathbf{x}_m(t) \in \mathbb{C}^{1\times N}$, can be expressed as a linear combination of the incident waveforms and noise. That is to say,

$$\mathbf{x}_m(t) = \sum_{l=0}^{l=D-1} a_m(\theta_l)\mathbf{s}_l(t) + \mathbf{w}(t), \tag{3.4}$$

where for all M-element array, the received matrix $\mathbf{X}(t) \in \mathbb{C}^{M\times N}$ is:

$$\mathbf{X}(t) = \begin{bmatrix} \mathbf{x}_1^t(t) \\ \mathbf{x}_2^t(t) \\ \vdots \\ \mathbf{x}_M^t(t) \end{bmatrix} = \begin{bmatrix} \mathbf{a}(\theta_0) & \mathbf{a}(\theta_1) & \dots & \mathbf{a}(\theta_{D-1}) \end{bmatrix} \begin{bmatrix} \mathbf{s}_0^t(t) \\ \mathbf{s}_1^t(t) \\ \vdots \\ \mathbf{s}_{D-1}^t(t) \end{bmatrix} + \mathbf{W}(t); \tag{3.5}$$

in other words,

$$\mathbf{X}(t) = \mathbf{A}(t)\mathbf{S}(t) + \mathbf{W}(t), \tag{3.6}$$

where

1. $\mathbf{S}(t) \in \mathbb{R}^{D\times N}$ is the matrix of incident signals' vectors.
2. $\mathbf{W}(t) \in \mathbb{C}^{M\times N}$ is the noise matrix.
3. $\mathbf{A} \in \mathbb{C}^{M\times D}$ is the array steering matrix.
4. $\mathbf{a}(\theta_j) \in \mathbb{C}^{M\times 1}$ is the array steering vector corresponding to the DOA of the jth signal.

For simplicity, we will drop the time arguments from **X**, **S** and **W** from this point onwards.

In geometric terms, at the instant n, the received vector $\mathbf{x}_m$ and the steering vectors $\mathbf{a}(\theta_j)$ can be visualized as vectors in the M dimensional space. From Equation 3.5, it is seen that $\mathbf{x}_m$ is a particular linear combination of the array steering vectors $\mathbf{a}(\theta_j)$, with $\mathbf{s}_0(n), \mathbf{s}_1(n), \ldots, \mathbf{s}_{D-1}(n)$ being the coefficients of the combination. In terms of the above data model, the input covariance matrix $\mathbf{R}_{xx} \in \mathbb{C}^{M\times M}$ can be expressed as

$$\mathbf{R}_{xx} = \mathbf{A}\mathbf{E}[\mathbf{S}\mathbf{S}^\dagger]\mathbf{A}^\dagger + \mathbf{E}[\mathbf{W}\mathbf{W}^\dagger] = \mathbf{A}\mathbf{R}_{ss}\mathbf{A}^\dagger + \mathbf{R}_{nn} \tag{3.7}$$

where

1. $\mathbf{R}_{ss} \in \mathbb{R}^{D\times D}$ is the signal correlation matrix $\mathbf{E}[\mathbf{S}\mathbf{S}^\dagger]$.
2. $\mathbf{R}_{nn} \in \mathbb{C}^{D\times D}$ is the signal correlation matrix $\mathbf{E}[\mathbf{W}\mathbf{W}^\dagger]$.

Assuming uncorrelated AWGN

$$\mathbf{R}_{xx} = \mathbf{A}\mathbf{R}_{ss}\mathbf{A}^\dagger + \sigma_n^2\mathbf{I} \tag{3.8}$$

The eigenvalue decomposition of $\mathbf{R}_{xx}$ produces the eigenvalues $\lambda_0, \lambda_1, \ldots, \lambda_{D-1}$ where similarly the eigenvalues v_i of $\mathbf{A}\mathbf{R}_{ss}\mathbf{A}^\dagger$ are

$$v_i = \lambda_i - \sigma_n^2. \tag{3.9}$$

Since **A** is comprised of steering vectors which are linearly independent, it has full column rank, and the signal correlation matrix $\mathbf{R}_{ss}$ is non-singular as the incident signals are not highly correlated. A full column rank **A** matrix and non-singular $\mathbf{R}_{ss}$ guarantees that, when $D < M$, the $M \times M$ matrix $\mathbf{A}\mathbf{R}_{ss}\mathbf{A}^\dagger$ is positive semi-definite with rank D. From elementary linear algebra, this implies that $M - D$ of the eigenvalues, v_i , of $\mathbf{A}\mathbf{R}_{ss}\mathbf{A}^\dagger$ are zero. Eq. 3.9 means that $M - D$ of the eigenvalues of R_{xx} are equal to the noise variance σ_n^2. We then sort the eigenvalues of $\mathbf{R}_{xx}$ such that λ_0 is the largest eigenvalue, and λ_{M-1} is the smallest eigenvalue. Therefore,

$$\lambda_D, \ldots, \lambda_{M-1} = \sigma_n^2. \tag{3.10}$$

In practice, however, when the autocorrelation matrix $\mathbf{R}_{xx}$ is estimated from a finite data sample, all the eigenvalues corresponding to the noise power will not be identical. Instead they will appear as a closely spaced cluster, with the variance of their spread decreasing as the number of samples used to obtain an estimate of $\mathbf{R}_{xx}$ is increased. Once the multiplicity, K, of the smallest eigenvalue is determined, an estimate of the number of signals, $\hat{D}$, can be obtained as $\hat{D} = M - K$. In practice, the number of incident signals D is known, thus the eigenvector $\mathbf{q}_i$ associated with a particular eigenvalue λ_i is given such that

$$\mathbf{R}_{xx} - \lambda_i \mathbf{I} = 0. \tag{3.11}$$

For eigenvectors associated with the $M - D$ smallest eigenvalues, we have

$$\mathbf{A}\mathbf{R}_{ss}\mathbf{A}^{\dagger}\mathbf{q}_i = \mathbf{0}; \tag{3.12}$$

since $\mathbf{A}$ has full rank and $\mathbf{R}_{ss}$ is non-singular, this implies that $\mathbf{A}^{\dagger}\mathbf{q}_i = \mathbf{0}$ that is

$$\begin{bmatrix} \mathbf{a}^{\dagger}(\theta_0)\mathbf{q}_i \\ \mathbf{a}^{\dagger}(\theta_1)\mathbf{q}_i \\ \vdots \\ \mathbf{a}^{\dagger}(\theta_{D-1})\mathbf{q}_i \end{bmatrix} = \begin{bmatrix} 0 \\ 0 \\ \vdots \\ 0 \end{bmatrix} \tag{3.13}$$

This means that the eigenvectors associated with the $M - D$ smallest eigenvalues are orthogonal to the D steering vectors that make up $\mathbf{A}$.

$$\{a(\theta_0), \ldots\ldots\ldots, a(\theta_{D-1})\} \perp \{q_D, \ldots\ldots\ldots, q_{M-1}\} \tag{3.14}$$

In fact, this is the essential observation of the MUSIC approach. It means that one can estimate the steering vectors associated with the received signals by finding the steering vectors which are most nearly orthogonal to the eigenvectors associated with the eigenvalues of $\mathbf{R}_{xx}$ that are approximately equal to σ_n^2.

This analysis shows that the eigenvectors of the covariance matrix $\mathbf{R}_{xx}$ belong to either of the two orthogonal subspaces, signal subspace or noise subspace. The steering vectors corresponding to the DOA lie in the signal subspace and are hence orthogonal to the noise subspace. By searching through all possible array steering vectors to find those which are perpendicular to the space spanned by the non-principle eigenvectors, the DOA can be estimated. To search the noise subspace, we form a matrix $\mathbf{U}_n \in \mathbb{C}^{M \times M - D}$ containing the noise eigenvectors:

$$\begin{bmatrix} \mathbf{q}_D & \mathbf{q}_{D+1} & \cdots & \cdots & \cdots & \mathbf{q}_{M-1} \end{bmatrix}. \tag{3.15}$$

Since the steering vectors corresponding to signal components are orthogonal to the noise subspace eigenvectors, $\mathbf{a}^{\dagger}(\hat{\theta})\mathbf{U}_n\mathbf{U}_n^{\dagger}\mathbf{a}(\hat{\theta})$ for $\hat{\theta}$ corresponding to the DOA of a multipath component. Then the DOAs of the multiple incident signals can be estimated by locating the peaks of a MUSIC spatial spectrum given by:

$$\Phi_{MUSIC}(\hat{\theta}) = \frac{1}{\mathbf{a}^{\dagger}(\hat{\theta})\mathbf{U}_n\mathbf{U}_n^{\dagger}\mathbf{a}(\hat{\theta})}. \tag{3.16}$$

The orthogonality between the noise subspace and the steering vectors will minimize the denominator and hence will give rise to peaks in the MUSIC spectrum defined in eq. 3.16. The largest peaks in the MUSIC spectrum correspond to the signals impinging on the array.

MUSIC in imaging: TR-MUSIC

In the last few decades, the problem of estimating the locations of point-like scatterers in open space have caught enormous attention. For this purpose, Devany in [135] applied for the first time the MUSIC concept for the goal of estimating the location of targets from the scattered field data by employing subspace methods used in signal classification and discrete spectrum estimation.

As a matter of fact, MUSIC technique as a subspace method, have been traditionally used in conjunction with the **A**uto**C**orrelation **F**unction (ACF) for the purpose of detecting and locating targets from *passive* antenna array data [135–137]. Although, they can be adapted to *active* arrays as used in **S**ynthetic **A**perture **R**adar (SAR) imaging, they start failing with the presence of multiple coherent targets due to the deficiency in the ACF estimating narrow band data [138, 139].

For an efficient dealing with this problem, MUSIC was applied in conjunction with TR processing enabling its application to the problem of locating M coherent point targets from the measured $N \times N$ multistatic response matrix $\mathbf{S}$ under the condition that $M < N$. It is worthy to note here that, MUSIC is applied in conjunction with TR processing and is not meant to *replace* it. Henceforth, the eigenvectors of the TRO $\mathbf{K} = \mathbf{S}^{\dagger}\mathbf{S}$ of the measured MDM $\mathbf{S}$ corresponding to the antenna array play the same role as the eigenvectors of the ACF in classical MUSIC. It follows, that the eigenspace of $\mathbf{K}$ can be partitioned into the direct sum of a *signal subspace* $\mathscr{S}$ and the *noise subspace* $\mathscr{N}$ in complete analogy with classical MUSIC. A pseudo-spectrum is then computed by the using a steering vector which is equal to the background Green function modeling the antenna received data from an isolated target at a "test" location. Significantly, the pseudo-spectrum produces super-resolved target locations similar to the closed spaced spectral lines produced in classical MUSIC [111, 140].

As a matter of fact, the coupling between the time reversal technique with subspace methods, particularly, with the MUSIC algorithm has led to the creation of what is referred to as the TR-MUSIC. This new concept has lead to a powerful approach for detecting and locating targets in homogeneous and non-homogeneous backgrounds especially in the cases of closely spaced targets or when using very sparse antenna arrays.

3.4.2 TR-MUSIC in Free Space

If we consider an array of N transceivers located in space, each transceiver can radiate into a reciprocal propagating medium in which M point targets having unknown positions $\mathbf{x}_m$ (m=1,2,...,M) are located. The imaging problem for any set of point targets can be roughly defined to be that of forming an "image" of the distribution of target scattering centers $\mathbf{x}_m$, which goes one step beyond with inverse problems that can additionally retrieve the target scattering strengths Γ_m from the available scattering field data. TR imaging is based on the availability of the multistatic data matrix which is given by

$$\begin{aligned} \mathbf{S}_{j,k} &= G(\alpha_j, \alpha_k) - G_0(\alpha_j, \alpha_k), \\ &= \sum_{m=1}^{M} \Gamma_m G_0(\alpha_j, x_m) G(x_m, \alpha_k), \end{aligned} \tag{3.17}$$

where G_0 is the background Green function of the medium where the targets are embedded while G is the full Green function of the combined background plus the medium containing the target, besides, α_j represents a field point at the jth receiver location while α_k is a source point at the kth transmitter location.

Generally, targets are mainly categorized in two main groups where they can be either "*well resolved*" that is they are sufficiently separated from each other so that they can be resolved by the transceiver array, or they are "*non-resolved*" that is multiple scattering occurs between various targets. Starting with the first case, a standard approximation proper to "*well resolved*" targets, is the distorted wave Born approximation (DWBA) [141] that is used in TR studies and is based on neglecting multiple scattering between various targets. Under this condition, $G(x_m, \alpha_k) \approx G_0(x_m, \alpha_k)$, which when used in eq. 3.17 yields the following expression of the MDM within the DWBA denoted here as $\mathbf{S}^b_{j,k}$ where

$$\begin{aligned} \mathbf{S}^b_{j,k} \approx \mathbf{S}_{j,k} &= \sum_{m=1}^{M} \Gamma_m G_0(x_m, \alpha_j) G_0(x_m, \alpha_k), \\ &= \sum_{m=1}^{M} \Gamma_m g_0(x_m) g_0^t(x_m), \end{aligned} \tag{3.18}$$

with $\mathbf{g}_0(x) = \left[G_0(x, \alpha_1), G_0(x, \alpha_2), ...G_0(x, \alpha_N)\right]^t$ is the *background Green function vector*, and $\mathbf{S}^b_{j,k} = \mathbf{S}_{j,k}$ is the DWBA approximation of the MDM. It was shown that within the DWBA the target locations $\mathbf{x}_m$ can be estimated from the MDM as long as $M \leq N$. This is accomplished by forming "TR images" from the singular vectors associated to the nonzero singular values using the background Green function. As for the target scattering strengths Γ_m, they can be determined from the set of singular values. In other words, this is what has been known with DORT method and was previously presented in this chapter.

The "*well resolved* " requirement of DORT method can be removed if instead of forming estimates of the target locations using TR imaging a generalized MUSIC algorithm is employed. In this approach, better known as TR-MUSIC, the singular vectors and singular values of the MDM are still employed as in standard DORT but the singular vectors associated to zero singular values are used instead in the image formation process rather than the singular vectors associated to nonzero singular values. As mentioned earlier DORT method requires that $M \leq N$ and that the targets be "*well resolved*". Notably, the TR-MUSIC scheme does not require that the targets be "*well resolved*" but it does require that the number of targets be less than the number of transceiver elements ($M \leq N$), which even holds in the presence of multiple scattering, as shown in [140, 142].

Both the DORT as well as the TR-MUSIC method are based on the SVD of the **S** matrix which can be written in the form

$$\mathbf{S} = \mathbf{U}\Lambda\mathbf{V}^{\dagger}, \tag{3.19}$$

where Λ is a real diagonal matrix of the singular values while **U** and **V** are unitary matrices whose columns are the left-singular vectors and right-singular vectors of **S** respectively. In fact, the SVD of **S** is equivalent to the eigenvalue decomposition of $\mathbf{K} = \mathbf{S}\mathbf{S}^{\dagger}$ where

$$\mathbf{K} = \mathbf{V}\Lambda^{2}\mathbf{V}^{\dagger}, \tag{3.20}$$

with Λ^2 being a real diagonal matrix of the eigenvalues, and **V** being the eigenvectors matrix.

The eigenvector matrix **V** can be divided into a signal space $\mathscr{S}$ and a noise space $\mathscr{N}$. $\mathscr{S}$ of the TRO **K** is formed by the eigenvectors with nonzero eigenvalues whereas $\mathscr{N}$ is formed by the remaining eigenvectors having almost zero eigenvalues. Consequently, $\mathscr{S} = \text{span}\{\mathbf{v}_i : \lambda_i^2 > 0\}$, while $\mathscr{N} = \text{span}\{\mathbf{v}_i : \lambda_i^2 \approx 0\}$, where $\mathbf{v}_i$ are columns of the unitary matrix **V**.

For homogeneous and isotropic media, and in the framework of DWBA, the signal space $\mathscr{S}$ is also spanned by the conjugation of background Green function $\mathbf{g}_0^*(x)$, with $(*)$ being the complex conjugate. Since $\mathscr{S}$ and $\mathscr{N}$ are orthogonal, their inner product is zero in theory. Consequently, the locations of the targets can be determined by the TR-MUSIC imaging pseudo-spectrum ,

$$\Phi(x) = \frac{1}{\displaystyle\sum_{\lambda_i^2 \approx 0} \left|\langle \mathbf{v}_i, \mathbf{g}_0^*(\mathbf{x}_m)\rangle\right|^2}, \tag{3.21}$$

which will peak (ideally to infinity) when $x = \mathbf{x}_m$, $m = 1, 2, ..., M$. In fact, $\left|\langle \mathbf{v}_i, \mathbf{g}_0^*(\mathbf{x}_m)\rangle\right|$ will vanish whenever a test location $\mathbf{x}_m$ happens to correspond to the actual position of one of the targets, since the significant eigenvectors of the TRO were demonstrated to be a linear combinations of the medium Green function sampled at the targets position [83, 110]; consequently, the pseudo-spectrum $\Phi(x)$ is singular at each scatterer position. More importantly, $\Phi(x)$ computed at any single frequency is capable of pointing the locations of the scatterers. In order to clarify this point, we will consider the example presented in Fig. 3.4 [9], as we can see there are two infinite peaks positing to the locations of two scatterers present in an open medium.

As a matter of fact, the target location within the DWBA reduces to finding the maxima of the pseudo-spectrum defined by eq. 3.21, generated using the background Green function $\mathbf{g}_0^*(\mathbf{x}_m)$ as a steering vector. It is important here to realize, that the pseudo-spectrum computed from either the DWBA or exact scattering, that is to say in other words for "*well resolved*" or "*non-resolved*" targets is

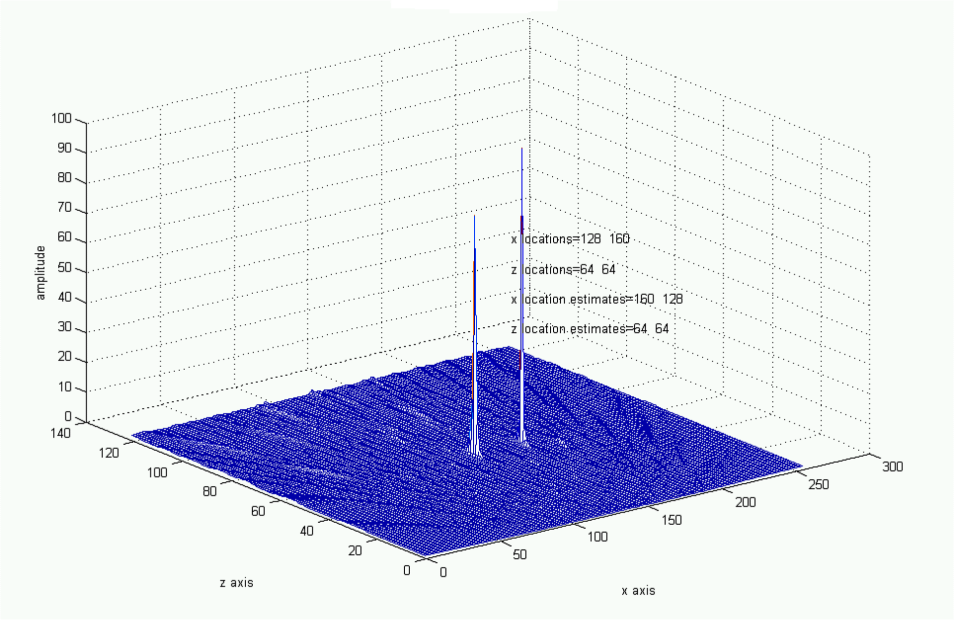

Figure 3.4 Mesh plot of the Pseudo-spectrum of a two well resolved scatterers present in an open medium. *Source: [9].*

the same. The reason is that TR-MUSIC employs the noise subspace, where $\mathscr{N}$ is always orthogonal to $\mathscr{S}$ regardless the "*well resolvedness*" criteria.

Generally speaking, it was shown that the TR-MUSIC pseudo-spectrum computed using the Green function as a steering vector yields accurate estimates of the target locations while achieving a *sub-wavelength resolution*. More importantly, this result pushed forward towards practical implementation for applications not limited to sonar, underwater communication, medicine, non destructive testing and imaging in general [105, 142, 143].

3.5 Concluding on TR Techniques

As discussed in the previous sections, TR techniques involve physical or synthetic retransmission of signals acquired by a set of transceivers in a time-reversed fashion, and can be used for a host of applications. For most of the TR-based applications, the analysis of the TR operator (TRO) is fundamental. Particularly, the eigenvalue decomposition of the TRO forms the basis for both the DORT and TR-MUSIC methods. These two approaches allow TR-based imaging via the use of complementary subspaces of the TRO. Specifically, DORT employs the signal subspace $\mathscr{S}$ whereas TR-MUSIC employs the null subspace $\mathscr{N}$. Furthermore, both the DORT as well as the TR-MUSIC have been considered under the Born approximation for the case of several targets, an approach which neglects multiple scattering between the targets [144].

In fact, it was shown that for well-resolved point-like scatterers, information on scatterer strength(s) and location(s) are partially encoded by the eigenvalues and associated eigenvectors of the TRO signal subspace [108]. Backpropagation of these eigenvectors (in the same background media) yields target images. However, DORT performance degrades if the "*well-resolvedness*" criterion is not met. In this case, the $\mathscr{S}$ eigenvectors become linear combinations of the Green function vectors connecting scatterers to the array of transceivers [110]. Backpropagation of such $\mathscr{S}$ eigenvectors creates overlapped image fields which hamper target imaging and localization. On the other hand, regardless of the "*well-resolvedness*" criteria, the TRO null subspace is orthogonal to the TRO signal subspace, i.e. the projection of any vector formed by the linear combination of the signal subspace eigenvectors onto the null subspace is (ideally) zero. This property is the basis of TR-MUSIC method which provides better detection and location properties than DORT even for poorly-resolved scatterers. It is worthy to note that, both algorithms are valid only when $N > M$ in acoustics.

In both DORT and TR-MUSIC for applications involving physical TR (i.e., where actual retransmission of signals occurs in the same physical medium in which the forward propagation was carried out), knowledge of the background Green function is not required to obtain the TRO. However, knowledge of the Green function is fundamental for imaging purposes (synthetic TR) where retransmission occurs numerically in a synthetic medium. In applications involving inhomogeneous media, the Green function is often not known in a deterministic fashion. The drawback is noisy and unreliable images are obtained [106, 111, 140, 145].

Since the problem of soft-fault detection and location in wiring networks is to a great extent similar to that of target location encountered in radar detection, DORT and TR-MUSIC method were adopted from acoustics to the case of guided wave propagation along transmission lines. In fact, DORT method has shown promising results in locating single soft faults in different complexity networks when applied in its standard version [73] but failed to locate multiple ones. With this in mind, the coming chapter will recall the basic principles of the standard DORT (SDORT) method while presenting some of the simulation and experimental results that validated it. Accordingly, the limitations SDORT faced with multiple faults will be illustrated, this will be followed by proposing a complementary technique based on the standard version permitting the location of multiple faults within different network configurations.

Chapter 4

Soft Fault Location Using DORT Method

Contents

4.1 Introduction

In the previous chapter, we studied the literature of time reversal in locating scatterers in open media, focusing our study on two of its varieties, the DORT and the TR-MUSIC techniques. In fact, both methods intend to locate several targets by using the elements of either the signal space $\mathscr{S}$ for DORT or the noise (null) space $\mathscr{N}$ for TR-MUSIC, of the multistatic data matrix of the system.

In the same fashion, the first two chapters presented a detailed study of the techniques present nowadays for detecting and locating faults in wiring networks. Despite the fact that many of these techniques have shown to be promising, reflectometry-based methods were still the most widely used, without having much changed in their scope and definition [146]. They are known to perform well when dealing with hard faults, which result in large reflections, but start failing with soft faults, characterized by a very weak reflectivity, producing echoes that can pass unnoticed compared to those caused, e.g., by junctions within a network under test (NUT) [4, 28, 147]. A recent work [53] aiming at locating multiple faults falls in this same group, as it mainly works for relatively hard faults.

Based on a radically different concept, the DORT method, allows defining signals bound to focus on one of the scatterers, thus providing a visual method for inferring the position of a previously unknown scatterer. This idea was first transposed to guided-wave propagation, e.g., wire networks, in [148] and has shown to precisely detect and locate single soft faults even within complex network configurations.

Accordingly, we will begin this chapter by introducing the main differences that occur for DORT between the case of free space propagation and that of guided nature along transmission lines. The adaptation of DORT to wiring networks in its standard version (SDORT) will be recalled, although it succeeded in locating single soft faults, it started failing when multiple faults are addressed. Therefore, the performance of SDORT with several faults will be investigated after which an analytical approach enabling separating the signature of different faults in single-fault response matrices will be presented. Notably, the new approach's significance is twofold, it allowed building an alternative DORT implementation (EDORT) which succeeded in detecting and locating multiple soft faults in different NUT complexities, additionally it enabled retrieving the faults' reflection coefficients. Meanwhile, this will be followed by introducing an experimental setup intending to show the practical validation of both the SDORT and EDORT techniques. Moreover, an estimation of the severities of the studied soft faults considered in the experimental validation according to our proposed analytical model will be investigated. The last section of this chapter is devoted to show the robustness DORT method has provided in noisy measuring environments. Last but not least, an assessment of the fault's position retrieved by DORT technique is examined towards issues related to variations in the lengths of cables composing the reference network model.

4.2 DORT Technique: from open media to guided wave propagation

From a formal point of view, a fault in a wiring network is nothing else than a discontinuity, i.e., a scatterer, typically of dimensions well below a wavelength. This simple observation implies that identifying the position (and eventually the nature) of a fault is essentially the same problem as locating a scatterer in a generic medium. Within this context, an entirely different approach to fault location, DORT method, was adopted from the acoustics to the case of guided wave propagation along transmission lines and has shown to be efficient in locating a single soft fault within different complexity networks [148, 149]. As a matter of fact, fundamental differences exist for DORT between the case of open media and that of guided wave propagation, where an adaptation of the method becomes essential to benefit from its advantages. In what follows, we will be illustrating some of the differences that exist between the two cases.

First of all, in free space, a normalized amplitude wave is identically reflected in all directions of a point-like scatterer target after being emitted from one of the transducers of an array of transducers. This wave is reflected by the reflection coefficient Γ_s of the scatterer as shown in Fig. 4.1(a); the target in this case acts as a secondary isotropic source. On the other hand, for the case of guided structures once an identical normalized wave emitted from one of the network testing ports reaches the fault, a similar reflection process takes place. The reflected wave is factored by the reflection coefficient Γ_f of the fault whereas, another $(1+\Gamma_f)$ factored part is transmitted through the network as shown in Fig. 4.1(b).

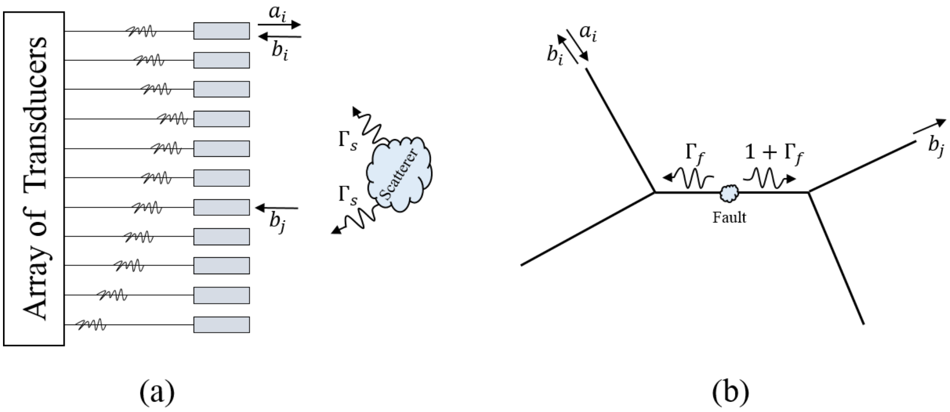

Figure 4.1 Comparison of the propagation phenomena underlying the multiport responses of (a) an electrically small scatterer in an open medium, with reflectivity Γ_s, and (b) a fault in a wire network with reflectivity Γ_f. In both cases, the jth output signal is generated by exciting the ith testing port with a unitary test signal, where in (a), signal b_j is basically related to the scattered field, while in (b), it is related to the total transmitted field, whereas the output signal observed at the ith port will be related to the reflected signal.

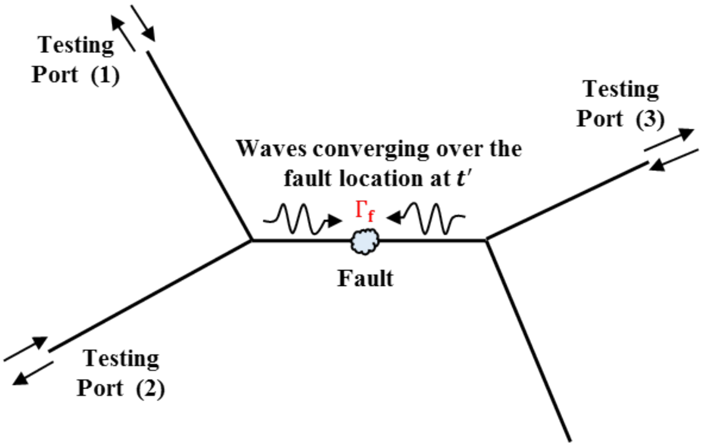

Figure 4.2 Schematic of how focusing signals can be used to locate a fault in a wire network. DORT-based signals are applied to three excitation ports in this example and lead to guided waves converging over the fault location at time t'. For $t > t'$, the same signals will continue propagating over the opposite sides of the fault and, after multiple reflections over the NUT discontinuities (e.g., junctions), will eventually cross again to form unwanted focal spots.

Besides, while in open media the signals that are reflected back to the transducers result from the backscattered field by the target with a negligible contribution from the original test waves generated by the array of transducers, in a wire network, output signals often involve a mix of the two. This situation is shown in Fig. 4.1, where the signal received over the jth port results from the transmission of the test signal applied at the ith port through the fault. Since the reflected and transmitted signals are intrinsically different, the fault's response will appear to differ, depending on the test port under consideration. This situation has no analogy in open media, making the use of the DORT method in guiding media critical.

Furthermore, if we consider the NUT demonstrated in Fig. 4.2, the multiport response of the network is measured through three testing ports. Applying DORT method will enable the generation of signals bound to focus on the position of the fault from the two sides of the branch containing the fault as schematically shown in Fig. 4.2. In fact, the focusing signals will converge on the fault's position at time t', after which for $t > t'$ these waves will continue propagating towards opposite directions of the NUT producing stray signals. Due to the guided structure of the network, these stray signals will eventually undergo interactions with other discontinuities in the NUT such as junctions. Consequently, they will be reflected back and transmitted over other paths of the NUT and thus be subject to constructive interferences producing artifact focal regions other than that of the fault. On the other hand, the intensity of radiated waves in open media weakens as a result of divergent propagation, where energy would spread over larger regions of the space, whereas their intensity can only diminish if the structure is lossy in the case of guided wave propagation. Regrettably, the chances of stray signals interfering as if focusing while maintaining an intensity similar to the true focal region is much higher in wire networks than in an open medium.

Despite the fact that DORT may have shown signs of weakness at some points when adapted to transmission lines, but the literature of existing fault location techniques have shown that they are not necessarily the best choice. This fact is also supported by the parallel that exist between the problem of fault location and inverse problems. Accordingly, DORT method as an inverse technique based on multiport scattering data is inevitably more efficient and accurate, as it is based on the simultaneous use of all available data, rather than a collection of separate tests as done in reflectometry. As a result, the advantages of the DORT makes it an interesting method to be applied for soft-fault detection and location in wire networks, where it has proven to be efficient when dealing with a single-soft fault in an NUT as firstly introduced and validated in [73, 148].

4.3 Application of SDORT for single fault location

We will begin this section by recalling the tools used for creating networks and faults numerically, along with presenting the standards followed to implement our methods and the tools used to produce the results. In fact, this will allow testing the SDORT technique on different network configurations as a first step and will be later used as a basis for the post-processing of experimental data. The main steps of the SDORT will then be recalled, along with presenting some of the simulation results that will validate the approach. In general, any technique might face some restrictions towards specific issues, particularly, SDORT suffers from an impasse whenever multiple soft faults are present in a network. Meanwhile, we will be introducing the limitations encountered by SDORT which will be later thoroughly explained in the next section of this chapter.

4.3.1 Standards and Tools

In order to support the DORT based methods, the same rules and standards that have been adopted in our study of section 2.4.2 & 2.4.3 will be followed in this chapter in order to organize the process of obtaining results and their display. Uniform two-wire transmission lines are reconsidered where the two conductors are 10 mm apart; each line has a total 1.5 mm cross-section distributed between a 1 mm core conductor and a 0.5 mm dielectric coating of relative permittivity $\epsilon_r = 3$. The lengths of the lines as well as the faults' positions are chosen arbitrarily or according to specific needs concerning illustration purposes as what will be shown in the SDORT limitations of sec. 4.4. The soft faults are modeled by a partial removal of the coating surrounding the 1 mm core conductor of the line, where a 0.45 mm radius coating removal will be considered for the SDORT numerical validation. In fact, we recall that the effect of such local modifications in the coating can be quantitatively assessed by computing the relative change R_f. In other words, $R_f = (\mid Z_f - Z_c \mid)/\mid Z_c \mid$ measures the deviation from the characteristic impedance Z_c of the line, after introducing a fault of impedance Z_f, where $R_f = 4\%$ is considered in our case study. It is important to state that the simulations were done on bandwidth of 2 GHz, a sampling frequency of 20 MHz, and a propagation velocity equal to two thirds the speed of light ($v = 2c/3$).

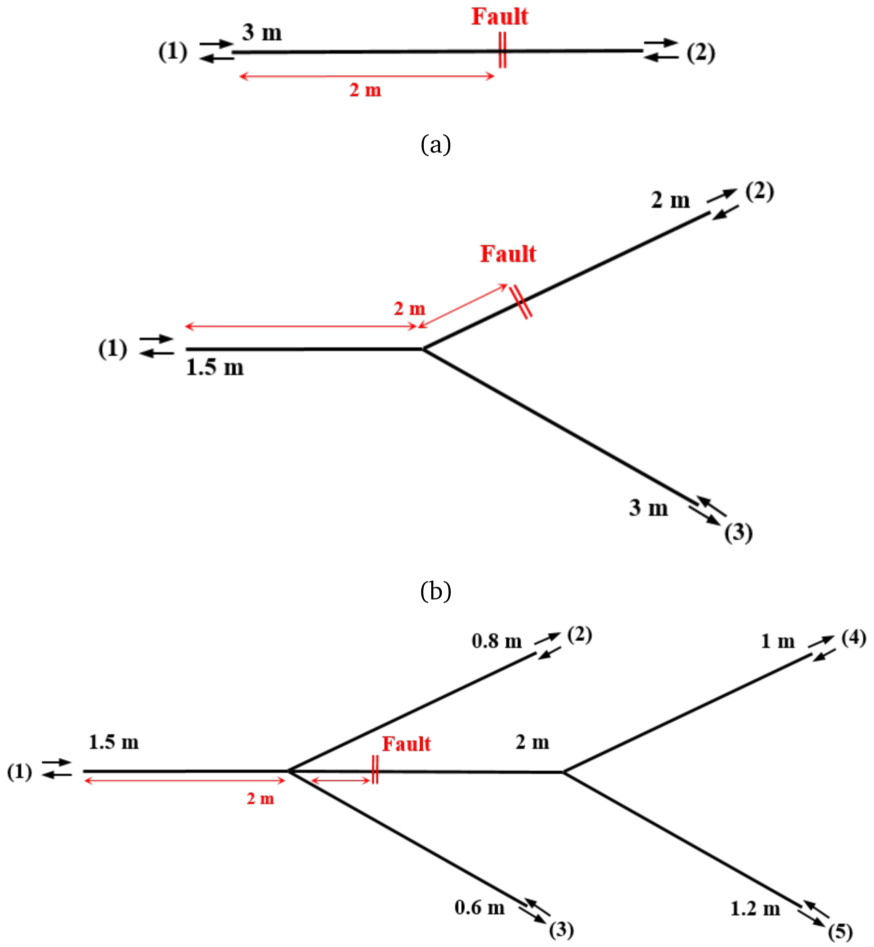

(a)

(b)

(c)

Figure 4.3 Layouts of the three NUTs considered for the numerical validation of the SDORT: (a) a single branch structure; (b) a single Y-junction configuration containing a soft fault on the second branch; (c) a double Y-junction NUT embedding a soft fault between the two junctions. The lengths of the branches were chosen arbitrarily, while considering the same intensity soft fault ($R_f = 4\%$) located at the same distance 2 m from the reference testing port (1) for all configurations.

All results obtained are done by frequency domain simulation on Matlab, using the transmission line theory (TLT) [54], where the transmission lines are considered to be uniform lossless lines with matched-ends. In order to display the results to determine the actual position of the fault, the space-time (ZT diagram) tool is reused which allowed observing the voltage propagation in the network both in space and time. Unfortunately, ambiguity surrounds the observations as the complexity of the network increases due to constructive interferences produced by stray signals. Regrettably, this leads to spurious crossings similar to the focal spots produced by the faults although with lower intensities. The instantaneous power, given by eq. (4.1), where $v^{-}(x,t)$ and $v^{-}(x,t)$ are the forward and backward voltage propagations, is an effective solution to this problem since its corresponding focal region is of higher intensity than that of the voltage waves .

$$p(x,t) = Z_c^{-1}[v^{-}(x,t) + v^{+}(x,t)]^2, \tag{4.1}$$

In fact, for the case of equal-amplitude signals, the instantaneous power will be four times higher than that of each signal. As a reference, if the total amplitude was considered, only a twofold increase would be observed. Therefore, the use of eq. (4.1) ensures a higher dynamics for the detection of the focal region. The detection of the focal region and, therefore, the position of the fault can be also greatly simplified by computing the total energy $E(x)$ observed at each position given by

$$E(x) = \int p(x,t)dt. \tag{4.2}$$

The main advantage of this operation consists in the removal of the temporal dimension where it will be plotted in the form of an energy diagram as function of the distance.

4.3.2 Process and Steps

The basic operations and properties involved in the use of SDORT technique in fault location are here recalled where a detailed study of this method could be found in [73, 148].

When dealing with an NUT displaying N testing ports, its corresponding scattering matrix allows a direct computation of the output signals generated by any testing signal applied to one or more of its N testing ports. As such, SDORT applied to fault detection is based on the availability of this matrix, which can be measured, either numerically or by means of a vector network analyzer (VNA). As it is often the case when dealing with soft faults, the SDORT procedure requires a baselining approach, i.e., taking the difference between the response of the NUT, containing an eventual fault, and a reference response of a healthy version of it [28, 150]. This operation ideally removes the spurious echoes generated by impedance discontinuities like junctions, leaving only those echoes initially generated by the interaction between the testing signals and the faults. For the case of SDORT, the NUT response after baselining will be $\mathbf{S} = \mathbf{S}_f - \mathbf{S}_h$, with $\mathbf{S}_f$ and $\mathbf{S}_h$ being the scattering matrices of the (eventually) faulty NUT and its healthy version, respectively.

Following the properties of the SDORT in free-space propagation, sets of input signals can be defined, such that when injected through the testing ports of a reference model of the NUT (without a fault), they will lead to waves focusing onto each fault. These signals can be computed by solving the eigenproblem $\mathbf{S}\mathbf{S}^{\dagger}\mathbf{U}_n = \lambda_n \mathbf{U}_n$. The number $n < N$ of most significant eigenvalues hints at the number of potential faults found in the NUT; if the properties proved for DORT [83] hold also for NUTs, then each fault could be spotted by monitoring the propagation of input signals whose Fourier spectra would be defined by the scalar components of each eigenvector $\mathbf{U}_n$. This operation is carried out by means of a numerical simulator for transmission lines, modeling the layout of the healthy NUT; the fault's position would be found by looking either for a focal spot in the ZT diagram or for the maximal energy peak in the energy diagram. It is worthy to note that, the sheer complexity of signal propagation through complex NUTs is a formidable obstacle to more general theoretical proofs. Since the basic idea behind any DORT method is to exploit the scattering nature of a fault and the time-reversal symmetry of wave propagation, there should be no doubt about the fact that DORT-based signals are bound to focus over the scatterer position, even in complex media.

4.3.3 SDORT Numerical Validation

Numerical results have been deducted using the network configurations presented in Fig. 4.3, where three different complexity NUT's have been considered, a single branch network, a single Y-junction structure, and a double Y-junction network configuration. These results are meant firstly to recall the potential benefits provided by the SDORT technique adapted to complex wire networks, as well as presenting several general aspects of the application of the method (eigendecomposition, testing signals, etc.).

We will first begin with the simple single-branch NUT of Fig. 4.3(a) where the soft fault is located at 2 m from the reference testing port (1) of a 3 m cable. In this simple case the TRO $\mathbf{K}$ could be analytically written as

$$\mathbf{K} = 2\Gamma_f^2 \begin{bmatrix} 1 & e^{-j\beta(L_1-L_2)} \\ e^{-j\beta(L_2-L_1)} & 1 \end{bmatrix}, \tag{4.3}$$

where L_1 and L_2 are the distance from ports (1) and (2) to the fault respectively. Applying an eigenvalue decomposition of $\mathbf{K}$ results in two eigenvalues λ_1 and λ_2 after forcing

$$det(\mathbf{K} - \lambda \mathbf{I} = 0) \tag{4.4}$$

with $\mathbf{I}$ being the identity matrix. According to the basics of DORT method, and since the network contains a single soft fault, one significant eigenvalue will be obtained; indeed, $\lambda_1 = 4\Gamma_f^2$ while $\lambda_2 \approx 0$. Consequently, the eigenvectors corresponding to λ_1 will form the components of the testing signals that shall be applied to the NUT. With this in mind, the signals shown in Fig. 4.4 will be applied to the two testing ports of a reference model of the single branch network. A time delay can be observed between the two testing signals which is intended to allow them interfere constructively on the position of the fault at the same time once injected in the reference model of the network. Accordingly, a focal spot can be seen at the fault's position as shown in the ZT diagram of Fig. 4.5.

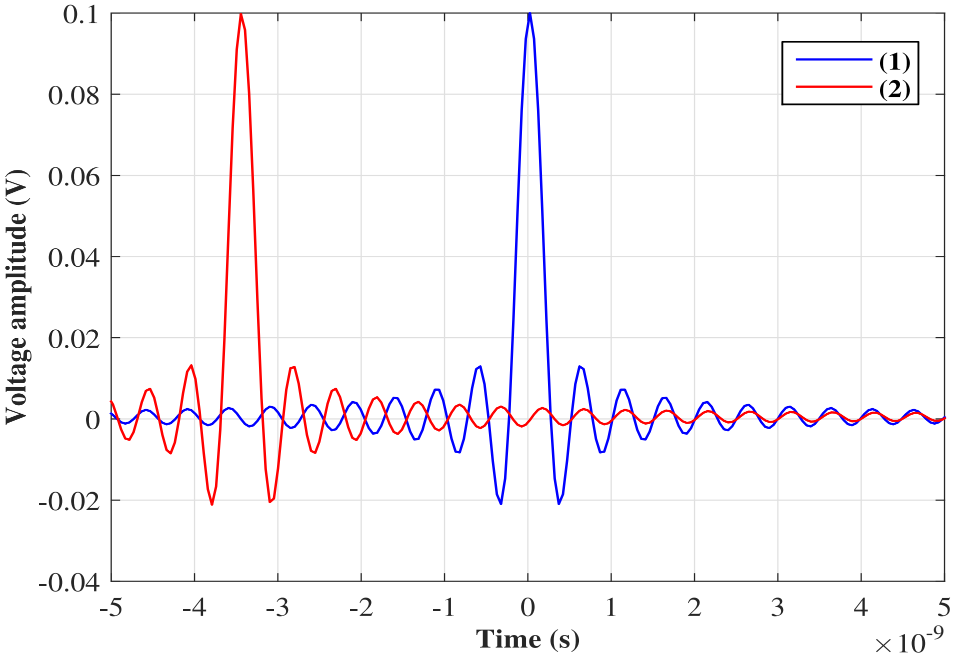

Figure 4.4 The injected signals resulting from the eigenvalue decomposition of the TRO of the NUT of Fig. 4.3 (a) as applied to the testing ports of its reference model and aiming to focus on the position of the fault.

In order to check the feasibility of SDORT on more complex networks, the single-junction network of Fig. 4.3 (b) is considered. A closed form computation of the TRO becomes more complex in this case, so we will proceed to a numerical calculation by the simulation model. The diagonalization of the 3 × 3 TRO matrix **K** of this configuration will produce three eigenvalues as shown in Fig. 4.6, where a significant non-zero eigenvalue ($\lambda_1 > 0$) is obtained along with two negligible ones ($\lambda_1 \approx \lambda_2 \approx 0$). The eigenvector components of λ_1 will form the testing signals that will be injected into the three testing ports of the corresponding reference NUT model. The position of the soft fault located at 2 m from port (1) along the second branch can be pinpointed by the focal spot obtained at its position when observing the voltage propagation along the second path on the ZT diagram of Fig. 4.7. Remarkably, SDORT has allowed retrieving the fault's position with respect to the NUT's configuration, where no focusing can be spotted along the third path of the network as obtained in the ZT diagram of Fig. 4.8. In fact, comparing the two ZT diagrams permits the elimination of any ambiguity regarding the fault's position where it can be inferred that it is located on the second branch of the tested network. This property exceeds in efficiency standard TDR techniques that are limited to knowing the distance at which the fault is located with respect

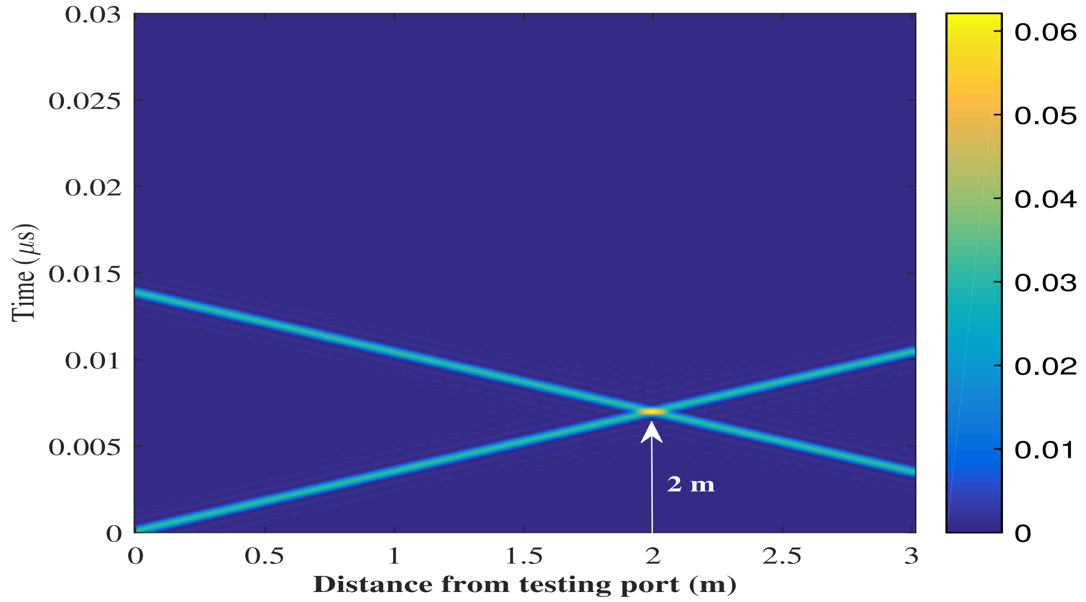

Figure 4.5 The space-time ZT diagram showing the voltage propagation along the single branch network of Fig. 4.3 (a). A focal spot can be seen at 2 m from the reference port (1) on the position of the fault.

to the used testing port. A simple conclusion, which is predictable with hindsight, is that to have focusing and, therefore, to locate the position of the fault, it is necessary to have at least two testing ports connected to the NUT in such a way as to have signals propagating toward the fault along opposite directions.

A more complex network composed of two Y-junctions is now considered and presented in Fig. 4.3 (c). This NUT is composed of five testing ports and a soft fault located on the branch linking the two junctions. Applying a numerical calculation of the TRO followed by an eigenvalue decomposition results in four negligible eigenvalues and a significant one. The eigenvectors corresponding to the dominant eigenvalue form the testing signals which are injected into the testing ports of the NUT to interfere constructively on the fault's position at the same time. As we have mentioned earlier, the increased complexity of the network leads to spurious constructive interferences at positions other than that of the fault although with weaker intensities; this is due to the guided nature of the propagation medium. Consequently, observing the power flow instead of the voltage propagation helps to a great extent in compensating this effect and enhances the visibility of the fault related focal spot which can be clearly observed in the power ZT diagram of Fig. 4.9.

As a matter of what we have recalled, SDORT presented a heuristic location criterion of a single soft fault in different complexity NUTs. It has stressed its ability to synthesize testing signals adapted to the tested network so as to directly focus on the fault's location, thus ensuring a direct estimation of the fault's position without the need of iterations. On the other hand, while passing from a single scatterer to several is trivial with waves propagating in homogeneous media, this is no longer true

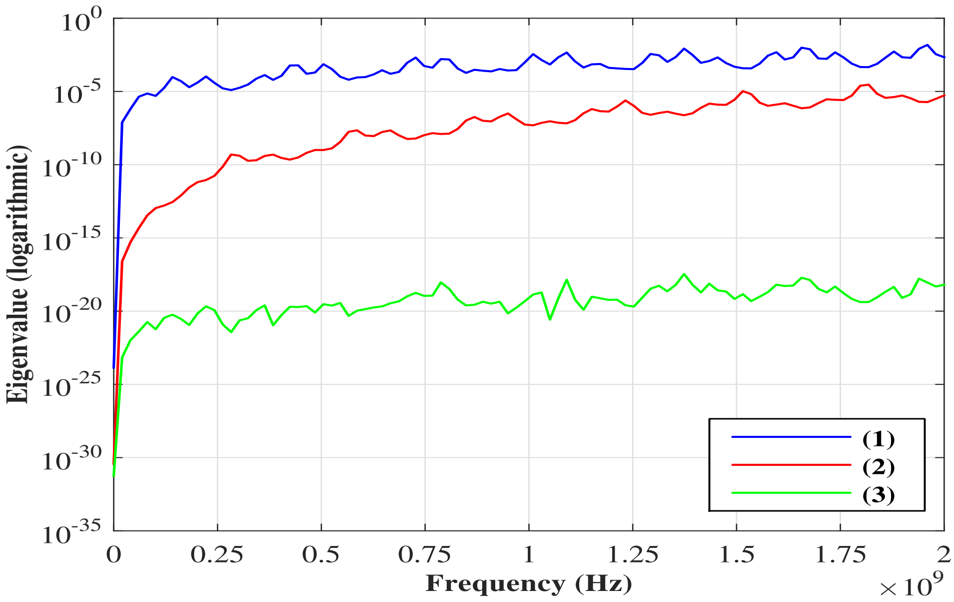

Figure 4.6 The eigenvalues of the TRO corresponding to the NUT of Fig. 4.3 (b) showing a significant eigenvalue (1), in addition to two almost negligible ones. The components of the dominant eigenvalue will form the testing signals intended to focus on the fault's position once injected in the NUT's reference model

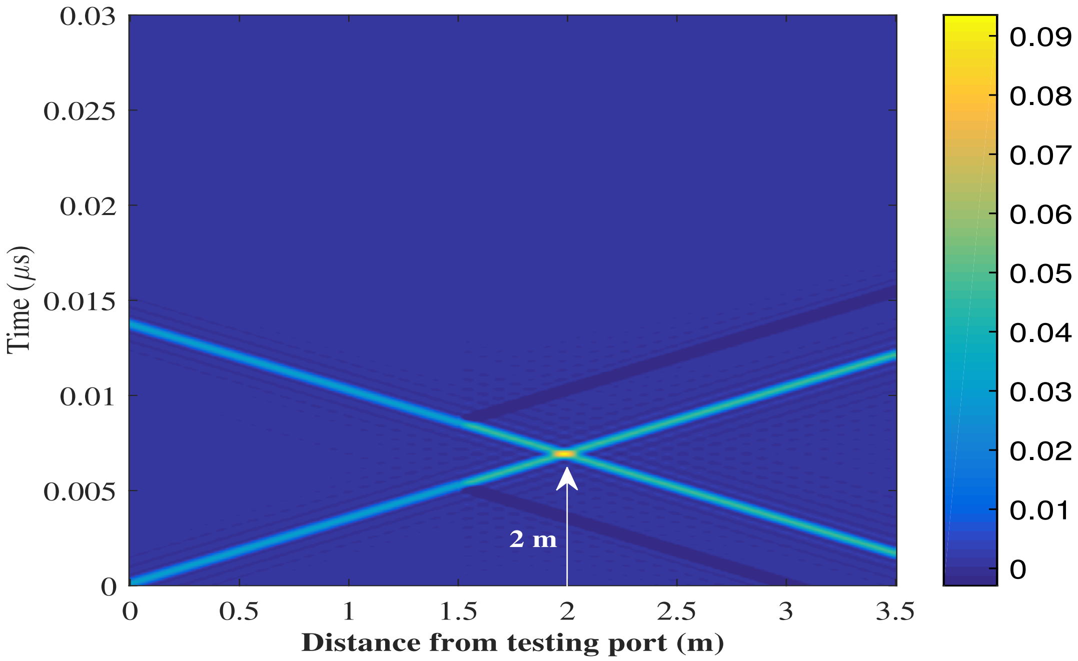

Figure 4.7 The space-time ZT diagram of the network presented in Fig. 4.3 (b) showing the voltage propagation along the second path of the network where a focal spot can be spotted at 2 m from the reference port on the position of the soft fault.

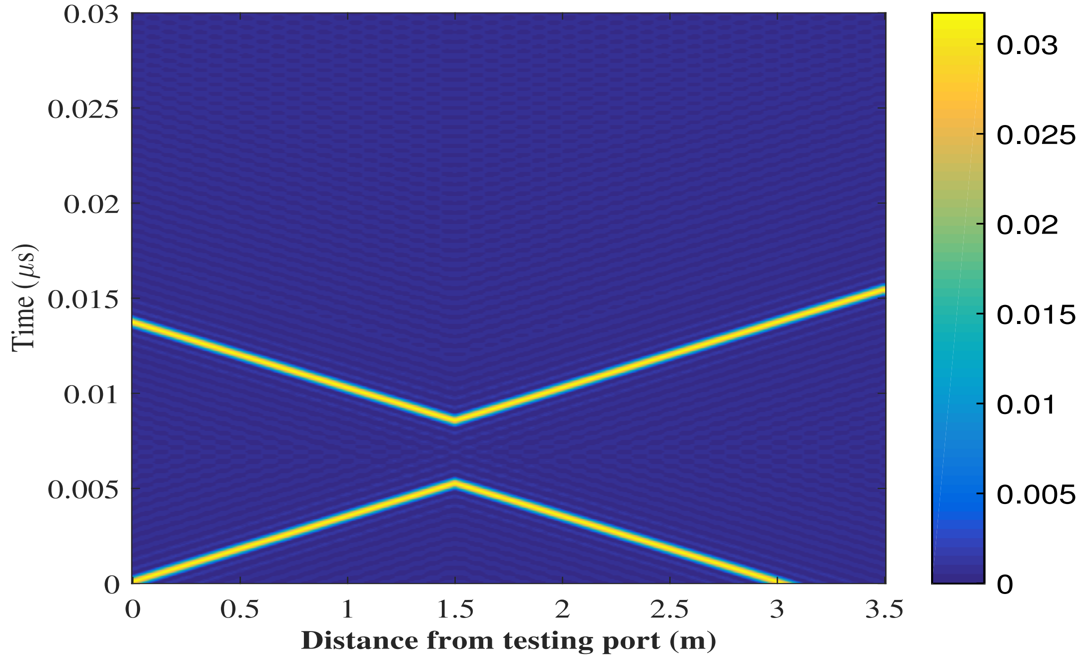

Figure 4.8 The ZT diagram of the NUT of Fig. 4.3 (b) showing no focusing when observed along the third path of the NUT which do not contain the fault.

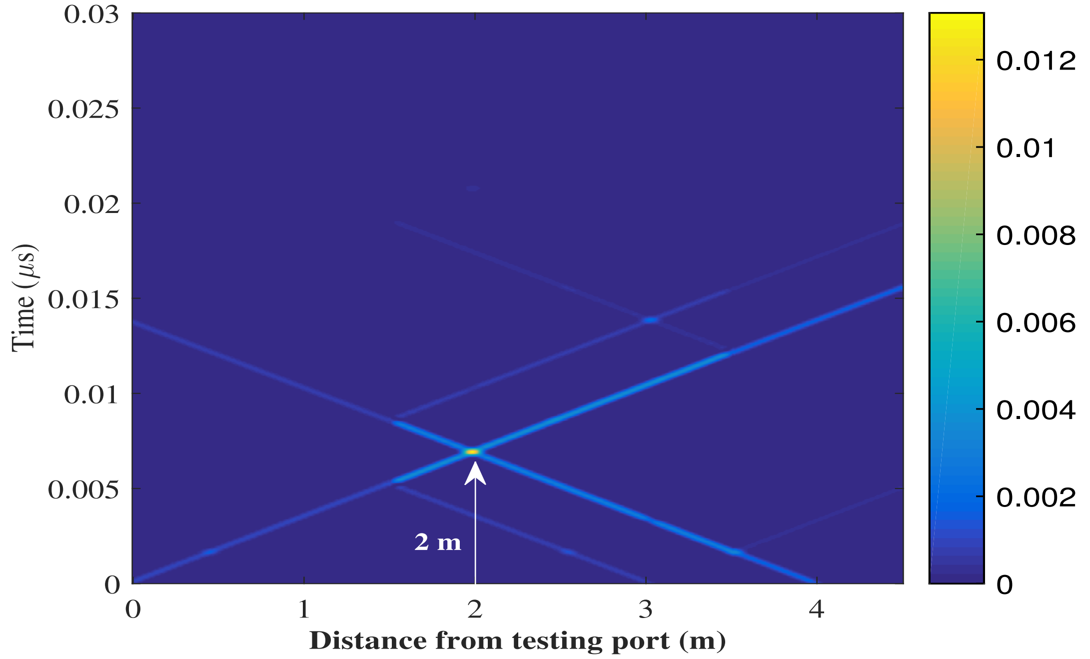

Figure 4.9 The ZT power summation observed along the fifth path of the reference model of Fig. 4.3 (c) intending to clarify the fault's position unambiguously.

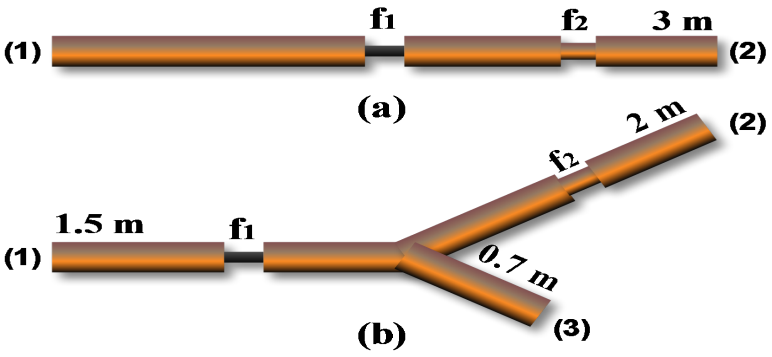

Figure 4.10 Layouts of the NUTs considered in the numerical studies intended to investigate the limitations of SDORT: (a) single-branch NUT; (b) single-junction network configuration. Both structures include the lengths of the branches and present two soft faults of different severity.

for the case of wiring networks. Multiple faults cannot be resolved separately, because of their strong coupling via guided propagation. For instance, this topic becomes a crucial research issue especially within todays wide spread of cumulated lengths of wiring networks that are susceptible to the occurrence of several faults in a row.

4.4 SDORT performance with multiple faults

The limitations SDORT faced in the case of multiple faults can be easily exposed by means of numerical simulations. Numerical results have been deducted using the network configurations presented in Fig. 4.10, where two different NUT's have been considered: a single cable and a single junction structure.

Dealing with the general network structure, illustrated in Fig. 4.10 (a), two soft faults are introduced, where the strongest is obtained by reducing the thickness of the coating from 0.5 mm to 0.45 mm over a length of 2 mm, whereas the weaker one is associated to a mere 0.05 mm coating removal producing an $R_{f1} = 4\%$ and $R_{f2} = 2\%$ respectively.

The first issue with SDORT is the lack of selective focusing. This can be demonstrated by tracking the voltage propagation both in time and space in the NUT, generated by applying to the testing ports the eigenvector corresponding to the most significant eigenvalue λ_n. According to [83], there should be a single spot appearing at the position of the most significant fault. In fact, for the NUT in Fig. 4.10 (a), the ZT diagram of Fig. 4.11 shows two focal spots where the faults were introduced.

Even though the faults are not excited individually, it could be argued that they are still visible and rightly located. That is where the second issue comes in: the ratio of the focal-spot intensities does not appear to represent the ratio of the fault severities. This means that it is not possible to use the focal-spot intensity as a proxy of a fault severity. Moreover, having focal-spot intensities spanning a large dynamical range can hinder the detection of faults associated to weaker focusing,

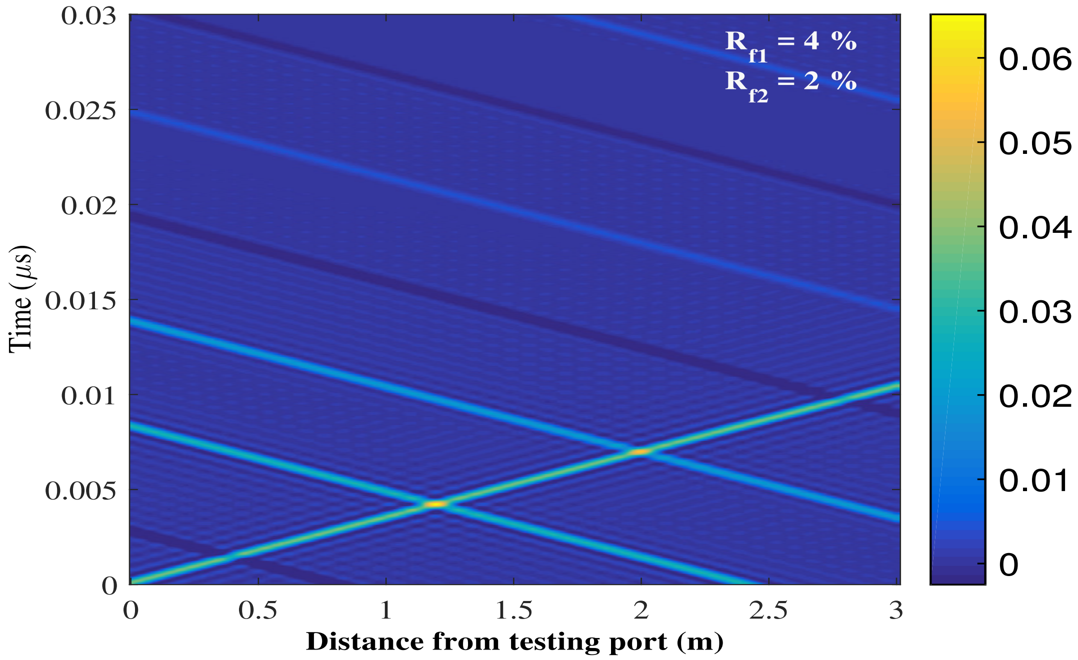

Figure 4.11 The space-time (ZT) diagram showing voltage propagation along the single-branch NUT in Fig. 4.10 (a). Two focal spots of different intensity can be observed at the positions of the two faults, at 1.15 and 2 meters.

particularly in the case of noisy signals. As an example, consider the NUT in Fig. 4.10 (a) with two faults of different intensities, placed at 1.15 m and 2 m, respectively. When choosing a weaker second fault (R_{f2} goes from 4% down to 0.5%), while keeping the first one fixed ($R_{f1} = 6$ %), the energy diagrams in Fig. 4.12 show a vanishingly low focusing over the weaker fault, resulting into a less likely identification. Moreover, the reduction in the energy at the second fault position does not seem to be related to the reduction in the fault intensity.

On the other hand, one of the most interesting properties of SDORT was its effectiveness in locating single faults within complex NUTs, composed of several junctions and branches [148]. This property is no longer guaranteed in the case of multiple faults. In order to better illustrate this point, the NUTs shown in Fig. 4.10 were considered, each with two faults where $R_{f1} = 6\%$ and $R_{f2} = 3\%$, found at the same distances with respect to the reference port (1 m for the stronger soft fault and 1.5 m for the weaker one). The objective is to assess how a changing the NUT complexity impacts the focusing capabilities of SDORT. The energy diagrams in Fig. 4.13 show that a more complex NUT introduces an ambiguity on the weaker fault's position, due to artifacts that appear as a result of junction-related echoes, in spite of the baselining procedure. This situation is expected to worsen with NUT's composed of several junctions and branches.

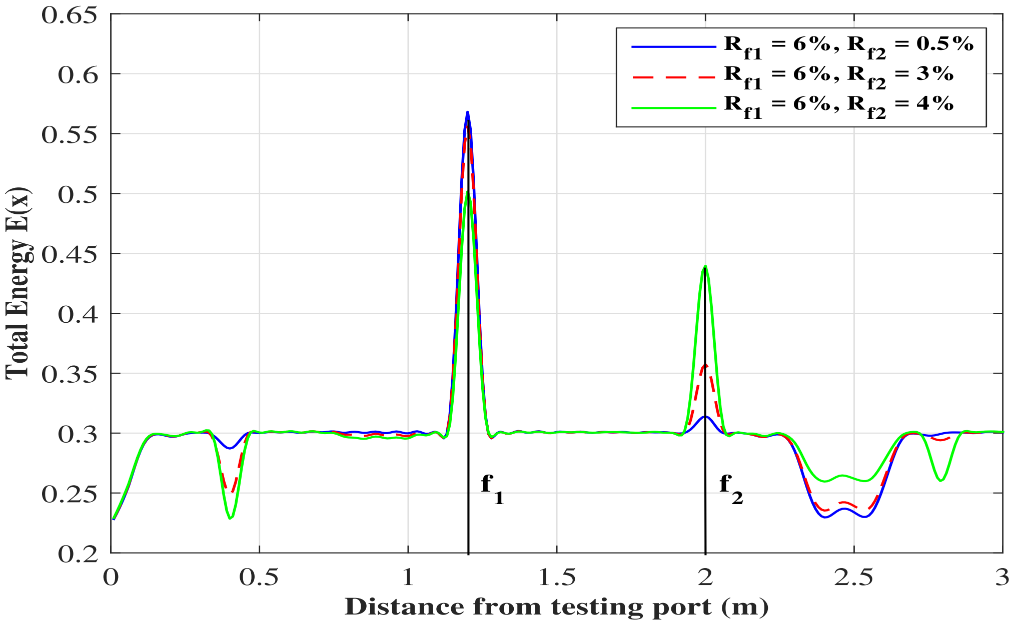

Figure 4.12 The total energy $E(x)$ as estimated along the path of network Fig. 4.10 (a) comparing three different fault severity configurations.

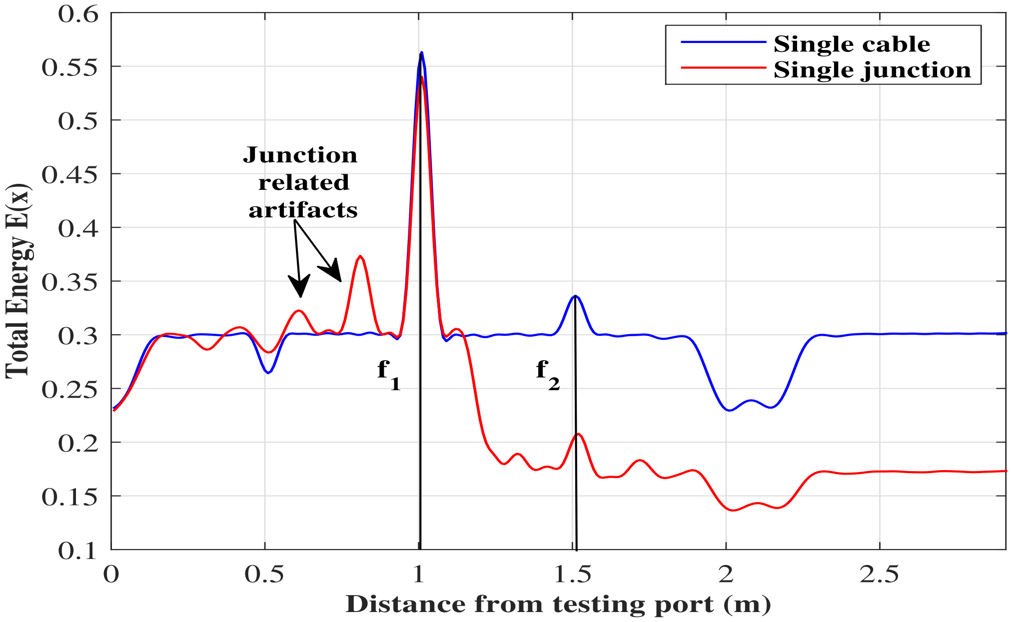

Figure 4.13 The total energy $E(x)$ obtained for the description comparing the responses of weak faults with respect to the network's complexity between the single-branch configuration of Fig. 4.10 (a) and the single-junction NUT of Fig. 4.10 (b) along its second path, while considering two soft faults at the same distances with respect to the reference port (1 m for the first soft fault and 1.5 m for the weaker one).

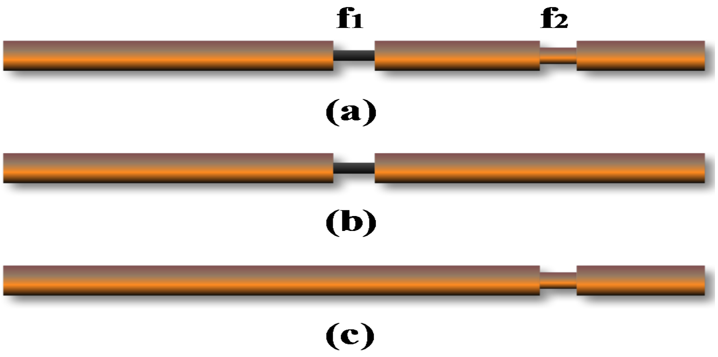

Figure 4.14 A single-branch NUT used for demonstrating the possibility of separating a multiple-fault scattering matrix containing two soft faults (a) into two replicas of the NUT presenting only fault 1 (b) or fault 2 (c).

4.5 Alternative iterative formulation

The issues SDORT faced in case of multiple faults can be ascribed to the coupling existing between the faults' responses, which in turn leads to simultaneous multiple focusing. If the signals relative to each fault could be separated, then individual focusing would be available again, making the detection and location of the faults more robust and precise. Moreover, without the separation of the fault responses, it is not possible to assess their severity, a major drawback in an early-warning technique.

4.5.1 Separation of a scattering matrix

The key element in addressing separately each fault is to understand how the response an NUT featuring only one fault at the time is related to the response of the multiple-fault case. In order to get a better insight into this problem, we start by considering the simple NUT in Fig. 4.14 (a) consisting of a single cable with two soft faults with reflection coefficients Γ_1 and Γ_2, respectively. Neglecting multiple reflections, its transmission coefficient can be expressed as

$$\begin{aligned} S_{ij}^{f} &= (1+\Gamma_1)(1+\Gamma_2)e^{-i\beta L} \\ &= e^{-i\beta L} + (\Gamma_2+\Gamma_2)e^{-i\beta L} + (\Gamma_1\Gamma_2)e^{-i\beta L} \end{aligned} \tag{4.5}$$

where β is the propagation constant and L the total length of the line, whereas for the case of the healthy configuration

$$S_{21}^{h} = e^{-j\beta L}. \tag{4.6}$$

Hence the baselined difference scattering transmission coefficient is

$$\begin{aligned} S_{21} &= S_{21}^{f} - S_{21}^{h} \\ &= e^{-i\beta L} + (\Gamma_1 + \Gamma_2)e^{-i\beta L} + (\Gamma_1\Gamma_2)e^{-i\beta L} - e^{-j\beta L} \\ &= (\Gamma_1 + \Gamma_2)e^{-j\beta L} + (\Gamma_1\Gamma_2)e^{-j\beta L}. \end{aligned} \tag{4.7}$$

Since we are dealing with soft faults, $|\Gamma_i| \ll 1, i = 1, 2$, so that $\Gamma_1\Gamma_2 \ll \Gamma_1 + \Gamma_2$, allows in turn to simplify the S_{21} expression to

$$\begin{aligned} S_{21} &\approx (\Gamma_1 + \Gamma_2)e^{-j\beta L} \approx \Gamma_1 e^{-i\beta L} + \Gamma_2 e^{-i\beta L} \\ &= S_{21}^{1} + S_{21}^{2}. \end{aligned} \tag{4.8}$$

where S_{21}^{i} is the scattering transmission coefficient of the single-fault NUT with only the ith fault appearing, as in Figs. 4.14 (b-c). The level of accuracy in neglecting the product $\Gamma_1\Gamma_2$ can be better grasped by taking the special case $\Gamma_1 = \Gamma_2 = \Gamma$, yielding $|\Gamma_1\Gamma_2|/|\Gamma_1 + \Gamma_2| = |\Gamma|/2$. Typical values of $|\Gamma|$ shown in sec. 4.6.4 are smaller than 0.01, implying a residual error of less than 1 %.

The same result can be found for the remaining terms in the baselined scattering matrix, i.e.,

$$\mathbf{S}_G \approx \sum_{i=1}^{N_f} \mathbf{S}_i. \tag{4.9}$$

where N_f is the number of faults in the NUT. This result is in general valid for any layout, as long as the faults can be regarded as soft, a property equivalent to the first Born approximation widely used in wave scattering [72].

The superposition (4.9) can be exploited in order to estimate the scattering matrix of the ith fault from the measured $\mathbf{S}_G$ matrix. To this end, let us recall that the SDORT does provide a very good estimate of the position of the faults. In particular, the position of strongest focusing typically coincides with the most severe fault. This observation can serve as a guess of the position of one of the faults. It is therefore possible to insert a dummy fault into the healthy-NUT model, previously used for baselining: the nature of this dummy fault is not important, as discussed later on. The scattering matrix of this modified NUT will be referred to as $\mathbf{S}_d^i$, for the ith fault. This would be the response of the NUT if only one fault was present. The idea is now to remove the contribution of $\mathbf{S}_d^i$ from $\mathbf{S}_G$, in order to be left with a scattering matrix containing only the remaining $N_f - 1$ faults.

To this end, we can exploit a fundamental property of SDORT: in case of a single-fault, the scattering matrix has only one eigenvalue. Since each $\mathbf{S}_i$ matrix is symmetric, it can be expressed exactly as [151].

$$\mathbf{S}_i = \nu_i \mathbf{w}_i \mathbf{w}_i^t, \tag{4.10}$$

where ν_i is the only non-zero eigenvalue of $\mathbf{S}_i$ and $\mathbf{w}_i$ the associated eigenvector. As shown in [108], the eigenvectors only depend on the position of the fault rather than its intensity, which is coded by ν_i. Therefore, assuming the guessed position of the fault is correct, the scattering matrix of the dummy-fault NUT is

$$\mathbf{S}_d^i = \mu_i \mathbf{w}_i \mathbf{w}_i^t \tag{4.11}$$

i.e., correct up to a scalar factor dependent on the unknown fault reflectivity, implying that $\mathbf{S}_i = \alpha_i \mathbf{S}_d^i$. Hence, from (4.9),

$$\mathbf{S}_G = \sum_{i=1}^{N_f} \alpha_i \mathbf{S}_d^i = \sum_{i=1}^{N_f} \alpha_i \mu_i \mathbf{w}_i \mathbf{w}_i^t. \tag{4.12}$$

The missing coefficients α_i can be estimated by noticing that

$$\mathbf{w}_i^t \mathbf{S}_G \mathbf{w}_i = \alpha_i \mu_i (\mathbf{w}_i^t \mathbf{w}_i)^2 + \sum_{k \neq i} \alpha_k \mu_k (\mathbf{w}_k^t \mathbf{w}_i)^2. \tag{4.13}$$

The first term in (4.13) provides direct access to α_i. In general, the remainder summation is different from zero when sampled at a given frequency; this is not expected to be an issue, since the scalar products lead to phase-shift angles that change with the frequency. As a result, the time-domain signals used for location involve an averaging effect that is expected to reduce the impact of the remainder, especially for complex networks.

We will therefore use

$$\begin{aligned} \hat{\alpha}_i &= \frac{\mathbf{w}_i^t \mathbf{S}_G \mathbf{w}_i}{\mu_i (\mathbf{w}_i^t \mathbf{w}_i)^2} \\ &= \alpha_i + \sum_{k \neq i} \alpha_k \frac{\mu_i (\mathbf{w}_k^t \mathbf{w}_i)^2}{\mu_k (\mathbf{w}_k^t \mathbf{w}_k)^2} \end{aligned} \tag{4.14}$$

as an estimate of α_i. Notice that (4.14) is based on the measured baselined scattering matrix of the multiple fault NUT, and the eigenexpansions of the dummy single-fault NUTs.

Finally, (4.14) yields an estimate of the single-fault scattering matrices, as

$$\hat{\mathbf{S}}_i = \hat{\alpha}_i \mathbf{S}_i^d. \tag{4.15}$$

As a matter of fact, $\hat{\mathbf{S}}_i$ contains only the signature of ith fault, where the eigenvalue decomposition of its corresponding TRO $\hat{\mathbf{K}}_i$ produces an eigenspace with only one significant eigenvalue. Accordingly, the components of this eigenvalue form the testing signals that will focus on the position of the ith fault separately once propagated in the reference model of the NUT. It is worthy to note that, access to the individual $\mathbf{S}_i$ not only allows energy focusing on individual faults, but also permitted estimating the fault's severity, as will discussed in sec. 4.5.3.

4.5.2 The EDORT algorithm

The previous discussion and results can be translated into an algorithm that iteratively extracts the individual scattering matrices of single faults of an NUT. The steps required are summarized in what follows:

1. measure the global scattering matrix $\mathbf{S}_G^1$ of the (eventually) multiple faulty NUT.
2. apply the SDORT method on $\mathbf{S}_G^i$, in order to estimate the position of the strongest soft fault
3. include a dummy soft fault on the guessed position and compute its scattering matrix $\mathbf{S}_d^i$
4. compute the only significant eigenvalue of $\mathbf{S}_d^i$ and its eigenvector
5. compute $\hat{\alpha}_i$ and $\hat{\mathbf{S}}_i$, according to (4.14) and (4.15)
6. remove the ith fault contribution by computing $\mathbf{S}_G^{i+1} = \mathbf{S}_G^i - \hat{\alpha}_i \mathbf{S}_d^i$
7. increase i and repeat from step 2) until the update $\mathbf{S}_G^i$ has no significant eigenvalue.

The stop criterion in this algorithm requires to set a threshold for negligible eigenvalues, a choice that really depends on the configuration, especially the noise level, numerical accuracy, etc. To better visualize this point, Fig. 4.15 shows the dominant eigenvalue of each EDORT iteration applied to the single branch NUT of Fig. 4.10 (b). In fact, two significant eigenvalues corresponding to the first and second iteration can be recognized, whose eigenvector components located the first and second soft fault present in the NUT. On the other hand, the third iteration leads to a negligible eigenvalue compared to the first two thus indicating the absence of any new considerable discontinuity in the structure. For instance, in the case of a purely numerical computation, one could also consider the machine epsilon. Besides from a more practical point of view, as the estimated severity gets very small, the user could stop the procedure as it is no longer worth continuing, since the fault would pose no threat to the proper functioning of the NUT.

4.5.3 Estimating the fault severity

Having provided an approximate procedure for extracting the single-fault matrices $\mathbf{S}_i$ as presented in sec. 4.5.1, the severity of each fault can be assessed without ambiguity, as these matrices have rank equal to one. Since the first Born approximation underpins soft-fault related scattering matrices, by defining $\tau_k = e^{-\beta L_k}$ the transmission function between the fault position and the kth port

$$S_{kj} = \Gamma_i \tau_k \tau_j, \tag{4.16}$$

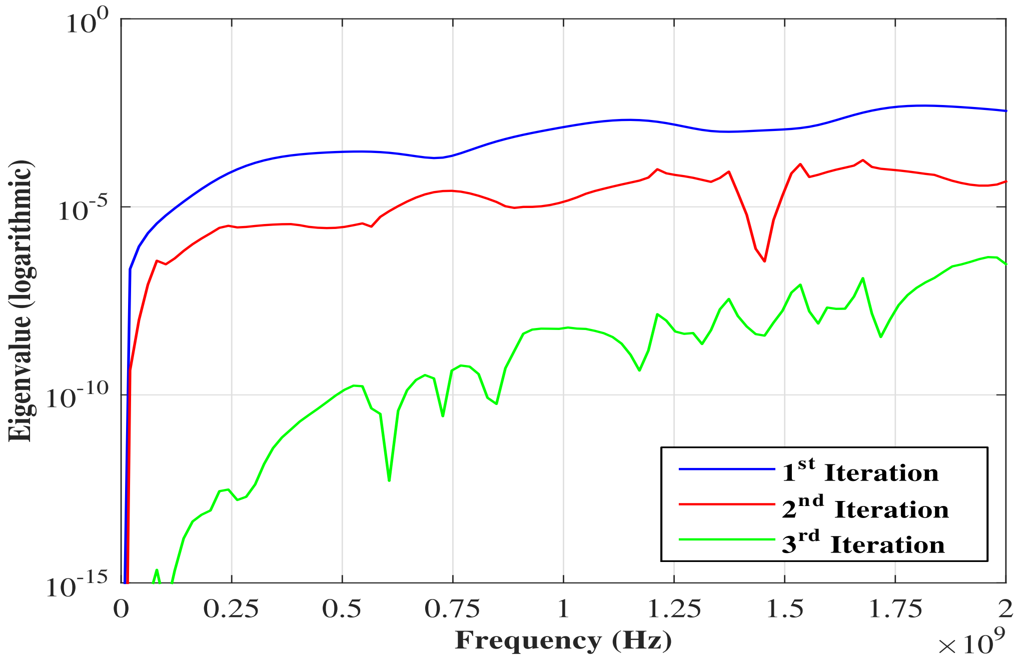

Figure 4.15 The most significant eigenvalue for the TRO, calculated for the single junction NUT of Fig. 4.10 (b) after applying the EDORT steps for the fist, second and third iterations.

where Γ_i is the reflection coefficient of the ith fault, and L_k being the distance between fault position and the kth port. This follows that

$$\begin{aligned}\sum_{i,j}|S_{ij}|^2 &= ||\Gamma_f||^2 \sum_{i,j}|\tau_i\tau_j|^2 \\ &= ||\Gamma_f||^2 \sum_{i}|\tau_i|^2 \sum_{j}|\tau_j|^2 \\ &= ||\Gamma_f||^2 (\sum_{i}|\tau_i|^2)^2.\end{aligned} \tag{4.17}$$

Noting that $||\mathbf{S}_i||_F$ is the Frobenius norm of $\mathbf{S}_i$, given by

$$||\mathbf{S}_i||_F = \sqrt{\sum_{i,j}|S_{ij}|^2}, \tag{4.18}$$

(4.16) yields

$$|\Gamma_i| = ||\mathbf{S}_i||_F \left(\sum_{k=1}^{N}|\tau_k|^2\right)^{-1}. \tag{4.19}$$

This last result requires a priori knowledge of the τ_i functions. In fact, these are known through the healthy NUT model used for baselining. The fact that only the moduli of the τ_i are required in (4.19) implies that errors in the positioning of the dummy fault have a minor impact on the accuracy of the estimated $|\Gamma_i|$, as long as the NUT is tested at frequencies where propagation can be regarded as subject to weak dissipation.

Departure from Born first approximation are shown in sec. 4.6.4 to lead to local errors that have in fact negligible impact on the overall performance of the procedure, as these errors have zero average (i.e., turning phase-shift angles).

4.6 Validation

The first part of this section will be devoted to provide the numerical support that will prove the efficiency of EDORT in locating multiple soft faults in complex wiring configurations. In fact, these numerical results will handle NUTs of high complexities that are hardly tested with experimental setups. After that, an experimental study will be conducted in order to validate the method and stress its feasibility for real-life practical network implementation. We will first begin by introducing the experimental setup used to perform the experimental measurements for applying the DORT methods. The successful results SDORT in locating single-soft faults will be recalled after which we will present the results obtained by EDORT that allowed locating multiple soft faults in different NUTs. After reinstating the ability of EDORT in testing and locating each fault separately, the accuracy of the estimation of the fault severity is tested in sec. 4.6.4.

4.6.1 EDORT Numerical Validation

The proposed EDORT procedure have been tested numerically using the same simulation setup previously utilized with the SDORT validation done in sec. 4.3.3. In fact, generating complex networks and testing them is usually easier when it comes to simulation platforms compared to the case of experimental setups, where several logistical impasses hinder this mission. Particularly, is the number of testing ports available in the VNA which is usually limited to four. As a result, we will consider in our simulations two non-trivial complex networks: a double-junction NUT composed of 6 branches and 5 testing ports in addition to a four-junction network configuration made up of 10 branches and 7 testing ports as shown in Figs. 4.16 (a), & (b) respectively. Notably, these two networks are rarely considered in fault location techniques, markedly the second NUT haven't been tested against faults to the best of our knowledge. Besides, it worthy to note that the reason behind testing such kind of complex networks, is to try to address the efficiency of EDORT in locating multiple faults against such kind of very complex networks, at least numerically if that's not possible experimentally in the meantime.

As earlier defined, all NUT configurations that will be studied are composed of cables with arbitrarily chosen lengths where each network contains two soft faults with different intensities. The soft faults considered are demonstrated by a partial removal of the coating surrounding the 1 mm core conductor of the line. The strongest soft fault is reproduced by a 0.45 mm radius coating removal producing a fault ratio $R_f = 4\%$, whereas the weaker fault is designated by a coating radius removal of 0.05 mm creating a $R_f = 2\%$.

All the following results are based on the procedure summarized at the end of section 4.5, which are meant to illustrate the potential benefits provided by the EDORT technique adapted to complex NUT's. The double Y-junction network presented in Fig. 4.16 (a), is composed of five extremities, in addition to two soft faults, the stronger is situated between the two junctions and referred to as f_{st} while the weaker f_{we} fault is located on the 6^{th} branch of the NUT. The first step begins by computing the global scattering matrix $\mathbf{S}_G^1$ of the network, for instance the eigenspace structure of its corresponding TRO contains the signature of both faults. Accordingly, the first iteration of EDORT will lead to the single-fault scattering matrix $\hat{\mathbf{S}}_1$, which contains now only the signature of the strongest fault f_{st}. Eventually, four negligible eigenvalues in addition to a significant one λ_1^1 will be obtained as a result of the eigenvalue decomposition of $\hat{\mathbf{K}}_1 = \hat{\mathbf{S}}_1\hat{\mathbf{S}}_1^\dagger$. Indeed, the eigenvector components of λ_1^1 will form the testing signals that will injected through the five testing ports of the reference NUT. Once again the time-delayed set of signals will focus on the strongest fault's position at the same instant, this can be seen on the power ZT diagram of Fig. 4.17, which is observed along the fifth path of the network, where the signals interfere constructively at the strongest fault's position with no focusing on the weaker one. In order to unambiguously pinpoint the location of the second fault, the second iteration of EDORT procedure removes the signature of the strongest fault f_{st} from $\mathbf{S}_G^1$ producing a new scattering matrix $\hat{\mathbf{S}}_2$ with nothing else than the signature of f_{we}. The eigenvalue decomposition of its corresponding TRO $\hat{\mathbf{K}}_2$ leads to an eigenspace containing a single dominant eigenvalue whose corresponding eigenvectors clearly focus on the position of the weak soft fault once propagated in the reference model of Fig. 4.16. Markedly, the power ZT diagram of Fig. 4.18 along the fifth path clarifies the result.

A more complex network as the one presented in Fig. 4.16 (b) is now considered. Here we have four junctions, the first one is linking four branches, while the second, third and fourth ones are linking three branches. Besides, two soft faults have been considered in this configuration, the strongest f_{st} is located between junctions (2) and (4) at a distance 2 m from the reference testing port (1), while the weaker fault f_{we} is positioned on the ninth branch after the fourth junction at 4m from (1). To the best of our knowledge, locating multiple soft faults not even single ones embedded in similar complex networks has never been addressed till the moment of writing this thesis. We assume having seven testing ports, situated at the extremities of the network, as indicated on the same figure. Under those circumstances, a numerical eigenvalue decomposition of the TRO obtained after the 1^{st} EDORT iteration leads to a significant eigenvalue whose components form the testing signals which once applied to the corresponding testing ports of the reference NUT model, will focus on the position of the strongest fault as shown in the power ZT diagram of Fig. 4.19 observed along the sixth path. Compared to previous cases, we can notice a focal spot at a distance of 2 m from the reference testing port identifying the position of the fault. Accordingly, the second iteration of the EDORT is capable of unleashing the location of the weaker fault which seems to be located at 4 m from (1) as shown in the power ZT diagram of Fig. 4.20.

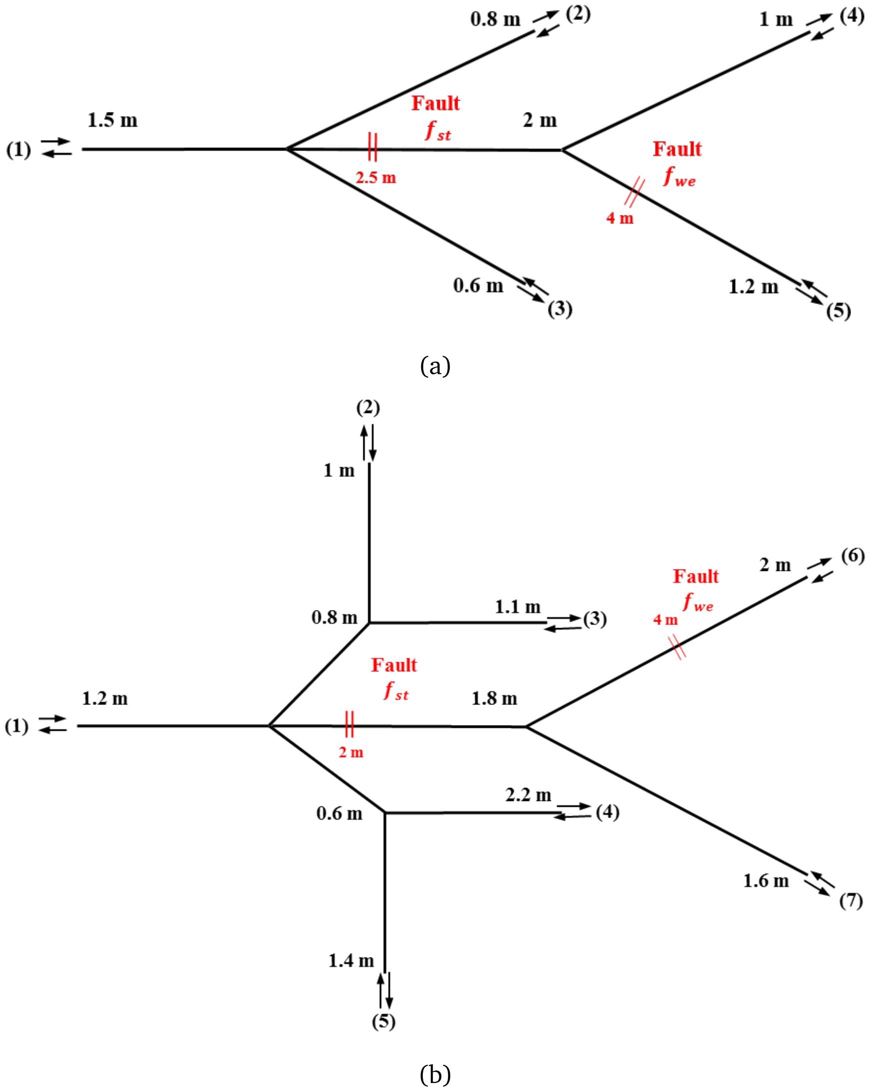

Figure 4.16 Layouts of the two NUTs considered for the numerical validation of the EDORT: (a) a double Y-junction NUT containing two soft faults with the first and second located at 2.5 m and 4 m from the reference port (1); (b) a four Y-junction NUT with 7 testing ports and two soft faults located at 2m from (1) for the stronger and at 4 m on the sixth branch for the weaker. The severity of the faults , represented here by two dashes, is characterized by the thickness of the dashes where increasing this thickness reflects a higher intensity of the soft fault, the strongest is referred to as f_{st} while the weaker fault by f_{we}.

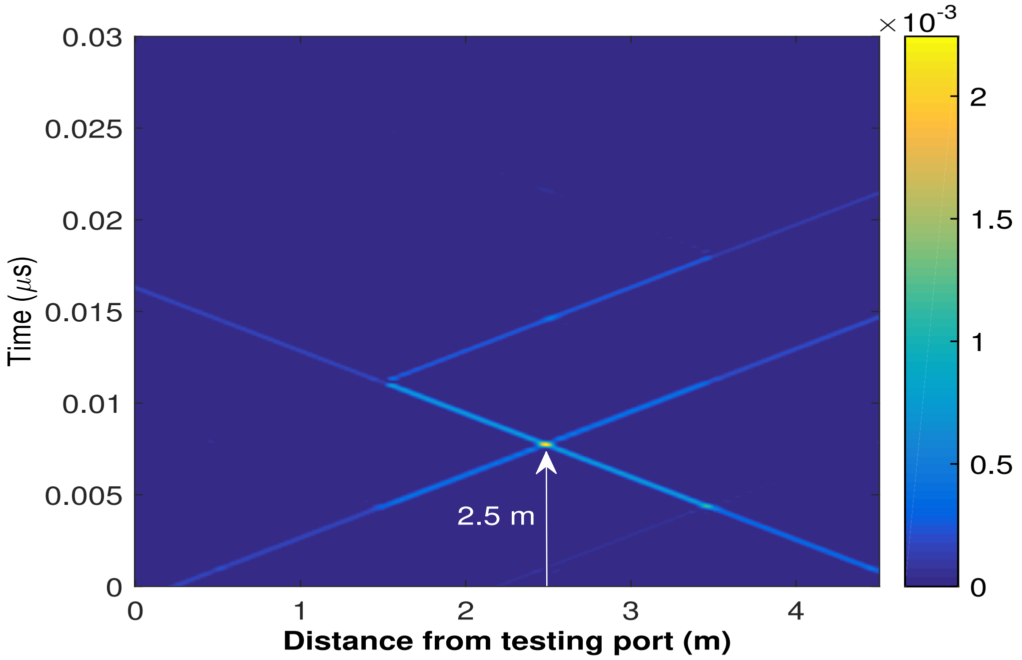

Figure 4.17 The ZT power summation observed along the fifth path of the reference model diagram of Fig. 4.16 (a) after performing the 1^{st} iteration of EDORT.

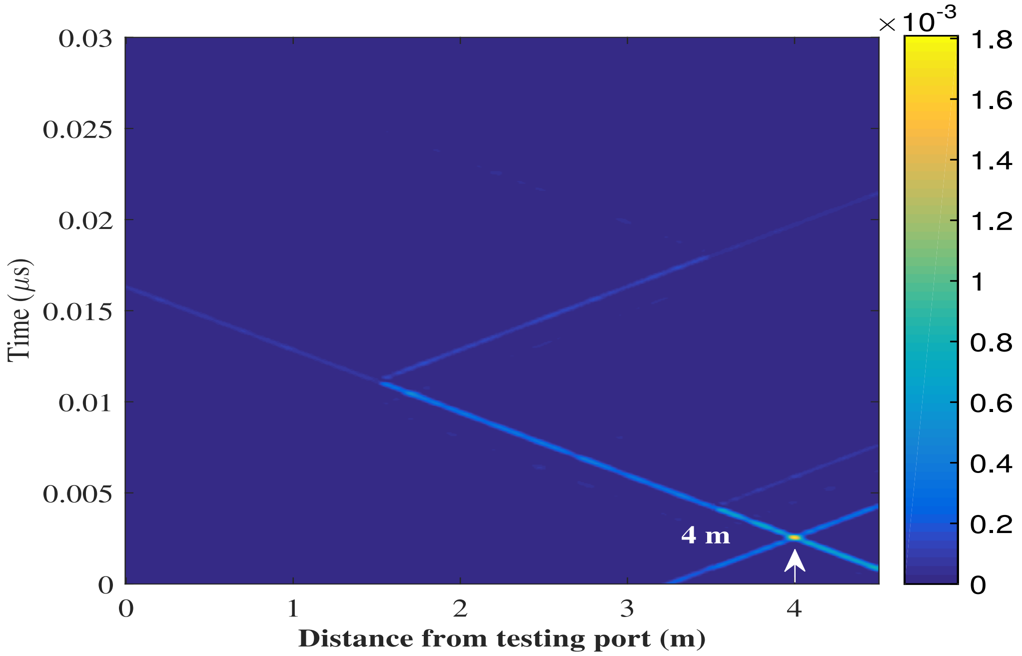

Figure 4.18 The ZT power summation observed along the fifth path of the reference model diagram of Fig. 4.16 (a) after performing the 2^{nd} iteration of EDORT. This step was sufficient to clearly pinpoint the location of the weaker soft fault in the NUT.

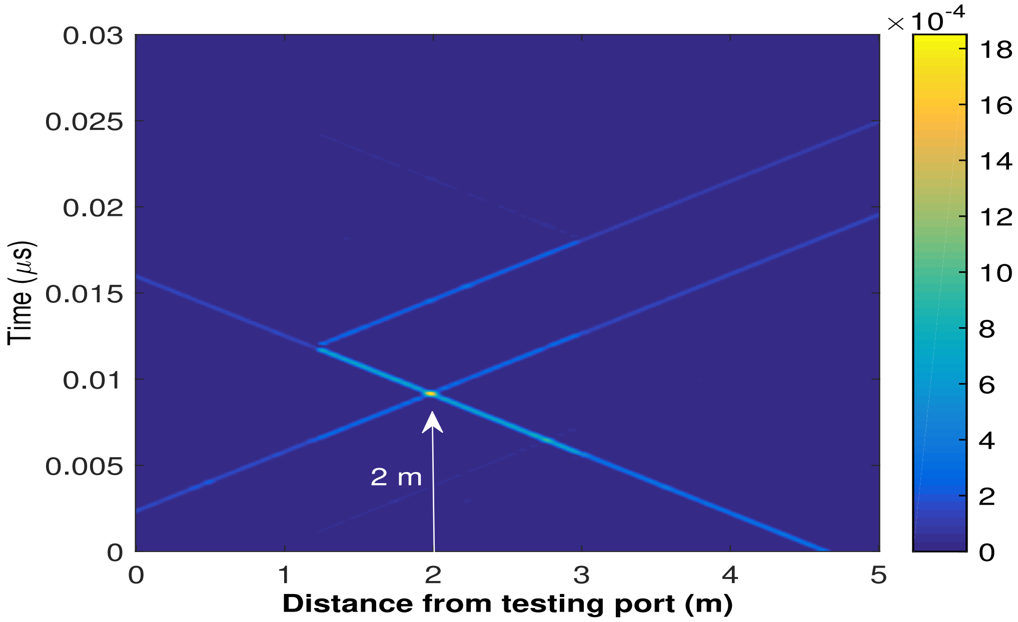

Figure 4.19 The ZT power summation observed along the sixth path of the reference model of Fig. 4.16 (b) intended to located the position of the first fault after performing the 1st iteration of EDORT.

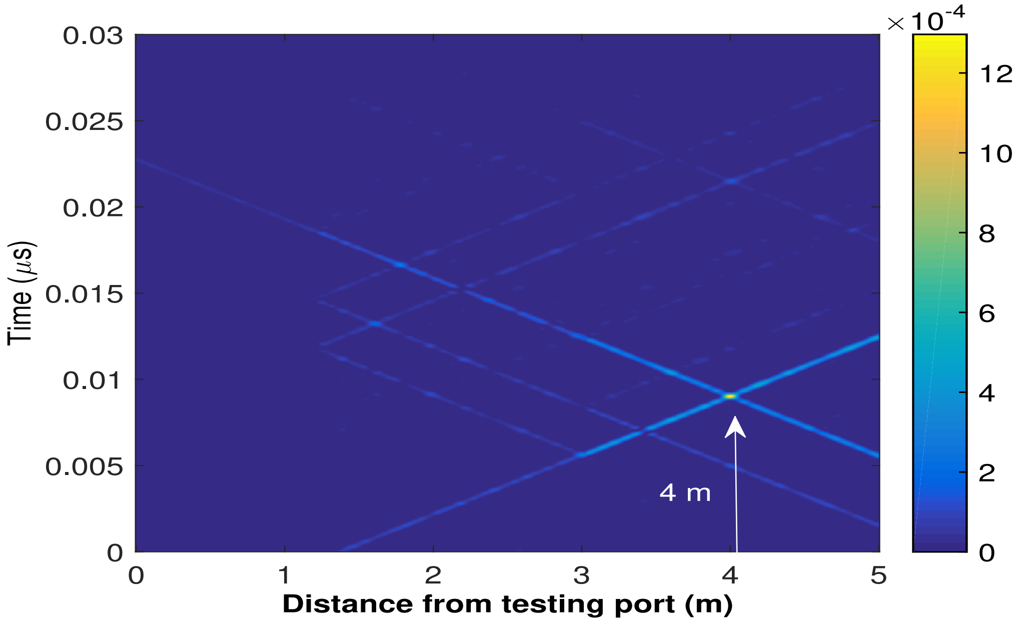

Figure 4.20 The ZT power summation observed along the sixth path of the four-junction NUT of Fig. 4.16 (b). The 2nd iteration of EDORT produces a single-fault scattering matrix whose eigenspace components form the testing signals that clearly pinpoint the location of the weaker soft fault one propagated in the reference model of the NUT.

It is important to realize that the proposed method has shown to be remarkably effective in locating the position of multiple soft faults within the tested wiring networks where significant focal spots appeared at their positions. Another key point, EDORT has proven to be robust when dealing with increased network complexity which was demonstrated by the results obtained when examining the latter complex wiring configurations. On the other hand, investigating EDORT's performance with real multiple soft faults embedded inside different complexity real-life NUTs would provide a profound support towards a practical implementation of the proposed technique. As a result, an experimental setup is conducted in order to validate the feasibility of EDORT with multiple faults as will be well detailed in the next section, nevertheless, this will be preceded by a part recalling the efficient results obtained with the SDORT for a single soft fault. In fact, this new method allowed as a by product to retrieve the faults' intensities through the single-fault matrices obtained at each iteration of EDORT, this will be demonstrated in sec. 4.6.4. Specifically, this step is an important feature when needing to decide whether a fault shall be checked more closely by a human operator or not, and in order to monitor how the fault's situation evolves in time.

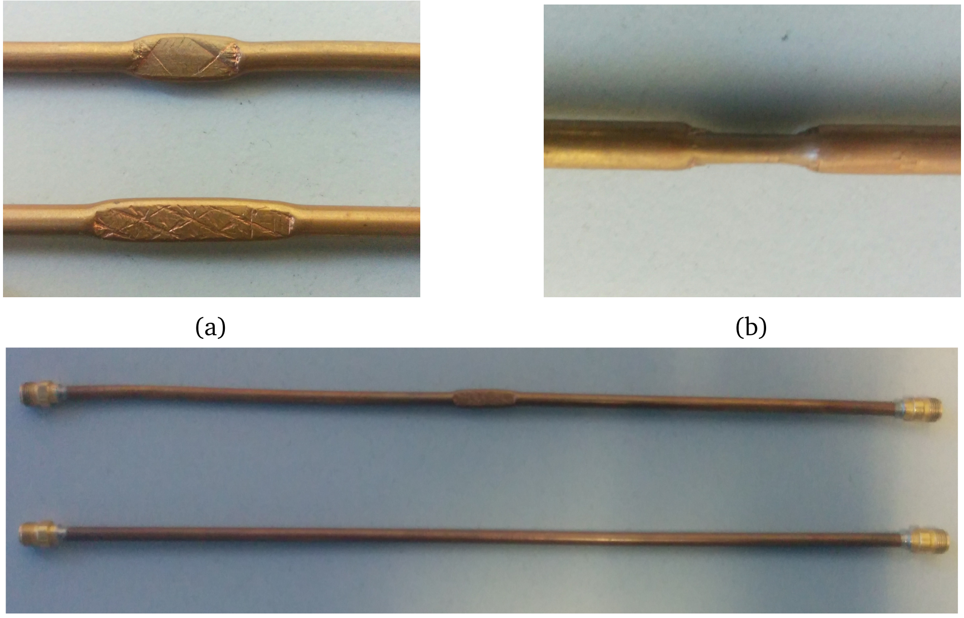

(a) (b)

(c)

Figure 4.21 The two soft faults considered in the experimental validations, as obtained by crushing a 2 cm and 1 cm long portions of a semi-rigid cable for the stronger f_{st} and weaker f_{we} faults respectively. The three pictures present: (a) a front view of the two soft faults; (b) a side view of one of faults, where the cable's cross-section is reduced from 3.4 mm to 2 mm for both; (c) the two samples used for the measurements, i.e., the reference semi-rigid cable without a fault and the one containing a fault. They share the same dimensions and features.

4.6.2 Experimental Setup

The experimental measurements we conducted tested three different NUTs: a single branch configuration, a single-Y junction structure, in addition to a double-Y junction network. The scattering matrices of the different considered network configurations were measured by means of a Vector Network Analyzer (VNA) whose testing ports were connected to the extremities of the NUTs, as shown in Fig. 4.23 (a). The VNA we used is a Rohde & Schwarz ZVB-8 network analyzer, with a frequency range from 300 kHz to 8 GHz, and four testing ports. The intermediate-frequency filter bandwidth was set to 100 kHz. The input power was set to a 0 dBm harmonic excitation signal: this ensured a strong rejection of noise, yielding very clean results that can be regarded as practically unaffected by any noise source. Using the VNA implies accessing the collected data in the frequency domain. Thus post-processing using Matlab was applied to the obtained results, in order to extract the time-domain responses, using the inverse Fourier transform which will be presented in the form of either a ZT or an energy diagram.

Networks were implemented using standard 50 Ω coaxial cables as transmission lines. Although coaxial cables are not routinely found in practical NUTs, they were chosen because of their excellent stability, in order to ensure reproducible results. The conclusions drawn in this section are not related to the type of lines used, since the proposed method is completely general. In our measurements, and for the sake of having flexibility in implementing our desired networks, we connected 50 Ω coaxial cables between the VNA's testing ports and the NUT's extremities. Henceforth, calibration was done for the extremities of these connected cables. Here it is important to point out that the fact of whether to calibrate the VNA or not, has strictly no impact on the results, as the goal here is to measure the echo-impulse response seen through the testing ports. This is not affected by calibration, which aims to compensate for the presence of a cable or any device between the measuring port (on the VNA side) and the wished testing port, on the NUT side.

Coaxial cables also offer another sizable advantage, since soft faults can be introduced (and removed) by using a set of 30 cm long samples made of semi-rigid coaxial lines terminated by two SMA connectors, as those shown in Fig. 4.21 (c). For instance, creating the soft faults was accomplished by crushing each sample by a different force over a different portion of length, thus producing a varying severity in the faults. Specifically, the strongest soft fault f_{st} is designated by a crushed length of 2 cm while for the weaker fault f_{we} the crushing was accomplished over 1 cm, this can be seen in the two faulty sections demonstrated in Fig. 4.21 (a). Furthermore, the crushing force applied on the cables reduced the thickness from its normal 3.4 mm cross-section to only 2 mm which can be seen in the cable side view photo of Fig. 4.21 (b).

Another key point is that in order to try to minimize the effect of the interconnections between the cable and the VNA and for the sake of making the fault's response more visible, the difference system will be considered. Thus, the need for a baseline measurement was satisfied by considering an unaltered sample as the reference one, and measuring the scattering matrix of the NUT using this reference sample, in order to be subtracted from the response of the faulty samples later. This kind of approach, where a portion of the faultless NUT is substituted with a faulty portion, rather than directly crushing the original cable, was intended as a way of ensuring reproducible results, in a controllable manner. As a matter of fact, the direct generation of a fault is hardly reproducible and does not allow double checking of results because it is an irreversible procedure. On the other side, the risk associated with our approach is the introduction of errors due to the positions of the faultless and faulty samples that are not perfectly identical; we have taken due care in keeping these errors negligible during our tests. It is worthy to note that, this same approach was also used in the experimental validation of the standard DORT done in [73, 148], where it allowed a practical and a reproducible framework.

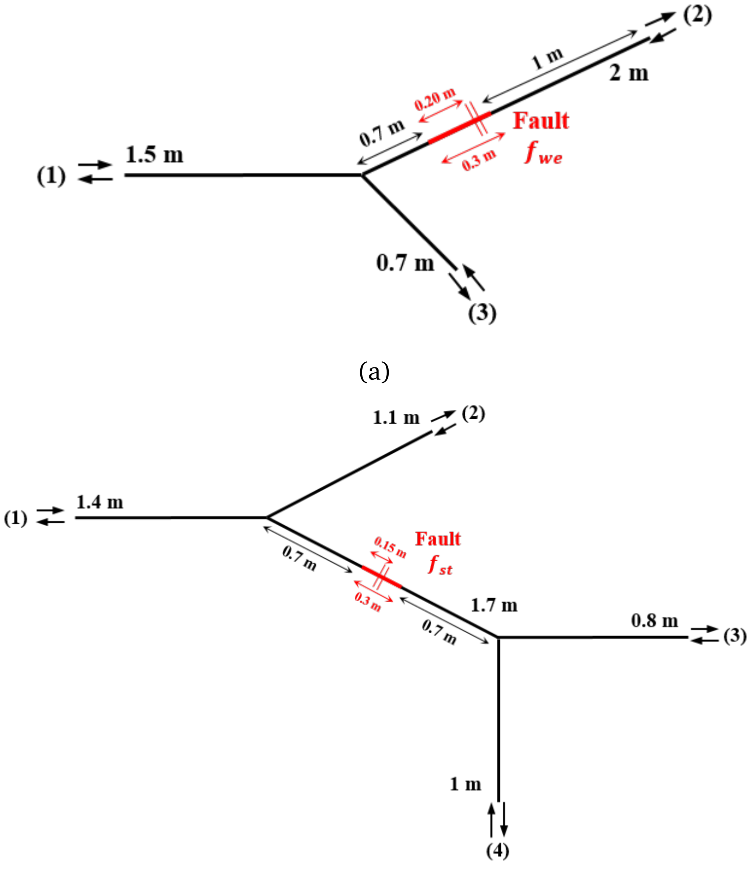

(a)

(b)

Figure 4.22 Layouts of the two NUTs considered for the experimental validation of SDORT: (a) a single Y-junction structure with a single f_{we} soft fault at a distance 2.4 m from (1) on the second branch; (b) a double Y-junction with an f_{st} soft fault situated between the two junctions at a distance 2.25 m from the reference port. Each branch of the NUT is implemented using flexible coaxial cables with a 50 Ω characteristic impedance, while the faults are implemented using semi-rigid coaxial samples. The lengths of the cables as well as the locations of the faults are indicated on the figures. The arrows and their attached numbering are meant to show the connections of the extremities to the testing ports of the VNA.

4.6.3 Experimental results

The studied configurations for the SDORT and EDORT are shown in Figs. 4.22& 4.26 respectively. We chose these configurations to first recall the efficiency of SDORT in precisely locating single-soft faults and then to prove experimentally the capacity of the EDORT to locate multiple-soft faults in different complexity network configurations where standard TDR and DORT techniques fail.

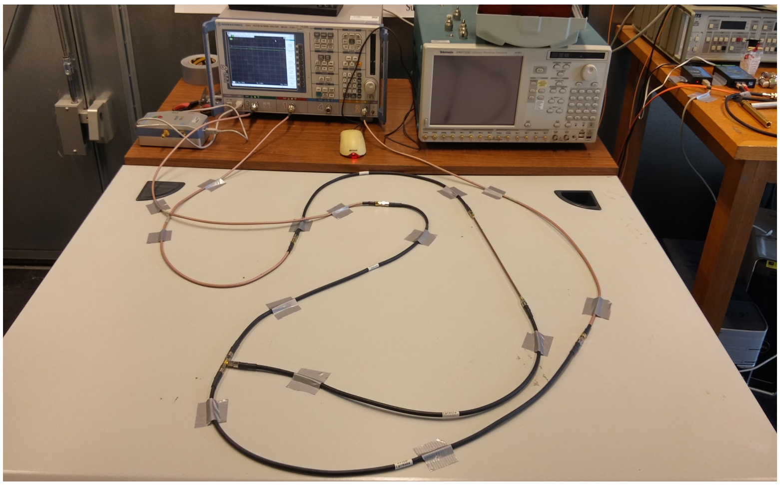

(a)

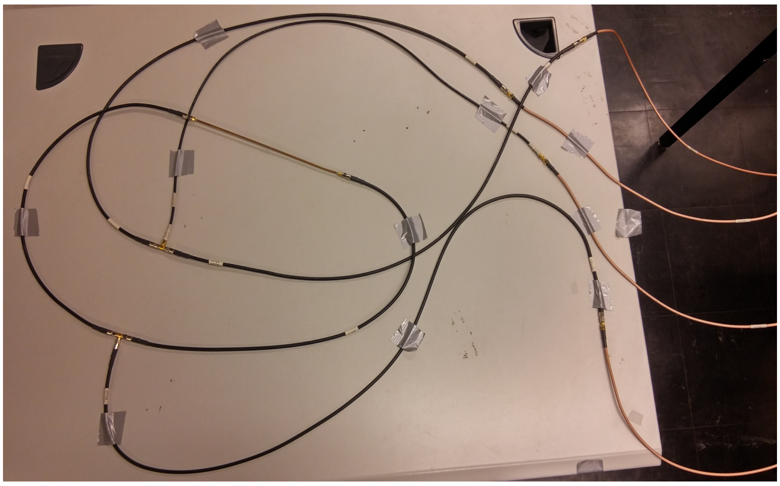

(b)

Figure 4.23 Experimental implementation of the networks represented in: (a) the single junction NUT of Fig. 4.22 (a), containing a weak single soft fault f_{we} at 2.4 m from (1) situated on the second branch, where the network's three extremities are connected to three testing ports of the VNA; (b) the double-junction NUT of Fig. 4.22 (b) composed of 5 branches and a single strong soft fault f_{st} at 2.25 m from the reference port located between the two junctions.

The need for a numerical model in order to inject the synthesized signals resulting from the eigenspace structure of TRO was satisfied by using the models we used earlier in the numerical validations. We also recall that the VNA used in our experiments had four testing ports, where different network extremities are connected each time to the VNA ports, in order to measure the NUT's scattering parameters. Besides, and due to the fact that we are considering a linear time-invariant system, we tried to minimize as much as possible the cables movement, in order to capture the faults' weak signatures. Consequently, we taped the cables to the bench on which the measurements are done, thus no perturbation would be introduced that could be seen as a secondary source in the difference system, and affecting the faults' locations.

The ends of the cables were used as testing ports and were connected to the ports of the Rohde & Schwarz ZVB8 VNA. The measurement of the scattering matrices was done over a total bandwidth of 2 GHz and a frequency step of 20 MHz. A first step in the measurement procedure is the calibration of the VNA. Thus we connected four identical 50 cm cables to the four testing ports, and calibrated the VNA according to these cables, using the calibration kit provided by the manufacturer. Three of these cables can be seen in Fig. 4.23 (a), connecting a single junction NUT to the network analyzer.

After the calibration step, we considered each of the studied networks and measured the scattering matrix of the difference system in each case. For each studied NUT, the measurement consisted of two steps:

- measurement of $\mathbf{S}_{Gh}$ of the reference healthy system (without faults).

We considered the network with unaltered 30-cm semi-rigid sections, and measured the scattering matrix of the system, for a frequency range from 300 kHz to 2 GHz. It can be seen from the photos of the NUT implementations of Figs. 4.23& 4.27 that we attached the cables to the table in order to minimize as much as possible their movements for the two measurements.

- Measurement of $\mathbf{S}_{Gf}$ of the faulty systems.

For this purpose, the unaltered 30-cm semi-rigid sections considered in the first step were replaced with the faulty sections on their positions. It is important to note that, a single section is replaced for the NUTs of Fig. 4.22 of the single-fault SDORT validation while two sections are replaced in the case of the double-fault EDORT validation of the networks of Fig. 4.26. In the event that we are dealing with soft faults which are basically characterized with weak responses, a particular attention was paid to the connection and disconnection of the semi-rigid cables. In fact, this was intended to minimize the effect of the connectors when considering the difference system, i.e., to avoid having residual responses that can mask the fault's signature.

Having measured the two scattering matrices of the considered NUTs, an averaging operation to both matrices is firstly done in order to obtain a symmetrical condition. As we have already stated, we will first begin by re-stressing the SDORT feasibility in locating single soft faults against experimental data. For this reason, the steps listed in sec. 4.3.2 detailing the SDORT procedure were applied, where signals propagating at each step throughout the NUT were computed by means of an in-house transmission-line solver, implemented under Matlab as the one used in the numerical validations.

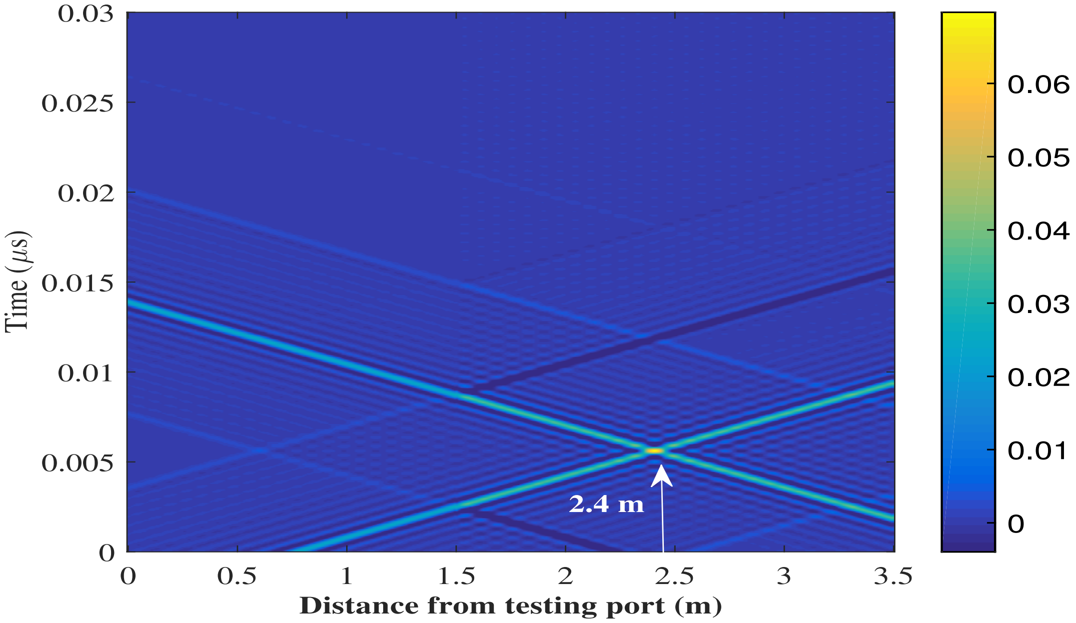

Figure 4.24 The ZT diagram corresponding to the single-fault single-junction NUT of Fig. 4.22 (a) observed along the second path. In fact, it shows signals focusing on the position of the soft fault located at 2.4 m from the reference port (1).

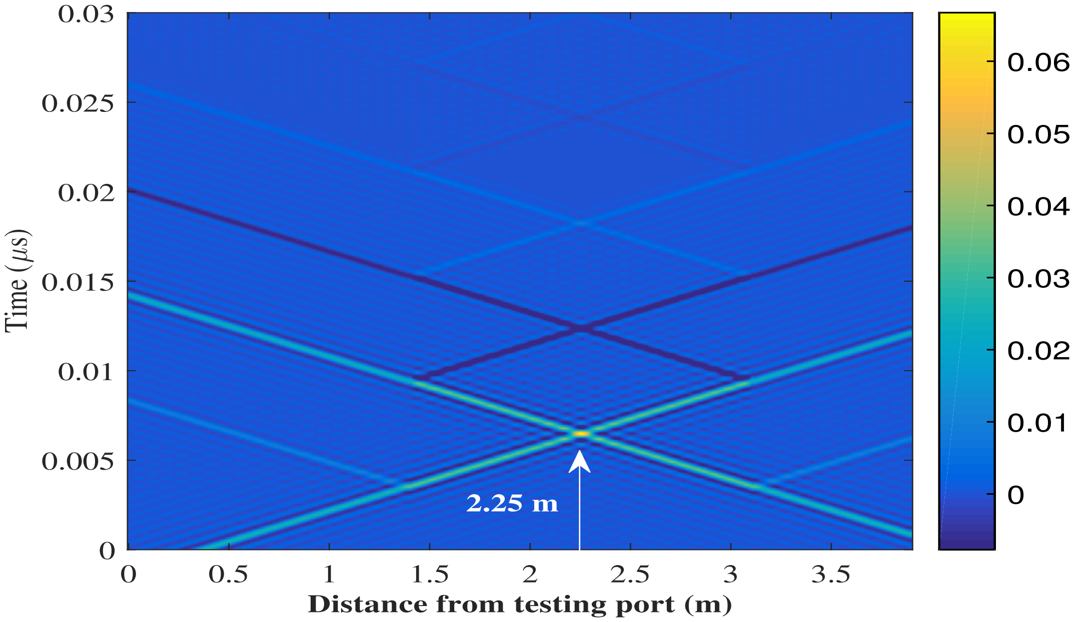

Figure 4.25 The ZT diagram corresponding to the single-fault double-junction NUT implemented in Fig. 4.22 (b). This network is composed of five branches and four testing ports. The voltage propagation is observed along the third path and shows the injected signals interfering constructively on the fault's position, which is situated at 2.25 m from (1).

Applying the SDORT procedure to the single junction NUT implemented in Fig. 4.23 (a) led to the definition of three testing signals that were subsequently applied to a numerical model of the corresponding NUT. From these numerical results, we computed the voltage propagation along the second path of the network where the ZT diagram of Fig. 4.24 shows a focal spot right at the position of the fault at 2.4 m from the reference testing port (1). Likewise, computing a closed form computation of the eigenvalue decomposition of the TRO corresponding to the double Y-junction NUT of Fig. 4.22 (b) after measuring the scattering matrices on the basis of five testing ports leads to five different eigenvalues. As a matter of fact, one dominant eigenvalue is obtained whose eigenvector components form the testing signals that will be propagated in the reference model of the network. Accordingly, a constructive interference shown in the ZT diagram of Fig. 4.25 along the third path, is obtained at 2.25 m from (1) thus pinpointing the location of the fault which is situated between the two junctions of the NUT. These experimental results validate the conclusions drawn from the previous numerical results for the feasibility of SDORT in locating a single soft fault in complex wire networks. Despite this fact, it started failing once multiple faults are encountered in an NUT, however, EDORT process provided an alternative solution for the DORT concept to embrace the location of multiple soft faults in guided wave structures of transmission lines.

Thereupon, the proposed EDORT procedure detailed in sec. 4.5 was first applied to the single-branch NUT of Fig. 4.26 (a) containing two soft faults situated at 1.15 m and 2 m from the reference port, and implemented as shown in Fig. 4.27 (a). The energy diagrams associated to the estimated single-fault scattering matrices in Fig. 4.28 are now characterized by a single dominant peak each, corresponding to the position of the two faults. In fact, the eigenvectors corresponding to the most significant eigenvalue of the TRO of the single-fault scattering matrix $\hat{\mathbf{S}}_1$ obtained after the first iteration of EDORT, form the testing signals intending to focus on the strongest fault once propagated in the reference model of the NUT of Fig. 4.27 (a) as shown in the ZT diagram of Fig. 4.29. Consequently, a similar focal spot shall be obtained on the position of the weaker fault in the network after applying EDORT's second iteration as presented in the ZT diagram of Fig. 4.30. These results show the outcome of selective focusing compared to the that obtained by the SDORT on the same NUT, featuring two peaks simultaneously on the faults' positions as can be also seen in the energy diagrams of Fig. 4.28. Furthermore, the ending point of the EDORT process for this case can be inferred from a negligible eigenvalue obtained after applying the third iteration of the process as presented in Fig. 4.31. Two significant eigenvalues were obtained after the first and second iteration of the process while a negligible one was obtained in the third iteration reflecting an empty eigenspace structure.

It is important to realize from Fig. 4.28, that some artifacts are still present. This phenomenon is due to the periodicity of wave propagation that is proper of single-branch structures. Indeed, this problem disappears as soon as more complex structures are considered, where the spatial periodicity is broken. The flat background observed in the two energy distributions can be understood by recalling that, in the case of single faults, excitation signals with equivalent intensity cross the NUT and interfere constructively at the fault position [148].

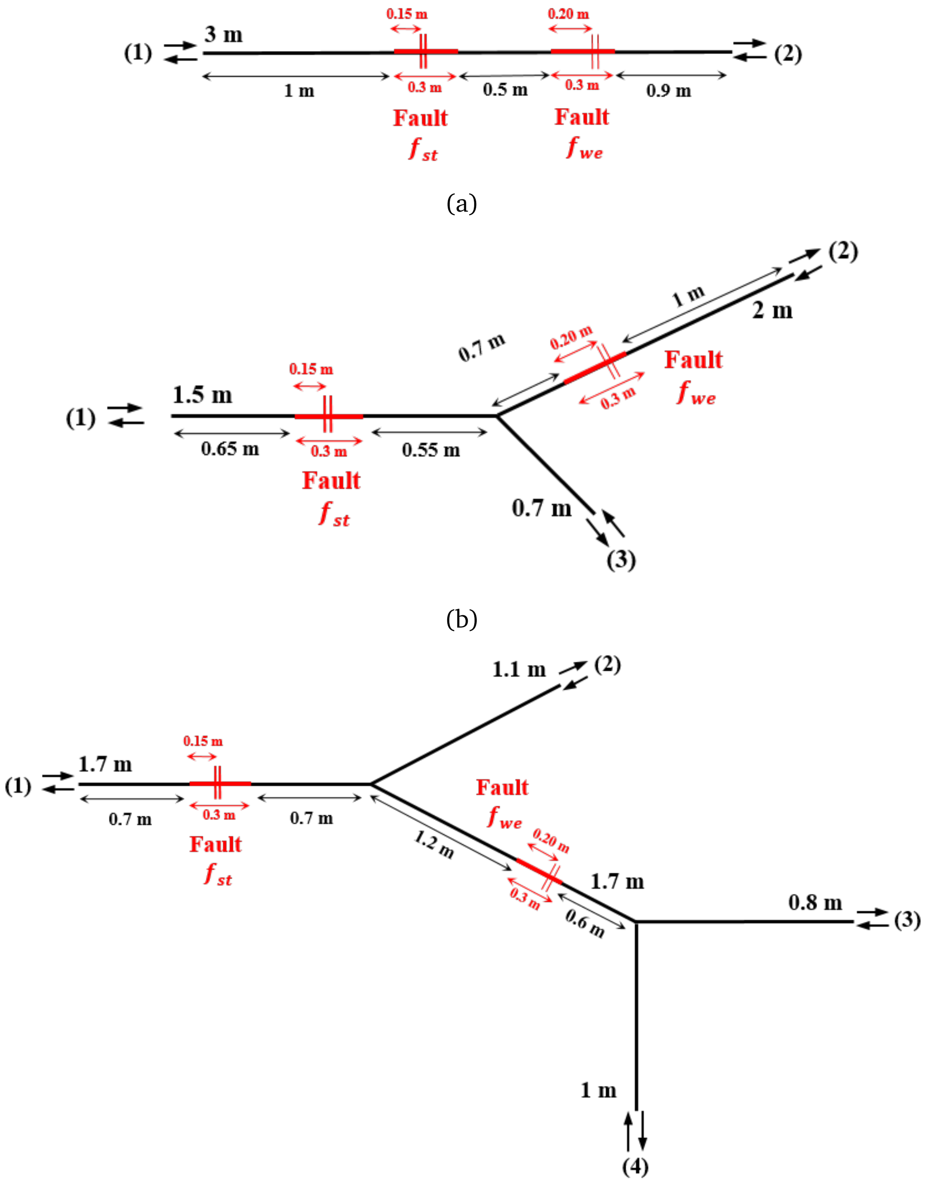

(a)

(b)

(c)

Figure 4.26 Layouts of the three NUTs considered for the experimental validation of the EDORT process: (a) a single branch structure with two soft faults: f_{st} at 1.15 m and f_{we} at 2 m from the reference testing port (1); (b) a single Y-junction configuration with the f_{st} located at 0.8 m from (1) while the f_{we} situated at 2.4 m from the reference port along the second branch; (c) a double Y-junction NUT with 4 testing ports and two soft faults: the stronger 0.85 m on from (1) while the weaker is embedded between the two junctions at 3.1 from the reference port. The severity of the faults share the same analogy considered in Fig. 4.16.

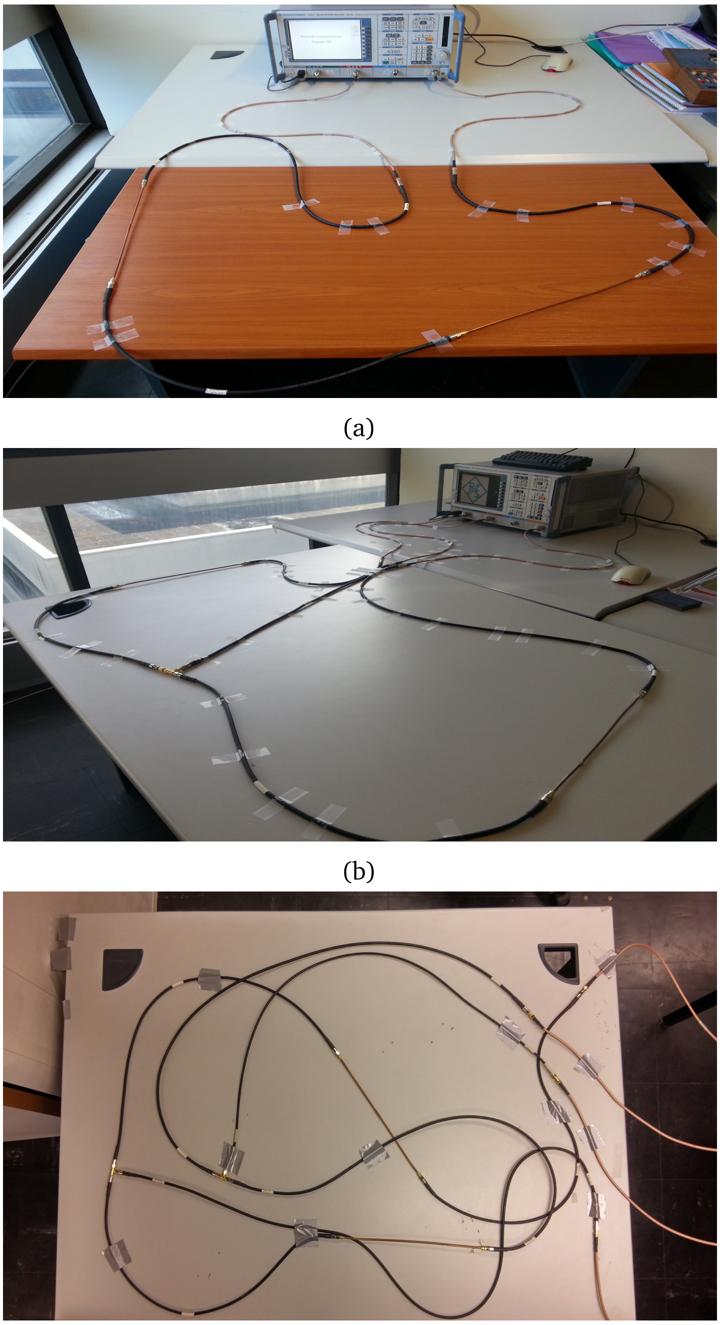
(a)

(b)

(c)

Figure 4.27 Experimental implementation of the layouts of the NUTs of Fig. 4.26: (a) the single cable NUT of Fig. 4.26 (a), containing two faulty sections (1.15 m and 2 m from the reference port), connected to the VNA for the experimental tests; (b) the single-junction NUT of Fig. 4.26 (b) presenting two faulty sections (0.8 m and 2.4 m from the reference port), whose three extremities are connected to three testing ports of the VNA. The 30-cm long semi-rigid cables containing the two faulty sample can be seen; and (c) the double junction NUT of Fig. 4.26 (c) composed of 5 branches and containing 2 soft faults, the f_{st} and the f_{we} at 0.85 m 3.1 m from (1).

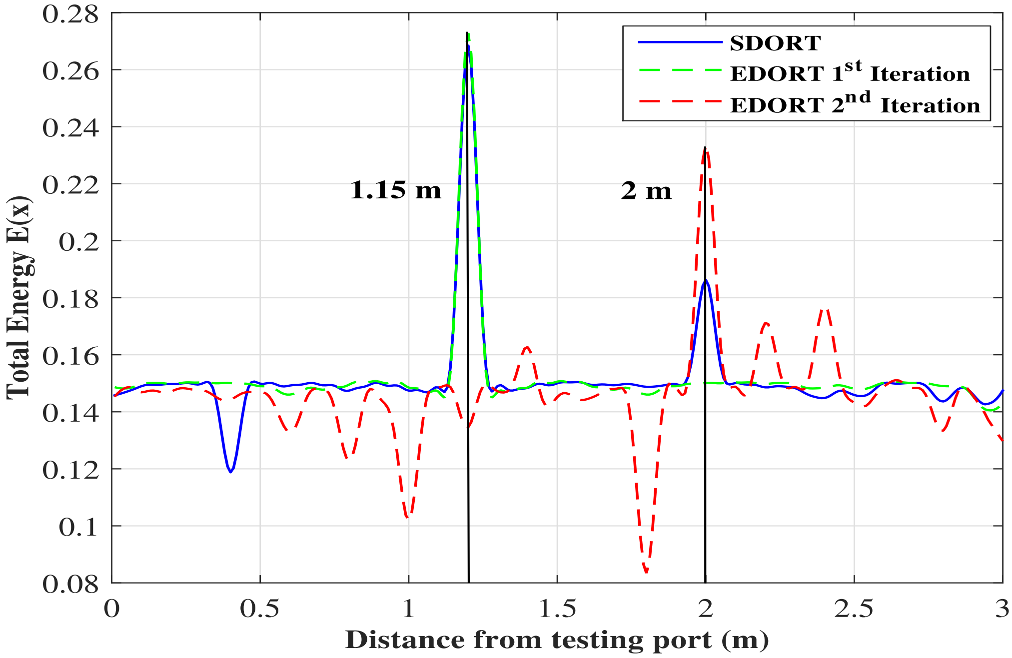

Figure 4.28 The total energy along the NUT in Fig. 4.26 (a), computed after applying the EDORT separation procedure. At each iteration the dominant energy peak corresponds to a fault not identified by the previous iterations. The energy distribution obtained when using the SDORT is also shown for reference, and contains two energy peaks at the position of the two faults.

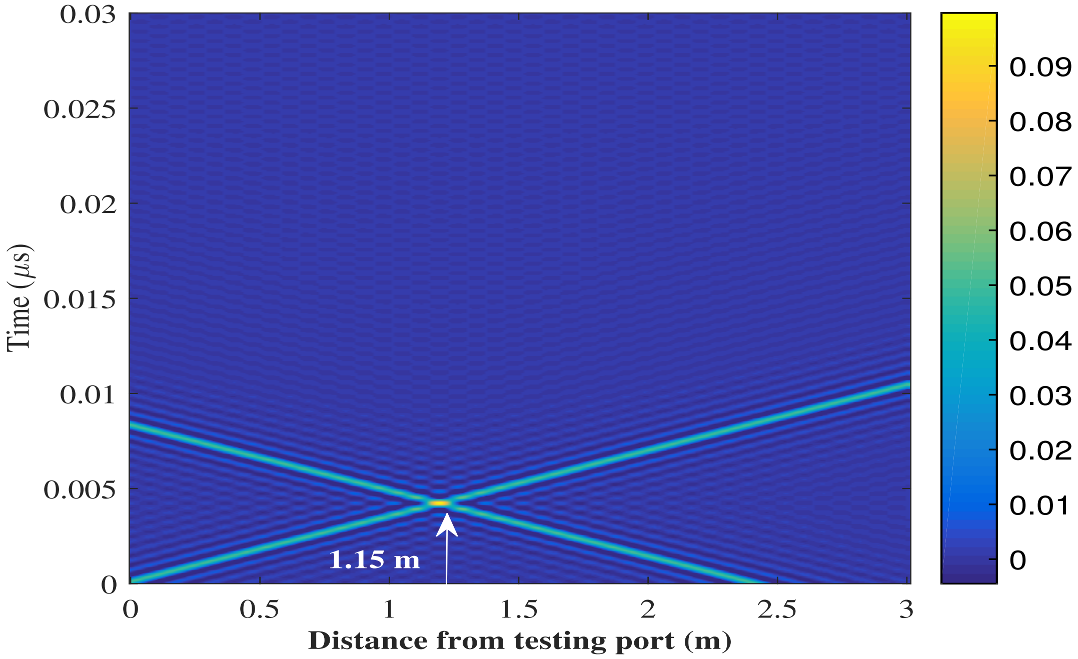

Figure 4.29 The ZT diagram corresponding to the single-branch NUT of Fig. 4.26 (a) and showing signals focusing on the position of the strongest soft fault after the first iteration of EDORT.

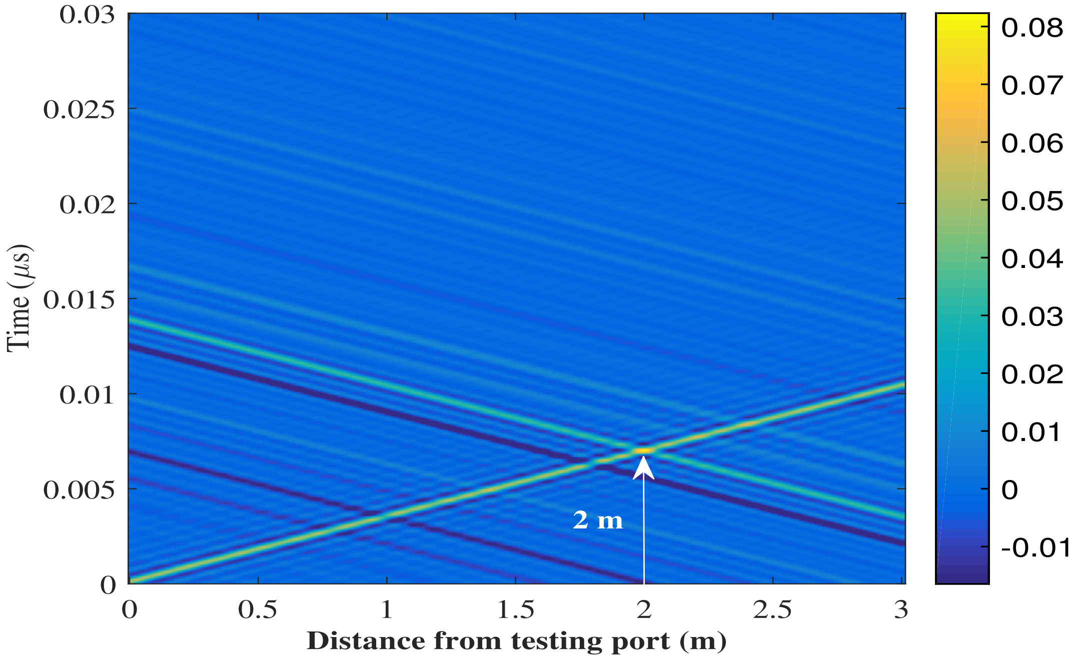

Figure 4.30 The ZT diagram corresponding to the single branch NUT implemented in Fig. 4.27 (a), where a focusing can be spotted at the position of the weaker soft fault after applying the 2^{nd} iteration of EDORT.

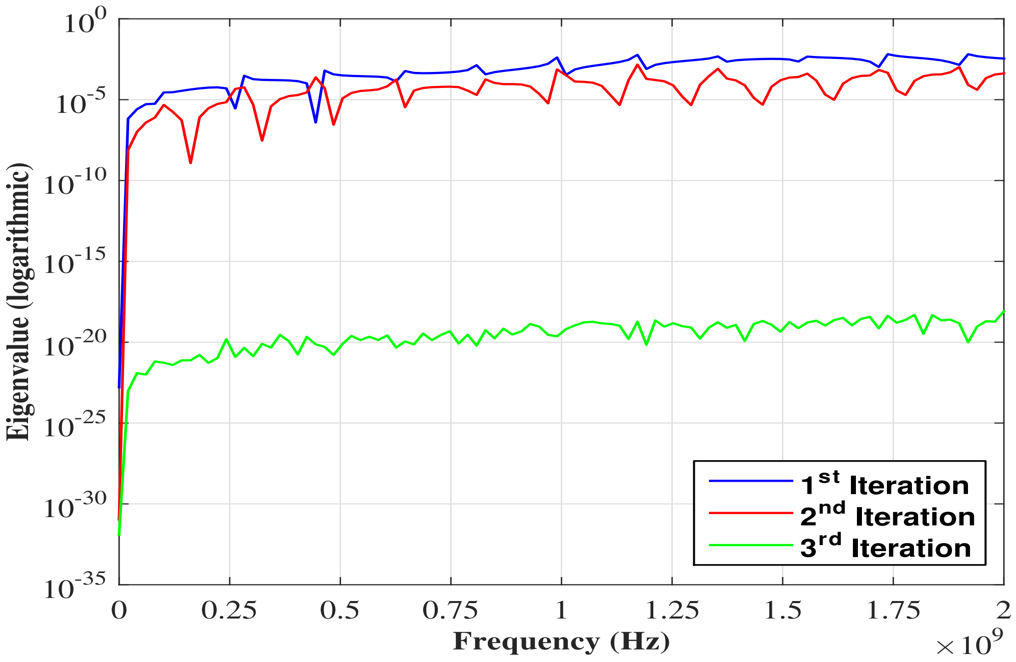

Figure 4.31 The most significant eigenvalue for the TRO, calculated for the single junction NUT of Fig. 4.26 (a) after applying the EDORT steps for the fist, second and third iterations.

In order to check the efficiency of the proposed method with more complex NUTs, the single-junction structure in Fig. 4.26 (b) was considered and implemented as presented in Fig. 4.27 (b) considering f_{st} at 0.8 m from the reference port and f_{we} at 2.4 m from (1) on the second path. Indeed, in this case artifacts are negligible with respect to the focusing peaks where the periodicity of waves was broken by the presence of the junction. The interest of applying the proposed procedure becomes clear when comparing the EDORT results in Fig. 4.32 with those from SDORT, shown in the same figure, where artifacts would have led to a wrong conclusion about the faults position. The separation of the fault responses yields similar features for the two faults, independently of their relative severity. In fact, the identification of both faults was possible after applying two iterations of the EDORT process where the third iteration led to an empty eigenspace structure demonstrated by a negligible value of its corresponding most significant eigenvalue as shown in Fig. 4.33. Under those circumstances, the ZT diagrams of Figs. 4.34& 4.35 show clearly two focal spots on the positions of the stronger and weaker soft faults after applying the first and second iteration of EDORT respectively.

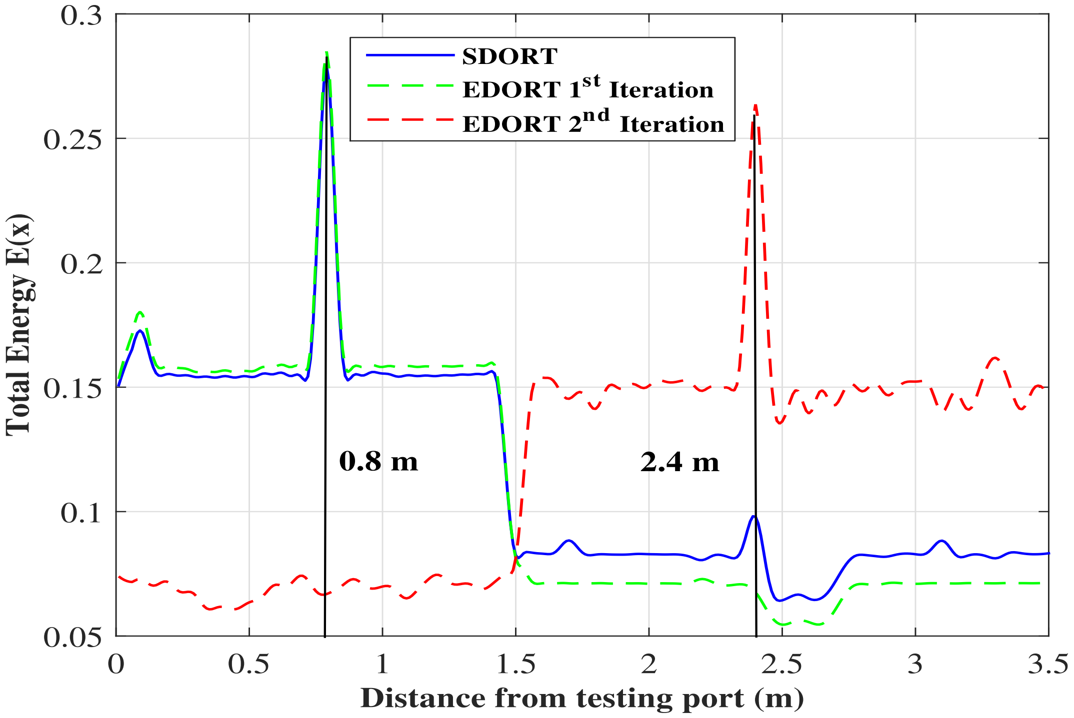

Figure 4.32 The total energy along the NUT in Fig. 4.26 (b), computed after applying the EDORT separation procedure. At each iteration the dominant energy peak corresponds to a fault not identified by the previous iterations. The energy distribution obtained when using the SDORT is also shown for reference, and contains two energy peaks at the position of the two faults.

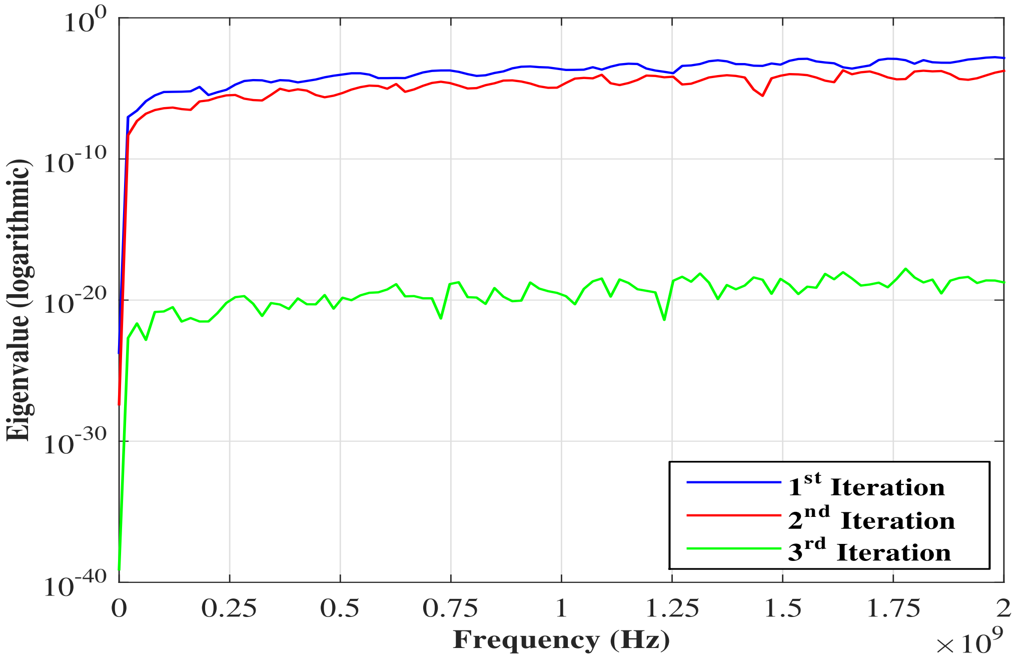

Figure 4.33 The most significant eigenvalue for the TRO, calculated for the single junction NUT of Fig. 4.26 (b) after applying the EDORT steps for the fist, second and third iterations.

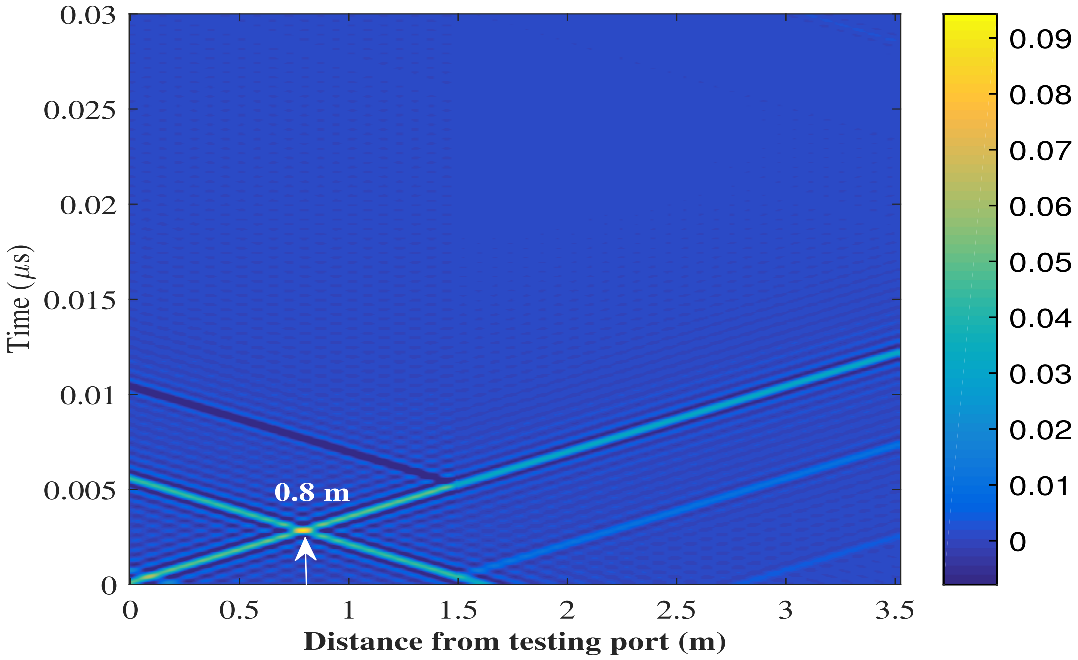

Figure 4.34 The ZT diagram tracking the voltage propagation in the single junction NUT of Fig. 4.26 (b) along the second path, where a focal spot can be observed at the strongest fault's position after the first iteration of the EDORT.

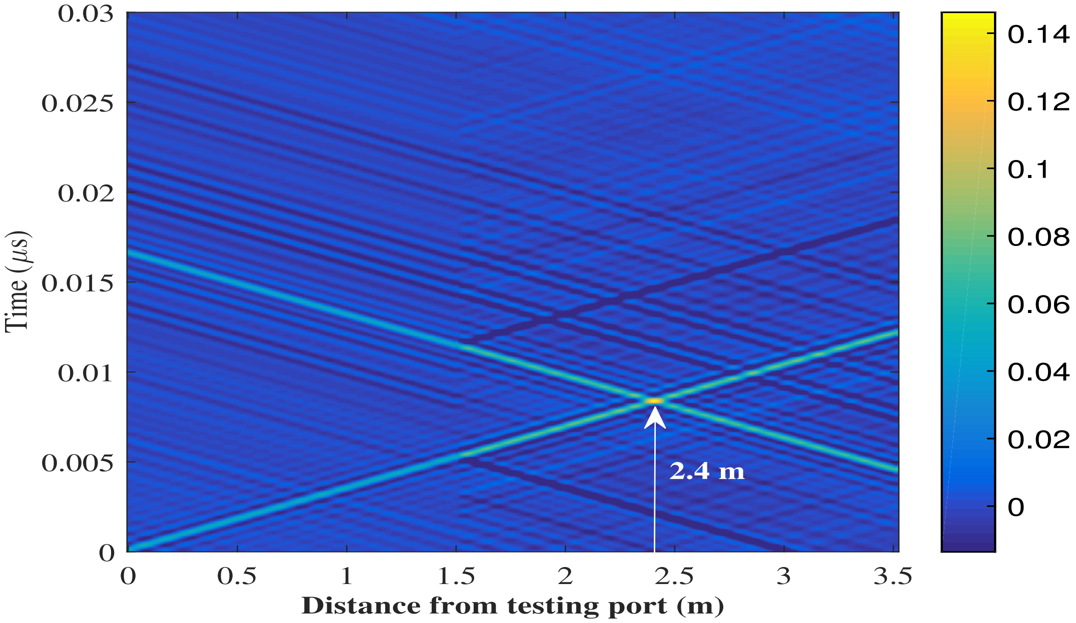

Figure 4.35 The ZT diagram corresponding to the network of Fig. 4.26 (b) tracking the voltage propagation along the second path. A focusing can be spotted at 2.4 m from the reference testing port pinpointing the location of the weaker fault after applying the second iteration of EDORT.

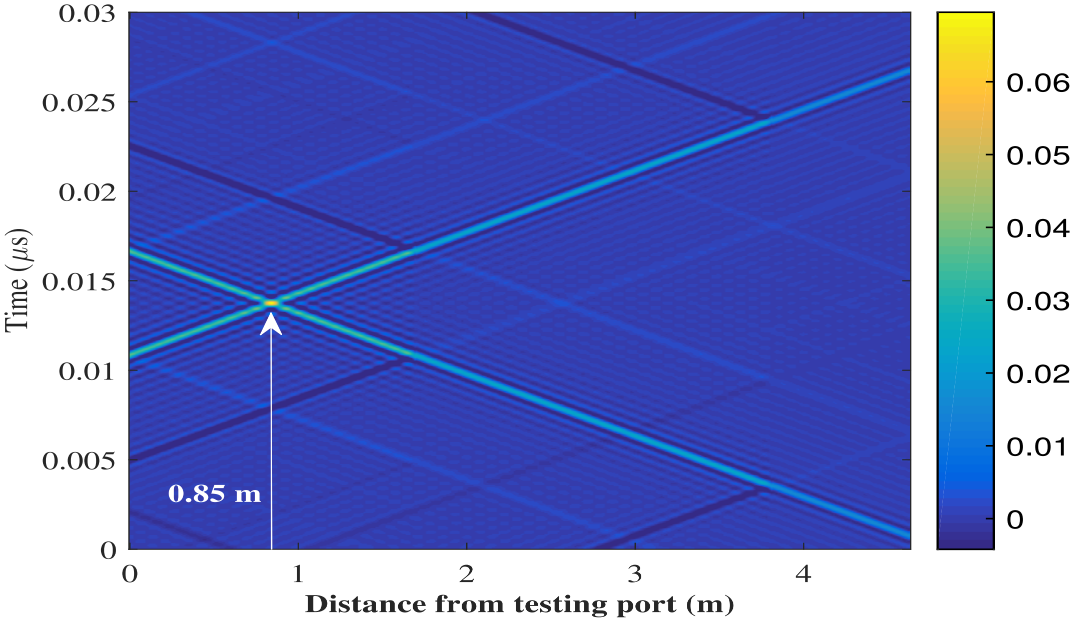

Figure 4.36 The ZT diagram corresponding to the double-junction network implemented in Fig. 4.27 (c) observed along the fourth path where measurements were done using four testing ports. Applying the EDORT procedure is capable of locating the strongest soft fault after the first iteration of the process.

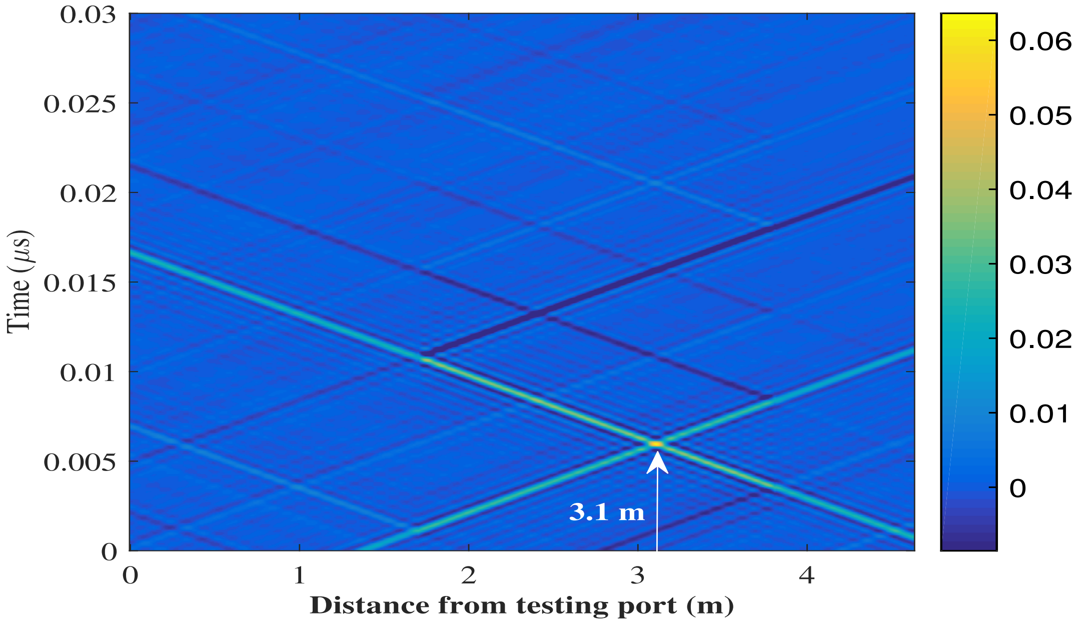

Figure 4.37 The ZT diagram corresponding to the double junction network of Fig. 4.26 (c) where the voltage propagation is observed along the fourth path of the NUT. The second iteration of EDORT is sufficient to create a focal spot at a distance of 3.1 m from port (1) thus locating the position of the weaker fault.

Let us now consider a more complex case, where a double junction NUT composed of 5 branches and 4 extremities and containing two soft faults at 0.85 m and 3.1 m from port (1), is presented in Fig. 4.26 (c) and implemented according to what is shown in Fig. 4.27 (c). Measuring the global scattering matrix $\mathbf{S}_G^1$ of this network is accomplished by connecting its four extremities to the four testing ports of the VNA, in fact $\mathbf{S}_G^1$ contains the signature of both faults present in the NUT. Accordingly, executing the EDORT steps on this matrix will lead to two single-fault scattering matrices $\hat{\mathbf{S}}_1$ and $\hat{\mathbf{S}}_2$ corresponding to the two soft faults f_{st} and f_{we} after applying the first and second iterations respectively. Consequently, applying the eigenvector components of the most significant eigenvalue of each of these two matrices into the reference model of the NUT will lead to two separate focal spots on the strongest and weakest faults' positions selectively as demonstrated in their ZT diagrams of Figs. 4.36&4.37 respectively. Significantly, the energy diagrams of Fig. 4.38 clearly demonstrate the ability of EDORT in creating energy peaks pinpointing the location of each of the faults' present in the network compared to the ambiguity obtained with SDORT. The ending point of this procedure is determined by the empty eigenspace structure demonstrated by a negligible eigenvalue obtained after the third iteration of EDORT as shown in Fig. 4.39.

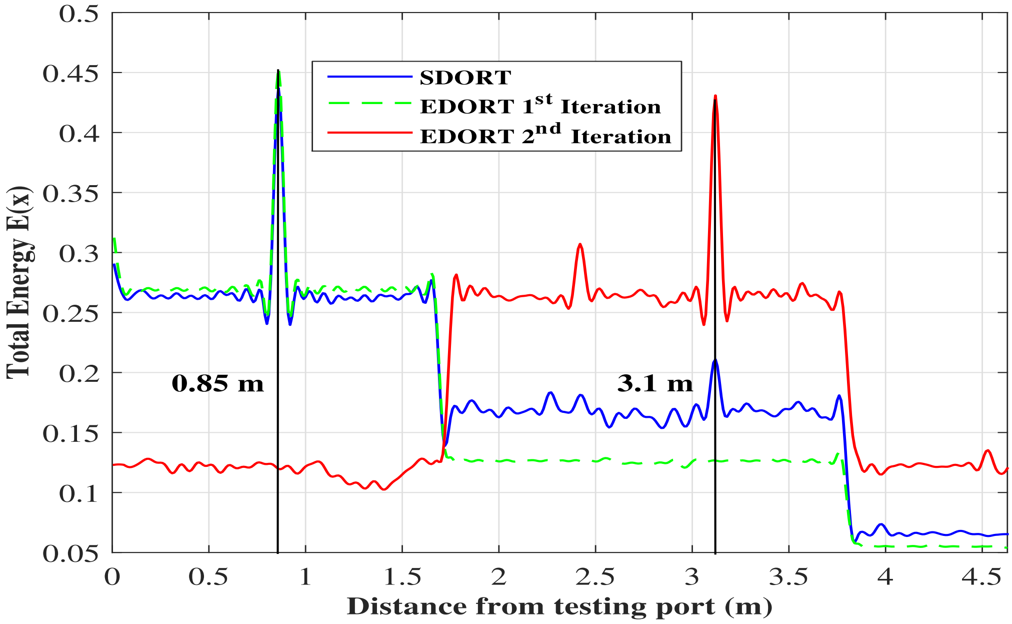

Figure 4.38 The total energy along the NUT in Fig. 4.26 (c), computed after applying the EDORT separation procedure. At each iteration the dominant energy peak corresponds to a fault not identified by the previous iterations. The energy distribution obtained when using the SDORT is also shown for reference, and contains two energy peaks at the position of the two faults.

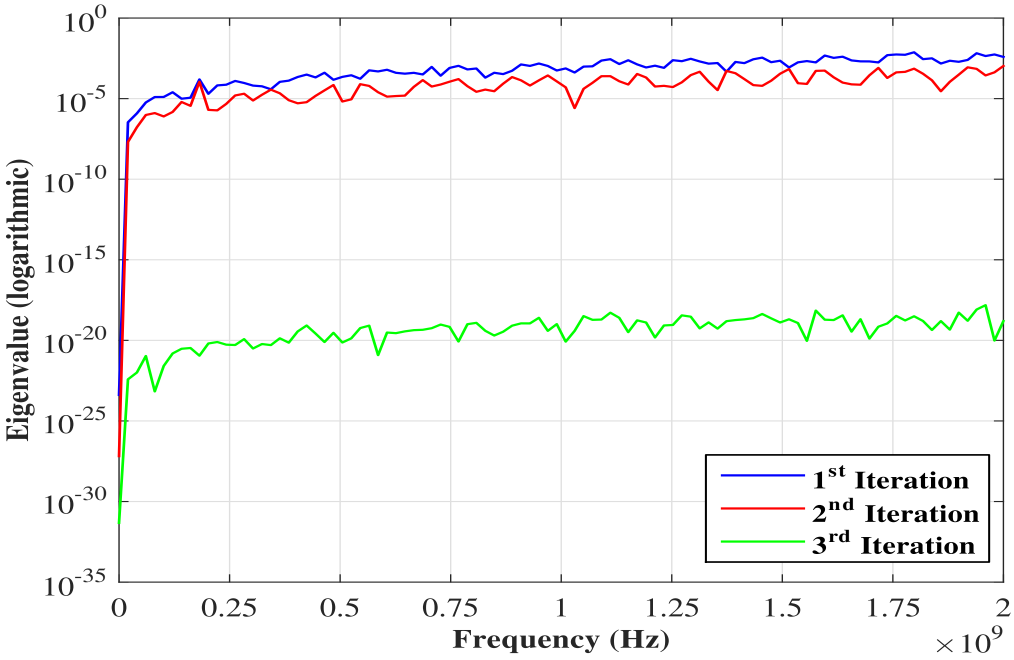

Figure 4.39 The most significant eigenvalue for the TRO, calculated for the double junction NUT of Fig. 4.26 (c) after applying the EDORT steps for the fist, second and third iterations.

4.6.4 Retrieving fault reflection coefficients

In order to assess the accuracy of eq. (4.19) in retrieving the reflection coefficients of the faults, their values were measured by directly connecting the faulty samples to one port of the VNA, while terminating the remaining port of the samples with a matched load. Eq. (4.19) was subsequently applied to the previously estimated single-fault scattering matrices where we firstly considered those corresponding to the double fault single branch NUT implemented in Fig. 4.26 (a). Results obtained are shown in Fig. 4.40, where we can see that the two sets of data of the measured and estimated reflection coefficients Γ_1 and Γ_2 closely agree.

The same operations were then carried out for the single-junction NUT in Fig. 4.26 (b). In this case, we can expect interactions between the faults and the discontinuity introduced by the junction. As a result, the simple model proposed in eq. (4.16) is expected to hold only on average. Fig. 4.41 shows the comparison between the measured and eq. (4.19)-based estimates of the reflection coefficients. It appears that the estimates oscillate around the true values that should have been retrieved.

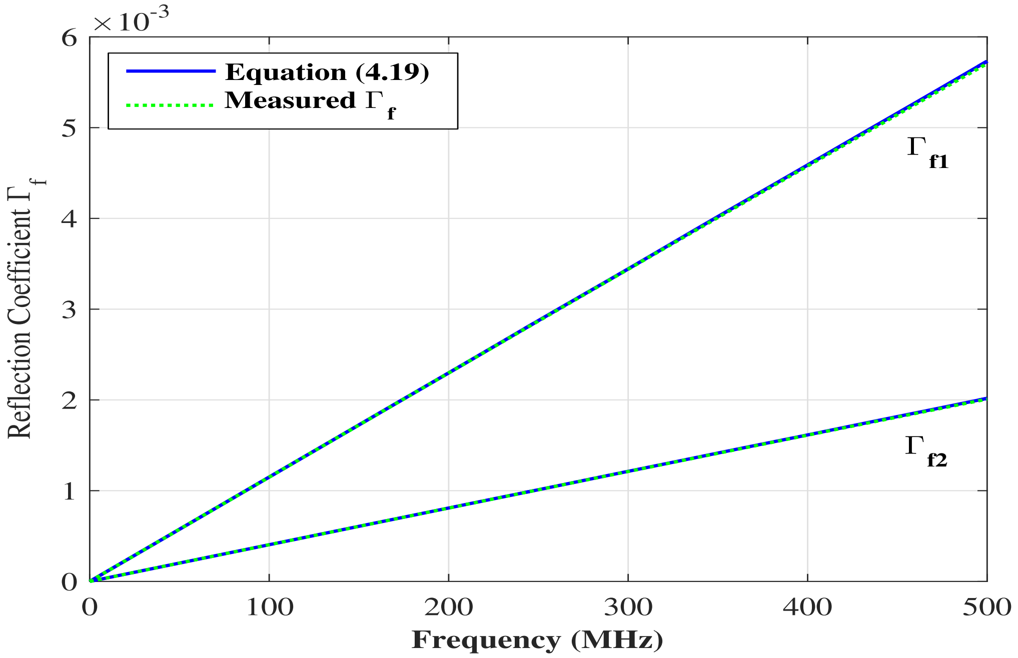

Figure 4.40 Amplitude of the measured reflection coefficients of the two faulty samples in Fig. 4.21 versus frequency. Estimates of these reflection coefficients obtained by means of the EDORT and (4.19) applied to experimental data from VNA measurements are also shown, corresponding to the setup in Fig. 4.26 (a).

Since this kind of behavior can be expected to have zero-average, because of phase rotation associated to frequency variations introduced by propagation delay, a simple linear regression through the estimate from (4.19) can be applied in order to reduce the impact of these oscillations.

The results in Fig. 4.41 confirm the effectiveness this procedure. Both reflection coefficients agree with the direct measurements.

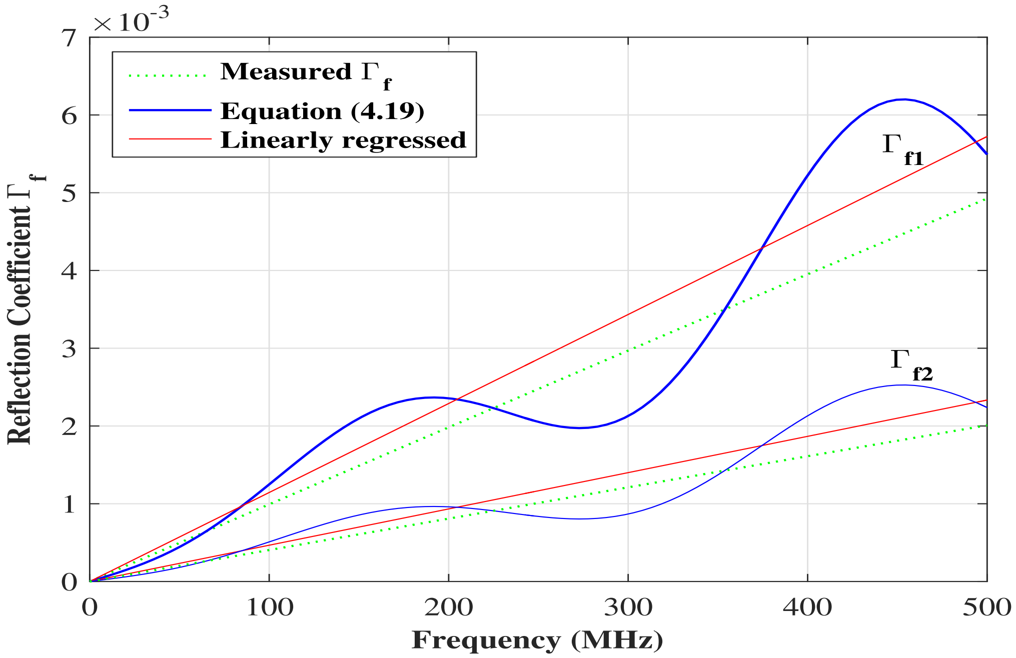

Figure 4.41 Same kind of results as in Fig. 4.40, but now dealing with the experimental setup in Fig. 4.27 (b). The results estimated by means of (4.19) are here also used as the basis for a linear regression, as explained in the body of the text.

4.7 Parametric Study

This section is devoted to provide an assessment of the applicability of DORT method towards some issues that might affect a network under test. Specifically, we will first begin by studying the effect noise can bring on the overall performance of DORT method in the precise detection and location of soft faults in complex wiring configurations. Afterwards, we will study the influence of changes in the lengths of branches composing the post-processing network model on the accuracy of the faults' positions.

4.7.1 Immunity towards Noise

Concepts and Tools

Real-life NUTs are always affected by some kind of background noise. Independently from its origin, the presence of noise puts a strong limit to the dynamic range of the signals that can be properly detected. In the case of soft faults, as their echoes can be expected to be quite weak, the possibility of having fault-related echoes beneath the level of background noise is clearly a critical configuration for standard TDR techniques. On the other hand, the ability of the DORT approach to ensure a maximization of the fault-related echo by maximizing the energy impinging on the fault position with respect to the rest of the system under test is a strong argument in its favor.

It is therefore important to assess how this energy maximization of the fault related peak translates into a corresponding improvement of the detection probability. In fact, the eventual presence of a fault in DORT method is inferred from the scattering matrix of the NUT rather than from echoes, as in TDR techniques. Besides, we have shown in the experimental validation that the process of obtaining the testing signals aiming to focus on the fault position after being applied to the post-processing network model are retrieved from the eigenvalue decomposition of the corresponding measured TRO. As such, it is convenient to compute the SNR at the level of the measured scattering matrix, where noise will be applied to all elements of the baselined matrix **S** before proceeding to the post-processing final step.

We consider an analysis based on the presence of an additive white Gaussian noise (AWGN), which does not bring any limitation to our conclusions, as the same analysis could be carried out considering other types of noise. The choice of an AWGN is just motivated by the simplicity of the related analysis.

In order to better understand the process of noise addition, let us consider **S** being the baselined scattering matrix collected from the experimental measurements, for instance **S** is measured independently at each frequency sample of the total considered bandwidth. Consequently, different levels of noise will be added to **S** at each frequency sample so that a fixed SNR value could be defined for **S** on the total bandwidth. In other words, if $\mathbf{S}^{f_k}$ is the scattering matrix at a frequency sample f_k, and $P_{sig}^{f_k}$ being the average power computed from all components of the corresponding scattering matrix as given in eq. 4.20, then for a value $x\ dB$ of the SNR, the noise power $P_{noise}^{f_k}$ will be computed according to eq. 4.21. It is noteworthy that the average power $P_{sig}^{f_i}$ becomes the square of the Frobenius norm of $\mathbf{S}^{f_k}$ as given in eq. 4.20, with n being the dimension of $\mathbf{S}^{f_k}$. Furthermore, the rational behind computing the average value of $\mathbf{S}^{f_k}$ as the signal power rather than choosing the maximum value is to avoid the total corruption of weak elements in $\mathbf{S}^{f_k}$. As a result, a unique SNR value will be defined for **S** at all frequency samples of the considered measuring bandwidth. The DORT technique will be then applied to the measured scattering matrices of the tested network configurations after numerically applying AWGN on different values of the SNR.

$$P_{sig}^{f_k} = \frac{1}{2n}\sum_{i=1}^{n}\sum_{j=1}^{n}|S_{ij}^{f_k}|^2 = \frac{1}{2n}\left(\|S^{f_k}\|_F\right)^2. \tag{4.20}$$

$$\text{SNR}_{dB} = \log_{10}\left(\frac{P_{sig}^{f_k}}{P_{noise}^{f_k}}\right). \tag{4.21}$$

In order to examine the problem of noise in DORT method, it is important to approach the detection probability which is characterized by the decision made on whether a fault is present or not. This decision directly depends on the value of the fault-related energy peak A^{max} at the instant of detection in the presence of noise $n(t)$. Applying the standard tools from the decision theory [152], the detection probability can be easily inferred by calculating the conditional probability of detection, hereafter referred to as the True Positive (TP) probability given by

$$P^{TP} = Pr(A^{max} + n(t)) > a_{th} | A^{max} > a_{th}). \tag{4.22}$$

Specifically, the TP is the conditional probability of having the amplitude of the fault-related energy peak A^{max}, affected by the instantaneous noise $n(t)$ at the eventual position of the fault, greater than the imposed detection threshold a_{th}, under the assumption of the fault's existence (noisy faulty NUT) that is $A^{max} > a_{th}$. The same rationale applies when calculating the conditional probability of detecting a fault when no fault exists (noisy faultless NUT), which is known as the false alarm rate and denoted to as the False Alarm (FA) probability.

$$P^{FP} = Pr(N_0 > a_{th}). \tag{4.23}$$

It is important to note that the detection threshold a_{th} is given as fraction of the maximum amplitude of the fault-related energy peak in the absence of noise A^{max}_{nless}, i.e, $a_{th} = \rho A^{max}_{nless}$ with $0 < \rho < 1$. With this in mind, AWGN will applied numerically to the considered measured baselined scattering matrices at SNR values ranging from -20 dB to 20 dB, while taking 10^4 different noise realizations at each SNR value, where a R^i_j will be denoted to each duet of a noise realization j at an SNR i, with j ranging from 1 to 10^4 while i from -20 dB to 20 dB with a step of 5 dB. Since the fault related energy peak and the added noise are independent scalar complex Gaussian processes which are independent ideally distributed (iid), the energy peak can be passed through a square law energy detector [153]. Consequently, and according to the Nehman-Pearson criterion, a detection threshold independent from the SNR is feasible because it only fixes the FA probability [153].

In our case study, A^{max}_{nless} is computed from the energy diagram of the faulty tested NUT under the assumption that no noise is present. Accordingly, the value of the energy peak found on the eventual position of the fault after applying the noise to the faulty and faultless cases at each R^i_j will be compared to a_{th} to decide whether a fault is present (1) or not (0), i.e is to compute the P^{TP} and P^{FA} probabilities respectively. This will be followed by computing the empirical P^{TP}_e and P^{FA}_e probabilities over the 10^4 realizations corresponding to a specific SNR at each value ρ.

Understanding the feasibility of the given probabilities necessitates introducing the Receiver Operating Characteristic curve (ROC) [154], which plots the TP probability in terms of the FA rate for different values of a parameter. Each point on the ROC curve represents a pair corresponding to a particular decision threshold, for a given SNR. In practical cases, the choice of this decision threshold is set as a compromise between the ability to detect the presence of the maximum peak and the need to provide a robust immunity with respect to noisy signals. The ROC curves can be useful to determine this detection threshold for a given SNR.

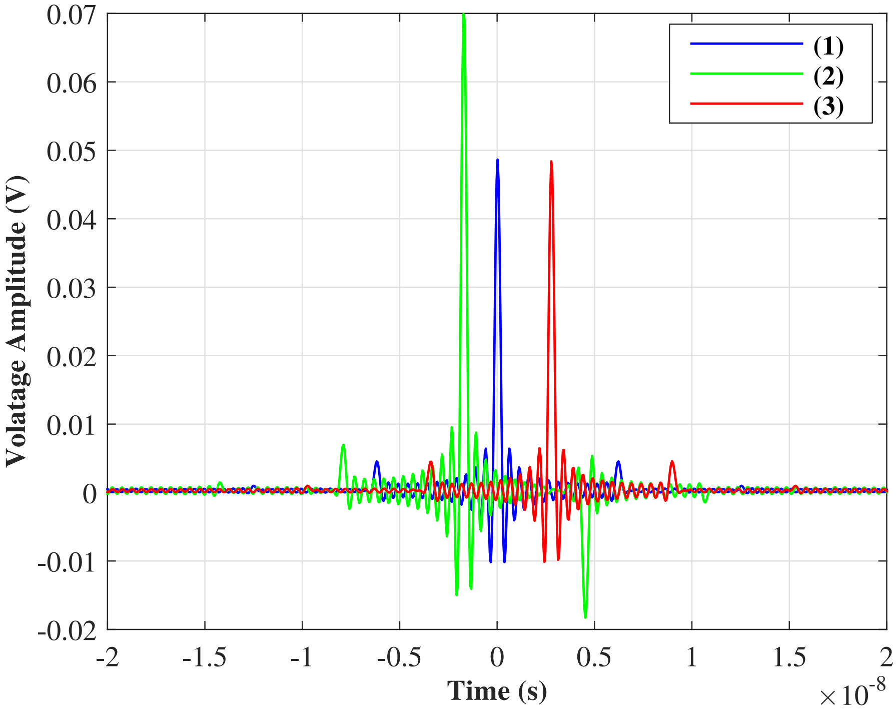

(a)

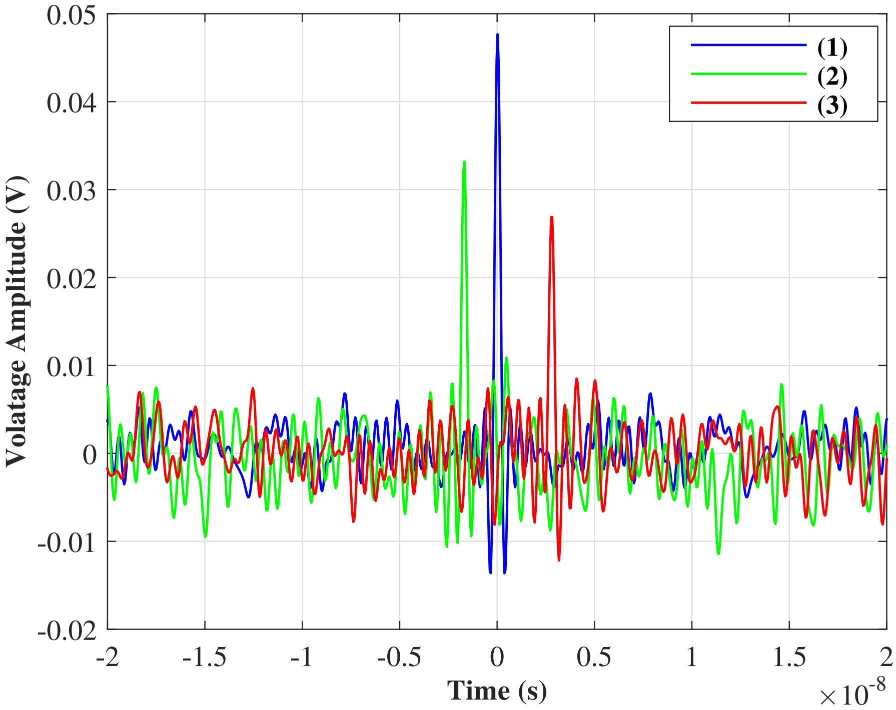

(b)

Figure 4.42 The testing signals resulting from the eigenvalue decomposition of TRO corresponding to the measured scattering matrix of the NUT of Fig. 4.22 (a), in the (a) noiseless case, and (b) at an SNR value of -5 dB.

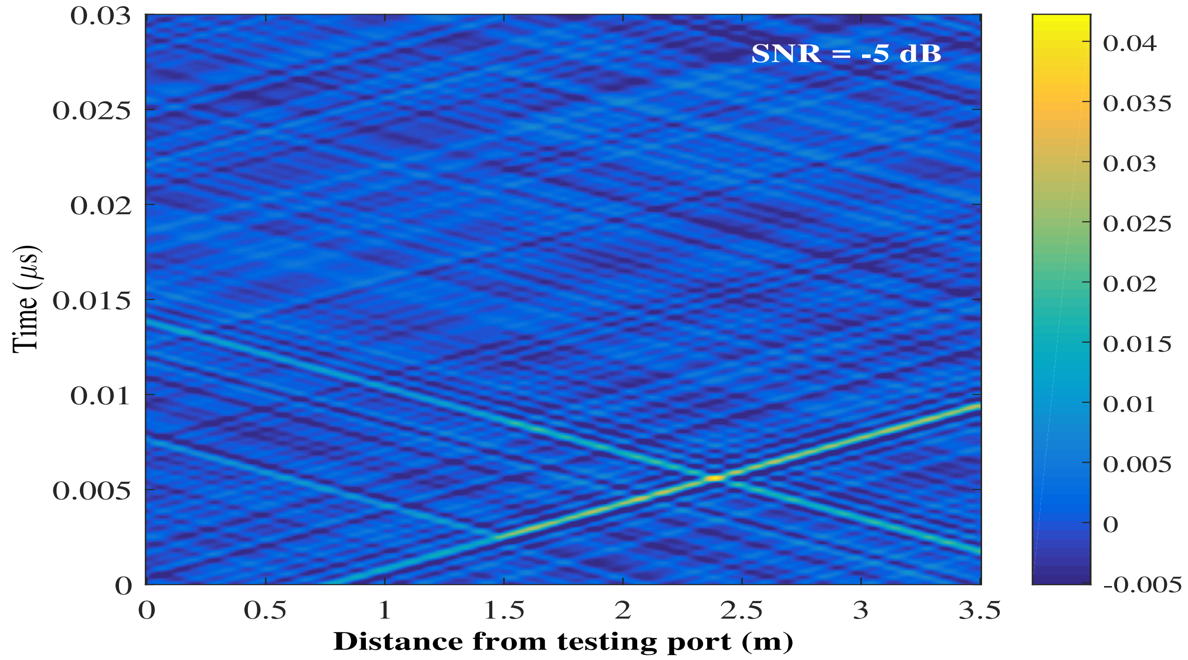

Figure 4.43 The ZT diagram corresponding to the single-junction single-fault NUT of Fig. 4.22 (a) at an SNR value of -5 dB observed along its second path. Notably, a focal spot can still be distinguished at the fault position although the noisy set of testing signals of Fig. 4.42 (b) are injected.

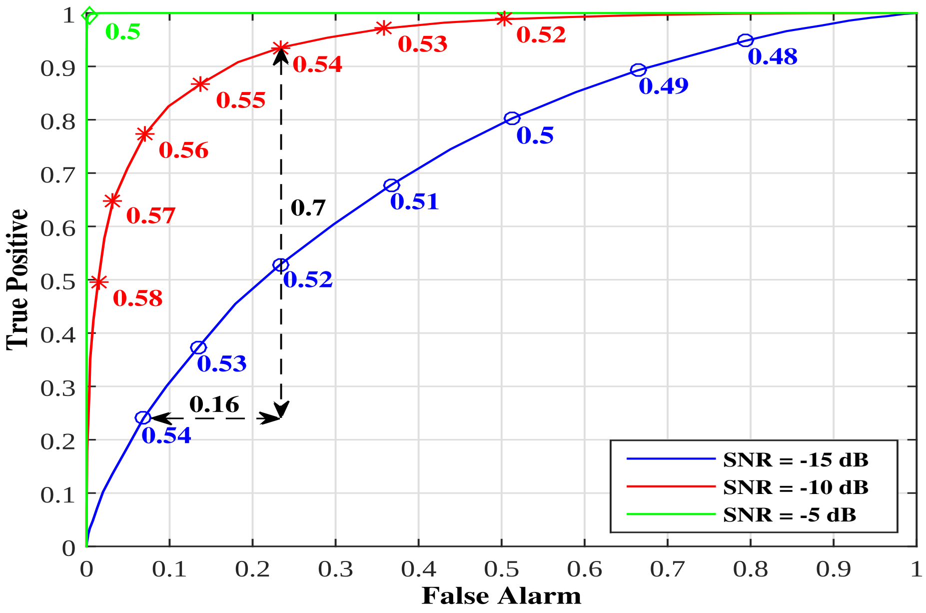

Figure 4.44 The ROC curve corresponding to the 2 m single-branch NUT with matched ends and a soft fault at 1.15 m. The TP is plotted versus the FA probabilities at different SNR values of -15 dB, -10 dB, and -5 dB, where the detection thresholds for each pair of TP and FA probabilities are marked on the figure.

Results and Discussions

In order to examine the robustness DORT method has provided in the domain of fault detection and location, we are going to examine three different complexity networks: a single-branch NUT of length 2 m with a single-soft fault at a position 1.15 m, in addition to the previously tested single-junction and double-junction networks of Figs. 4.22 (a), & (b) respectively.

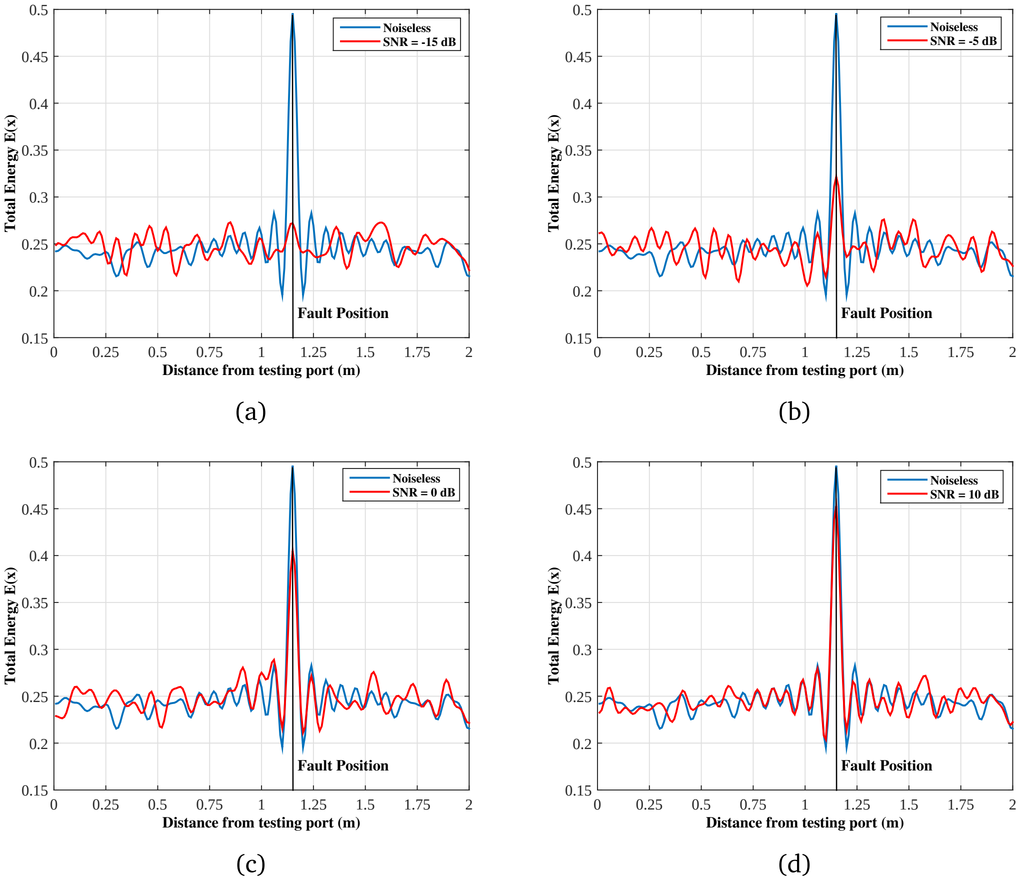

Figure 4.45 The total energy computed along a 2 m matched ends single-branch NUT containing a soft fault at a distance 1.15 m from the reference port. AWGN was applied to its baselined scattering matrix at different SNR values of (a) -15 dB, (b) -5 dB, (c) 0 dB and (d) 10 dB. The faulty noiseless case is also plotted on each figure for the sake of comparison.

We will first begin by studying the effect noise has introduced on the testing signals resulting from the eigenvalue decomposition of the TRO. To better illustrate this point, Fig. 4.42 (a), & (b) shows the three testing signals corresponding to the single junction NUT of Fig. 4.22 (a) in the noiseless case and at an SNR value of -5 dB respectively. Comparing the two sets of signals show that although the noisy case is affected by some perturbations, the signals' time delays are still the same. In particular, DORT method is based on these time delays as its mode of operation is to focus the testing signals on the position of the fault at the same time. With this in mind, applying the set of noisy testing signals to a reference model of the tested NUT leads to the ZT diagram of Fig. 4.43; markedly a focal spot can be still distinguished at the eventual position of the fault.

We will now examine the ROC curves of Fig. 4.44 corresponding to the single-branch single-fault network configuration of Fig. 4.22 (a) which are plotted at different values of the SNR at -15 dB, -10 dB, and -5 dB. If we consider the ROC curve at -10 dB, we can notice that it can be divided into three regions: the first one corresponds to the case when the TP and FA probabilities are both close to zero which are relative to a high detection threshold, the second one when both probabilities are close to 1, which means the detection threshold is set very low. The third region is the one between these two regions; it is the one we are interested in for an eventual analysis of the curve.

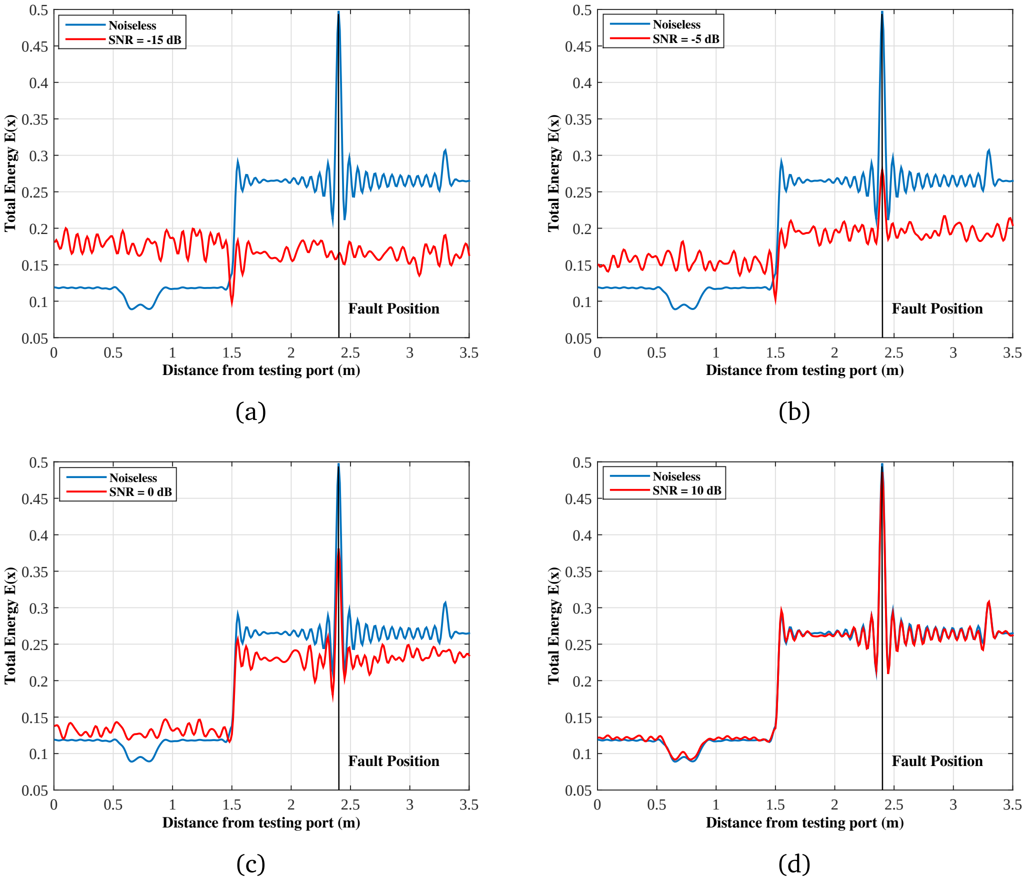

(a) (b) (c) (d)

Figure 4.46 The total energy computed along the second path of the single-junction NUT of Fig. 4.22 (a). AWGN was applied to its baselined scattering matrix at different SNR values of (a) -15 dB, (b) -5 dB, (c) 0 dB and (d) 10 dB. The faulty noiseless case is also plotted on each figure for the sake of comparison.

To determine the optimal detection threshold, we reconsider the same ROC curve of Fig. 4.44 plotted at different values of the detection threshold ρ at an SNR of -10 dB. Notice that for the values of ρ set between 54 % and 56 % of the maximal peak value, the TP probabilities range between 0.77 and 0.93, with the FA probabilities not exceeding 0.23, thus a detection threshold ranging between these two values can be chosen, $\rho = 0.55$ can be a good choice. Applying the same rational to the ROC curve obtained at an SNR of -15 dB we can infer that an optimal performance is reached at a detection threshold of 0.51.

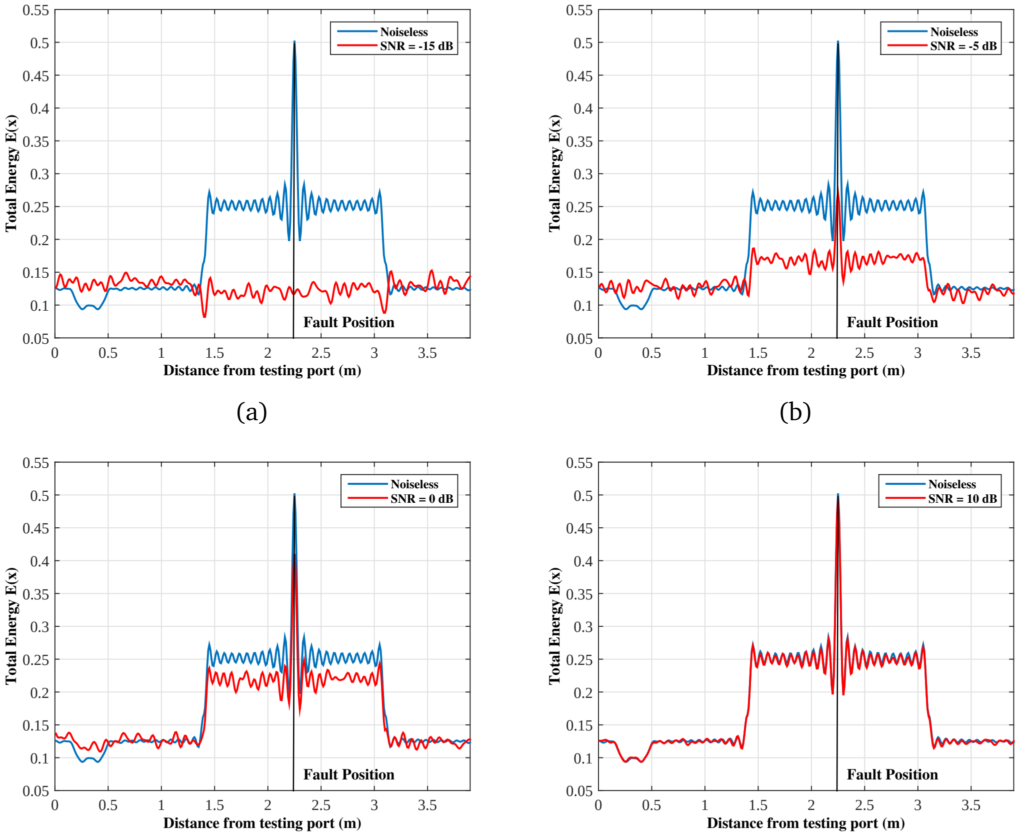

(a) (b)

(c) (d)

Figure 4.47 The total energy computed along the third path of the double-junction NUT of Fig. 4.22 (b). AWGN was applied to its baselined scattering matrix at different SNR values of (a) -15 dB, (b) -5 dB, (c) 0 dB and (d) 10 dB. The faulty noiseless case is also plotted on each figure for the sake of comparison.

Remarkably, for a detection threshold of $\rho = 0.54$, the FA and TP probabilities are 0.06 and 0.24 respectively at an SNR=-15 dB whereas they are 0.23 and 0.93 for an SNR = -10 dB. In other words, a 5 dB SNR gain led to a TP gain of 0.7 for an only 0.16 FA loss. This shows a significant improvement in the performance of the detection gain even at low SNR values typically below 0 dB. Furthermore, it can be noted that by increasing the SNR, the ROC curves show a fast convergence towards a step function which was a perfectly obtained at an SNR of -5 dB.

As an illustration, and in order to examine the effect noise introduces on the proper detection of a fault, the energy is traced at different SNR values for the single-fault single-branch NUT as shown in Fig. 4.45 where each case presents the noiseless faulty result compared to that of the noisy case at a specific value of the SNR. Fig. 4.45 (a) shows that for a low SNR = -15 dB the peak value obtained at the position of the fault is relatively masked by those caused by the AWGN which can explain the low detection probabilities obtained in the corresponding ROC curve of Fig. 4.44. Notably, the energy peak's detectability appears to have been improved with a higher SNR = -15 dB where Fig. 4.45 (b) shows that it is more visible relative to the noise background. Significantly, the situation improves where higher energy peaks are obtained at SNR values of 0 dB and 10 dB as shown in Figs. 4.45 (c), & (d) respectively.

We turn our attention now to more complex NUTs at the single junction and double junction networks of Figs. 4.22 (a), & (b) respectively. The extremities of the networks are terminated by matched ends. The energy diagrams of Fig. 4.46 correspond to the NUT of Fig. 4.22 (a), where increasing the SNR value from -15 dB, where no peak can be distinguished at the fault position due to the strong noise background, to a value of -10 dB leads to better probability of detection, which is predicted to be more evident at higher SNR values of 0 dB and 10 dB as Figs. 4.46 (c)& (d) attest. In fact, this same result is obtained in the energy diagrams of Fig. 4.47 corresponding to the double junction configuration of Fig. 4.22 (b).

The ROC curves of Figs. 4.48 (a), (b) &(c) are meant to investigate the effect increasing the network's complexity can have on the evolution of the TP and FA probabilities. Accordingly, three different SNR values of -15 dB, -10 dB, and -5 dB were considered for the three different studied networks. Significantly, the results obtained imply that for the same level of applied AWGN, the detection probability is substantially higher with an increased complexity for the network. Notably, a perfect step function is obtained for the three NUT configurations at a very low SNR value of -5 dB.

In fact, the enhancement in the robustness of DORT while increasing the complexity of the network might be returned to two main reasons. For instance, this can be a result of the increase in the number of testing ports proper to increasing the network's complexity, which in turn increases the number of signals supposed to interfere constructively at the position of the fault and thus leading to higher energy peaks than the background noise. With this in mind, if we consider the simplest NUT configuration designated by the single-branch NUT, two testing signal can be defined. Accordingly, if one of these two signals is totally corrupted by noise it is surely impossible to have a constructive interference on the position of the fault. On the other hand, this is no longer the case with NUTs composed of several junctions where this increased complexity is accompanied by an increase in the number of testing signals, thus a high noise perturbation of any of the signals do not imply a total loss of focusing as other signals can still accomplish the mission. Another key point, is that the presence of junctions can in turn scatter to a great extent the echo focusing of noisy signals at different positions of the network rather than focusing more strongly on the fault's position.

Generally speaking, results have shown a remarkable robustness of DORT method to noise which proved to afford optimal performances in relatively noisy measuring environments characterized by low SNR (below 0 dB). Moreover, it was shown that the increasing the complexity of the network improved the performance of DORT method, as an increasingly number of junctions

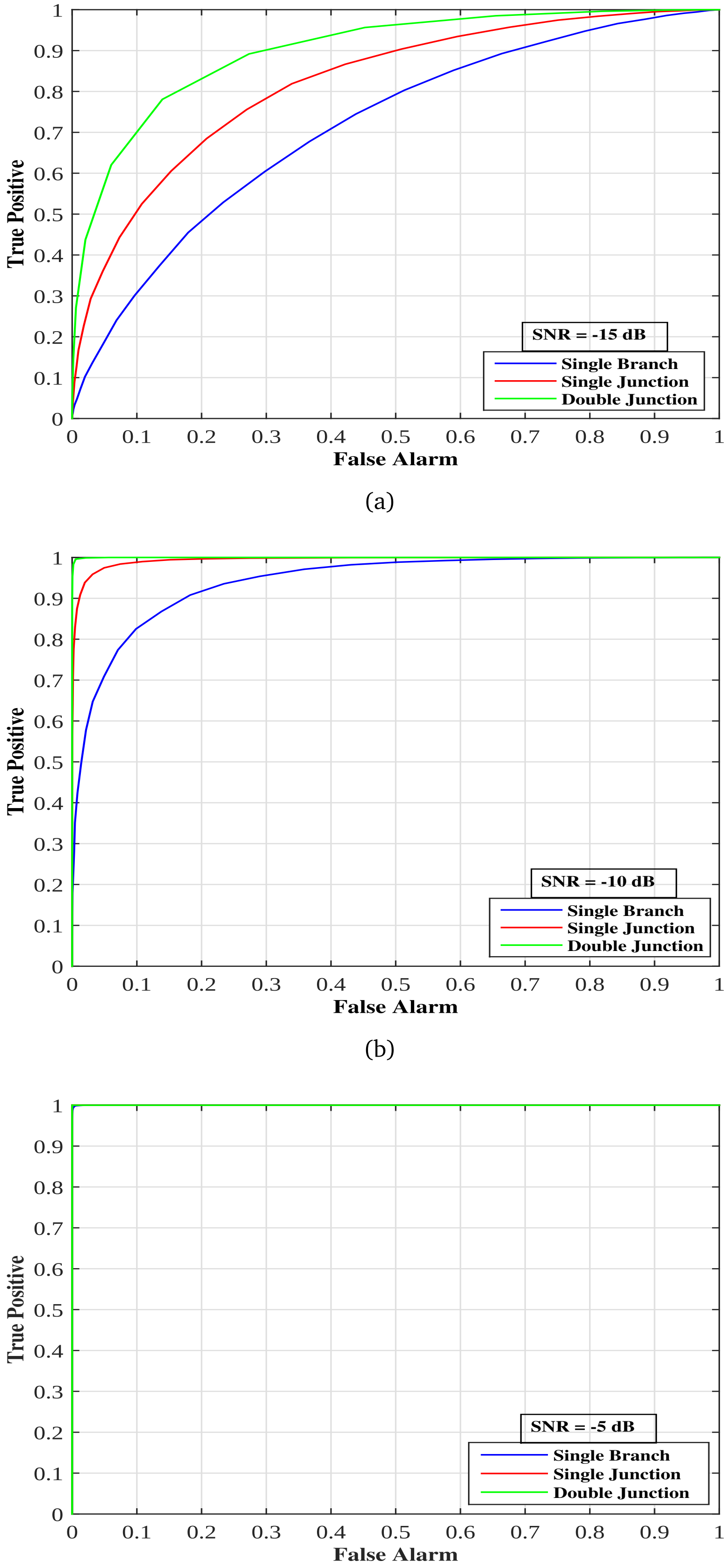

(a)

(b)

(c)

Figure 4.48 The ROC curves plotting TP versus the FA probabilities and comparing the results between the single-branch, single-junction, and double-junction configurations at three different SNR values of (a) -15 dB, (b) -10 dB, and -5 dB.

systematically scatters noise related constructive interferences throughout the network. Besides, this was accompanied by increasing the number of testing signals corresponding to the increase in the number of testing ports which result in a more significant constructive interference on the fault position.

As a matter of fact, this significant robustness of DORT to noisy measured data unveils an important feature in the domain of fault detection and location. In other words, standard reflectometry techniques necessitate measuring conditions with high SNR values in order to return accurate locations of soft faults in wiring networks. On the other hand, DORT method while operating on low SNR values (below 0 dB) can still return good estimates of their positions. With this in mind, the VNA's sweep time, i.e the time needed to return a complete measurement of the tested network's scattering matrix, increases whenever high SNR (noiseless) measurements are needed. Specifically, this sweep time is directly controlled by the VNA's averaging function which is adjusted by the intermediate frequency bandwidth (IF BW) where the noise floor can be improved by reducing the system's IF BW. Notably, the SNR is ameliorated by 3 dB for every factor of 2 increase in averages. Although, it is a powerful method for reducing noise floor, it also reduces measurement speed which in turn increases the measurement time. Markedly, DORT method presented a great performance at low SNR values, thus noisy measured scattering matrices can still be used while returning good estimates of the fault's position as the obtained results attest. Consequently, lower VNA IF BW can be set which means lower measurements periods. With this in mind, intermittent soft faults, which always appear with short durations and low magnitudes, could be potentially detected and located with DORT method.

4.7.2 Tolerances to length change

We have discussed in the last section of chapter 2 the importance of baselining, i.e taking the difference between the faulty and non-faulty versions of the same NUT, on the performance of fault detection and location methods while considering the standard reflectometry case as an example. In fact, any slight change in the baseline model would make the detection of a soft fault impossible. As for DORT methods, the essentiality of baselining is two fold; first it allows considering the soft fault as a secondary source which is an important condition for the applicability of DORT method, second it makes detecting soft faults possible, a feature shared with other fault detection and location techniques.

In our numerical and experimental investigations, we have considered the case of perfect baselining in order to obtain precise estimates of the positions of soft faults in different NUTs. In fact, the process of computing the testing signals was accomplished by numerical post-processing on Matlab, where they were also injected to a reference model of the tested NUT created on the same simulation platform. In other words, this reference model is of the same dimensions and topology as the studied network. But what if wrong estimates of the lengths of the branches composing the reference NUT model occurred? To answer this question we reconsidered the same three network

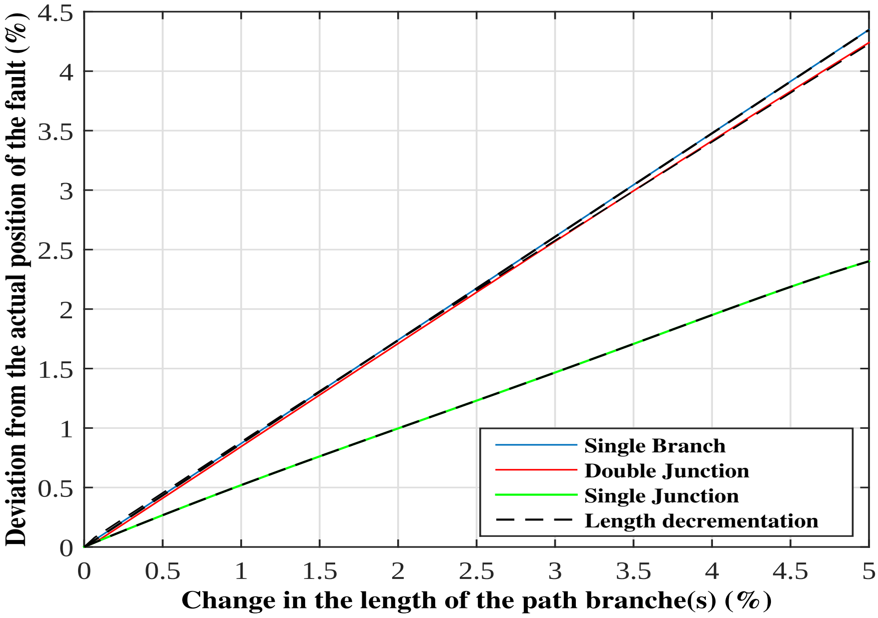

Figure 4.49 The percentage deviation of the position of the fault plotted as a function of the percentage change (incremental and decremental) in the lengths of the cables linking the fault for a single-branch, single-junction and double-junction NUTs. The decremental case is showed in black while the original colors are for the incremental case.

configurations of the previous sec. 4.7.1 where changes were applied to the lengths of the cables composing the network models. Meanwhile, two different changes were considered: an incremental and another decremental in the length of one the branches in the network. Specifically, alterations ranging to 5% of the length of the considered branch were accounted for both cases (incremental and decremental) and accordingly the DORT post-processing was applied to each studied network.

The results corresponding to a length manipulation in the branch containing the fault are summarized in Fig. 4.49, where we can see that a linear variation in the fault's position occurs as consequence of the branch's length alteration. Notably, a smaller deviation is observed for the eventual position of the fault with respect to that of the reference model's change, where the same result can be spotted for the incremental and decremental cases proving that the latter has no effect on the overall response of the process. In fact, the performance seems to improve as the network's complexity increases where a slight gain is obtained for the single-junction configuration compared to that of the single-branch network. Surprisingly, a much better performance is obtained for the double-junction case, which seems to be less sensitive to changes in the NUT model length variations.

To better understand the reasoning behind this kind of performance, we will first begin with the scheme of Fig. 4.50 which shows the single-branch network with its corresponding two testing signals. Normally, in a healthy network model, a constructive interference is expected on the fault

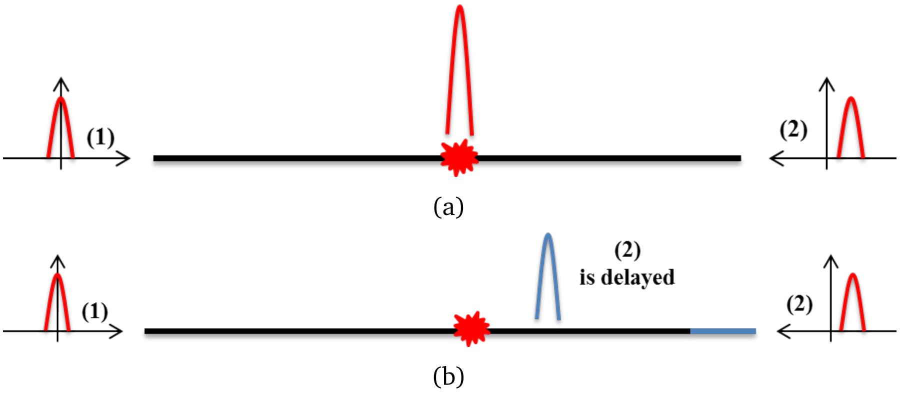

Figure 4.50 A demonstration of the effect of branch length variations of the NUT single-branch model on the precise location of the fault where (a) shows a perfect reference network model leading to a constructive interference of the two testing signals on the position of the fault, (b) a change in the branch length results in a delay of arrival of the corresponding testing signal and consequently an interference of the signals on a position other than that of the fault.

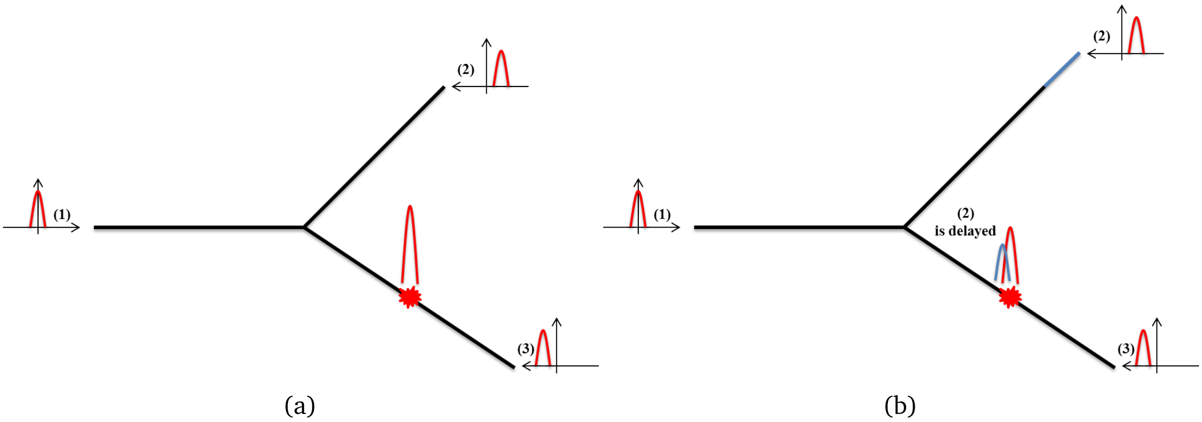

Figure 4.51 A demonstration of the effect of branch length variations of the NUT single-junction model on the precise location of the fault where (a) shows a perfect reference network model leading to simultaneous constructive interference of all testing signals on the position of the fault at the same time, (b) a changed branch length of one of the branches composing the NUT model leading to a delay of arrival of the corresponding testing signal and consequently an overlapping with the components of the constructive interference on the eventual position of the fault.

position which can be inferred from Fig. 4.50 (a). Unfortunately, any change in the length of the branch will be accompanied with a delayed or an advanced testing signal thus leading to an interference on a position other than that of the fault as shown in Fig. 4.50 (b).

Significantly, it was noted that the performance has improved with the increase in the network's complexity. This result can be understood if we consider the demonstration of Fig. 4.51 examining the single-junction network. In fact, three testing signals are defined in this case where injecting them into an unaltered model of the NUT will lead to a constructive interference on the fault position as presented in Fig. 4.51 (a). On the other hand, if the length of one of the branches composing the network is changed, the testing signal injected in its corresponding branch will be either delayed or advanced in time. Although this occurs, but the other two testing signals injected in the unaltered branches can still reach the fault's position at the same time. Consequently, a constructive interference resulting from the unmodified signals will occur at the fault position in addition to an overlapping with the time modified testing signal as shown in Fig. 4.50 (b). This effect is predicted to become smaller with more complex networks as more testing signals are present whose interference effect would mask the overlapping produced by the altered signal. Eventually, this explains the improved performance obtained with the increase in the network's complexity shown in Fig. 4.49.

4.8 Conclusion

We began this chapter by recalling the standard DORT technique (SDORT) which was capable of effectively locating single soft faults in different network configurations. This was supported by numerical and experimental results that validated the standard method. Although, SDORT has shown to be promising in locating single soft faults, it faced several limitations when multiple ones appeared in an NUT. For this reason, the shortcomings of SDORT in this case were detailed, meanwhile an alternative formulation based on an updating scheme was presented. The input signals used for imaging the faults were shown to focus selectively on single faults, allowing a clear identification. No spurious focusing was observed, thus reducing the probability of false alarms. Experimental validations also confirmed these conclusions, when considering both very weak faults and non-trivial NUT layouts. These results give credibility to the practical usefulness of the proposed method in real-life network configurations that are hardly addressed in current literature.

Additionally, the proposed methodology allowed an accurate estimate of the severity of each fault, which enabled retrieving its reflection coefficient in a precise manner. In fact, this feature is of practical interest when monitoring the state of cables in wiring networks especially in nowadays' systems where wires became responsible of control and safety operations. Accordingly, this feature permitted anticipating the degree of seriousness of the wiring fault for a better assessment of the level of intervention needed for fixing or repairing the wire before the occurrence of drastic consequences. In the last section of this chapter, we performed a parametric study of DORT method handling two important issues: noise and changes in the lengths of cables composing the post-processing network model. Significantly, DORT method has shown great performance and an excellent robustness in locating soft faults in noisy measurement conditions along with an increasing immunity and better achievements when dealing with an increased network complexity. Notably, the eminent effectiveness of DORT technique with noisy measured data allow accomplishing measurements in relatively very short durations, which in turn will encourage the potential efforts for locating intermittent soft faults. Equally important, is the results DORT presented with changes in the lengths of branches composing the simulation network model. As a matter of fact, we have shown that these changes are confronted with lower ones in the fault position whose effect decreases with an increasing complexity of the tested wiring networks.

Despite the fact that, the study we conducted in this chapter showed the feasibility of DORT method with its both versions, the standard and enhanced techniques, in precisely locating single as well as multiple soft faults in different complexity network configurations, it still shared limitations encountered by time domain fault location techniques. As a matter of fact, DORT-based methods use a sub-space approach in defining signals that, once fed into a numerical model of the NUT, will focus back to the position of a fault; this propagation phase is carried out in the time domain, and therefore undergo most of the same limitations of any other time-domain method, particularly the need for large bandwidth to create spatial resolution. On the contrary, TR-MUSIC, as will be presented in the next chapter, does operate on a different sub-space approach, based on the Green function of the NUT; no back-propagation phase is used and actually a correlation process is defined. TR-MUSIC operates on phase patterns provided by Green function as a mean of identifying positions in a complex medium.

Chapter 5

Soft Fault Location Using TR-MUSIC Method

Contents

5.1 Introduction

In the previous chapter, we studied fault location based on the properties of the time reversal DORT concept, where we introduced two approaches: the SDORT and the EDORT techniques. We started by recalling the main principles of the standard version of DORT in precisely locating single soft faults in complex wiring networks. However, we showed that this method started failing once multiple faults are addressed in an NUT. As a result, we proposed an alternative formulation based on the tenets of SDORT but in a complementary manner that efficiently provided accurate estimates of the positions of multiple faults in different complexity wiring configurations.

It is worthy to note that, DORT based methods are essentially based on a time domain approach, thus as any method based on time-domain analysis, belonging to TDR methods or not, rely on the availability of potentially large bandwidths, in order to create the conditions for spatial resolution. The spatial resolution Δs enabled by a test signal is directly proportional to its spatial support or that of its autocorrelation function, given by

$$\Delta s = k\frac{v}{B_T}, \tag{5.1}$$

where v is the speed of propagation of electrical signals along the cables of the NUT and B_T is the bandwidth of the test signals; k is a constant of the order of unity, dependent on the shape of the test signals. Limitations are thus introduced by the ability of cables in an NUT to support such bandwidths, as in the case of low-frequency networks such as power grids.

With this background in mind, we studied the possibilities offered by time-reversal (TR) multiple signal classification [110, 126], also known as TR-MUSIC [111]. It has already been applied with success to other detection problems and appears to bring an effective answer to all of the limitations recalled so far [155, 156]. TR-MUSIC is mainly applied for detecting and locating scatterers in a background medium; indeed, soft faults can also be treated as weak scatterers. The most striking feature of TR-MUSIC is that it ensures *sub-wavelength spatial resolution* while working on a single-frequency basis [157], which is in contradiction with (5.1). Besides, it works independently of the *well-resolvedness* criteria for multiple scatterers already discussed in sec. 3.4.2 and returns *super-resolution* estimates for their locations.

TR-MUSIC shares the same foundations as DORT-based methods, namely, the availability of a mutistatic (or multiport) characterization of the NUT, but they follow two distinguished ways to translate multistatic data into a fault position. DORT-based methods use a sub-space approach in defining signals that, once fed into a numerical model of the NUT, will focus back to the position of a fault; this propagation phase is carried out in the time domain, and therefore undergo most of the same limitations of any other time-domain method, particularly the need for large bandwidth to create spatial resolution. On the contrary, TR-MUSIC, does operate on a different sub-space approach, based on the Green function of the NUT; no back-propagation phase is used, and a correlation with the noise subspace is defined instead. TR-MUSIC operates on phase patterns provided by the Green function as a mean of identifying positions in a complex medium.

In this chapter, the performance of TR-MUSIC is studied for detecting and locating single as well as multiple soft faults in different network configurations. Numerical and experimental results are conducted in order to confirm the practical potential applicability of this novel approach. TR-MUSIC is also shown to allow retrieving the reflection coefficient of each fault without having to measure the reflections of testing signals, thus giving a direct evaluation of the risk they pose to the integrity of the NUT. Notably, TR-MUSIC has provided an effective performance in the presence of noise, where a good robustness was revealed starting for a SNR as low as 0 dB. In fact, a heuristic approach is presented which allowed returning good estimates of the positions of the faults at low SNR values in different complexity NUTs.

5.2 TR-MUSIC in Guided wave Propagation

The application of DORT to fault detection and location was introduced earlier in the previous chapter, proving to have advantages compared to standard TDR techniques and showing to be efficient in locating single as well as multiple soft faults in different network configurations. Yet, it is also a time-domain method, where spatial resolution can only be gained by means of pulsed signals, i.e., large bandwidths. In what follows we will focus on TR-MUSIC, as it has presented major advantages over the remaining methods, in particular *super-resolution* imaging while using single frequency excitation signals.

5.2.1 TR-MUSIC: Application to wiring networks

In the last section of chapter 3 we have thoroughly detailed the basic principles of TR-MUSIC in free space where we have noticed that it employs the noise space $\mathscr{N}$ of the system's multi-static data matrix whereas DORT utilizes the components of the signal space $\mathscr{S}$. As such, TR-MUSIC returns precise estimates of the target's locations regardless their *well resolvedness* criteria, since $\mathscr{N}$ is always orthogonal to $\mathscr{S}$. Accordingly, TR-MUSIC adapted to guided wave propagation along transmission lines is capable of locating single as well as multiple soft faults in different wiring configurations. This is due to the fact that TR-MUSIC is not sensitive to fault coupling compared to a high sensitivity with the standard DORT method.

As it is typically the case when dealing with soft faults, the baselining approach shall be applied where its significance becomes twofold in TR-MUSIC. First, it is an effective solution to remove the spurious echoes generated by impedance discontinuities like junctions, leaving only those echoes initially generated by the interaction between the testing signals and the faults [28, 150]. Besides, removing the echoes generated by junctions is also beneficial in order to increase the maximum number of faults M that TR-MUSIC can detect, which is theoretically limited to $N-1$, where N is the number of testing ports. As a matter of fact, a junction is nothing else than a scatterer, thus its presence in an NUT limits the number of faults that can be possibly detected to $N_{det} = M - n_{jun}$ (N_{det} being the number of faults that could be detected while n_{jun} being the number of junctions). Consequently, increasing the networks complexity to NUT's composed of several branches leads in turn to an increase in the number of junctions; regrettably this increase in n_{jun} will be faced with a decrease in N_{det}. Therefore, applying the baselining process removes the junctions' effect leaving a scattering matrix with nothing else than the signature of the faults. Accordingly, the NUT's response after baselining will be $\mathbf{S} = \mathbf{S}_f - \mathbf{S}_h$, with $\mathbf{S}_f$ and $\mathbf{S}_h$ the scattering matrices of the (eventually) faulty NUT and its healthy (reference) version, respectively.

The baselined scattering matrix is then used to compute the TR operator (TRO) $\mathbf{K} = \mathbf{S}^\dagger\mathbf{S}$. TR-MUSIC was shown to be capable of locating M faults from the knowledge of the TRO under the condition that $N > M$ [110, 157]. It does so by computing the eigenvalue decomposition of $\mathbf{K}$ according to eq. (5.2), which is also equivalent to the singular value decomposition of $\mathbf{S}$ [158] where the number $M < N$ of the non-negligible eigenvalues hints at the number of potential faults found in the NUT. Henceforth, there are at most $N - M$ negligible eigenvalues indexed from $M + 1$ to N where the maximum number of faults that can be addressed by TR-MUSIC is $N_{max} = N - 1$.

$$\mathbf{K} = \mathbf{U}\mathbf{\Lambda}\mathbf{U}^\dagger, \tag{5.2}$$

The quantity Λ is a real-valued diagonal matrix containing the eigenvalues, while $\mathbf{U}$ is the eigenvector matrix. In fact, $\mathbf{U}$ can be divided into a signal space $\mathscr{S}$ and a noise space $\mathscr{N}$; the latter can be seen as an approximation of the null space of $\mathbf{K}$. $\mathscr{S}$ is identified by the eigenvectors associated with the most significant eigenvalues, with respect to a threshold λ_{th}, i.e., $\mathscr{S} = \text{span}\{\mathbf{u}_i : \lambda_i > \lambda_{th}\}$, whereas $\mathscr{N}$ is formed by the remaining eigenvectors deemed to have negligible eigenvalues $\mathscr{N} = \text{span}\{\mathbf{u}_i : \lambda_i < \lambda_{th}\}$, with λ_i and $\mathbf{u}_i$ are the eigenvalues and their corresponding eigenvectors, respectively; λ_{th} is set by analyzing the scree plot of the eigenvalues of $\mathbf{K}$.

Following the properties of TR-MUSIC in open media, each fault can be spotted by observing the singularities in the pseudo-spectrum $\Phi(X_p)$ computed according to eq. 3.21 of chapter 3, where its denominator is simply the magnitude square of the projection of the Green function at a position X_p onto the noise space $\mathscr{N} = \text{span}\{\mathbf{u}_i : \lambda_i < \lambda_{th}\} = \text{span}\{\mathbf{u}_i, i = M + 1, ..., N\}$. Therefore, to perform this projection a reference model of the NUT is needed in order to deliver the Green function vector which will serve as a steering vector for a fault located at the test location X_p.

For guided wave propagation in wiring networks, the reference model is computed by means of a numerical simulator for transmission lines, modeling the layout of the healthy NUT. The Green function here relates the voltage at a position X_{p_j} along the healthy NUT with the N excitation voltages applied to its N testing ports where the distances are measured relative to the reference port j. The projection operation is then performed between the eigenvectors of $\mathscr{N}$ and the forward propagating voltage $\mathbf{v}(X_{p_j})$ taken with respect to j which is observed throughout the numerical model of the network at each position X_{p_j}, i.e. $< \mathbf{u}_{(\lambda > \lambda_{th})}, \mathbf{v}^*_{X_{p_j}} >$.

To this end, the fault's positions would be found by looking for singularities in $\Phi^{Guided}(X_{p_j})$.

$$\Phi^{Guided}(X_{p_j}) = \frac{1}{\sum_{i=M+1}^{N} | < \mathbf{u}_i, \mathbf{v}(X_{p_j})^* > |^2}. \tag{5.3}$$

5.2.2 Estimating a fault severity

Once the position of each fault in the NUT is found thanks to the pseudo spectrum given by eq. 5.3, it is possible to estimate the NUT response $\mathbf{S}_i$ that would be measured if only one fault at a time appeared. As discussed in the fault retrieval procedure accomplished in the previous chapter for EDORT, as long as soft faults are considered, the first Born approximation holds [72], thus the global scattering matrix of any faulty NUT can be broken down as

$$\mathbf{S}_G \approx \sum_{i=1}^{M} \mathbf{S}_i. \tag{5.4}$$

The main limitation in (5.4) is its neglecting interactions between multiple faults, which can induce errors, as discussed in sec. 4.6.4 of chapter 4.

Now the problem is that the fault reflection coefficients $\{\Gamma_i\}$ are unknown. As long as the faults are soft, i.e., $|\Gamma_i| \ll 1, \forall i$, the propagation of voltage waves within the NUT would be hardly affected, again under Born first approximation. This observation implies that a dummy fault of known value $\Gamma_{d,i}$ can be used instead of the real unknown fault Γ_i, yielding a scattering matrix $\mathbf{S}_{d,i}$. This latter is ideally identical to $\mathbf{S}_i$, but for the factor $\Gamma_i/\Gamma_{d,i}$. Introducing the matrices $\tilde{\mathbf{S}}_i = \mathbf{S}_{d,i}/\Gamma_{d,i}$, the $\{\Gamma_i\}$ can be estimated by solving the least-square problem

$$\min_{\{\Gamma_i\}} \left\| \mathbf{S}_G - \sum_{i=1}^{M} \Gamma_i \tilde{\mathbf{S}}_i \right\|^2, \tag{5.5}$$

i.e., by using the $\{\tilde{\mathbf{S}}_i\}$ as regressors for the measured scattering matrix $\mathbf{S}$.

It is worthy to note here that $\mathbf{S}_i$ in the case of EDORT presented in chapter 4 is computed at each iteration of the method by extracting its components from the corresponding global scattering matrix. This will be followed by a post-processing enabling the location of the faults' positions and retrieving their corresponding reflection coefficients. On the other hand, TR-MUSIC plays the way round where it allows first determining the positions of the faults which will form the basis for a following extraction of the $\mathbf{S}_i$'s to retrieve their severities as presented in this section.

5.3 Results and analysis

The performance of TR-MUSIC as presented in sec. 5.2.1 is tested against numerical and experimental data measured from NUTs affected by a single as well as multiple soft faults. Accordingly, having extracted the position of the faults, the analytical model explained in sec. 5.2.2, will allow retrieving their corresponding reflection coefficients.

5.3.1 Numerical Results

We will begin our study of the TR-MUSIC method by conducting numerical simulations using the network configurations presented in Figs. 5.1&5.2, where we have considered three different network topologies: a single-branch configuration, a single Y-junction structure, and a double Y-junction network configuration. Besides, two different fault-network configurations were examined: one considering a single-fault and another studying a double-fault embedded in the NUT. The results obtained are meant to prove the potential benefits provided by the TR-MUSIC adapted to guided wave propagation along transmission lines in locating the position of single as well as multiple soft faults in different complexity network configurations. The feasibility of TR-MUSIC in retrieving the position of a fault while using a single frequency component (the monochromatic case) is also checked, a property provided uniquely by this technique compared to any other existing fault location method.

In order to support the validation of TR-MUSIC, the same rules and standards that have been adopted in the study of the SDORT and EDORT methods in the previous chapter are considered. We will recall briefly the main concepts taken into account where the same simulation platform using the transmission line theory (TLT) is considered, which models uniform two-wire transmission lines, with two conductors 10 mm apart. The core conductor has a radius of 1 mm surrounded by a 0.5 mm dielectric coating of relative permitting $\epsilon_r = 3$; all results obtained are done by frequency domain simulation on Matlab. The lengths of the branches were chosen in accordance with the experimental setup that will be presented in the next section. Furthermore, the soft faults were demonstrated by a partial removal of the 0.5 mm radius coating. The strongest soft fault f_{st} is given by a 0.45 mm radius coating removal producing a fault ratio $R_f = 4\%$, whereas the weaker fault f_{we} is designated by a coating radius removal of 0.05 mm creating a $R_f = 2\%$.

As defined, all network configurations that will be studied are either composed of a single soft fault f_{st} with a fault ratio $R_f = 4\%$ as presented in the NUTs of Fig. 5.1, or containing two different severity soft faults f_{st} and f_{we} as examined in the configurations of Fig. 5.2. All the following results are based on the procedure summarized in sec. 5.2.1, which are meant to illustrate the feasibility of TR-MUSIC technique in locating soft faults adapted to complex NUTs.

We will start our study by considering the case of a single soft fault embedded in three different network configurations presented in Figs. 5.1 (a), (b), & (c) respectively where simulations were done on a bandwidth ranging from 1 MHz to 1 GHz with a sampling frequency of 1 MHz. The eigenvalue decomposition of the TRO $\mathbf{K}$ of the single-branch NUT of Fig. 5.1 (a) produces an eigenspace structure with two eigenvalues, a significant eigenvalue belonging to the signal space $\mathscr{S}$ in addition to a negligible eigenvalue in $\mathbf{K}$'s corresponding noise space $\mathscr{N}$ as shown in Fig. 5.3. In fact, the eigenvectors associated to the negligible eigenvalue once correlated with the network's

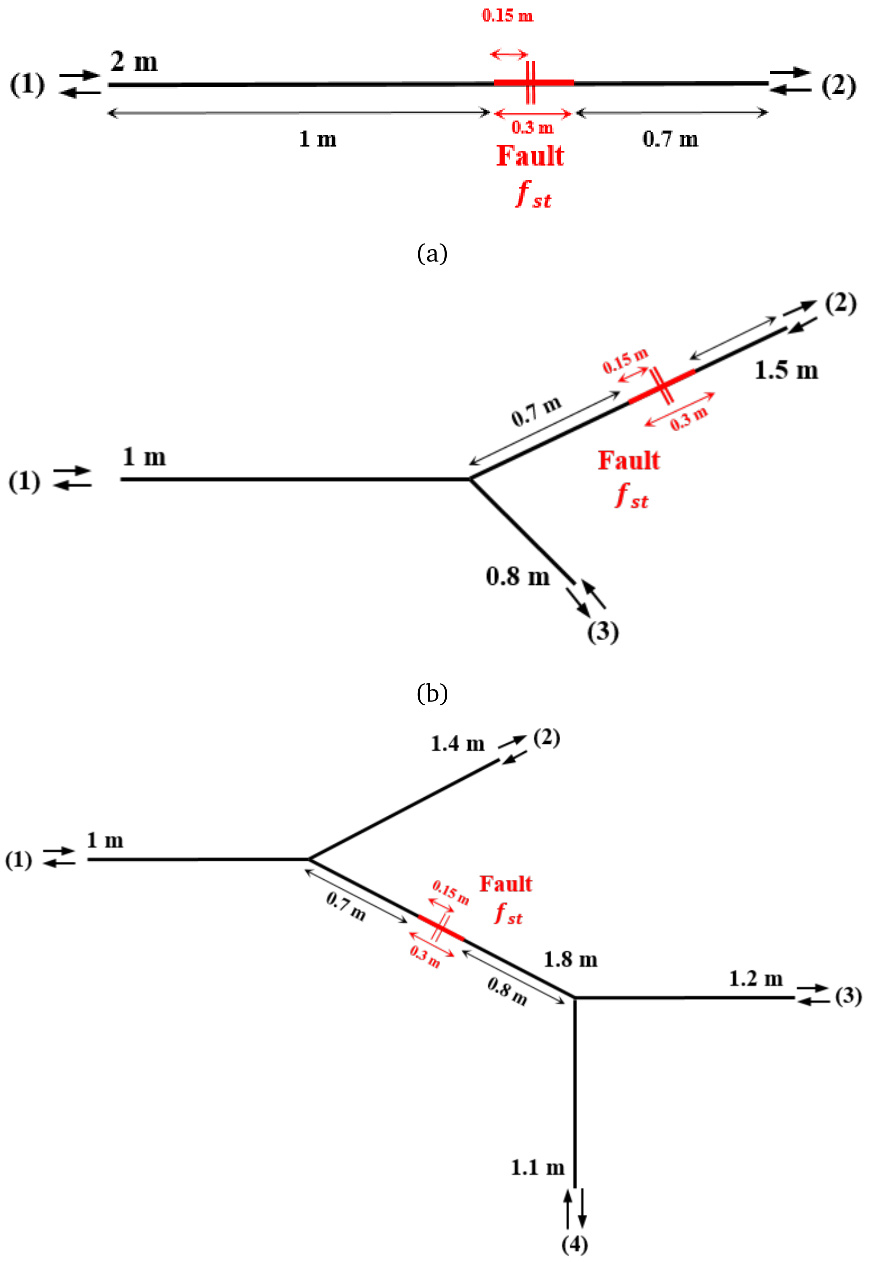

(a)

(b)

(c)

Figure 5.1 Layouts of the three NUTs considered for both the numerical and experimental validations of the TR-MUSIC: (a) a single-branch structure; (b) a single Y-junction configuration, (c) and a double Y-junction NUT. All network structures contain a single soft fault where the lengths of the branches in addition to the location of the faults, which are indicated on the figure, were chosen in accordance with the available cable and fault utilities used in the experimental setup. The extremities of the lines are terminated with matched ends.

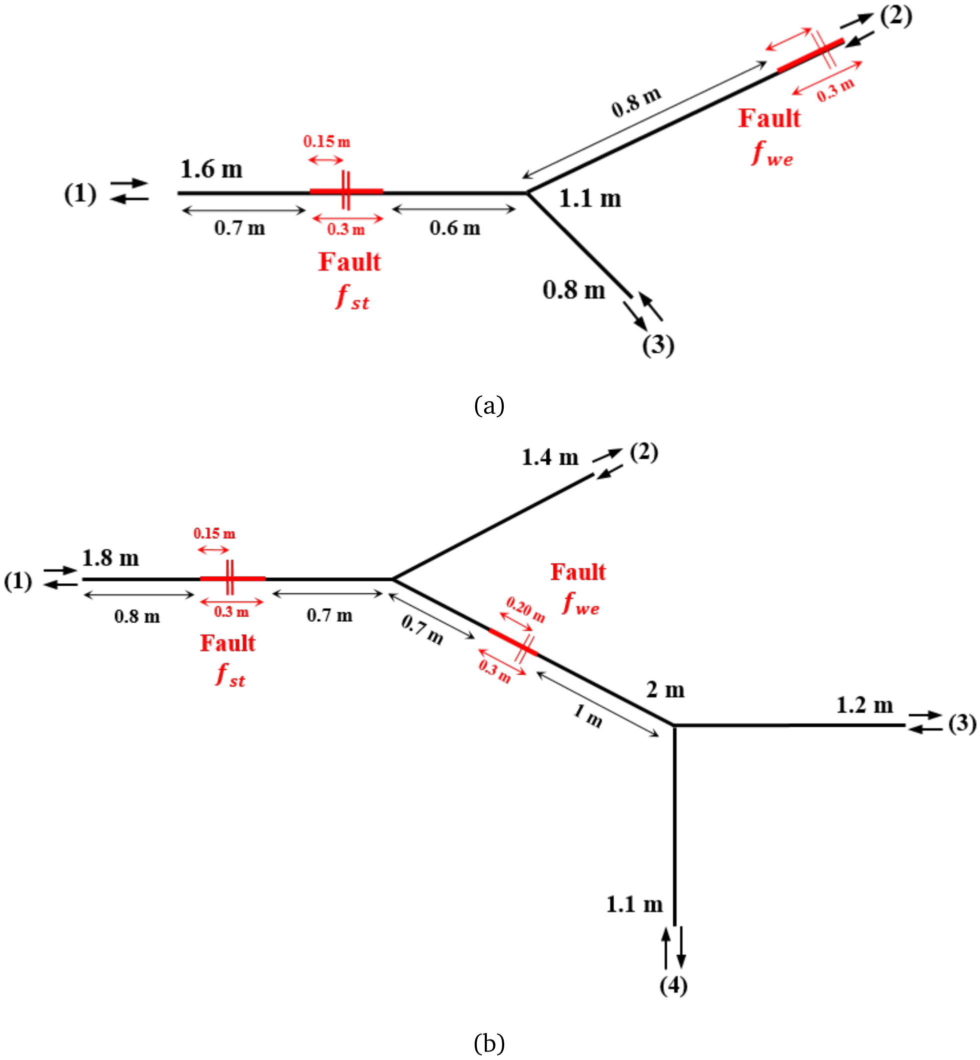

Figure 5.2 Layouts of the two NUTs considered for both the numerical and experimental validations of the TR-MUSIC: (a) a single Y-junction configuration, (b) and a double Y-junction NUT. Both network structures contain two soft faults where the lengths of the branches in addition to the location of the faults, which are indicated on the figure, were chosen in accordance with the available cable and fault utilities used for the experimental setup. The extremities of the lines are terminated with matched ends.

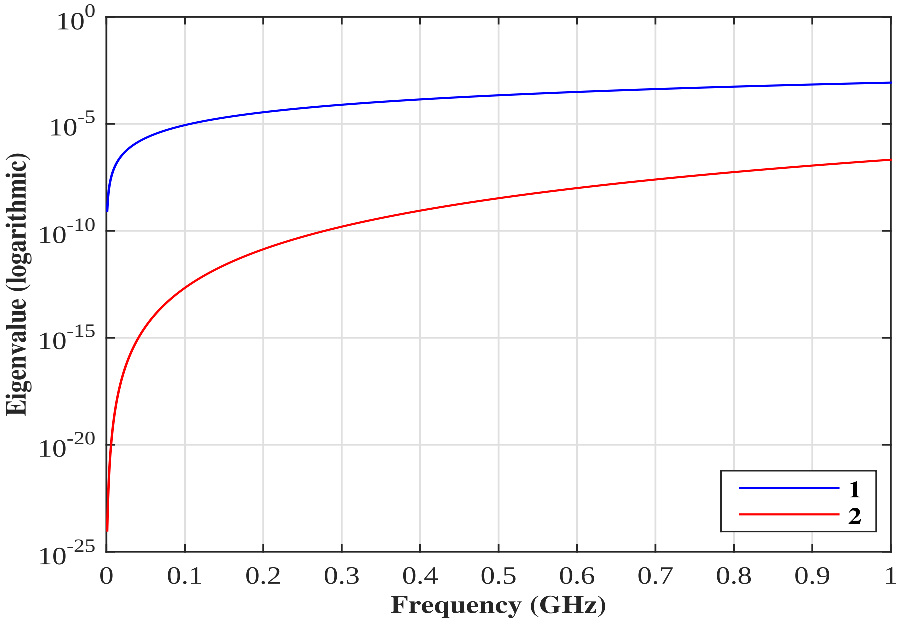

Figure 5.3 The eigenvalues of the TRO corresponding to the single branch NUT of Fig. 5.1 (a) showing a significant eigenvalue (1) belonging to the signal space $\mathscr{S}$ in addition to a negligible eigenvalue (2) of the noise space $\mathscr{N}$.

Green function demonstrated by its forward propagation voltage will vanish at the position of the fault when computed using a single-frequency excitation signal. In other words, a singularity at its positions is obtained from the the pseudo-spectrum calculated according to eq. 5.3. To better illustrate this point, the pseudo-spectrum is computed at several frequencies ranging from 1 MHz to 100 MHz as shown in the pseudo-spectra of Fig. 5.4. Notably, accurate estimates in the *sub-wavelength spatial resolution* are obtained on the fault's position by using different single frequency excitations. It is also important to realize, that the results obtained are not affected by the frequency of the excitation wave (as long as it is below a maximal frequency to be illustrated later in this section), a prominent feature proving the method's effectiveness in locating soft faults based on a monochromatic signal. Eventually, this demonstrates the technique's applicability in band limited systems without the need of complex testing setups requiring pulse generators and fast electronics.

In order to check the method's applicability with more complex NUTs, the continuous wave excitation feature is examined on the single and the double Y-junction networks of Figs. 5.2 (b), & (c). Significantly, sharp peaks are obtained on the positions of the faults given by the singularities obtained in the pseudo-spectra of Figs. 5.5 (a), &(b) as a result of a 1 MHZ single frequency signal.

Meanwhile, applying TR-MUSIC for network configurations composed of two soft faults will allow checking the method's feasibility with multiple faulty structures based on monochromatic excitations. Significantly, two singularities were obtained on the faults' position in the double-fault

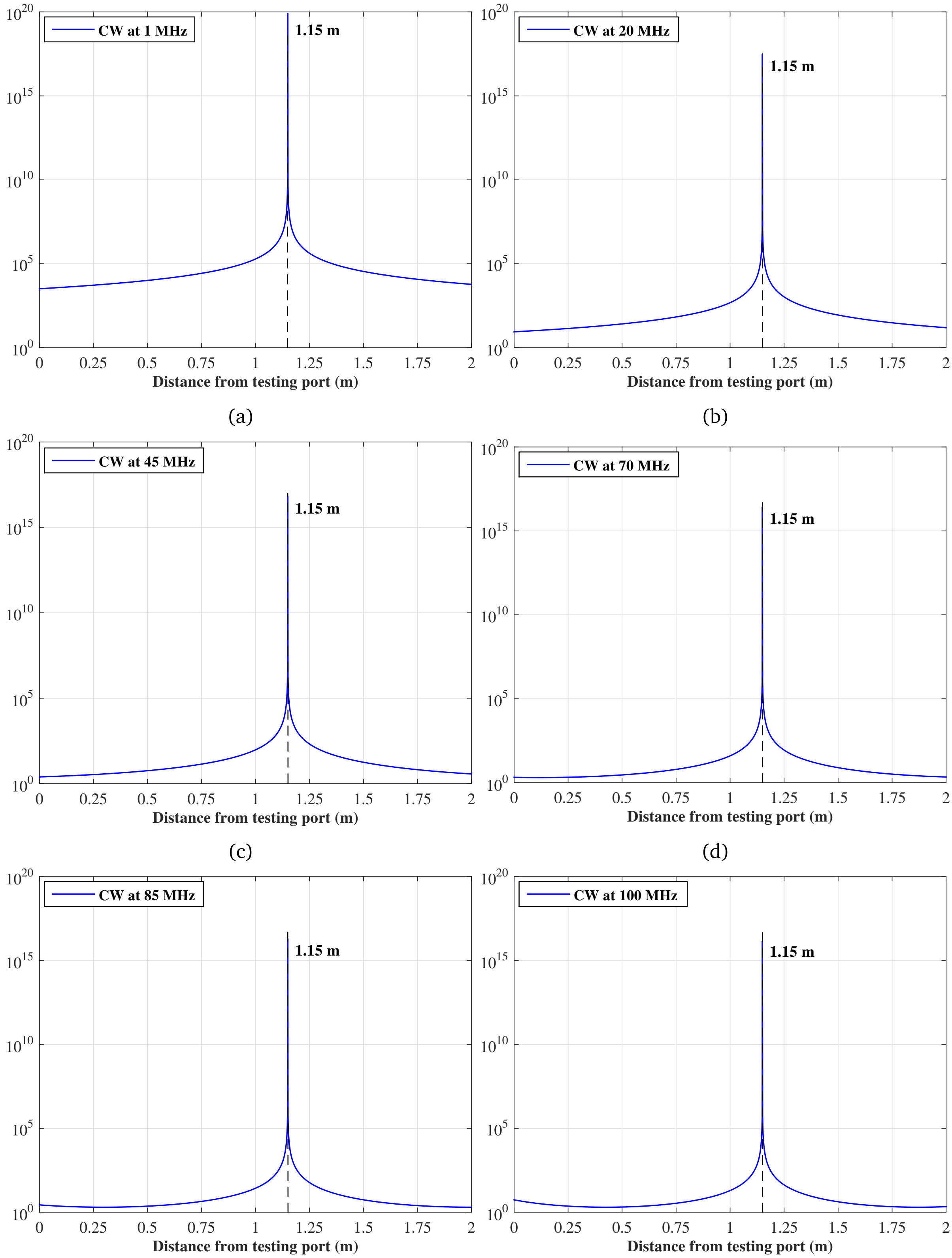

(a) (b) (c) (d) (e) (f)

Figure 5.4 Pseudo-spectra of the TR-MUSIC applied on the single-branch single-fault NUT of Fig. 5.2 (a) computed on the basis of a continuous wave excitation on several frequencies. A single singularity was obtained on the position of the fault regardless the frequency used.

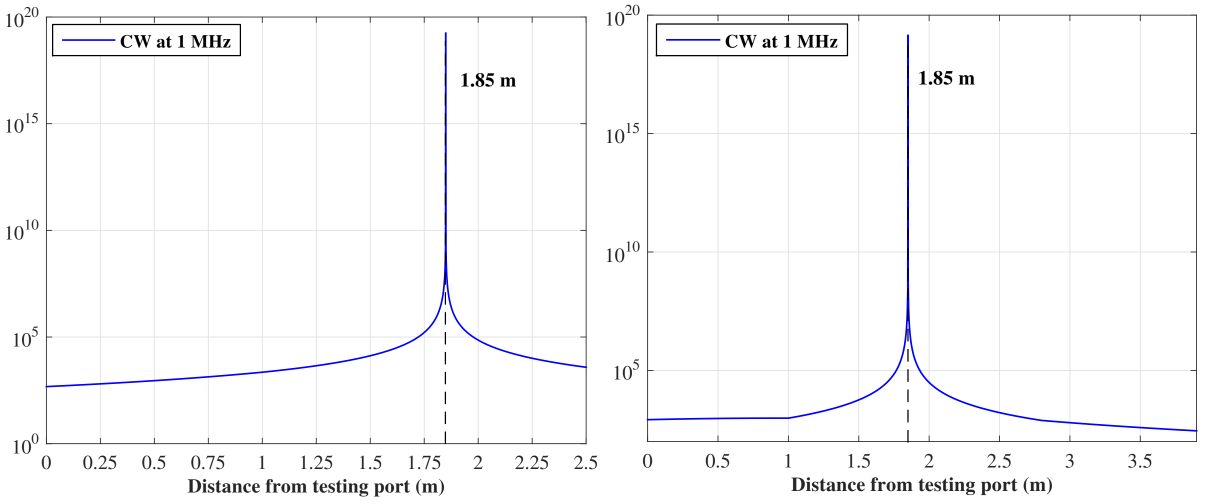

(a) (b)

Figure 5.5 Pseudo-spectra of the single and double Y-junction NUTs of Figs. 5.1 (b)&(c) respectively containing a single soft fault, after applying the TR-MUSIC method on a 1 MHz single frequency excitation. It can be noted that a single singularity is obtained on the position of the fault.

configuration of the single and double Y-junction networks of Figs. 5.2 (a), & (b) with a 1 MHz continuous wave as shown in the pseudo-spectra of Figs. 5.6 (a), & (b) respectively. Indeed, the obtained results prove the eligibility of TR-MUSIC technique in ensuring a *sub-wavelength spatial resolution* of the fault's positions while working on a monochromatic excitation basis.

The computation of TR-MUSIC on multiple frequencies is possible in theory, so it would be interesting to asses the effect frequency can have on the performance of the method. As a result, the single-fault single-branch NUT of Fig. 5.1 (a) was reconsidered where simulations were done on a predefined bandwidth ranging from 1 MHz to 1 GHz. Fig. 5.7 (a) shows the resulting pseudo-spectrum where the distances on the horizontal axis are measured from the reference port (1). As a matter of fact, several features need to be commented. First, a number of singularities appear at each frequency, but only one keeps constant, at a position corresponding to the fault, at 1.15 m, with a standard deviation through the entire set of frequencies well below the millimeter. This observation confirms the claims of the possibility of locating very accurately a fault while working at a single frequency, as opposed to time-domain methods. The remaining singularities are reminiscent of ghosts found in radar applications in multipath media. The fact that their position changes with the frequency and that for a given frequency they are periodically spaced is a direct indication of their origin. It is important to realize that these ghosts can be understood by recalling the periodicity of wave propagation of harmonic signals, proper to single-branch structures. Indeed, the spatial period of the Green function corresponds to a an integer multiple of a wavelength at each frequency tested, where the same result is obtained at each λ whereas a changed sign result will be obtained at $\lambda/2$. In other words, the periodicity of the Green function along a cable imply that the pseudo-spectrum will also be periodic, but it will change with the frequency. Besides, the

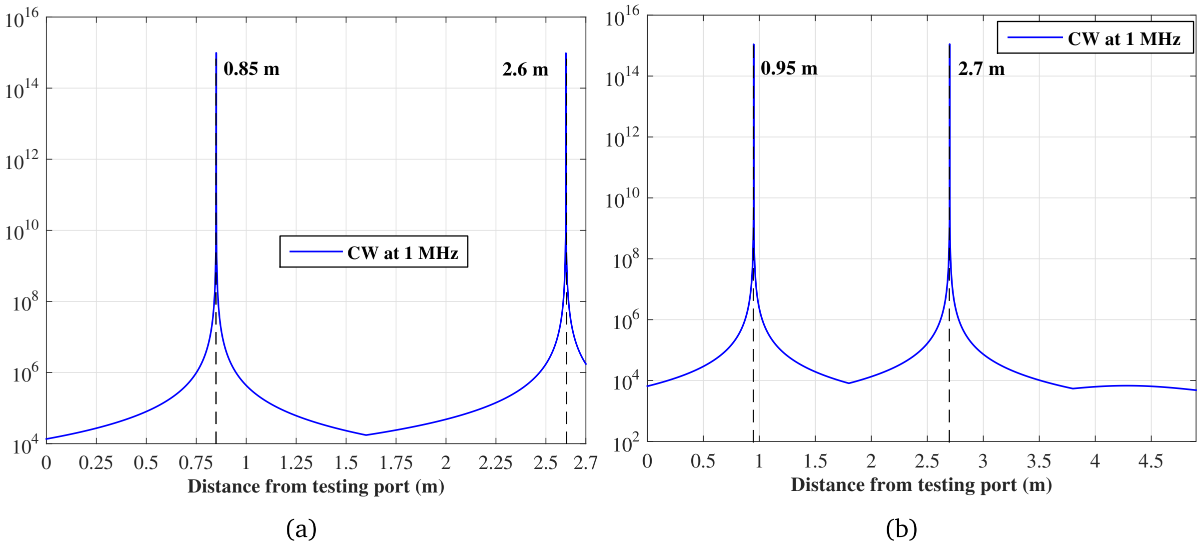

Figure 5.6 Pseudo-spectra of the single and double Y-junction NUTs of Figs. 5.2 (a)&(b) respectively containing two soft faults, after applying the TR-MUSIC method on a 1 MHz monochromatic excitation. It can be noted that two singularities were obtained on the positions of the two faults.

periodicity in the pseudo-spectrum is expected to be at half a wavelength ($\lambda/2$) due to the squaring of the correlation in its corresponding denominator. Accordingly, a singularity will be achieved at each $\lambda/2$. In fact, the appearance of junctions prior to complex wiring configurations breaks down this periodicity and consequently their corresponding resulting ghosts. Notably, this can be inferred from the pseudo-spectra of Figs. 5.7 (b), & (c) of the single and double-junction networks of Figs. 5.1 (b)& (c), where ghosts appear to be collapsed starting from the position of the junction.

For instance, these ghosts are confusing and cannot be distinguished from the actual position of a fault, when observed at a single frequency. Therefore they need to be avoided by ensuring that for a maximal length L found through an NUT, the test frequency is $f \lesssim v/(2L)$, with v being the speed of the wave along the NUT.

So as to check the feasibility of this proposed condition, the methodology of TR-MUSIC was applied to the networks of Fig. 5.1 containing a single soft fault. Simulations were done on a frequency bandwidth ranging from 1 MHz to a maximum of 100 MHz, which seemed to be compatible with the proposed condition and the maximum lengths of the cables of the tested networks. As a result, the pseudo-spectra obtained in Figs. 5.8 shows the disappearance of the ghosts accompanied with a unique singularity at the fault's position. Similarly, under the same conditions the process effectively located the two soft faults present in the single and double Y-junction network configurations of Fig. 5.2, which is demonstrated with two singularities at their positions as shown in the pseudo-spectra of Figs. 5.8. It is worthy to note that peak value corresponding tot the actual position of the singularity peaks at 18 in the color bar of the corresponding pseudo-spectrum. But, the obtained spatial resolution from the considered sampling frequency made it hard to resolve the fault's very thin line from its background.

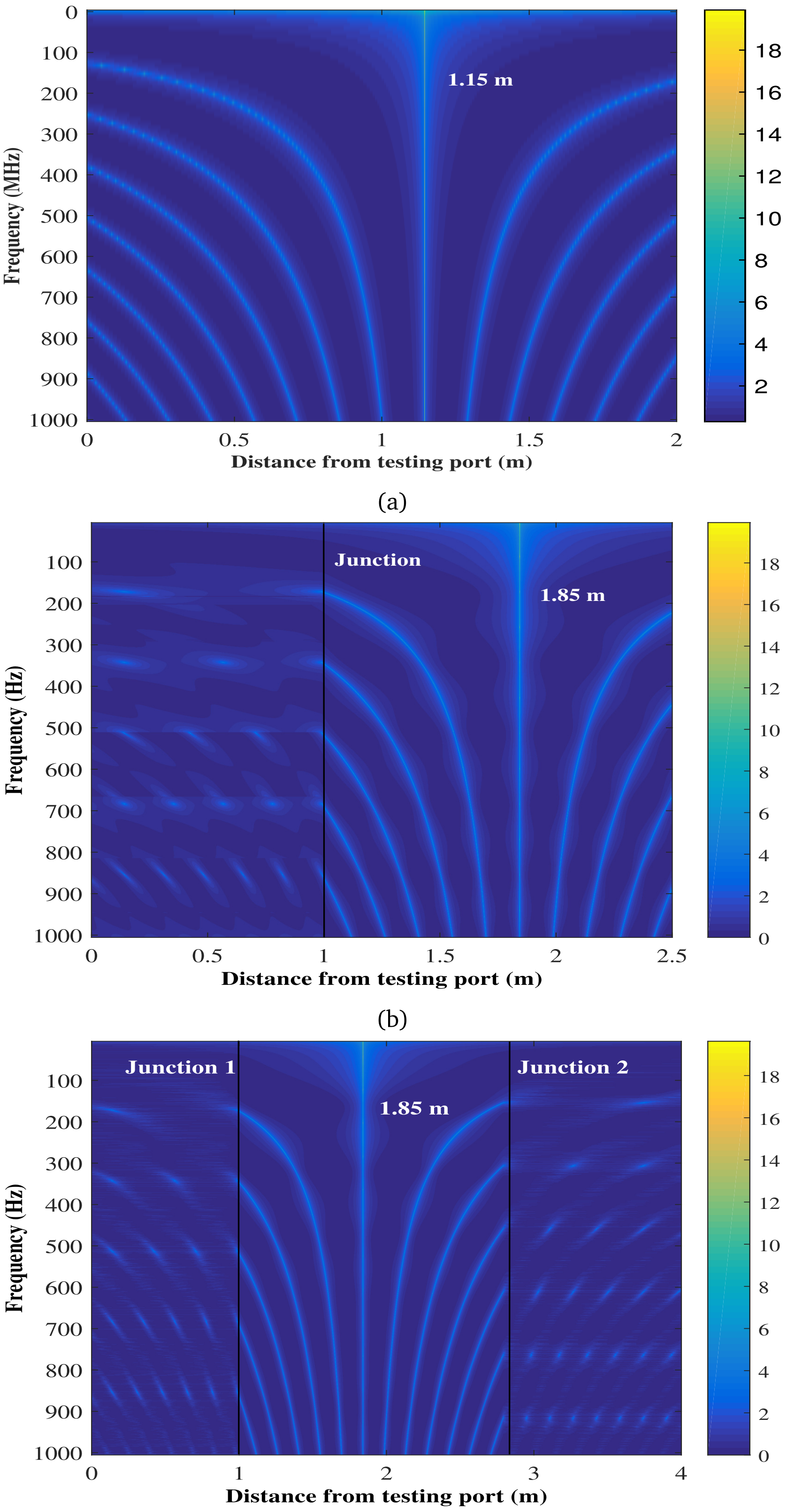

(a)

(b)

(c)

Figure 5.7 Pseudo-spectra of the single-branch, single Y-junction and double Y-junction network configurations of Figs. 5.1 (a), (b) & (c) respectively containing a single-soft fault, after applying the TR-MUSIC method on a frequency range from 1 MHz to 1 GHz. It can be noted that a unique singularity is obtained on the fault's position in addition to the appearance of ghosts prior to the periodicity of waves. In fact, the appearance of ghosts is expected to breakdown with the presence of junctions.

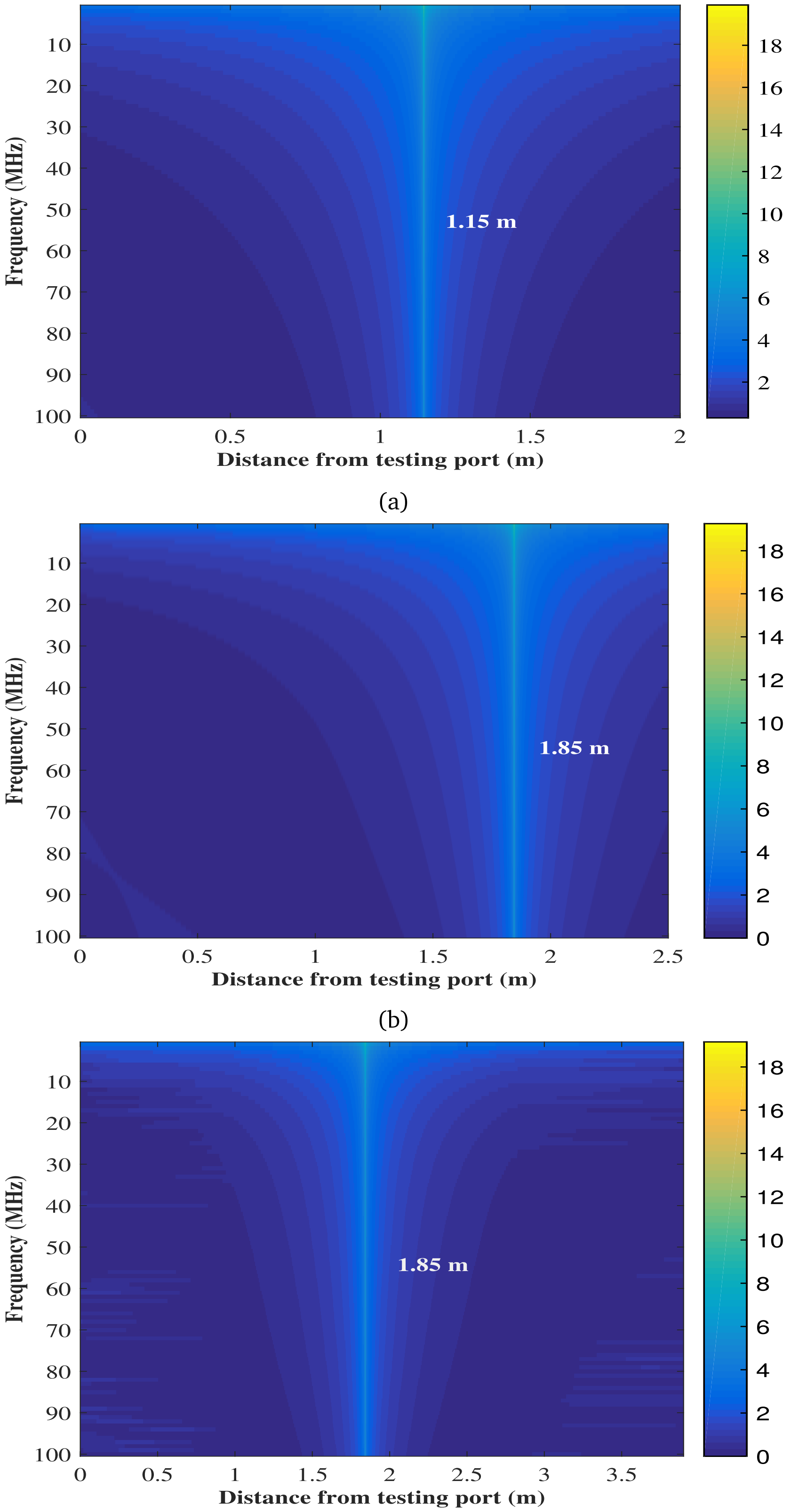

(a)

(b)

(c)

Figure 5.8 Pseudo-spectra of the single-branch in addition to the single and double Y-junction NUTs of Figs. 5.1 (a), (b) & (c) respectively containing a single-soft fault, after applying the TR-MUSIC method on a frequency range from 1 MHz to 100 MHz. It can be noted that a single singularity with no ghosts is obtained on the position of the fault.

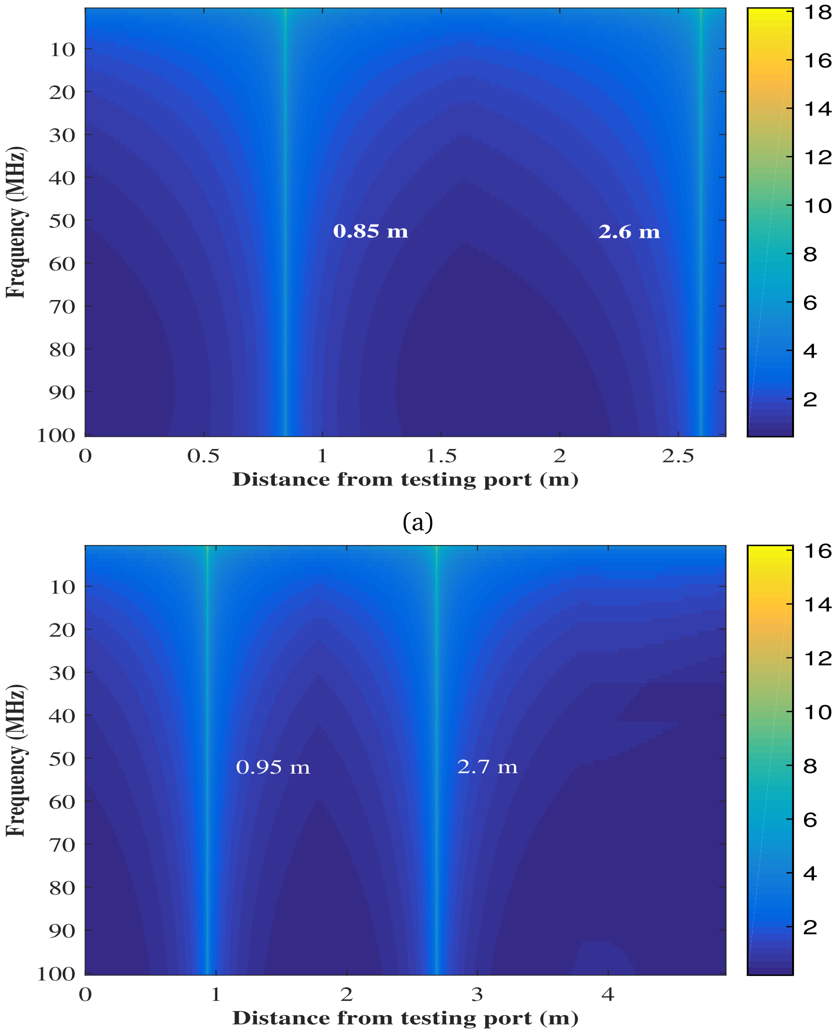

(a)

(b)

Figure 5.9 Pseudo-spectra of the single and double Y-junction NUTs of Figs. 5.2 (a) &(b) respectively containing two soft faults, after applying the TR-MUSIC method on a frequency range from 1 MHz to 100 MHz. No ghosts appear in the spectra, on the contrary two clear obvious singularities pinpoint the locations of the two soft faults.

As opposed to TDR techniques, TR-MUSIC has proved not to suffer from the ambiguity created by the existence of multiple echoes in cable networks, which can be easily misinterpreted as multiple faults, leading to false alarms. TR-MUSIC is intrinsically adapted to dealing with multiple faults, handing a direct estimate of the number of faults found in a network under test. Furthermore, the detection capabilities of TR-MUSIC are insensitive to the severity of a fault, as faults are not detected based on the intensity of their echoes as done in TDR techniques, but on a sub-space approach mostly dependent on phase patterns. It is worthy to note that TR-MUSIC revealed a significant feature designated by its ability to pinpoint the locations of single as well as multiple soft faults with *super resolution* by using continuous wave excitations.

5.3.2 Experimental Validation

The conducted numerical study in the previous section has validated the feasibility of the proposed method in locating soft faults in different network configurations. In order to examine the performance of TR-MUSIC with real soft faults, we propose to conduct an experimental study to assess the accuracy of the location method in practical situations.

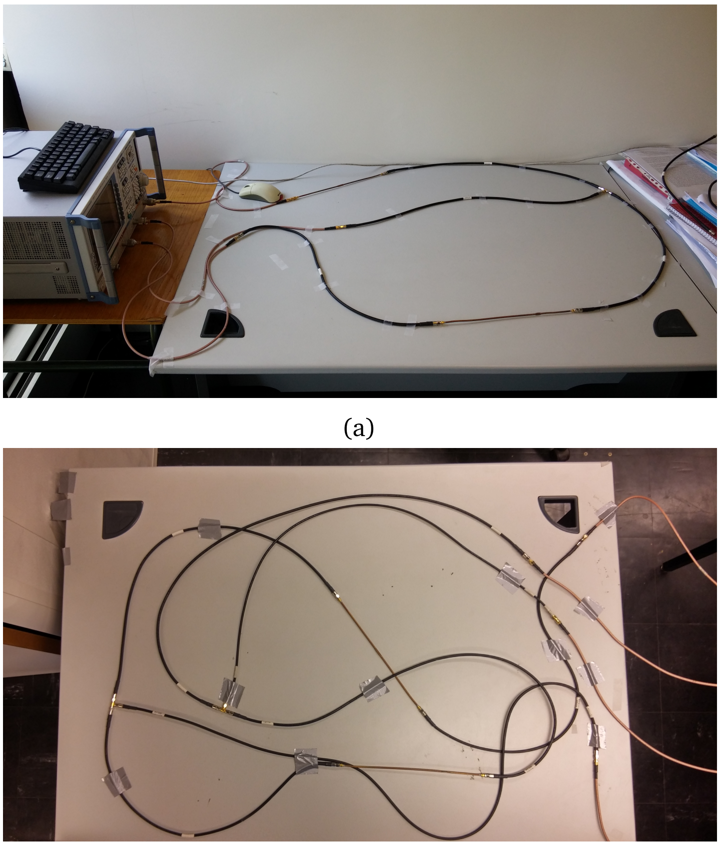
(a)

(b)

Figure 5.10 Experimental implementation of the layouts of the NUTs of Fig. 5.2 (a) &(b) containing two different severity soft faulty sections f_{st} and f_{we}, as connected to the vector analyzer for experimental work. The 30 cm long semi-rigid cables implementing the fault sections are clearly visible.

The experimental measurements were conducted on the networks of Figs. 5.1 & 5.2 for the single and double soft fault configurations respectively. It is worthy to note that the same materials considered for the EDORT experimental validations as well as the same procedure of measuring the scattering matrices will be followed for the TR-MUSIC investigation. However, we will recall briefly these elements for the sake of clarity.

The NUTs are implemented using standard 50 Ω coaxial cables as transmission lines. Two types of soft faults were created by applying a crushing force to the samples: the strongest soft fault f_{st}

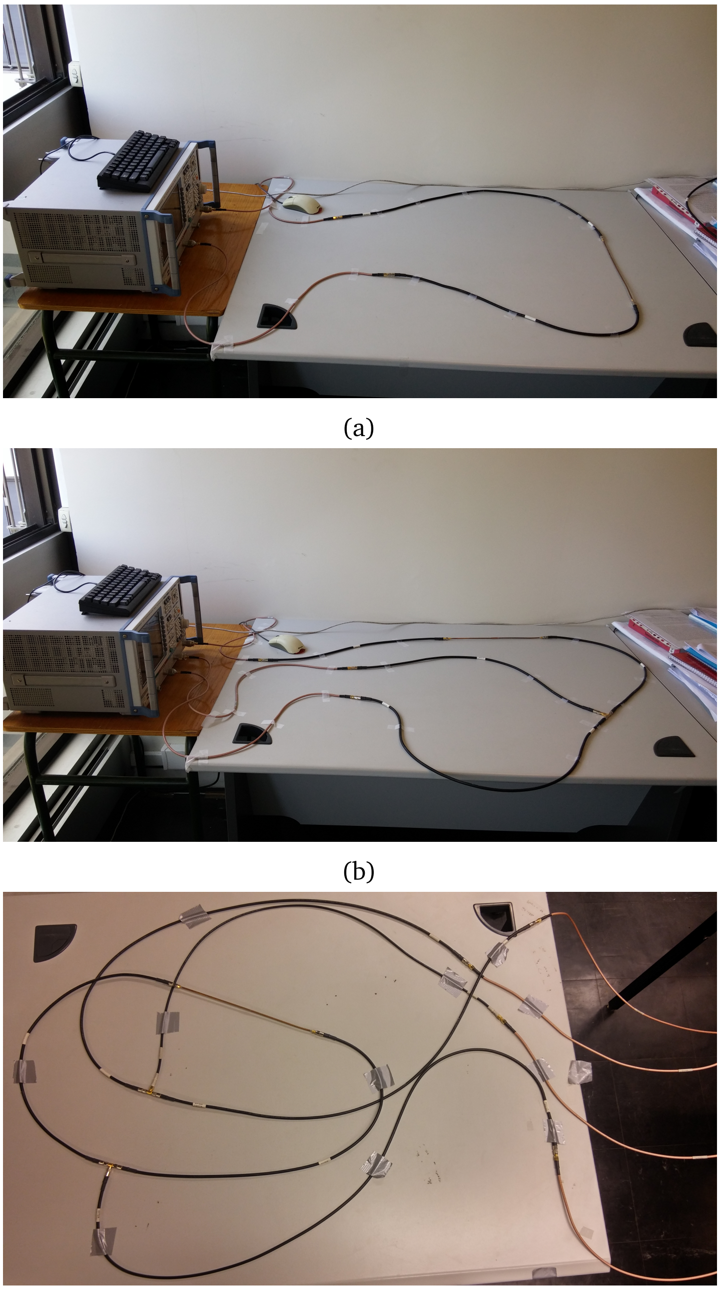

(a)

(b)

(c)

Figure 5.11 Experimental implementation of the layouts of the NUTs of Fig. 5.1: (a) the single 2 m cable NUT of Fig. 5.1 (a), containing a single soft fault at 1.15 m from the reference port (1), whose extremities are connected to the ports of the VNA for the experimental tests; (b) the single-junction NUT of Fig. 5.1 (b) embedding a soft faulty section at 1.85 m on the second branch from (1), whose three extremities are connected to three testing ports of the VNA. The 30-cm long semi-rigid cable containing the faulty sample can be seen; and (c) the double junction NUT of Fig. 5.1 (c) composed of 5 branches and containing a soft fault at 1.85 m from (1) between the two junctions. The same intensity soft fault f_{st} is considered in the three network configurations.

was designated by a crushed area of 2 cm while the weaker one f_{we} by 1 cm. As matter of fact, the results obtained in the previous chapter has shown that $\Gamma_{f1} \simeq 2.7\Gamma_{f2}$, with Γ_{f1} and Γ_{f2} being the reflection coefficients of the stronger and the weaker faults, respectively.

The ends of the cables making up each NUT were used as testing ports, by connecting them to a Rohde & Schwarz ZVB8 vector network analyzer, covering a frequency range from 300 kHz to 8 GHz, with four testing ports. The measurement of the scattering matrices was done over a predefined bandwidth ranging from 1 MHz to 100 MHz in accordance with the results obtained in the numerical validation as we will be considering the same network configurations in our experimental study. After calibrating the VNA using the calibration kit provided by the manufacturer, studying the network consisted of two steps:

1. measurement of $\mathbf{S}_h$ of the reference healthy system with the unaltered 30-cm semi-rigid sections;
2. measurement of $\mathbf{S}_f$ of the NUT, after replacing the reference samples with the crushed ones.

After measuring the two scattering matrices of the tested networks, post-processing was done by using Matlab where several steps are followed to obtain the results. First of all, we applied an averaging operation to have both matrices symmetrical which was the same process followed for the DORT methods in the previous chapter. After that, the TRO of the difference system is computed, where performing an eigenvalue decomposition allows the derivation of the eigenvalues and their corresponding eigenvectors. The following step, allows separating the eigenspaces into a signal space $\mathscr{S}$ and a noise space $\mathscr{N}$, where the eigenvectors corresponding to $\mathscr{N}$ are used to compute the pseudo-spectrum of the studied network. Henceforth, the procedure described in sec. 5.2.1 is applied. Consequently, in order to compute the pseudo-spectrum of each wiring network the corresponding Green functions must be retrieved. An in-house transmission-line solver, implemented under Matlab, allows computing the forward propagating voltage $\mathbf{v}_i(x)$ which is the voltage applied at the ith testing port and serves as the network's Green function.

TR-MUSIC was first applied to the networks of Fig. 5.1 which are built according to a single soft fault f_{st} configuration and are implemented as shown in Fig. 5.11. The resulting pseudo-spectra are presented in Fig. 5.12, where the first pseudo-spectrum shows a single singularity obtained at the position of the soft fault situated at 1.15 m from (1) for the single-branch NUT of Fig. 5.1(a), a similar singularity can be inferred from Fig. 5.12 (b) at 1.85 m from the reference port for the NUT implemented in Fig. 5.11 (b) along its second branch. Notably, TR-MUSIC has unambiguously uncovered the fault's position with respect to the NUT's branches, where no singularity is acquired in pseudo-spectrum of Fig. 5.13 corresponding to the same single junction network of Fig. 5.12 (b) when computed from the Green function along the third path of the network. In fact, comparing the two pseudo-spectra permits the elimination of any vagueness regarding the fault's position where it can be inferred that it is located on the second branch of the network. This property has been also validated by the DORT methods. Significantly, it exceeds in efficiency standard TDR

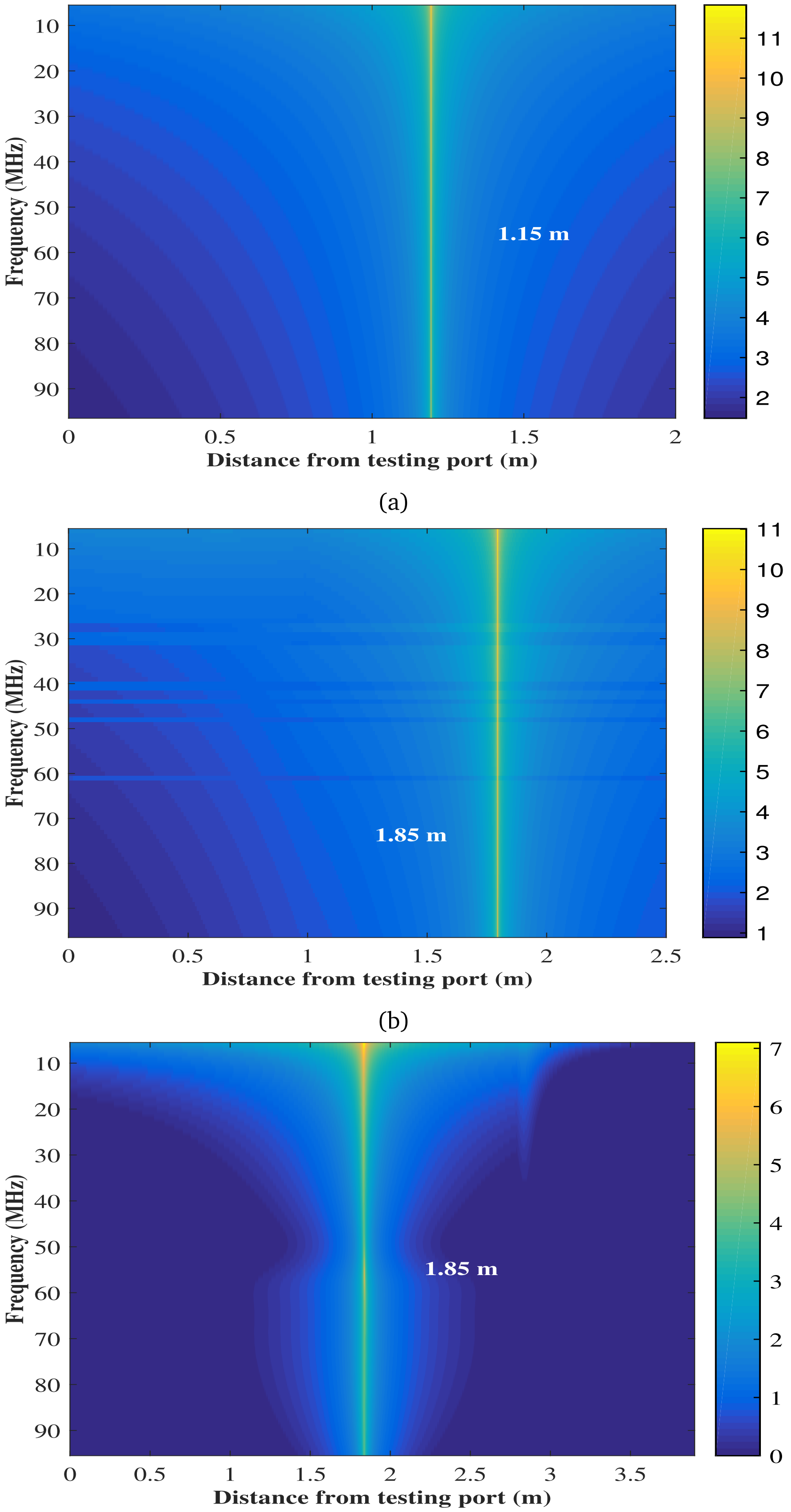

(a)

(b)

(c)

Figure 5.12 Pseudo-spectra of the single-branch in addition to the single and double Y-junction NUTs of Figs. 5.1 (a), (b) &(c) respectively containing a single soft fault, after applying the TR-MUSIC method on the experimental data collected on a frequency range from 1 MHz to 100 MHz. It can be noted that a single singularity is obtained on the position of the fault.

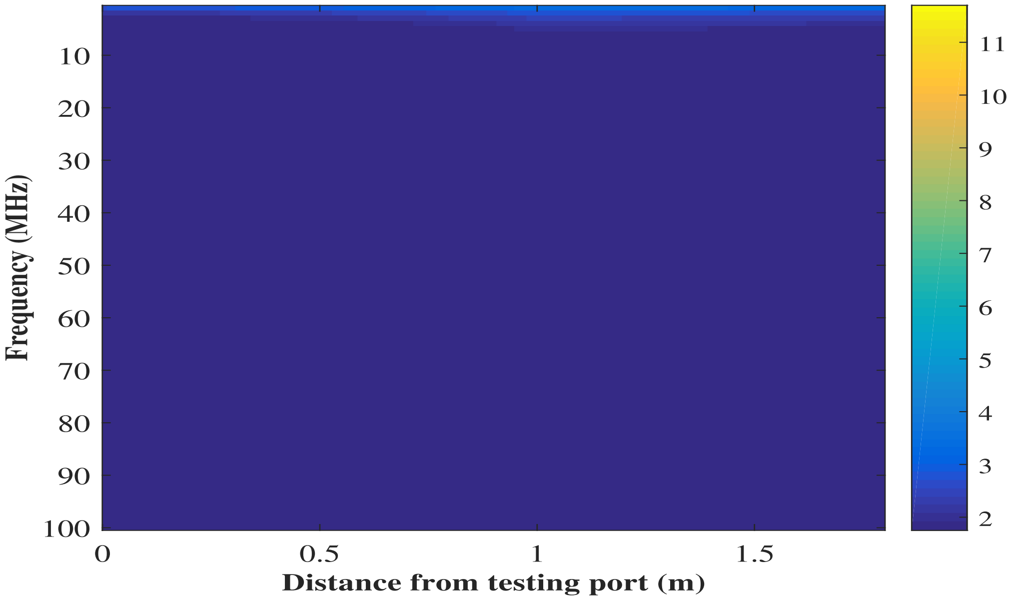

Figure 5.13 The pseudo-spectrum of the single Y-junction NUT of Fig. 5.1 (b) showing no singularity when computed along the third path of the network thus removing any ambiguity on the location of the fault with respect to the configurations branches.

techniques that are limited to knowing the distance at which the fault is located with respect to the used reference testing port. Eventually, considering the complex double Y-junction network implemented in Fig. 5.11 (c) stresses the efficiency of TR-MUSIC in locating the position of a soft fault with increased network complexity which is viable in the clear singularity obtained at the fault's position as shown in the pseudo-spectrum of Fig. 5.12 (c).

Another key point was revealed where passing from one to two faults does not modify in any aspect the interpretation of the pseudo-spectra, proving the robustness of TR-MUSIC to multiple-scatterer configurations. As a matter of fact, the pseudo-spectra of Fig. 5.14 corresponding to the single and double Y-junction wiring configurations implemented in Fig. 5.10 show two unique singularities at the position of the two soft faults in each configuration. This seamless passage from single to multiple faults is in sharp contrast with the efforts reported in the literature for TDR techniques, where multiple faults can lead to ambiguity in their localization, particularly when dealing with complex network structures.

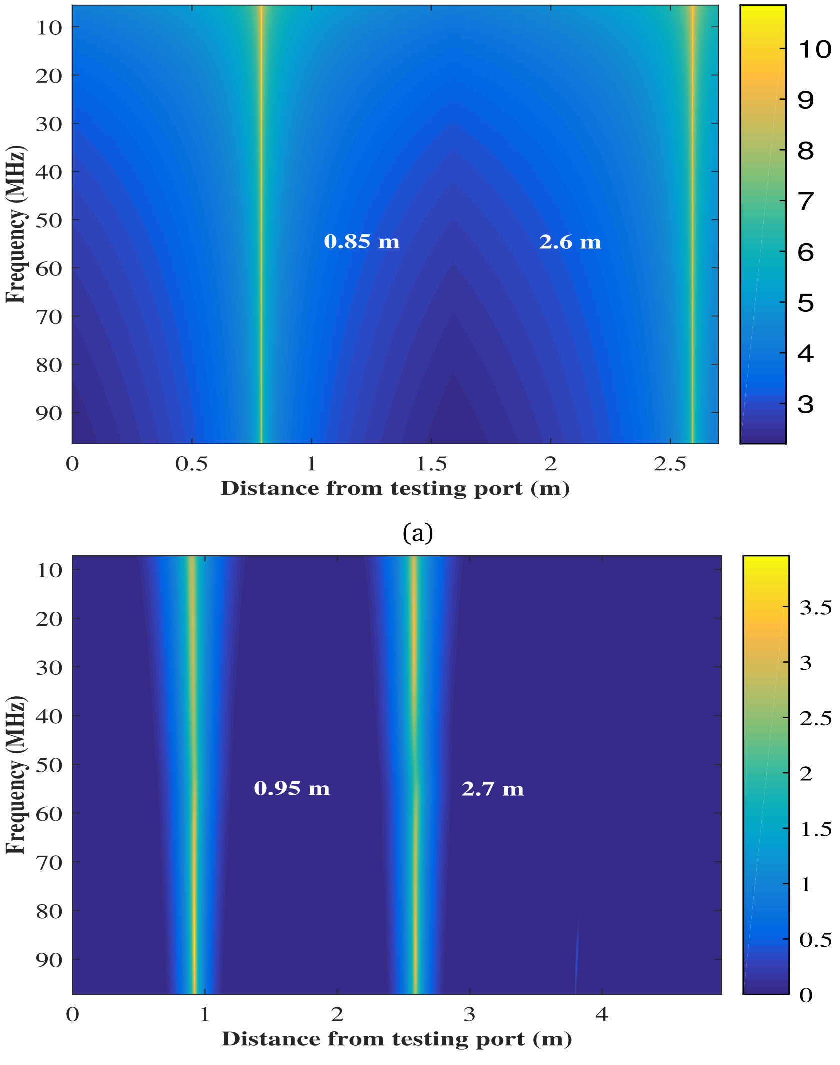

(b)

Figure 5.14 Pseudo-spectra of the measurements done on the single as well as the double Y-junction NUTs of Figs. 5.2 (a) &(b) respectively containing two soft faults, after applying the TR-MUSIC method on a frequency range from 1 MHz to 100 MHz. No ghosts appear in the spectra, on the contrary two singularities pinpoint the locations of the two soft faults in the network.

5.3.3 Retrieving a fault's reflection coefficient

Having inferred the position of the faults in each of the tested NUTs, the reflection-coefficient estimation technique proposed in sec. 5.2.2 was applied for each frequency tested. The longer and stronger soft fault f_{st} is first considered, as found in the experimental setups of Fig. 5.1 (a) & (b); along with similar experimental measurements done on the same configurations but with the shorter weak fault f_{we} where the results obtained are shown in Fig. 5.15. The estimate provided by (5.5) closely agrees with the measured reflection coefficients for the single-branch and the single

Y-junction NUTs with a single fault configuration. The worst estimate error is 8.5% when considering the single-junction single-fault case (a maximum of 8.3% for the stronger and 6.8% for the weaker).

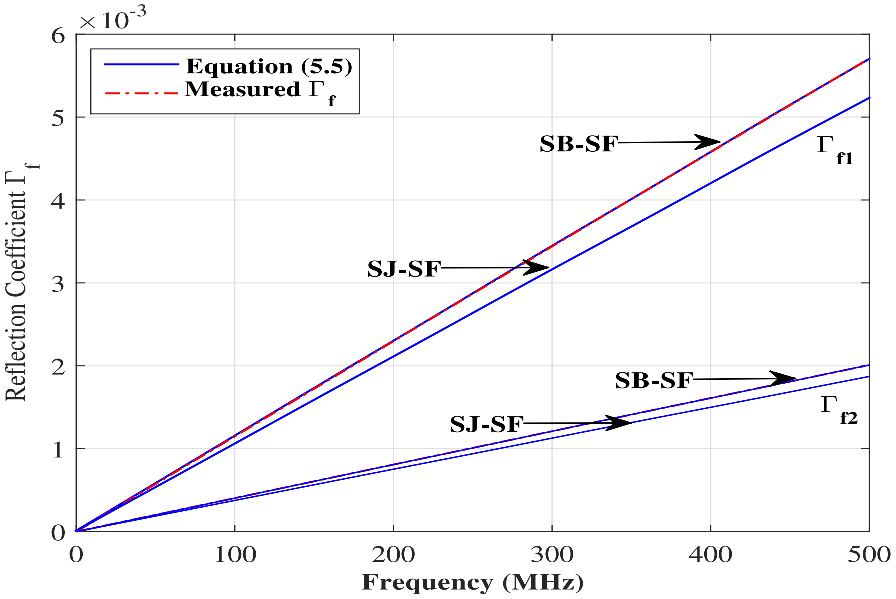

Figure 5.15 Amplitude of the measured reflection coefficient of the stronger f_{st} as well as the weaker f_{we} faulty sections versus the frequency used in the experimental validation of the single branch and single Y-junction NUTs. Estimates are obtained by means of (5.5) applied on the experimental data and direct measurements from the VNA. The single branch, single junction, and single fault are denoted as SB, SJ, and SF respectively

The same operations were applied to the single Y-junction double fault NUT of Fig. 5.2 (a), in order to assess the accuracy of the estimation for both faults in multiple faulty complex networks. Fig. 5.16 shows the reflection coefficients of the two faulty samples as obtained from the measured and the (5.5)-based estimates whose values appear to oscillate around the true values. In fact, this behavior is likely caused by the interactions between the two faults and also with the junction, and was also observed with DORT method in the previous chapter, when attempting to estimate fault severity using a eigenvector-based projection approach. To better understand this point, we recall that (5.5) used for retrieving the fault's reflection coefficient was based on (5.4) which provided a linear approximation of separating the network's global scattering matrix $\mathbf{S}_G$ into single-fault scattering matrices $\mathbf{S}_i$ each containing a single ith fault's signature. In fact, (5.4) was based on Born approximation which neglects multiple scattering between faults inside a network given that we are dealing with soft ones. Accordingly, each fault's reflection coefficient Γ_{f_i} is retrieved from its corresponding scattering matrix $\mathbf{S}_i$, but in practice $\mathbf{S}_i$ contains contributions from the other faults present in the network. Consequently, this explains the oscillations obtained in the computed values of the reflection coefficient. The systematic error introduction by the interactions represents a problem when testing an NUT with a single frequency, since the estimate can locally deviate rather strongly. Interestingly, interactions have an impact only on the estimate of the faults severity, not on their positions.

On the other hand, repeating tests at multiple frequencies and applying a simple linear regression, the intensity of these oscillations can be reduced, as shown in Fig. 5.16 where one fifth of the frequency points were used for this sake (100 out of 500 samples). This need for multiple-frequency regression could clearly be avoided by looking for the entire set of reflection coefficients at once, rather than separating the system into single-fault contributions, as done in sec. 5.2.2. The price to pay would be a non-linear optimization process as the Jacobi method. Nonetheless, the estimates obtained are rather precise. More importantly, they are not based on any measure of the intensity of signals reflected by faults, but are rather entirely based on sub-space computations, which are intrinsically more robust to noise and multiple reflections observed in complex NUTs.

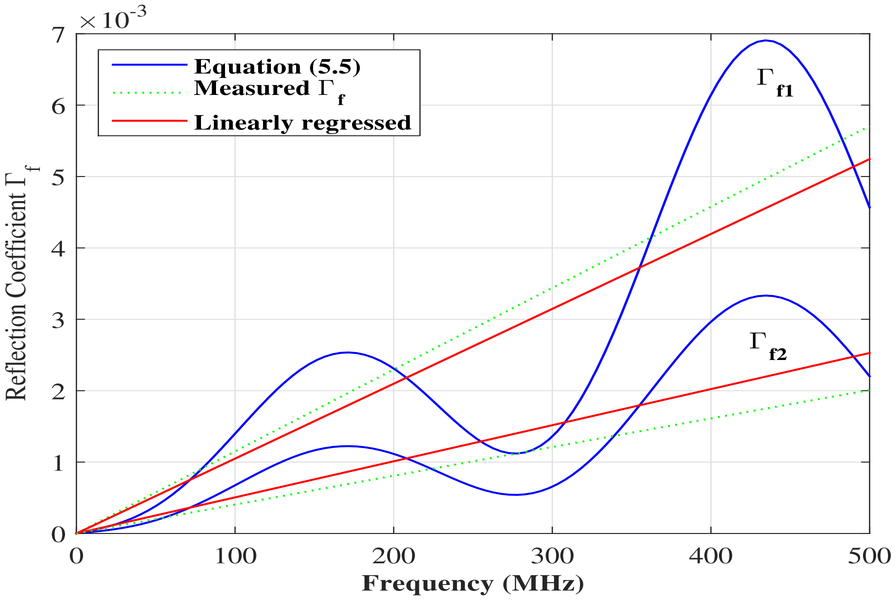

Figure 5.16 The reflection coefficients of the two faulty sections used in the experimental setup of double fault single Y-junction NUT of Fig. 5.2 (a). The results are estimated by means of (5.5) with an application of a linear regression as discussed in the body of the text along with direct VNA measurements.

5.4 Parametric Study

After introducing the TR-MUSIC approach, we have witnessed a significant ability of obtaining *super resolution* estimates of the faults' locations in different complexity wiring networks, while using continuous wave excitations. Therefore, it would be interesting to quantify and assess the response of such a technique in noisy measuring environments which will enable studying its applicability in real-life testing setups.

5.4.1 Immunity to Noise

As we have discussed earlier in the previous chapter, real-life wiring networks are always affected by disturbing energy that interfere with the useful measured signals leading to unwanted modifications. Notably, DORT method has showed to provide a surprising robustness in the presence of AWGN where a good performance was obtained in the precise location of the faults at relatively low SNR values well below 0 dB. On the other hand, the literature of TR-MUSIC in open media, states that this method is highly sensitive to noise, where unlimited resolution can be achieved in the absence of noise, nevertheless increasing the level of noise degrades the quality of *sub-wavelength imaging* [112]. The aim of this section is to explore the influence of noise level on both the imaging resolution of the pseudo-spectra and the accuracy of the fault's position.

TR-MUSIC technique computes the pseudo-spectrum resulting from the correlation of the medium's Green function to the components of the noise subspace $\mathscr{N}$ of the multi-static data matrix (MDM). In fact, the scattering matrix of the network is collected by measurements done at the level of the vector network analyzer, thus noise will be added numerically to the measured scattering matrices in order to assess its effect on the applicability of the method. It is worthy to note that the same procedure of adding AWGN to the measured scattering matrices described in chapter 4.7.1 will be followed in our investigation. As a result, a unique SNR value will be defined for $\mathbf{S}$ at all frequency samples of the studied bandwidth. After that, the TR-MUSIC procedure described in section 5.2.1 will be applied to the noisy scattering matrices corresponding to each tested network configuration on different values of the SNR.

In our study, we will examine the NUTs of the experimental validation accomplished on the single-branch, single-junction and double-junction networks of Fig. 5.1, where we will consider the single-soft fault configuration in our study. In our investigation, AWGN was added to the initially measured baselined scattering matrices (on a bandwidth ranging from 1 MHz to 500 MHz and a sampling frequency step of 1 MHz) of all NUTs while considering SNR values ranging from 0 dB till 35 dB with a step of 5 dB. Thereafter, the TR-MUSIC method will be applied in the post-processing to the resulting noisy scattering matrices of the three studied networks in order to determine the effect noise can bring on the applicability of the technique. Figs. 5.17, 5.18 &, 5.19 show the pseudo-spectra corresponding to the NUTs of Figs. 5.1 (a), (b), & (c) respectively at different values of the SNR along with the noiseless case for the sake of comparison. It is important to note here that the 0 dBm input power set for the VNA ensured a strong rejection of noise thus results obtained from the measured data are considered to be noiseless ones. Indeed, adding noise has led to a scattering effect of the peaks whether corresponding to the fault's singularity or to the ghosts, in the neighborhood of their eventual position. Regrettably, this effect seems to be severer at low SNR values where we can barely distinguish the position of the fault at 0 dB. Fortunately, the situation is expected to improve with an increase in the SNR where the range of the scattered peaks gather towards the true position of either the fault or the ghost. Notably, the position of the fault can be clearly distinguished from the ghosts starting from 10 dB, an SNR value relatively very low

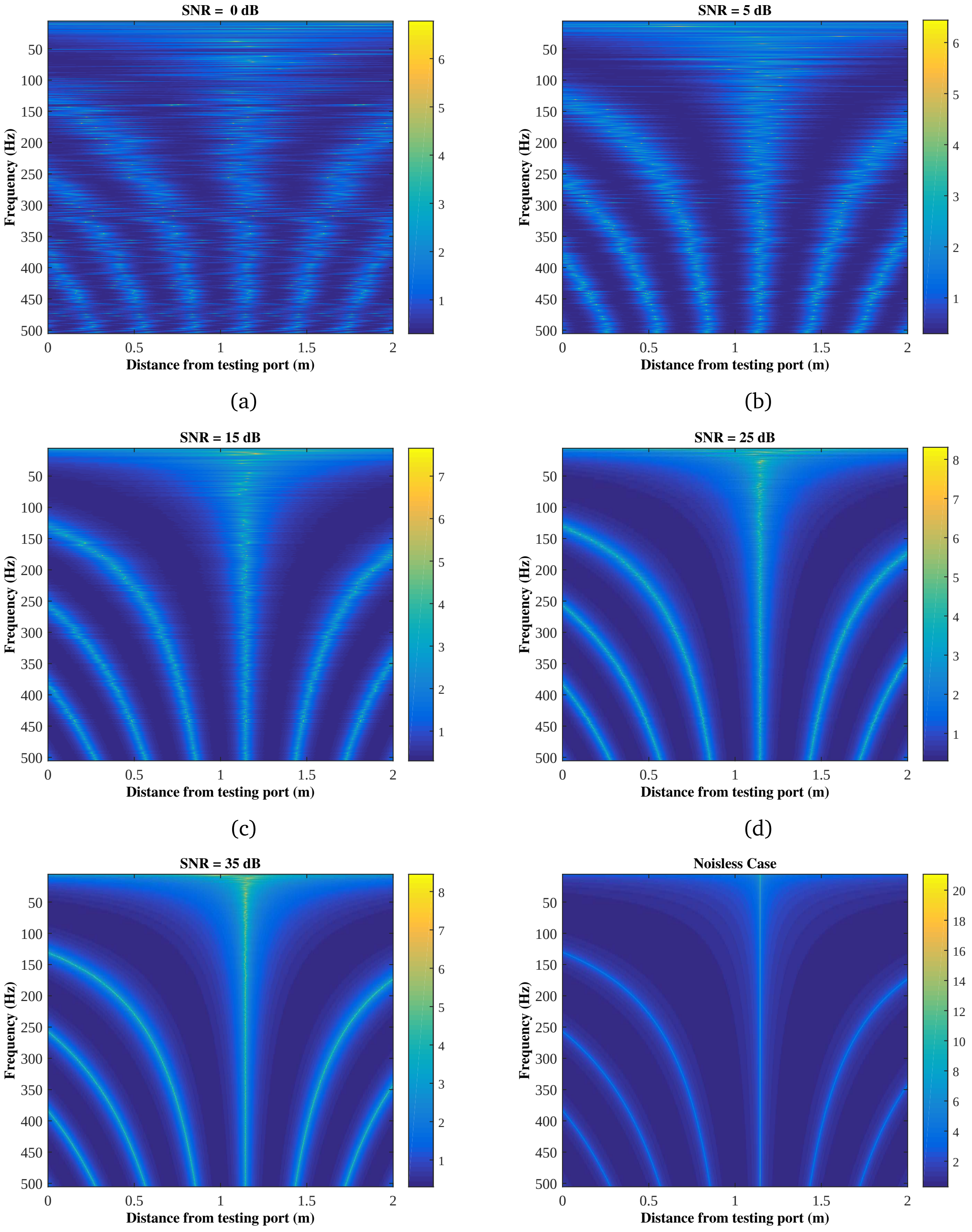

(a) (b) (c) (d) (e) (f)

Figure 5.17 Pseudo-spectra of the single branch NUT of Fig. 5.1 (a) containing a single soft fault, after applying the TR-MUSIC method on the experimental data collected on a frequency range from 1 MHz to 500 MHz for the noiseless case and after applying AWGN on different values of the SNR listed on the top of each figure.

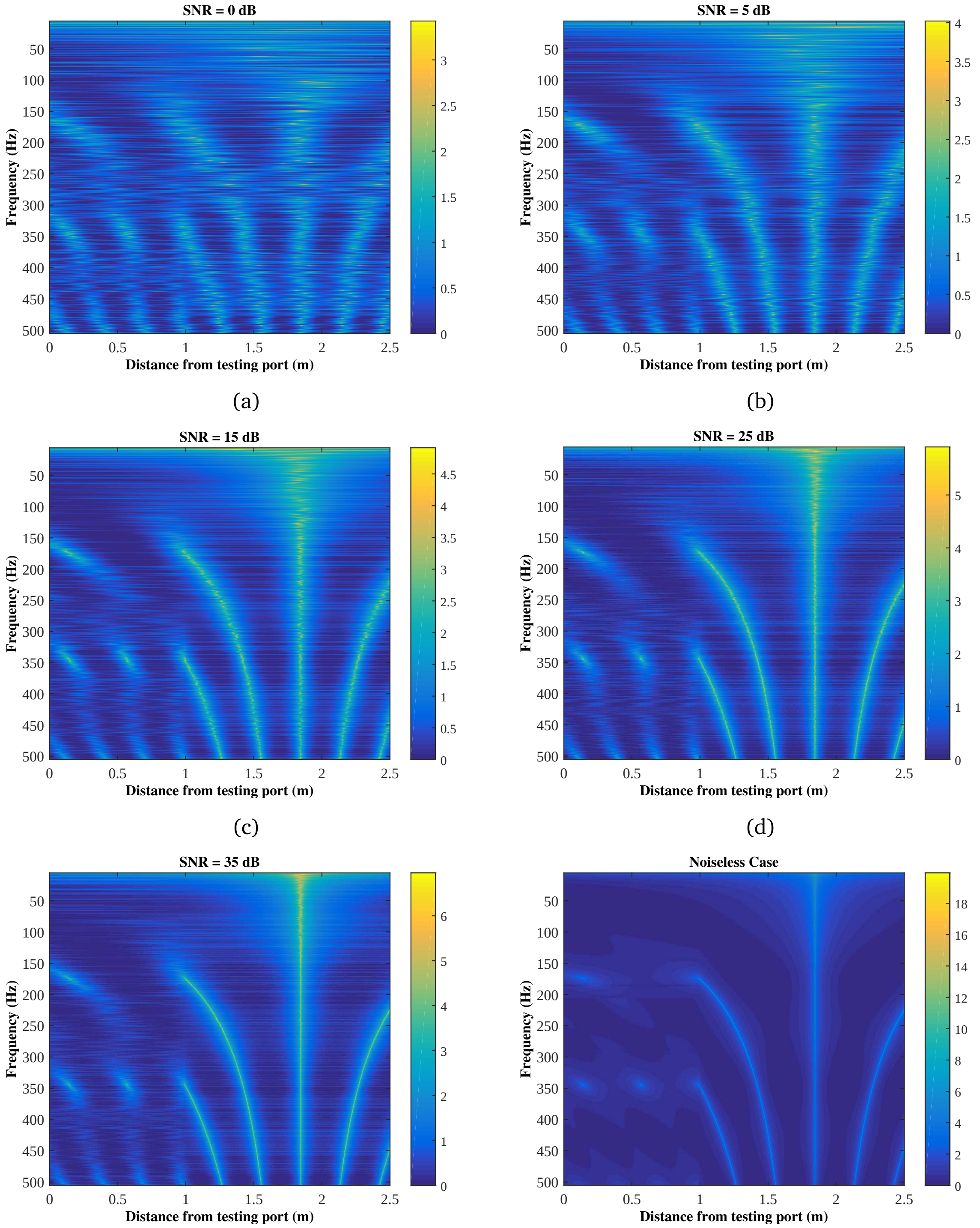

(a) (b) (c) (d) (e) (f)

Figure 5.18 Pseudo-spectra of the single Y-junction NUT of Fig. 5.1 (b) containing a single soft fault, after applying the TR-MUSIC method on the experimental data collected on a frequency range from 1 MHz to 500 MHz for the noiseless case and after applying AWGN on different values of the SNR listed on the top of each figure.

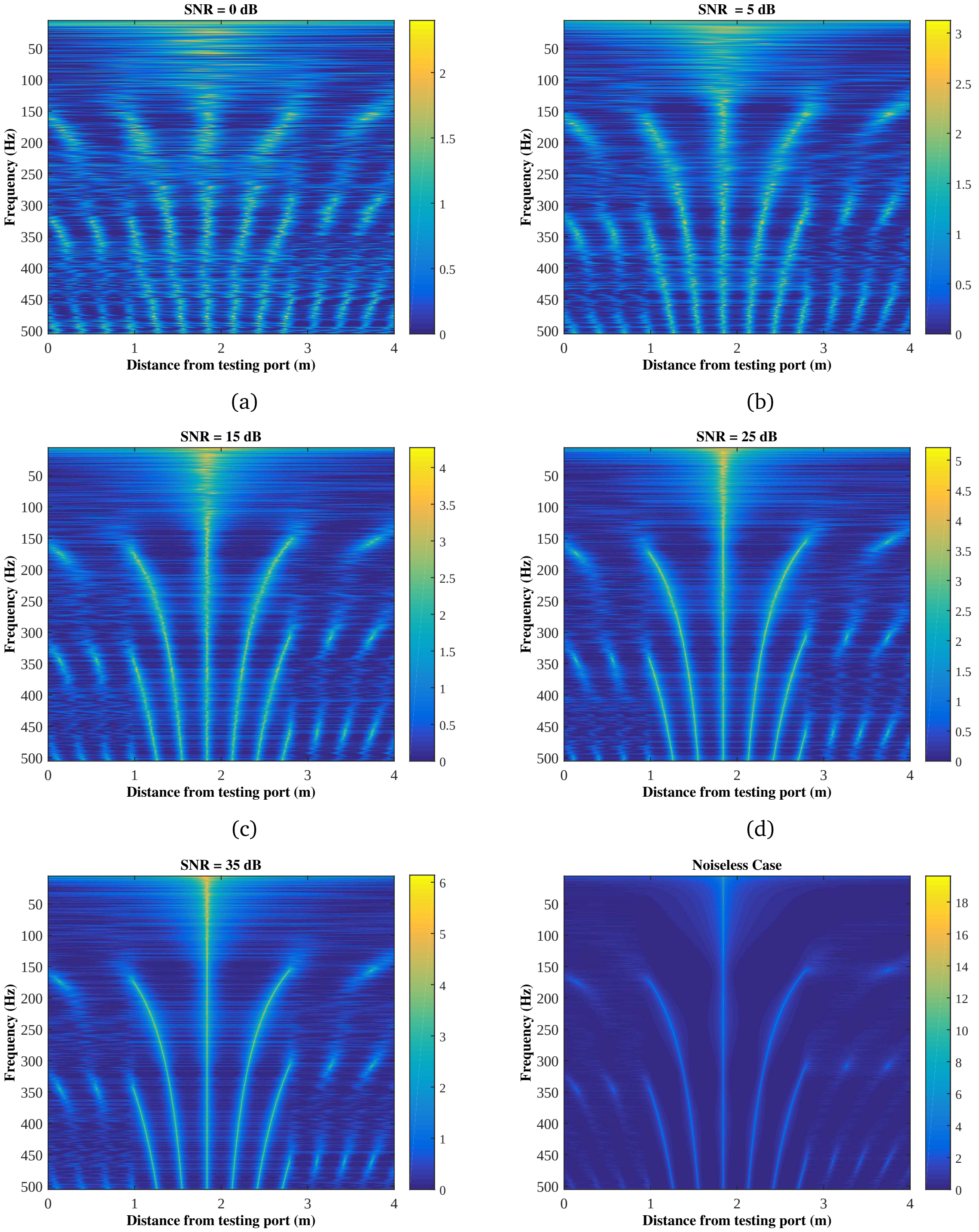

(a) (b)

(c) (d)

(e) (f)

Figure 5.19 Pseudo-spectra of the double Y-junction NUT of Fig. 5.1 (c) containing a single soft fault, after applying the TR-MUSIC method on the experimental data collected on a frequency range from 1 MHz to 500 MHz for the noiseless case and after applying AWGN on different values of the SNR listed on the top of each figure.

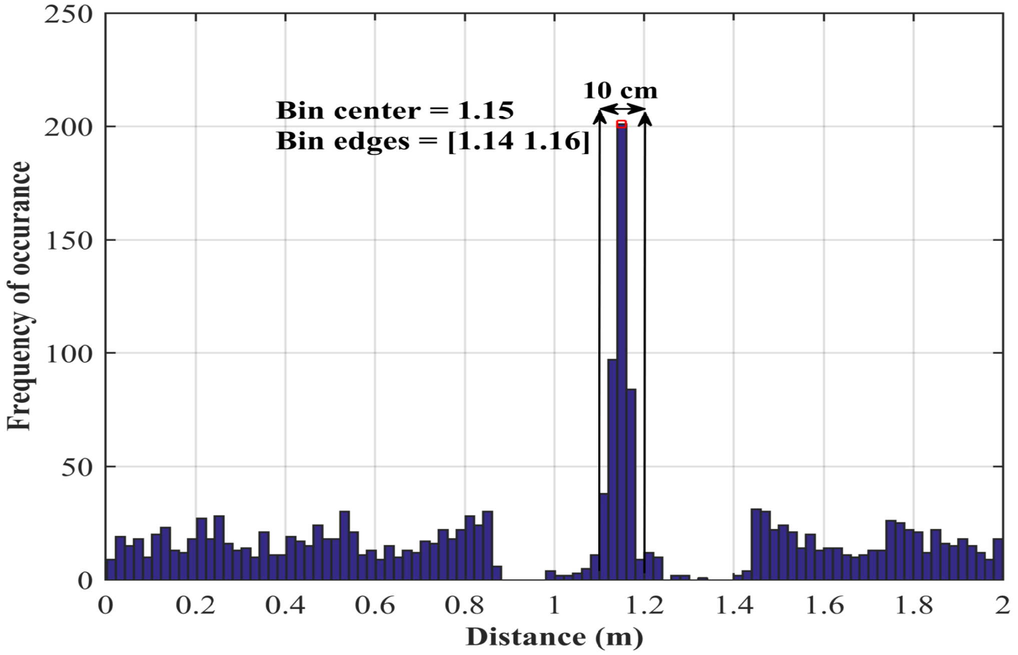

Figure 5.20 The histogram of the peaks corresponding to the pseudo-spectrum of the NUT of Fig. 5.1 (a) at 10 dB.

if compared to 35 dB considered in open media applications as done in [112]. Significantly, the results start confining to the noiseless case with an increase in the SNR value where for an SNR of 35 dB a notable resemblance can be observed. Besides, it can be noted that the appearance of junctions relative to complex wiring structures improved the performance in the presence of noise, in the event that these junctions serve in breaking down the periodicity phenomenon relative to simple single-branch structures. Therefore, ghosts seem to collapse once a junction appears, which can be inferred from the pseudo-spectra of Figs. 5.18&, 5.19 corresponding to the single and double-junction networks respectively, a property facilitating the process of isolating the fault's singularity.

As a matter of fact, several features based on the presented results need to be commented. First, uncertainty is obtained in the case of a single frequency excitation in the presence of noise when observing the pseudo-spectra of all tested networks at low SNR values well below 15 dB. Regrettably, in this case we can't resolve the fault's singularity neither at low frequencies where heavy clutter is present especially that low frequency components are less tolerant to noise nor at high frequencies where distinguishing the fault's singularity from ghosts is impossible. Besides, we have realized that the peaks were symmetrically scattered around the true position of the singularities. Therefore, studying the pseudo-spectrum based on several frequency samples would allow an estimation of the fault's position by applying an averaging operation. However, peaks scattered from ghosts can pollute the useful data used for the averaging process thus applying a clustering procedure would allow collecting each set of peaks corresponding to a position to one group, in particular those corresponding to the neighborhood of the fault's singularity.

To better illustrate this point, let us consider the case of the single-branch network of Fig. 5.1 (a) at an SNR value of 10 dB, the histogram of Fig. 5.20 shows the distribution of peaks on different positions of the network. Markedly, 25 % of the total peak locations occur within a bin width of 10 cm centered at the position of the fault (1.15 m from the reference testing port). The remaining peaks are distributed all over the positions of the network prior to the presence of ghosts. On the other hand, one can argue that depending on the width of the bin a different precision of the fault's position could be obtained. In fact, this might be true as long as a specific algorithm is not defined, but in our case study a heuristic approach is considered.

Based on the fact that the worse ghost scenario occurs in simple network structures, and knowing that these ghosts appear as a multiple of half the wavelength, we can expect that the maximum number of singularities including the one pointing on the position of the fault is achieved on the maximal frequency step. In other words, for a simple structure wiring configuration of length L and operating at a maximum frequency F_{max} the maximum number of singularities is

$$N_{sing} = \frac{L}{\lambda/2}, \tag{5.6}$$

with $\lambda = v_p/F_{max}$ being the wavelength at F_{max}. Consequently, the maximal distance between a ghost and another is $W = L/N_{sig}$. Specifically, for the single 2 m branch network of Fig. 5.1 (a), $N_{max} = 8$ for a maximal frequency step of 500 MHz, while W $\approx$ 0.25 m. After computing W, a bin width $W_b = W/10$ is set, the bin center corresponding to the most frequent bin would be a preliminary estimate P_f^{pr} of the fault's position. Accordingly, the fault's position would be the mean value of the peak locations lying in an interval W and centered at P_f^{pr}. It is important to note here that the reason behind choosing W as an onset interval is to try as much as possible to collect only peaks related to the fault's position otherwise a larger W would probably pollute our data with peak locations from the ghosts.

In order to better understand the procedure of obtaining the fault's position, let us reconsider the case of the single-branch NUT of Fig. 5.1 (a) at a SNR value of 10 dB. For instance, we have already computed W=0.25 m, thus for a threshold of $W_b = W/10 = 0.025$ m, the histogram of Fig. 5.21 (a) is obtained. The most frequent bin occurs at a bin center of 1.14 m with a bin width of $\approx$ 0.25 m, thus P_f^{pr}=1.14 m will form the preliminary position of the fault. This will be followed by collecting all the peak locations centered at the obtained P_f^{pr} within an interval $W \approx 0.25$ m. The distribution of these peak locations is shown in the histogram of Fig. 5.1 (b), where we can notice that they have a bell shaped distribution, whose mean value $\mu = 1.147\ m$ reflects the estimated position of the fault. With this in mind, 1000 different noise realizations are considered at each SNR value where an estimate fault position P_f^{es} is computed at each of these realizations. This will followed by an averaging operation done over all noise realizations where according to the law of large numbers (LLN) in probability theory [159], the sample average converges almost surely to

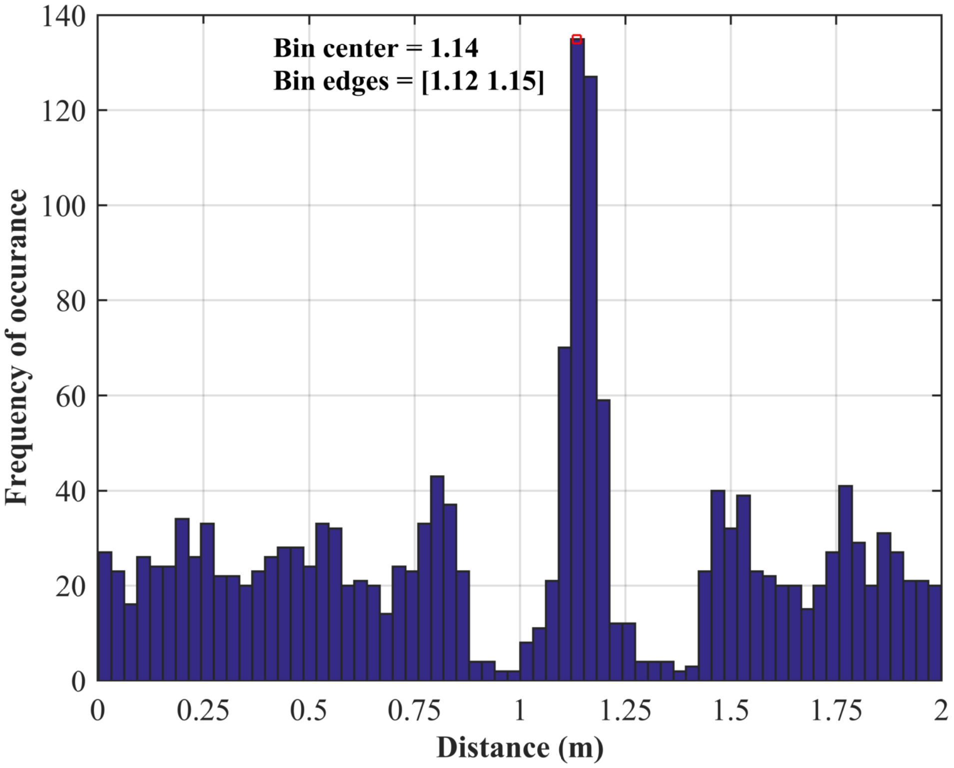

(a)

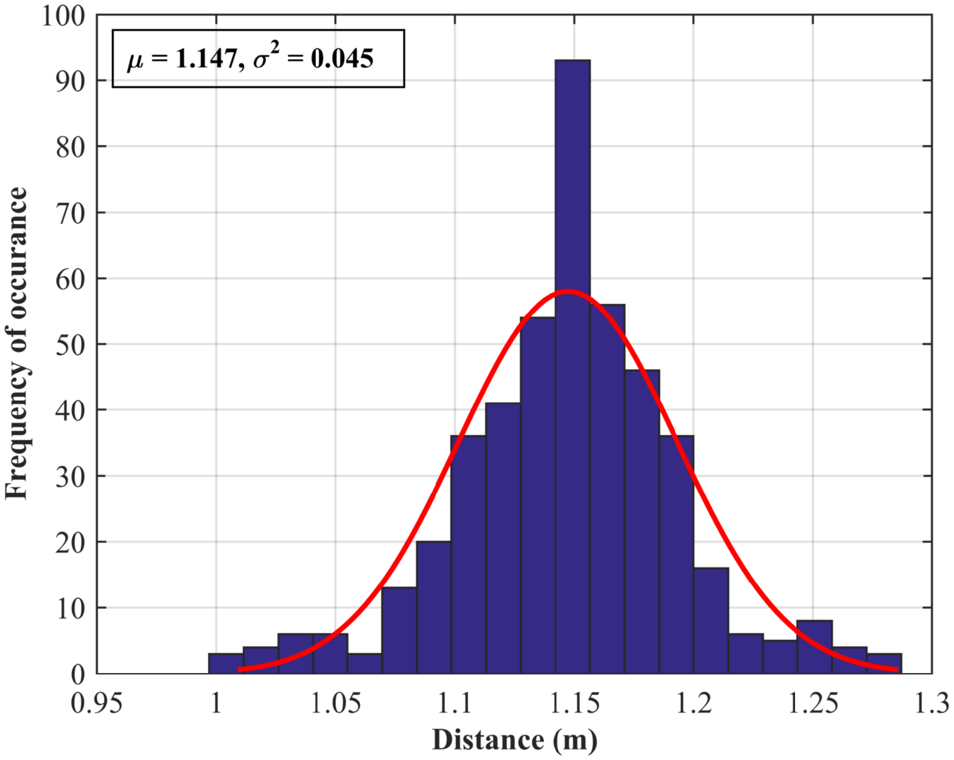

(b)

Figure 5.21 The histograms of peaks corresponding to the pseudo-spectrum of the NUT of Fig. 5.1 (a) at an arbitrarily chosen noise realization and an SNR value of 10 dB. (a) Shows the result obtained after setting a bin width of 0.025 m prior to obtained maximal ghost interval W = 0.25 m, (b) shows the distribution of the peaks in an interval of 0.3 m around the preliminary fault's position referring to 1.14 m.

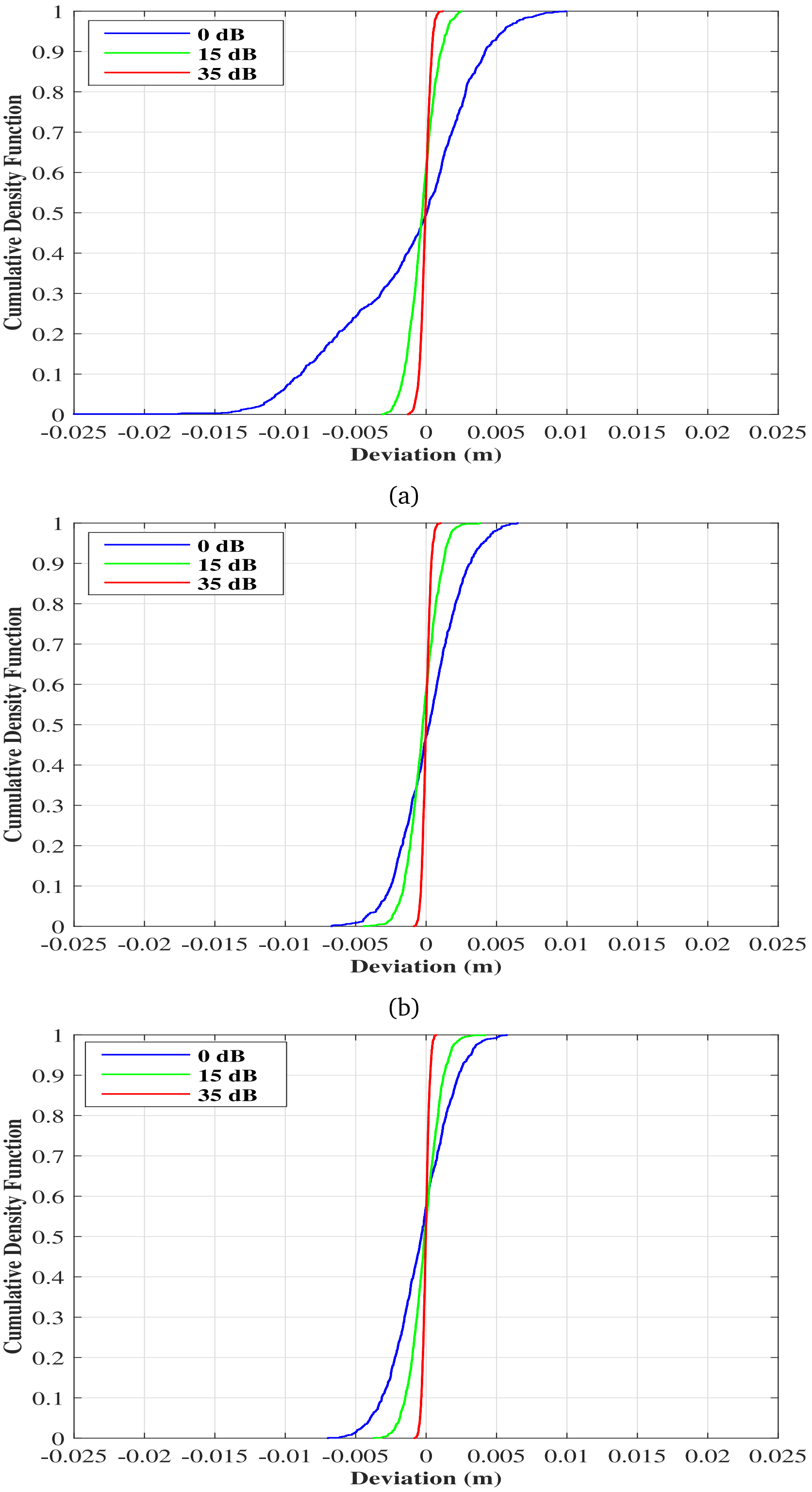

(a)

(b)

(c)

Figure 5.22 The cumulative distribution function (CDF) of the deviation of the faults's position for different values of the SNR in the (a) single-branch configuration, (b) single-junction network, and (c) double-junction NUT of Figs. 5.1(a) ,(b),& (c) respectively.

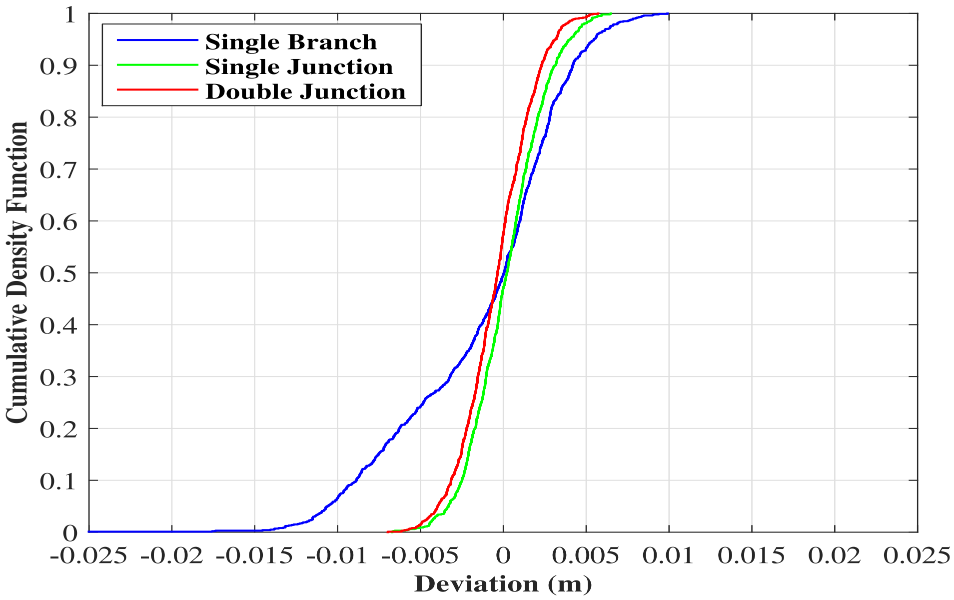

Figure 5.23 The cumulative distribution function (CDF) of the deviation of the faults's position for an SNR value of 0 dB comparing the performance with an increased network's complexity starting from the single-branch configuration to the single-junction network and the double-junction NUT of Figs. 5.1(a) ,(b),& (c) respectively.

the expected value at a large number of realizations. Accordingly, this would return a better, more precise estimation of the fault's position at a specified value of the SNR. Furthermore, it would be interesting to observe the distribution of P_f^{pr} over all the noise realizations for a given value of the SNR. The cumulative distribution function (CDF) forms a proper tool for this purpose.

The CDFs in Fig. 5.22 (a) are computed for several values of the SNR for the single branch NUT of Fig. 5.1 (a). It can be noted that the steepness of the CDF increases with an increase in the SNR, which is accompanied by a faster convergence towards the eventual position of the fault. In this event, the same result is obtained with the single and double-junction NUTs of Figs. 5.1 (b), & (c), where the corresponding CDFs are shown in Figs. 5.22 (b), & (c). With this in mind, Fig. 5.23 compares the CDFs of the three NUTs computed at an SNR value of 0 dB, where it can be inferred that increasing the network's complexity is accompanied by an increase in the steepness of the curve. Accordingly, a faster convergence towards the actual position of the fault is obtained. In brief, this result is expected as the appearance of ghosts is broken down by the presence of junctions prior to the increase in the complexity of the network. In other words, less peak locations are obtained in the data of the corresponding pseudo-spectrum starting from the position of the junction.

In order to quantify the variation of the estimated fault's position for a given SNR, its mean value is observed along with its upper and lower bound estimates. A 95% confidence interval is considered, i.e. the significance level is set to 0.05 where the lower and upper bound estimates are taken at a 2.5% and 97.5% of the CDF corresponding to the studied network at a predefined SNR. To better

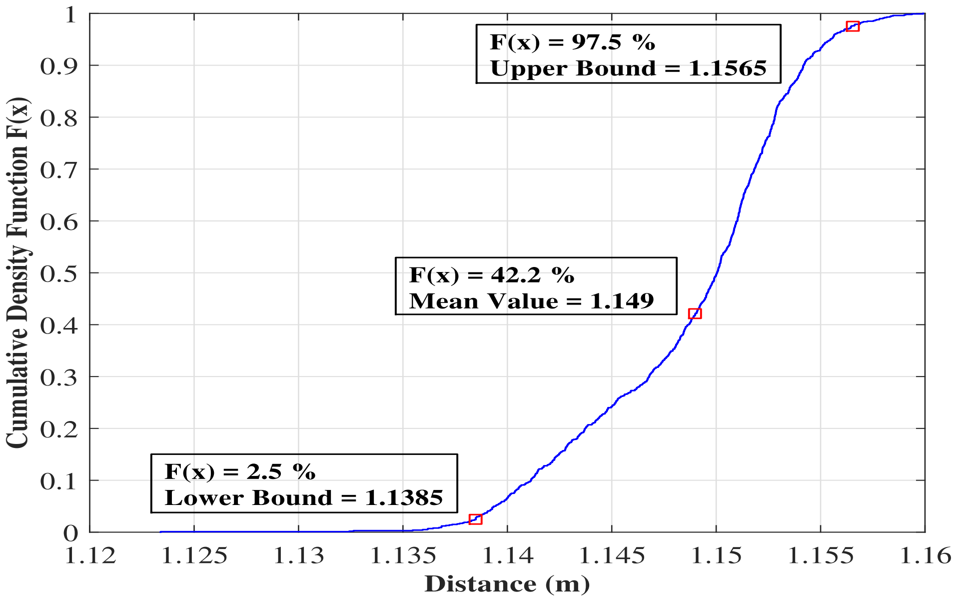

Figure 5.24 The cumulative distribution function (CDF) of the deviation of the faults's position for an SNR value of 0 dB of the single branch NUT of Fig. 5.1(a) showing the mean value of the fault's position along with the upper and lower bound limits taken on a 95% confidence interval.

clarify this point, Fig. 5.24 shows the CDF of the single branch NUT at 0 dB, where the corresponding mean value of the fault's position is 1.149 m, with a lower bound limit of 1.1385 m and an upper bound limit of 1.1565 m for a 95% interval of confidence. Accordingly, the evolution of these values is observed for the NUTs of Figs. 5.1 (a), (b), & (c) as presented in Figs 5.25(a) ,(b), & (c) respectively. It can be noticed that for a low SNR value of 0 dB, the difference between the upper and lower bounds decreased from 17 mm for the single-branch configuration to 9 mm for the single-junction NUT and finally to an 8 mm difference for the double-junction network. A significant decrease in this difference is observed with an increase in the SNR which is in the range of 1 mm at 35 dB, where additionally this increase in the SNR is accompanied by a converging in the mean value of the fault's position towards the eventual location of the fault.

It shall be worthy to note that, TR-MUSIC has provided an effective robustness with noisy data where precise estimates of the fault's position were returned at low SNR. Most importantly, the error didn't exceed the range of 2 cm at very low SNR of 0 dB, a striking result in the domain of fault detection and location.

5.4.2 Conclusions

This chapter has investigated the potential of TR-MUSIC as a single-frequency fault detection technique. Experiments have shown that this technique is effective in detecting and locating single

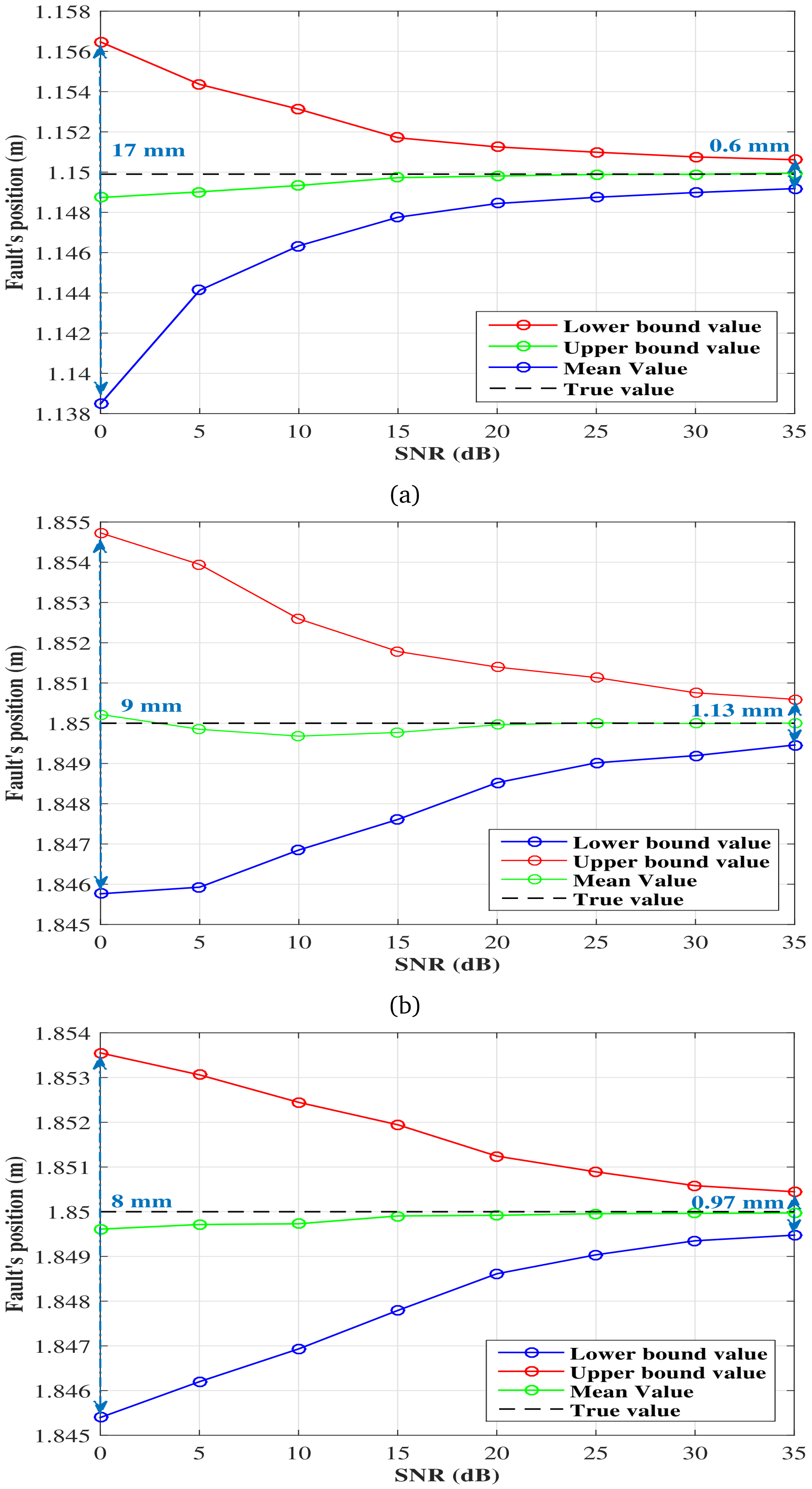

(a)

(b)

(c)

Figure 5.25 The cumulative distribution function (CDF) of the deviation of the faults's position computed for different values of the SNR in the (a) Single branch configuration, (b) single junction network, and (c) double junction NUT of Figs. 5.1(a) ,(b),& (c) respectively.

as well as multiple soft faults in three NUTs of different complexity. Of practical importance is its ability to retrieve a fault's reflection coefficient even though a reflectogram is not defined.

The appearance of ghosts in pseudo-spectra was shown to be avoidable by imposing a maximum test frequency, according to the length of the NUT. The surprising ability of TR-MUSIC to ensure a *sub-millimeter resolution* while using relatively low test frequencies is good news, as similar performance with TDR techniques would require much higher test frequencies and wider bandwidths, which may be hampered by attenuation in cables. Furthermore, since this chapter has shown that the performance of TR-MUSIC does not depend on the chosen test frequency, TR-MUSIC appears as more readily adaptable to the case of live testing, where the NUT would be under use over a given set of frequencies and thus test signals could ideally be allocated outside these frequencies. The same rationale clearly applies to EMC constraints.

Additionally, TR-MUSIC has shown a great performance in the presence of noise, where a significant robustness has been obtained at low SNR. This, promising achievement proves the technique's applicability for real-life NUTs where data are usually collected in noisy environments. In fact, the obtained results form an excellent incentive towards the practical implementation of the method. Despite the fact that good results have been obtained, an optimization of the heuristic approach is needed in order to take advantage from all information provided by the pseudo-spectrum data which might enable working on lower SNR values.

Future work will need to deal with the robustness of the TR-MUSIC and its sensitivity to tolerances in the topology of the network which is used in the post-processing as a reference model for computing the system's Green function.

5.5 Conclusion

Time-Reversal multiple signal classification (TR-MUSIC) was here applied to testing cable networks in order to detect and locate soft faults. TR-MUSIC has shown to provide spatial resolution in the millimeter range while using continuous-wave test signals, even at frequencies with guided wavelengths much larger than cables length. State of the art time-domain reflectometry (TDR) methods would require bandwidths in the order of hundreds of MHz for a similar performance. As opposed to TDR, TR-MUSIC does not suffer from the ambiguity created by the existence of multiple echoes in cable networks, which can be easily misinterpreted as multiple faults, leading to false alarms. TR-MUSIC is intrinsically adapted to dealing with multiple faults, handing a direct estimate of the number of faults found in a network under test. Furthermore, the detection capabilities of TR-MUSIC are insensitive to the severity of a fault, as faults are not detected based on the intensity of their echoes as done in TDR techniques, but on a sub-space approach mostly dependent on phase patterns. Accurate identification of faults from continuous-wave signals points to the possibility of designing simpler test systems, not requiring pulse generators and fast electronics. TR-MUSIC accuracy is demonstrated experimentally for locating both single as well as multiple soft faults in different networks. The proposed method also gives access to the reflection coefficient of each fault, thus enabling an estimate of its severity. Notably, TR-MUSIC has provided a good performance in the presence of noise, where good estimates of the fault's positions were returned at low SNR in different complexity NUTs. In fact, this robustness towards noisy measuring environments would allow as the case of DORT method to accomplish measurements in short periods of times and would additionally permit detecting intermittent faults.

Given that the studies we conducted in this chapter and the previous one were a feasibility study of TR-based methods of both DORT and TR-MUSIC techniques, for locating single as well as multiple soft faults in different complexity network configurations, a more extended analysis should be conducted. In fact, a wider database should be considered, including more network configurations, and more real soft fault models, as well as an extension of the influencing parameters to include the bandwidth, losses, model perturbations, etc. A comparison of the both DORT and TR-MUSIC with other existing methods in given scenarios is also useful to asses the configurations where our method presents advantages over the existing one. The practical implementation of the method should be further investigated, depending on the configuration of the NUT. For example, if we consider networks that are extended over wide distances, their extremities cannot be connected to one VNA in order for the **S** matrix to be measured. In such scenarios, several measuring devices must be used, and thus the synchronization of these devices in order to obtain a time origin for the injected and received signals is necessary (which can be done by means of the GPS network for example). This shows that the practical implementation of the method for a given network needs to be investigated.

General Conclusion and Perspectives

Conclusion

The research conducted in this thesis aim to propose and develop new diagnostic techniques for complex wired networks to meet the need and the problem of detecting and locating faults that manufacturers and users face today in electrical systems. The critical importance of the problem of soft faults has been emphasized and explained, while showing the shortcomings existing methods faced in this domain.

In fact, the literature study achieved during the three years of the thesis allowed us to acquire a set of methods, techniques and procedures necessary and helpful to successfully accomplish our objective. The state of the art performed in the beginning of our journey permitted forming a conviction of the importance of time reversal (TR) methods in fulfilling our aim.

In the event that the problem of soft-fault detection and location in wiring networks is to a great extent similar to the problem of target location encountered in radar detection, TR techniques can ensure a maximization of the fault-related echo by maximizing the energy impinging on the fault position with respect to the rest of the system under test. Within this context, DORT method adopted from acoustics to the case of guided wave propagation along transmission lines showed the ability to synthesize testing signals adapted to the network under test so as to directly focus signals on the fault location, thus enabling the direct estimation of the fault's position. Despite the fact that the standard form of DORT (SDORT) has shown a great feasibility is locating single soft faults in different complexity network configurations, it started failing once multiple faults are addressed in an NUT. For this reason, the limitations of SDORT were detailed, during which an analytical approach enabling separating the faults' responses was illustrated. Notably, this new approach enabled extracting the signature of each soft fault in a unique single-fault scattering matrix which was presented as an EDORT technique. Equally important, was the ability to set the basis of computing the reflection coefficients of the corresponding faults. Experimental validations confirmed the applicability of EDORT is the precise detection and location of multiple soft faults in simple and non-trivial NUT layouts, and in retrieving the severities of the tested faults. These results give credibility to the practical usefulness of the proposed method in critical real-life configurations that are hardly addressed in current literature. Meanwhile, a substantial concern that might affect the practical implementation of the method in real-life applications, namely noise, is investigated.

DORT method has demonstrated an unrivaled robustness in providing excellent performance with noisy collected data along with a boosted effectiveness with an increased network complexity, thus enabling fast measuring operations and opening the potential opportunity to locate intermittent soft faults. Furthermore, we have shown that length changes in the NUT reference model are confronted with smaller variations in the position of the fault whose effect seems to decrease with an increasing complexity of the tested wiring networks.

As a matter of fact, DORT-based methods use a sub-space approach in defining signals that, once fed into a numerical model of the NUT, will focus back to the position of a fault; this propagation phase is carried out in the time domain, and therefore undergo most of the same limitations of any other time-domain method, particularly the need for large bandwidth to create spatial resolution. On the contrary, TR-MUSIC, which formed the pivot of our research study in the second part of our work, does operate on a different sub-space approach, based on the Green function of medium; no back-propagation phase is used and actually a correlation process is defined. TR-MUSIC operates on phase patterns provided by Green function as a mean of identifying positions in a complex medium. It is mainly applied for detecting and locating scatterers in a background medium; indeed, soft faults can also be treated as weak scatterers. In the last part of the thesis, TR-MUSIC is adopted to soft fault detection and location in transmission lines which presented a striking feature demonstrated by ensuring *sub-wavelength spatial resolution* while working on a single-frequency basis. Besides, it works independently of *well-resolvedness* criteria for multiple scatterers and returns *super-resolution* estimates for their locations. Notably, it is by far less sensitive to fault coupling which is possible as the TR-MUSIC is based on a sub-space approach. Numerical and experimental results conducted, confirm the practical potential of this novel approach in locating single as well as multiple soft faults in different network complexities. TR-MUSIC has also shown to allow retrieving the reflection coefficient of each fault, thus giving a direct evaluation of the risk they pose to the integrity of the NUT. This step is accomplished without having to measure the reflections of testing signals. Notably, TR-MUSIC has provided an efficient performance in the presence of noise, where a significant robustness was revealed starting from an SNR of 0 dB. In fact, a heuristic approach was derived which allowed returning good estimates of the positions of faults at low SNR values in different complexity NUTs.

Perspectives

We opted to work in this thesis on adopting TR properties to the problem of fault detection and location in transmission line networks. As a matter of fact, efficient and significant results have been obtained with single as well as multiple soft faults in different network structures. With this in mind, an extended study could be conducted to continue or handle other features that we weren't able to address in our work. Some of these perspectives are listed in the following:

- when addressing multiple soft fault location with EDORT method in the first part of the thesis, we accomplished our investigations on a limited number of network topologies and a specific type of wiring soft faults. Consequently, a wider database handling more complex network configurations while considering other types of real soft faults, namely resistive, capacitive or even inductive defects as well as an extension of the influencing parameters to include the bandwidth, losses, model perturbations, etc., should be addressed.

- Based on the examples considered in the EDORT validations, we saw the necessity of finding an adequate criterion to describe whether or not we located a fault in a complex network. In fact, determining the fault's position was accomplished by monitoring either the focal spot location in the ZT diagram or the energy peak in the energy diagrams. Therefore, there arises a need to calculate some kind of contrast, between the fault's peak and its background to return more accurate estimates of the positions of the detected faults along with their locations with respect to the network's topology.

- Previous literature of DORT method show that its performance is influenced by the number of testing ports and their positions; this factor is one of many other factors that might influence the method's performance, hence it is necessary to analyze these parameters and their possible effects on the EDORT performance through a statistical study handling the number of testing ports and the positions of the faults.

- One of the paramount aspects we proposed for the DORT and TR-MUSIC methods is their feasibility in retrieving the reflection coefficients of the tested soft faults. Soft defects can be seen as the premises of future hard faults which have irreversible consequences and require repair to restore the quality of service. Consequently, using the reflection coefficient computation along with cable data sheets provided by the manufacturer could be beneficial to estimate the remaining useful lifetime (RUL) of a cable.

- The same rationals of extended study of DORT method should be applied for the TR-MUSIC method that showed an important efficiency in detecting and locating single as well as multiple soft faults in different complexity networks. Therefore, a wider database of network topologies along with different types of real soft faults in addition to the same statistical study previously considered for DORT shall be addressed. Furthermore, it is important to monitor TR-MUSIC's response towards changes in the lengths of cables composing the reference network model, in order to analyze its tolerance towards such changes and compare it to the results obtained for DORT's method.

- The significant robustness DORT and TR-MUSIC methods have provided in the presence of noise while returning good estimates of the positions of faults at low SNR encourages the practical implementation of these techniques in real-life applications. In fact, real-life systems are always susceptible to a variety of noise sources (thermal, mechanical, etc.) which might return noisy measured data at low SNR. Besides, we have shown that this robustness was accompanied by a short duration measurement process which promotes a deeper detailed research study for detecting and locating intermittent faults.

- The heuristic approach presented in the last part of the TR-MUSIC shows that it needs to be optimized, where better estimates of the fault's positions could be returned. As a matter of fact, several clustering techniques, namely the k-means method, could be a good candidate in its favor.
- DORT and TR-MUSIC are among the many existing methods for the detection and location of faults in wiring networks. Thus, a comparison of the both DORT and TR-MUSIC with other methods, namely reflectometry, in given scenarios is also useful to asses the configurations where our method presents advantages over these methods.
- The paradigm shift of technology to the evolution of smaller electrical systems which are easy to handle and carry led to the development of portable VNA's with small dimensions but with still high frequency ranges up to 6 GHz (MS2036C). Notably, this allows implementing our methods in small kits that can be integrated in the body parts of many applications (vehicles, airplanes, etc.) to accomplish automatic and frequent monitoring for the health of the wiring networks of the tested systems.
- The practical implementation of the method should be further investigated, depending on the configuration of the NUT. For example, if we consider networks that are extended over wide distances (power lines), their extremities cannot be connected to one VNA in order for the **S** matrix to be measured. In such scenarios, several measuring devices must be used, and thus the synchronization of these devices in order to obtain a time origin for the injected and received signals is necessary (which can be done by means of the GPS network for example). This shows that the practical implementation of the method for a given network needs to be investigated.
- An extended study of the DORT and TR-MUSIC methods in the case of multiconductor transmission lines (MTL) is interesting to study, since a wide range of cables consist of multiconductor lines that are packed together into bundles. When considering MTLs, several parameters such as the coupling between the conductors should be taken into account, and also the way to adapt and implement the methods should be investigated.
- DORT and TR-MUSIC were here applied to electrical cables and have shown interesting and promising results. Another line of research for these methods could be conducted to handle fault location in railways, pipelines, etc. during which acoustic signals could be used for the purpose.

Glossary

Abbreviations

- **DORT**: Décomposition de l'Opérateur de Retournement Temporel.
- **EVD**: Eigen Value Decomposition.
- **FA**: False Alarm.
- **FDR**: Frequency Domain Reflectometry.
- **MDM**: Multi-static Data Matrix.
- **MTL**: Multi-conductor Transmission Line.
- **MUSIC**: Multiple Signal Classification.
- **NUT**: Network Under Test.
- **ROC**: Receiver Operating Curve.
- **SNR**: Signal to Noise Ratio.
- **SVD**: Singular Value Decomposition.
- **TDR**: Time Domain Reflectometry.
- **TP**: True Positive.
- **TR**: Time Reversal.
- **TRO**: Time Reversal Operator.
- **VNA**: Vector Network Analyzer.
- **ZT**: Space-Time Diagram.

Publications

Journal Papers

- **Moussa Kafal**, Andrea Cozza, and Lionel Pichon. "*Locating Multiple Soft Faults in Wire Networks Using an Alternative DORT Implementation*." IEEE Transactions on Instrumentation and Measurement 65, no. 2 (2016): 399-406.
- **Moussa Kafal**, Andrea Cozza, and Lionel Pichon. "*Locating Faults with High Resolution Using Single-Frequency TR-MUSIC Processing*." IEEE Transactions on Instrumentation and Measurement (2016).
- **Moussa Kafal**, Andrea Cozza, and Lionel Pichon. "*An Efficient Technique Based on DORT Method to Locate Multiple Soft Faults in Wiring Networks*." IEEE Instrumentation and Measurement Magazine (2016).

International Conference Papers

- **Moussa Kafal**, Andrea Cozza, and Lionel Pichon. "*An Enhanced DORT Approach for Locating Multiple Soft-Faults in Complex Wire Networks*." IEEE First Atlantic Radio Science Conference (URSI AT-RASC), May 2015.
- **Moussa Kafal**, Andrea Cozza, and Lionel Pichon. "*An Efficient Technique Based on DORT Method to Locate Multiple Soft Faults in Wiring Networks*." IEEE AUTOTESTCON, November 2015. *Best Student Technical Paper Award*.

Bibliography

[1] T. Edison, “Electric conductor,” Mar. 15 1892. US Patent 470,924.

[2] http://www.nexans.fr/.

[3] K. R. Wheeler, I. X. Twombly, K. F. Goebel, P. F. Wysocki, *et al.*, “Aging aircraft wiring fault detection survey,” 2007.

[4] C. Furse, Y. C. Chung, C. Lo, and P. Pendayala, “A critical comparison of reflectometry methods for location of wiring faults,” *Smart Structures and Systems*, vol. 2, no. 1, pp. 25–46, 2006.

[5] P. Smith, C. Furse, and J. Gunther, “Analysis of spread spectrum time domain reflectometry for wire fault location,” *Sensors Journal, IEEE*, vol. 5, no. 6, pp. 1469–1478, 2005.

[6] J. Wang, P. Crapse, J. Abrams, Y.-J. Shin, R. Dougal, T. Mai, L. Tran, and J. Molnar, “Diagnostics and prognostics of wiring integrity via joint time-frequency domain reflectometry,” in *10th Joint FAA/DoD/NASA Conference on Aging Aircraft*, 2007.

[7] N. Ravot, F. Auzanneau, Y. Bonhomme, M. Olivas, and F. Bouillault, “Distributed reflectometry-based diagnosis for complex wired networks,” *EMC: Safety, Reliability and Security of Communication and Transportation Syst*, 2007.

[8] M. Fink *et al.*, “Time-reversed acoustics,” *Scientific American*, vol. 281, no. 5, pp. 91–97, 1999.

[9] W. Zhang, A. Hoorfar, and L. Li, “Through-the-wall target localization with time reversal music method,” *Progress In Electromagnetics Research*, vol. 106, pp. 75–89, 2010.

[10] F. Auzanneau, “Wire troubleshooting and diagnosis: Review and perspectives,” *Progress In Electromagnetics Research B*, vol. 49, pp. 253–279, 2013.

[11] R. R. Yarlagadda, R. K. R. Yarlagadda, and R. K. R. Yarlagadda, *Analog and digital signals and systems*, vol. 1. Springer, 2010.

[12] S.-Y. King and N. Halfter, “Underground power cables,” *S. Y. King and N. A. Halfter, Book, 1982, Many figs. and tables, 411, Longman Group Limited, Longman House, Burnt Mill, Harlow, Essex, 30 Pounds*, 1982.

[13] L. Rochester, *Coaxial Cables Application Data*. Technical Publishers Incorporated, 1969.

[14] T. J. Siekierka and R. D. Kenny, “Twisted pair cable,” Mar. 31 1998. US Patent 5,734,126.

[15] A. G. Bell, “Telephone-circuit,” July 19 1881. US Patent 244,426.

[16] A. A and L. Espenschied, “Concentric conducting system,” Dec. 8 1931. US Patent 1,835,031.

[17] C. Furse and R. Haupt, “Down to the wire [aircraft wiring],” *Spectrum, IEEE*, vol. 38, no. 2, pp. 34–39, 2001.

[18] A. J. Hebert, “When aircraft get old,” *Air Force Magazine*, vol. 86, no. 1, p. 30, 2003.

[19] F. Global. https://www.flightglobal.com/, 2006.

[20] http://www.thespacereview.com/article/662/1.

[21] C. Teal and C. Satterlee, “Managed aircraft wiring health directly relates to improved avionics performance,” in *Digital Avionics Systems Conference, 2000. Proceedings. DASC. The 19th*, vol. 1, pp. 3B6–1, IEEE, 2000.

[22] C. Buccella, M. Feliziani, and G. Manzi, “Identification and localization of defects in shielded cables by a numerical/experimental procedure,” in *Electromagnetic Compatibility, 2003 IEEE International Symposium on*, vol. 1, pp. 213–218, IEEE, 2003.

[23] S. P. Cygan and J. R. Laghari, “Effects of multistress aging (radiation, thermal, electrical) on polypropylene,” *Nuclear Science, IEEE Transactions on*, vol. 38, no. 3, pp. 906–912, 1991.

[24] Y. Mecheri, L. Boukezzi, A. Boubakeur, and M. Lallouani, “Dielectric and mechanical behavior of cross-linked polyethylene under thermal aging,” in *Electrical Insulation and Dielectric Phenomena, 2000 Annual Report Conference on*, vol. 2, pp. 560–563, IEEE, 2000.

[25] J. Schonfeld, O. Greulich, A. Patterson-Hine, L. Lee, J. Cockrell, and L. Hofland, “Wire integrity research (wire) research study,” *Doc. No. A0SP-0001-XB1*, 2000.

[26] C. Smith, “Transport aircraft intrusive inspection project (an analysis of the wire installations of six decommissioned aircraft),” *Aging Transport Systems Rulemaking Advisory Committee (ATSRAC) Final Report*, 2000.

[27] P. Smith, P. Kuhn, and C. Furse, “Intermittent fault location on live electrical wiring systems,” *SAE International Journal of Aerospace*, vol. 1, no. 1, pp. 1101–1106, 2009.

[28] L. A. Griffiths, R. Parakh, C. Furse, and B. Baker, “The invisible fray: A critical analysis of the use of reflectometry for fray location,” *Sensors Journal, IEEE*, vol. 6, no. 3, pp. 697–706, 2006.

[29] NASA, “Wire integrity research pilot study final report,” 2000.

[30] Y. C. Chung, N. Amarnath, C. Furse, and J. Mahoney, “Capacitance and inductance sensors for location of open and short circuited wires,” *IEEE Trans Instrum. Meas*, pp. 604–613, 2009.

[31] V. C. Camara and D. Laux, “Moisture content in honey determination with a shear ultrasonic reflectometer,” *Journal of Food Engineering*, vol. 96, no. 1, pp. 93–96, 2010.

[32] T. Gumprecht, G. Roeder, M. Schellenberger, and L. Pfitzner, “Measurement strategy for dielectric ultra-thin film characterization by vacuum ultra-violet reflectometry,” in *Advanced Semiconductor Manufacturing Conference (ASMC), 2012 23rd Annual SEMI*, pp. 82–87, IEEE, 2012.

[33] M. Kaczmarek, P. SAFINOWSki, and B. Piwakowski, “Non-contact ultrasonic porosimetry,” in *7th International Symposium on Non Destructive Testing in Civil Engineering, NDTCE’09*, pp. 529–534, 2009.

[34] J. A. Ware and K. Aki, “Continuous and discrete inverse-scattering problems in a stratified elastic medium. i. plane waves at normal incidence,” *The journal of the Acoustical Society of America*, vol. 45, no. 4, pp. 911–921, 1969.

[35] S. Kharkovsky and R. Zoughi, “Microwave and millimeter wave nondestructive testing and evaluation-overview and recent advances,” *Instrumentation & Measurement Magazine, IEEE*, vol. 10, no. 2, pp. 26–38, 2007.

[36] L. A. Pereira Dos Santos, *Développement d’une nouvelle méthode de détermination des profils de teneur en eau dans les sols par inversion d’un signal TDR*. PhD thesis, 1997.

[37] R. J. Woodward, *Using frequency domain reflectometry for water level measurement*. 2000.

[38] W. Liu, R. Hunsperger, M. Chajes, and E. Kunz, “An overview of corrosion damage detection in steel bridge strands using tdr,” in *Proc., 2nd Int. Symp. on TDR for Innovative Applications*, Citeseer, 2001.

[39] C. Neus, P. Boets, and L. Van Biesen, “Channel capacity estimation of digital subscriber lines: a frequency domain approach.,” in *ICC*, pp. 2676–2681, Citeseer, 2007.

[40] Y. C. Chung, C. Furse, and J. Pruitt, “Application of phase detection frequency domain reflectometry for locating faults in an f-18 flight control harness,” *Electromagnetic Compatibility, IEEE Transactions on*, vol. 47, no. 2, pp. 327–334, 2005.

[41] C. Furse, Y. C. Chung, R. Dangol, M. Nielsen, G. Mabey, and R. Woodward, “Frequency-domain reflectometry for on-board testing of aging aircraft wiring,” *Electromagnetic Compatibility, IEEE Transactions on*, vol. 45, no. 2, pp. 306–315, 2003.

[42] P. J. Medelius and H. J. Simpson, “Non-intrusive impedance-based cable tester,” Nov. 2 1999. US Patent 5,977,773.

[43] C. Furse and N. Kamdar, “An inexpensive distance measuring system for navigation of robotic vehicles,” *Microwave and Optical Technology Letters*, vol. 33, no. 2, pp. 84–87, 2002.

[44] A. Lelong, M. O. Carrion, V. Degardin, and M. Lienard, “Characterization of electromagnetic radiation caused by on line wire diagnosis,” in *URSI Conference*, Citeseer, 2008.

[45] V. Taylor, M. Faulkner, A. Kalam, and J. Haydon, “Digital simulation of fault location on ehv lines using wideband spread spectrum techniques,” in *Generation, Transmission and Distribution, IEE Proceedings-*, vol. 142, pp. 73–80, IET, 1995.

[46] C. Furse, P. Smith, C. Lo, Y. C. Chung, P. Pendayala, and K. Nagoti, “Spread spectrum sensors for critical fault location on live wire networks,” *Structural Control and Health Monitoring*, vol. 12, no. 3-4, pp. 257–267, 2005.

[47] P. Smith, C. Furse, and J. Gunther, “Fault location on aircraft wiring using spread spectrum time domain reflectometry,” *IEEE Sensors Journal*, vol. 5, no. 6, pp. 1469–1478, 2005.

[48] P. Crapse, J. Wang, Y.-J. Shin, R. Dougal, T. Mai, J. Molnar, and L. Tran, “Design of optimized reference signal for joint time-frequency domain reflectometry-based wiring diagnostics,” in *AUTOTESTCON, 2008 IEEE*, pp. 195–201, IEEE, 2008.

[49] J. Wang, P. E. Stone, D. Coats, Y.-J. Shin, and R. A. Dougal, “Health monitoring of power cable via joint time-frequency domain reflectometry,” *Instrumentation and Measurement, IEEE Transactions on*, vol. 60, no. 3, pp. 1047–1053, 2011.

[50] Q. Shi, U. Troeltzsch, and O. Kanoun, "Detection and localization of cable faults by time and frequency domain measurements," in *Systems Signals and Devices (SSD), 2010 7th International Multi-Conference on*, pp. 1–6, IEEE, 2010.

[51] M. Franchet, *Réflectométrie appliquée à la détection de défauts non francs dans les torons de câbles*. PhD thesis, Université Paris-Est, 2012.

[52] M. Franchet, N. Ravot, and O. Picon, "The use of the pseudo wigner ville transform for detecting soft defects in electric cables," in *Advanced Intelligent Mechatronics (AIM), 2011 IEEE/ASME International Conference on*, pp. 309–314, IEEE, 2011.

[53] H. Boudjefdjouf, R. Mehasni, A. Orlandi, H. Bouchekara, F. De Paulis, and M. Smail, "Diagnosis of multiple wiring faults using time-domain reflectometry and teaching–learning-based optimization," *Electromagnetics*, vol. 35, no. 1, pp. 10–24, 2015.

[54] C. R. Paul, *Analysis of multiconductor transmission lines*. John Wiley & Sons, 2008.

[55] C. M. Studio, "v5. 0," *Computer Simulation Technology*, 2003.

[56] K. S. Yee *et al.*, "Numerical solution of initial boundary value problems involving maxwell's equations in isotropic media," *IEEE Trans. Antennas Propag*, vol. 14, no. 3, pp. 302–307, 1966.

[57] K. S. Kunz and R. J. Luebbers, *The finite difference time domain method for electromagnetics*. CRC press, 1993.

[58] T. P. Montoya, "Modeling 1-d fdtd transmission line voltage sources and terminations with parallel and series rlc loads," in *Antennas and Propagation Society International Symposium, 2002. IEEE*, vol. 4, pp. 242–245, IEEE, 2002.

[59] M. K. Smail, L. Pichon, M. Olivas, F. Auzanneau, and M. Lambert, "Detection of defects in wiring networks using time domain reflectometry," *Magnetics, IEEE Transactions on*, vol. 46, no. 8, pp. 2998–3001, 2010.

[60] F. T. Ulaby, E. Michielssen, and U. Ravaioli, *Fundamentals of Applied Electromagnetics 6e*. Prentice Hall, 2001.

[61] T. Instruments, "The bergeron method: A graphic method for determining line reflections in transient phenomena," *Texas Instruments, Dallas, TX*, 1996.

[62] S. C. Wu, *An iterative inversion method for transmission line fault location*. PhD thesis, The University of Utah, 2011.

[63] C. Lo and C. Furse, "Modeling and simulation of branched wiring networks," *Applied Computational Electromagnetics Society Journal*, vol. 23, no. 2, p. 143, 2008.

[64] K. M. Fidanboylu, N. Korkmaz, and K. Korkmaz, "A transmission line modeling technique using time domain," in *Electromagnetic Compatibility, 2003. EMC'03. 2003 IEEE International Symposium on*, vol. 1, pp. 331–334, IEEE, 2003.

[65] C. Christopoulos, "The transmission-line modeling (tlm) method in electromagnetics," *Synthesis Lectures on Computational Electromagnetics*, vol. 1, no. 1, pp. 1–132, 2005.

[66] K. Kurokawa, "Power waves and the scattering matrix," *Microwave Theory and Techniques, IEEE Transactions on*, vol. 13, no. 2, pp. 194–202, 1965.

[67] P. L. Peres, C. R. de Souza, and I. S. Bonatti, "Abcd matrix: a unique tool for linear two-wire transmission line modelling," *International Journal of Electrical Engineering Education*, vol. 40, no. 3, pp. 220–229, 2003.

[68] D. M. Pozar, *Microwave engineering*. John Wiley & Sons, 2009.

[69] S. J. Orfanidis, *Electromagnetic waves and antennas*. Rutgers University New Brunswick, NJ, 2002.

[70] M. B. Steer, *Microwave and RF design: a systems approach*. SciTech Pub., 2010.

[71] A. Cozza, *Railways EMC: Assessment of infrastructure impact*. PhD thesis, Université des Sciences et Technologie de Lille-Lille I, 2005.

[72] M. Born and E. Wolf, *Principles of optics: electromagnetic theory of propagation, interference and diffraction of light*. Cambridge university press, 1999.

[73] M. A. COZZA, *Layane ABBOUD*. PhD thesis, Citeseer, 2013.

[74] H. W. Ott, *Electromagnetic compatibility engineering*. John Wiley & Sons, 2011.

[75] A. Parvulescu and C. Clay, "Reproducibility of signal transmissions in the ocean," *Radio and Electronic Engineer*, vol. 29, no. 4, pp. 223–228, 1965.

[76] B. Y. Zel'Dovich, N. F. Pilipetsky, and V. V. Shkunov, *Principles of phase conjugation*, vol. 42. Springer, 2013.

[77] C. R. Giuliano, "Applications of optical phase conjugation," *Physics Today*, vol. 34, pp. 27–35, 1981.

[78] D. R. Jackson and D. R. Dowling, "Phase conjugation in underwater acoustics," *The Journal of the Acoustical Society of America*, vol. 89, no. 1, pp. 171–181, 1991.

[79] M. Fink, C. Prada, F. Wu, and D. Cassereau, "Self focusing in inhomogeneous media with time reversal acoustic mirrors," in *Ultrasonics Symposium, 1989. Proceedings., IEEE 1989*, pp. 681–686, IEEE, 1989.

[80] M. Fink, "Time reversal of ultrasonic fields. i. basic principles," *Ultrasonics, Ferroelectrics, and Frequency Control, IEEE Transactions on*, vol. 39, no. 5, pp. 555–566, 1992.

[81] F. Wu, J.-L. Thomas, and M. Fink, "Time reversal of ultrasonic fields. il. experimental results," *Ultrasonics, Ferroelectrics, and Frequency Control, IEEE Transactions on*, vol. 39, no. 5, pp. 567–578, 1992.

[82] D. Cassereau and M. Fink, "Time-reversal of ultrasonic fields. iii. theory of the closed time-reversal cavity," *Ultrasonics, Ferroelectrics, and Frequency Control, IEEE Transactions on*, vol. 39, no. 5, pp. 579–592, 1992.

[83] C. Prada and M. Fink, "Eigenmodes of the time reversal operator: A solution to selective focusing in multiple-target media," *Wave motion*, vol. 20, no. 2, pp. 151–163, 1994.

[84] M. Fink and C. Prada, "Acoustic time-reversal mirrors," *Inverse problems*, vol. 17, no. 1, p. R1, 2001.

[85] J.-L. Thomas, F. Wu, and M. Fink, "Time reversal focusing applied to lithotripsy," *Ultrasonic imaging*, vol. 18, no. 2, pp. 106–121, 1996.

[86] G. Montaldo, P. Roux, A. Derode, C. Negreira, and M. Fink, “Ultrasound shock wave generator with one-bit time reversal in a dispersive medium, application to lithotripsy,” *Applied physics letters*, vol. 80, no. 5, pp. 897–899, 2002.

[87] M. Tanter, J.-L. Thomas, and M. Fink, “Focusing and steering through absorbing and aberrating layers: application to ultrasonic propagation through the skull,” *The Journal of the Acoustical Society of America*, vol. 103, no. 5, pp. 2403–2410, 1998.

[88] C. Le Floch, M. Tanter, and M. Fink, “Self-defocusing in ultrasonic hyperthermia: Experiment and simulation,” *Applied physics letters*, vol. 74, no. 20, pp. 3062–3064, 1999.

[89] M. Persson and H. Trefna, “Method and system relating to hyperthermia,” May 23 2007. US Patent App. 12/302,119.

[90] D. M. Pepper, G. J. Dunning, and D. S. Sumida, “Time-reversed photoacoustic system and uses thereof,” Aug. 15 2006. US Patent 7,089,796.

[91] P. Kosmas and C. M. Rappaport, “Time reversal with the fdtd method for microwave breast cancer detection,” *Microwave Theory and Techniques, IEEE Transactions on*, vol. 53, no. 7, pp. 2317–2323, 2005.

[92] B. Guo, L. Xu, and J. Li, “Time reversal based microwave hyperthermia treatment of breast cancer,” *Microwave and optical technology letters*, vol. 47, no. 4, pp. 335–338, 2005.

[93] C. Larmat, J.-P. Montagner, M. Fink, Y. Capdeville, A. Tourin, and E. Clévédé, “Time-reversal imaging of seismic sources and application to the great sumatra earthquake,” *Geophysical Research Letters*, vol. 33, no. 19, 2006.

[94] M. Saillard, P. Vincent, and G. Micolau, “Reconstruction of buried objects surrounded by small inhomogeneities,” *Inverse Problems*, vol. 16, no. 5, p. 1195, 2000.

[95] N. Maaref, P. Millot, X. Ferrières, C. Pichot, and O. Picon, “Electromagnetic imaging method based on time reversal processing applied to through-the-wall target localization,” *Progress In Electromagnetics Research M*, vol. 1, pp. 59–67, 2008.

[96] T. Leutenegger and J. Dual, “Non-destructive testing of tubes using a time reverse numerical simulation (trns) method,” *Ultrasonics*, vol. 41, no. 10, pp. 811–822, 2004.

[97] T. Leutenegger and J. Dual, “Detection of defects in cylindrical structures using a time reverse method and a finite-difference approach,” *Ultrasonics*, vol. 40, no. 1, pp. 721–725, 2002.

[98] N. Chakroun, M. A. Fink, and F. Wu, “Time reversal processing in ultrasonic nondestructive testing,” *Ultrasonics, Ferroelectrics, and Frequency Control, IEEE Transactions on*, vol. 42, no. 6, pp. 1087–1098, 1995.

[99] G. F. Edelmann, T. Akal, W. S. Hodgkiss, S. Kim, W. A. Kuperman, and H. C. Song, “An initial demonstration of underwater acoustic communication using time reversal,” *Oceanic Engineering, IEEE Journal of*, vol. 27, no. 3, pp. 602–609, 2002.

[100] G. F. Edelmann, H. Song, S. Kim, W. Hodgkiss, W. Kuperman, and T. Akal, “Underwater acoustic communications using time reversal,” *Oceanic Engineering, IEEE Journal of*, vol. 30, no. 4, pp. 852–864, 2005.

[101] W. Higley, P. Roux, W. Kuperman, W. Hodgkiss, H. Song, T. Akal, and M. Stevenson, “Synthetic aperture time-reversal communications in shallow water: Experimental demonstration at sea,” *The Journal of the Acoustical Society of America*, vol. 118, no. 4, pp. 2365–2372, 2005.

[102] O. Dorn, "Time-reversal and the adjoint imaging method with an application in telecommunication," in *Inverse Problems and Imaging*, pp. 135–170, Springer, 2008.

[103] L. A. Sheridan, G. S. Kovener, B. Ostrofsky, and H. J. Nebelsiek, "Ultrasonic testing device and method," Oct. 11 1977. US Patent 4,052,887.

[104] G. Lerosey, J. De Rosny, A. Tourin, A. Derode, G. Montaldo, and M. Fink, "Time reversal of electromagnetic waves," *Physical review letters*, vol. 92, no. 19, p. 193904, 2004.

[105] M. Fink, D. Cassereau, A. Derode, C. Prada, P. Roux, M. Tanter, J.-l. Thomas, and F. Wu, "Time-reversed acoustics," *Reports on progress in Physics*, vol. 63, no. 12, p. 1933, 2000.

[106] L. Borcea, G. Papanicolaou, C. Tsogka, and J. Berryman, "Imaging and time reversal in random media," *Inverse Problems*, vol. 18, no. 5, p. 1247, 2002.

[107] G. Micolau, M. Saillard, and P. Borderies, "Dort method as applied to ultrawideband signals for detection of buried objects," *Geoscience and Remote Sensing, IEEE Transactions on*, vol. 41, no. 8, pp. 1813–1820, 2003.

[108] C. Prada, S. Manneville, D. Spoliansky, and M. Fink, "Decomposition of the time reversal operator: Detection and selective focusing on two scatterers," *The Journal of the Acoustical Society of America*, vol. 99, no. 4, pp. 2067–2076, 1996.

[109] D. Clorennec, J. De Rosny, J.-G. Minonzio, C. Prada, M. Fink, T. Folégot, P. Billand, S. Tauvry, S. Hibral, and L. Bernière, "First tests of the dort method at 12 khz in a shallow water waveguide," in *Oceans 2005-Europe*, vol. 2, pp. 1205–1209, IEEE, 2005.

[110] H. Lev-Ari and A. Devancy, "The time-reversal technique re-interpreted: Subspace-based signal processing for multi-static target location," in *Sensor Array and Multichannel Signal Processing Workshop. 2000. Proceedings of the 2000 IEEE*, pp. 509–513, IEEE, 2000.

[111] A. Devaney, "Time reversal imaging of obscured targets from multistatic data," *Antennas and Propagation, IEEE Transactions on*, vol. 53, no. 5, pp. 1600–1610, 2005.

[112] M. Davy, J.-G. Minonzio, J. de Rosny, C. Prada, and M. Fink, "Influence of noise on subwavelength imaging of two close scatterers using time reversal method: Theory and experiments," *Progress In Electromagnetics Research*, vol. 98, pp. 333–358, 2009.

[113] E. A. Marengo, F. K. Gruber, and F. Simonetti, "Time-reversal music imaging of extended targets," *Image Processing, IEEE Transactions on*, vol. 16, no. 8, pp. 1967–1984, 2007.

[114] A. Baussard and T. Boutin, "Time-reversal rap-music imaging," *Waves in Random and Complex Media*, vol. 18, no. 1, pp. 151–160, 2008.

[115] C. Prada, E. Kerbrat, D. Cassereau, and M. Fink, "Time reversal techniques in ultrasonic nondestructive testing of scattering media," *Inverse Problems*, vol. 18, no. 6, p. 1761, 2002.

[116] S. Flax and M. O'Donnell, "Phase-aberration correction using signals from point reflectors and diffuse scatterers: Basic principles," *Ultrasonics, Ferroelectrics, and Frequency Control, IEEE Transactions on*, vol. 35, no. 6, pp. 758–767, 1988.

[117] R. Mallart and M. Fink, "Adaptive focusing in scattering media through sound-speed inhomogeneities: The van cittert zernike approach and focusing criterion," *The Journal of the Acoustical Society of America*, vol. 96, no. 6, pp. 3721–3732, 1994.

[118] R. Mittra and T. Habashy, "Theory of wave-front-distortion correction by phase conjugation," *JOSA A*, vol. 1, no. 11, pp. 1103–1109, 1984.

[119] C. Prada, F. Wu, and M. Fink, "The iterative time reversal mirror: A solution to self-focusing in the pulse echo mode," *The Journal of the Acoustical Society of America*, vol. 90, no. 2, pp. 1119–1129, 1991.

[120] M. Fink, "Time-reversal mirrors," *Journal of Physics D: Applied Physics*, vol. 26, no. 9, p. 1333, 1993.

[121] C. Prada, J.-L. Thomas, and M. Fink, "The iterative time reversal process: Analysis of the convergence," *The Journal of the Acoustical Society of America*, vol. 97, no. 1, pp. 62–71, 1995.

[122] H. Tortel, G. Micolau, and M. Saillard, "Decomposition of the time reversal operator for electromagnetic scattering," *Journal of Electromagnetic Waves and Applications*, vol. 13, no. 5, pp. 687–719, 1999.

[123] E. Kerbrat, C. Prada, D. Cassereau, and M. Fink, "Ultrasonic nondestructive testing of scattering media using the decomposition of the time-reversal operator," *Ultrasonics, Ferroelectrics, and Frequency Control, IEEE Transactions on*, vol. 49, no. 8, pp. 1103–1113, 2002.

[124] M. E. Yavuz and F. L. Teixeira, "Full time-domain dort for ultrawideband electromagnetic fields in dispersive, random inhomogeneous media," *Antennas and Propagation, IEEE Transactions on*, vol. 54, no. 8, pp. 2305–2315, 2006.

[125] E. Barbieri and M. Meo, "Time reversal dort method applied to nonlinear elastic wave scattering," *Wave Motion*, vol. 47, no. 7, pp. 452–467, 2010.

[126] R. O. Schmidt, "Multiple emitter location and signal parameter estimation," *Antennas and Propagation, IEEE Transactions on*, vol. 34, no. 3, pp. 276–280, 1986.

[127] H. Krim and M. Viberg, "Two decades of array signal processing research: the parametric approach," *Signal Processing Magazine, IEEE*, vol. 13, no. 4, pp. 67–94, 1996.

[128] L. C. Godara, *Smart antennas*. CRC press, 2004.

[129] M. D. Zoltowski, G. M. Kautz, and S. D. Silverstein, "Beamspace root-music," *Signal Processing, IEEE Transactions on*, vol. 41, no. 1, p. 344, 1993.

[130] B. D. Rao and K. Hari, "Performance analysis of root-music," *Acoustics, Speech and Signal Processing, IEEE Transactions on*, vol. 37, no. 12, pp. 1939–1949, 1989.

[131] R. Roy and T. Kailath, "Esprit-estimation of signal parameters via rotational invariance techniques," *Acoustics, Speech and Signal Processing, IEEE Transactions on*, vol. 37, no. 7, pp. 984–995, 1989.

[132] J. Foutz, A. Spanias, and M. K. Banavar, "Narrowband direction of arrival estimation for antenna arrays," *Synthesis Lectures on Antennas*, vol. 3, no. 1, pp. 1–76, 2008.

[133] Y. Bresler and A. Macovski, "Exact maximum likelihood parameter estimation of superimposed exponential signals in noise," *Acoustics, Speech and Signal Processing, IEEE Transactions on*, vol. 34, no. 5, pp. 1081–1089, 1986.

[134] F. Scholz, "Maximum likelihood estimation," *Encyclopedia of Statistical Sciences*, 1985.

[135] A. J. Devaney, "1super-resolution processing of multi-static data using time reversal and music," 2000.

[136] C. W. Therrien, *Discrete random signals and statistical signal processing*. Prentice Hall PTR, 1992.

[137] P. Stoica and R. L. Moses, *Introduction to spectral analysis*, vol. 1. Prentice hall Upper Saddle River, 1997.

[138] H. Wang and M. Kaveh, “Coherent signal-subspace processing for the detection and estimation of angles of arrival of multiple wide-band sources,” *Acoustics, Speech and Signal Processing, IEEE Transactions on*, vol. 33, no. 4, pp. 823–831, 1985.

[139] H. Hung and M. Kaveh, “Focussing matrices for coherent signal-subspace processing,” *Acoustics, Speech and Signal Processing, IEEE Transactions on*, vol. 36, no. 8, pp. 1272–1281, 1988.

[140] F. K. Gruber, E. A. Marengo, and A. J. Devaney, “Time-reversal imaging with multiple signal classification considering multiple scattering between the targets,” *The Journal of the Acoustical Society of America*, vol. 115, no. 6, pp. 3042–3047, 2004.

[141] M. Born and E. Wolf, *Principles of optics: electromagnetic theory of propagation, interference and diffraction of light*. Cambridge university press, 1999.

[142] C. Prada and J.-L. Thomas, “Experimental subwavelength localization of scatterers by decomposition of the time reversal operator interpreted as a covariance matrix,” *The Journal of the Acoustical Society of America*, vol. 114, no. 1, pp. 235–243, 2003.

[143] T. Miwa and I. Arai, “Super-resolution imaging for point reflectors near transmitting and receiving array,” *Antennas and Propagation, IEEE Transactions on*, vol. 52, no. 1, pp. 220–229, 2004.

[144] M. Born and E. Wolf, *Principles of optics: electromagnetic theory of propagation, interference and diffraction of light*. CUP Archive, 2000.

[145] J. G. Berryman, L. Borcea, G. C. Papanicolaou, and C. Tsogka, “Statistically stable ultrasonic imaging in random media,” *The Journal of the Acoustical Society of America*, vol. 112, no. 4, pp. 1509–1522, 2002.

[146] T.-W. Pan, C.-W. Hsue, and J.-F. Huang, “Time-domain reflectometry using arbitrary incident waveforms,” *Microwave Theory and Techniques, IEEE Transactions on*, vol. 50, no. 11, pp. 2558–2563, 2002.

[147] Y.-J. Shin, E. J. Powers, T.-S. Choe, C.-Y. Hong, E.-S. Song, J.-G. Yook, and J. B. Park, “Application of time-frequency domain reflectometry for detection and localization of a fault on a coaxial cable,” *Instrumentation and Measurement, IEEE Transactions on*, vol. 54, no. 6, pp. 2493–2500, 2005.

[148] L. Abboud, A. Cozza, and L. Pichon, “A noniterative method for locating soft faults in complex wire networks,” *Vehicular Technology, IEEE Transactions on*, vol. 62, no. 3, pp. 1010–1019, 2013.

[149] L. Abboud, A. Cozza, and L. Pichon, “A matched-pulse approach for soft-fault detection in complex wire networks,” *Instrumentation and Measurement, IEEE Transactions on*, vol. 61, no. 6, pp. 1719–1732, 2012.

[150] G. Cerri, R. De Leo, L. Della Nebbia, S. Pennesi, V. M. Primiani, and P. Russo, “Fault location on shielded cables: Electromagnetic modelling and improved measurement data processing,” *IEE Proceedings-Science, Measurement and Technology*, vol. 152, no. 5, pp. 217–226, 2005.

[151] R. A. Horn and C. R. Johnson, *Matrix analysis*. Cambridge university press, 2012.

[152] P. B. Kahn, *Mathematical methods for scientists and engineers: linear and nonlinear systems*. Courier Corporation, 2004.

[153] D. W. Ricker, *Echo signal processing*, vol. 725. Springer Science & Business Media, 2012.

[154] F. Gorunescu, *Data Mining: Concepts, models and techniques*, vol. 12. Springer Science & Business Media, 2011.

[155] M. E. Yavuz and F. L. Teixeira, "Ultrawideband microwave sensing and imaging using time-reversal techniques: A review," *Remote Sensing*, vol. 1, no. 3, pp. 466–495, 2009.

[156] D. Ciuonzo, G. Romano, and R. Solimene, "Performance analysis of time-reversal music," *Signal Processing, IEEE Transactions on*, vol. 63, no. 10, pp. 2650–2662, 2015.

[157] A. J. Devaney, "Super-resolution processing of multi-static data using time reversal and music," *J. Acoust. Soc. Am*, 2000.

[158] W. GAO, X. WANG, and B. Wang, "Review of time reversal imaging techniques,"

[159] E. W. Weisstein, *CRC concise encyclopedia of mathematics*. CRC press, 2002.

ÉCOLE DOCTORALE
Physique et ingénierie : électrons, photons, sciences du vivant (EOBE)

Titre : Techniques d'imagerie pour la localisation des défauts non francs dans différents réseaux de câblage.

Mots clés : Réseaux de câblage, Défauts non francs, Méthode DORT, méthode TR-MUSIC

Résumé : Les câbles électriques sont partout dans de nombreux domaines où le transfert d'énergie et de l'information est nécessaire pour garantir une bonne performance d'un système. Un jour ou l'autre, un câble dans un réseau va montrer des signes de faiblesse qui conduit à l'apparition de défauts soit francs ou non francs. Malgré le fait que plusieurs méthodes de diagnostic de fil électriques et non-électriques ont été étudiés et mis au point au cours des dernières décennies, les techniques basées réflectométrie-ont fourni des résultats efficaces avec des défauts difficiles, mais ont montré moins fiables à chaque fois que des erreurs légères sont traitées.

Basé sur un concept radicalement différent, la méthode DORT, développé à l'origine en acoustique a récemment été transposée à la propagation à ondes guidées, par exemple, les réseaux de fils, et montré pour détecter avec précision et localiser les défauts mous simples même dans les configurations de réseau complexes. D'autre part, plusieurs défauts ne peuvent être résolus séparément. Désormais une formulation alternative du DORT basée sur un système de mise à jour est proposée. Notamment, cette nouvelle approche, appelée EDORT, a permis de localiser plusieurs défauts non francs dans différents réseaux de câblage et a permis l'extraction de l'intensité de chaque défaut uniquement.

D'autre part, ces méthodes dans le domaine temporel comptent sur la disponibilité de potentiellement importantes largeurs de bande, afin de créer les conditions pour la résolution spatiale. Retournement temporel (TR) classement de signaux multiples, également connu sous le TR-MUSIC, assurée sous-longueur d'onde résolution spatiale des emplacements des défauts tout en travaillant sur une base mono-fréquence. TR-MUSIC a montré une bonne performance dans la localisation unique, ainsi que de multiples défauts non francs dans différentes configurations de réseau. Il a également montré pour permettre la récupération du coefficient de réflexion de chaque défaut séparément.

Title : Imaging techniques for soft fault location in different wiring networks

Keywords : Wiring networks, Soft faults, DORT method, TR-MUSIC method

Abstract : Electrical cables are everywhere in many fields where the transfer of energy and information is necessary to guarantee a good performance of a system. One day or another, a cable in a network will show signs of weakness leading to the appearance of either hard or soft faults. Despite the fact that several electric and non-electric wire diagnosis methods have been studied and developed throughout the last few decades, reflectometry-based techniques have been providing effective results with hard faults, but have shown to be less reliable whenever soft faults are addressed.

Based on a radically different concept, the DORT method, originally developed in acoustics was recently transposed to guided-wave propagation, e.g., wire networks, and shown to precisely detect and locate single soft faults even within complex network configurations. On the other hand, multiple faults cannot be resolved separately. Henceforth an alternative formulation of the DORT based on an updating scheme is proposed. Notably, this novel approach, referred to as EDORT, allowed locating multiple soft faults in different wiring networks and enabled extracting the intensity of each fault solely.

On the other hand, such time domain methods rely on the availability of potentially large bandwidths, in order to create the conditions for spatial resolution. Time-reversal (TR) multiple signal classification, also known as TR-MUSIC, ensured sub-wavelength spatial resolution of the faults' locations while working on a single-frequency basis. TR-MUSIC has shown a good performance in locating single as well as multiple soft faults in different network configurations. It has also shown to allow retrieving the reflection coefficient of each fault separately.